THE PREDICTION OF TURBULENT STABLY-STRATIFIED BUOYANT FLOWS

COSTAS PAPADIMITRIOU

DIPL. ENG. , M.Sc.

Thesis submitted for the degree of

Doctor of Philosophy

In the University of London

and for the

Diploma of Membership of the Imperial College

Imperial College of Science and Technology

(Department of Mechanical Engineering)

October, 1985

ABSTRACT

Theoretical research work is presented on the prediction of turbulent buoyant stably-stratified flows. The work is based on the numerical solution of the governing mean field and turbulence transport equations by the finite difference method. The final aim of the work is the prediction of the two-dimensional buoyant vertical jet in a shallow water body of large horizontal extent. In order to fulfill this aim a series of intermediate tasks had to be accomplished.

Numerical prediction of buoyant flows is hampered by numerical instabilities associated with the buoyancy coupling of the momentum and temperature or species concentration equations. The source and mechanism of instability were investigated and practical measures adopted which allowed stable solutions for all buoyant flows examined. The numerical accuracy of the finite difference method was also improved by the introduction of a third order accurate convection discretisation scheme (QUICK).

Two turbulence closures were applied in this work. The two equation k-ϵ model extended for buoyant flows and the Reynolds stress-scalar flux transport equation model of Launder, Reece and Rodi (1975) and Gibson and Launder (1978). The performance of the models was initially tested in the prediction of two non-buoyant recirculating flows. The second moment closure improved the mean velocity field predictions.

Predictions are also presented for a series of buoyant and non-buoyant flows closely related to the vertical

buoyant discharge in shallow water: for the buoyant surface jet, the internal hydraulic jump, the vertical non-buoyant discharge in shallow water and for the buoyant jet impinging on the free surface of a semi-infinite water body. Both turbulence models predict satisfactorily the buoyant surface jet and the internal hydraulic jump though the second moment closure produced significant improvements. The vertical non-buoyant discharge was equally well predicted by both models. Numerical problems did not allow the application of the transport equation model to the vertical buoyant jet in a shallow or semi-infinite water body and these flows were calculated by the buoyancy extended k-ϵ model only; for both flows promising agreement with experimental data was obtained.

Predictions of the vertical buoyant jet in shallow water reproduced the main features of the flow observed in experiments. The dominance of the discharge Froude number on the evolution of the flow was succesfully demonstrated and both forms of the flow, stable and unstable, could be predicted. A model of the flow is suggested based on the predictions and the limited amount of data available. This model is compared with the one suggested by Jirka and Harleman (1979) and substantial differences emerge concerning the interpretation of the stable form.

ACKNOWLEDGEMENTS

I wellcome the opportunity to express my gratitude to all those who provided help, in many different ways, during the period of my Ph.D. research.

Firstly I would like to thank my supervisor, Dr J.J. McGuirk who initiated the work and who was throughout my studies a constant source of advice, constructive criticism, guidance and optimism. I should also like to thank Mr A. Gorashi, Mr J. De Palma, Dr A. Taylor and Dr B. Yunis for their useful discussion of parts of my work of common interest.

I wellcome the opportunity to acknowledge the financial support provided by the Greek Government for the first two years of my studies. In particular, I would like to thank the staff of the Greek state scholarship foundation for their assistance and cooperation. I also wellcome the opportunity to acknowledge the financial support provided by the British council during the third year of my studies.

TABLE OF CONTENTS

ABSTRACT I

ACKNOWLEDGMENTS.....III

TABLE OF CONTENTS.....IV

LIST OF FIGURES.....VII

NOMENCLATURE.....XV

CHAPTER 1 : INTRODUCTION 1

1.1. Vertical buoyant discharges in environmental shallow water bodies 2
1.2. The aspect of the problem dealt with here.....6
Previous work 7
1.3. Non-buoyant 2-D vertical jet in shallow water.....7
1.3.1. Experimental work 9
1.3.2. Previous numerical predictions.....12
1.4. Buoyant vertical 2-D jet in shallow water.....14
1.4.1. Description of the flow and previous experimental work 14
1.4.2. Stabiltiy analysis of Jirka, Lee and Harleman (1979). 20
1.4.3. Related experimental work.....22
1.4.4. Previous numerical predictions.....22
1.5. Assesment: objectives and strategy of present contribution 23
1.6. Outline of the thesis 26

CHAPTER 2 : THE MATHEMATICAL MODEL.....28

2.1. Mean flow equations 30
2.2. The turbulence closure problem.....34
2.2.1. The k-ϵ model 38
2.2.2. The RSFT model 40
2.3. Boundary conditions 47
2.4. Numerical solution of the governing PDE's.....51
2.4.1. The QUICK discretisation.....53
2.4.2. The buoyancy related instability.....57
2.4.3. The incorporation of the RSFT model in the computer code.....61

CHAPTER 3 : A STUDY OF THE PERFORMANCE OF THE RST MODEL IN TWO NON-BUOYANT RECIRCULATING FLOWS. 63

3.1. Introduction (the flows considered).....64
3.2. Computational details, boundary conditions and numerical tests 69
3.3. Results and discussion 77
3.3.1. Step flow 77
3.3.2. Disc flow 83
3.4. Summary.....87

CHAPTER 4 : THE PREDICTION OF THE BUOYANT SURFACE LAYER 89

4.1. Physical phenomena occuring in buoyant surface layers 91
4.2. The prediction of the fully entraining buoyant surface jet..... 95
4.2.1. The mathematical model 96
4.2.2. Computational details 100
4.2.3. Results and discussion 102
4.3. The prediction of the internal hydraulic jump.....107
4.3.1. Computational details 108
i . Numer. instab. problems 108
ii . Boundary conditions 110
iii. Grid and CPU times 111
4.3.2. Results and discussion 112
i . k-ϵ predictions 112
ii. RSFT predictions 114
4.4. Conclusions.....116

CHAPTER 5 : THE PREDICTION OF THE VERTICAL 2-D NON-BUOYANT DISCHARGE IN SHALLOW WATER.....118

5.1. Computational details 120
Solution domain and boundary conditions.....120
Grid 122
5.2. k-ϵ results and discussion 124
Centreline velocity decay 124
Vertical velocity profiles 125
Horizontal velocity profiles 126
Surface elevation 127
Streamline pattern, recirculation strength 130
5.3. Transport equation results and discussion 133
5.4. Conclusions.....137

CHPTER 6 : THE PREDICTION OF THE VERTICAL BUOYANT JET IN SHALLOW WATER 139

6.1. The performance of the RSFT model in confined vertical buoyant jet flows 140
6.2. The prediction of the vertical buoyant jet experiments of Pryputniewicz and Bowley (1975).....146
6.3. The simulation of the experimental situation.....154
6.4. Axisymmetric discharge H/D=11.1 159
6.5. A stable shallow axisymmetric discharge (H/D=2.2, Fd=8) 170
6.6. An unstable axisymmetric discharge (H/D=1Ø, Fd=2Ø5) 175
6.7. A plane unstable discharge (H/D=19Ø.6, Fd=8Ø) 178
6.8. A model of the flow based on the predictions; comparisons with the model of Jirka e.a. 181
6.9. Summary.....187

CHAPTER 7 : ACHIEVEMENTS, CONCLUSIONS AND SUGGESTIONS FOR FUTURE WORK 190

7.1. Outline of the work, achievements and conclusions 191
7.2. Suggestions for future work 197

APPENDIX A1 : THE SET OF GOVERNING PARTIAL DIFFERENTIAL EQUATIONS 201

1.The mean variable equations..... 203
2.The buoyancy extended k-ϵ model 204
3.The transport equation model..... 205

APPENDIX A2 : THE QUICK DISCRETISATION SCHEME 211

A2.1. A mathematical definition of QUICK 213
A2.2. The treatment of negative coefficients in QUICK 218
A2.3. The laminar flow in a plane channel with a symmetric contraction 221
A2.4. Wiggles in QUICK predictions. "Remedial" measures..... 224

APPENDIX A3 : THE BUOYANCY RELATED INSTABILITY PROBLEM 233

A3.1. Analytical study of unstable error growth..... 235
Stability through under-relaxation 239
Transient solution 240
A3.2. Simultaneous solution of the momentum and temperature equation 241
A3.3. Application of the simultaneous solution algorithm:..... 244
i .The stratified convection problem 244
ii.The buoyancy driven square cavity laminar flow 247
A3.4. Small amplitude persistent oscillations..... 250
A3.5. The practice adopted in this project..... 254

REFERENCES..... 259

FIGURES 272

LIST OF FIGURES

FIGURE 1.1 : Non-buoyant plane jet. Flow configuration. Page 273.

FIGURE 1.2 : Non-buoyant plane jet with high initial momentum. Page 273.

FIGURE 1.3 : Non-buoyant plane jet. Flow-pattern suggested by Jirka and Harleman (1979). Page 273.

FIGURE 1.4 : Buoyant vertical jet in shallow water. Temperature profiles for three axisymmetric configurations. Page 274.

FIGURE 1.5 : Buoyant vertical jet in shallow water. Temperature profiles for two plane configurations. Page 274.

FIGURE 1.6 : Buoyant vertical jet in shallow water: definition of flow field configurations. Page 275.

FIGURE 2.1 : Control volumes for the scalar fluxes and the shear stress. Page 276.

FIGURE 3.1 : Flow configurations considered.
(A): Plane single sided expansion.
(B): Axisymmetric disc blockage in a pipe.
Page 277.

FIGURE 3.2 : Zones of the flow-domain where upwind discretisation was applied. Page 277.

FIGURE 3.3 : Grid independence checks, step-flow, k-ϵ predictions. Page 278.

FIGURE 3.4 : Grid independence checks, step-flow, RST prediction. Page 279.

FIGURE 3.5 : Plane single-sided step. Definition of wall effects function f. Page 279.

FIGURE 3.6 : Grid independence checks, disc-flow, k-ϵ predictions. Page 280.

FIGURE 3.7 : Disc-flow. Selective refinement of the grid from the (24*29) level to the (42*50) level. Page 281.

FIGURE 3.8 : Recirculation zone, step-flow. Page 281.

FIGURE 3.9 : Axial velocity profiles, step-flow. Page 282.

FIGURE 3.10: Experimental data of Pronchick et al (1983). Longitudinal velocity profiles before and past reattachment. Page 283.

FIGURE 3.11: Static pressure coefficient at the expansion wall of the channel. Page 283.

FIGURE 3.12: Cross-sectional maximum value of turbulence kinetic energy. Step-flow. Page 284.

FIGURE 3.13: Turbulence kinetic energy profiles, step-flow. Page 284.

FIGURE 3.14: Axial normal Reynolds stress ($\overline{u^2}$) profiles. Step-flow. Page 285.

FIGURE 3.15: Shear stress profiles. Step-flow. Page 286.

FIGURE 3.16: Cross-sectional maxima of $\overline{u^2}$, $\overline{v^2}$, $\overline{w^2}$ and k. Step-flow. Page 287.

FIGURE 3.17: Recirculation zone, disc-flow. Page 288.

FIGURE 3.18: Axial velocity profile at x/Rp=Ø.4, disc-flow. Page 288.

FIGURE 3.19: Centreline velocity development, disc-flow. Page 289.

FIGURE 3.2Ø: Turbulence kinetic energy profiles, disc-flow. Page 289.

FIGURE 3.21: Centreline turbulence kinetic energy, disc-flow. Page 29Ø.

FIGURE 3.22: Normal (P_N) and shear stress (P_S) contribution to the production of turbulence kinetic energy at a cross-section close to the stagnation point. Disc-flow. Page 29Ø.

FIGURE 3.23: Turbulence anisotropy along the axis of symmetry. Disc-flow. Page 291.

FIGURE 4.1 : Sketch of the experimental apparatus. Experiments of Chu and Baddour (1984). Page 292.

FIGURE 4.2 : Parametric study of the form of the production term in the dissipation rate equation. Surface jet, Fd=12. Page 292.

FIGURE 4.3 : Surface jet experiments of Chu and Baddour (1984). Experimental data compliance with the integral constraints of the flow. Page 292.

FIGURE 4.4 : Londitudinal development of the flow. Surface jet, Fd=12. Surface velocity and buoyancy, jet-width and mass-flowrate in the layer. Page 293.

FIGURE 4.5 : Relation of the cross-sectional Richardson

number with the entrainment coefficient. Surface jet, Fd=12. Page 293.

FIGURE 4.6 : Velocity profiles. Surface jet, Fd=12. Page 294.

FIGURE 4.7 : Mean buoyancy profiles. Surface jet, Fd=12. Page 294.

FIGURE 4.8 : Vertical component ($\overline{v^2}/k$) profiles for various Richardson numbers. Surface jet, Fd=12. Page 295.

FIGURE 4.9 : Free surface effects function f. Surface jet Fd=12. Page 295.

FIGURE 4.10: Prandtl number (σ_T) across the layer. Surface jet, Fd=12. Page 295.

FIGURE 4.11: Layer width . Surface jet, Fd=12. Page 296.

FIGURE 4.12: Comparison between k-ϵ and RSFT predictions. Mixing layer, Fd=2.3. Page 296.

FIGURE 4.13: Velocity profiles. Mixing layer, Fd=2.3. Page 296.

FIGURE 4.14: Mean buoyancy profiles. Mixing layer, Fd=2.3. Page 297.

FIGURE 4.15: Longitudinal development of the cross-sectional peak value of $\overline{u^2}$. Mixing layer, Fd=2.3. Page 297.

FIGURE 4.16: Axial normal stress profiles. Mixing layer, Fd=2.3. Page 298.

FIGURE 4.17: Longitudinal development of the cross-sectional peak value of $\overline{b^2}$. Mixing-layer, Fd=2.3. Page 298.

FIGURE 4.18: Longitudinal layer development. Centreline and boundaries. Page 298.

FIGURE 4.19: Internal Hydraulic jump. Solution domain and boundary conditions. Page 299.

FIGURE 4.20: Surface jet, Fd=12. Comparison of the prediction of two parameters using elliptic and parabolic codes. Surface velocity and jet-width. Page 299.

FIGURE 4.21: Internal hydraulic jump, Fd=4.9, k-ϵ prediction. Streamline pattern. Page 300.

FIGURE 4.22: Internal Hydraulic jump, Fd=4.9, k-ϵ prediction. Velocity and mean buoyancy profiles. Page 301.

FIGURE 4.23: The influence of the downstream control on the evolution of a buoyant surface layer. Fd=6.39. Page 301.

FIGURE 4.24: Internal Hydraulic jump, Fd=4.9. Location of the limiting streamline. k-ϵ and RSFT predictions. Page 302.

FIGURE 4.25: Internal Hydraulic jump, Fd=4.9. Mean buoyancy profiles and interface of the layer. k-ϵ and RSFT predictions. Page 302.

FIGURE 4.26: Internal Hydraulic Jump, Fd=4.9. Turbulence anisotropy and Prandtl number across the layer. Page 302.

FIGURE 5.1 : 2-D vertical non-buoyant discharge in shallow water. Solution domain and boundary conditions. Page 303.

FIGURE 5.2 : The influence of the inlet turbulence intensity on the centreline velocity decay. Page 304.

FIGURE 5.3 : Grid independence checks. Plane discharge $V_{\emptyset}$=0.6 m/s, D=4 cm, H/D=10. Page 304.

FIGURE 5.4 : Symmetry plane velocity decay, plane configuration. Page 305.

FIGURE 5.5 : Centreline velocity decay, axisymmetric configuration. Page 305.

FIGURE 5.6 : Round discharge $V_{\emptyset}$=0.512 m/s, H/D=4, D=12.44 cm. Vertical velocity close to the axis of symmetry. Page 306.

FIGURE 5.7 : Vertical velocity profiles. Plane configuration. Page 307.

FIGURE 5.8 : Horizontal velocity profiles, plane configuration. Page 308.

FIGURE 5.9 : Horizontal velocity profiles, axisymmetric configuration. Page 308.

FIGURE 5.10: Surface shape, plane configuration. Page 309.

FIGURE 5.11: Round jet $V_{\emptyset}$=0.512 m/s, D=12.44 cm, H/D=4. Surface velocity evolution. Page 310.

FIGURE 5.12: Round jet $V_{\emptyset}$=0.512 m/s, D=12.44cm, H/D=4. Surface shape. Page 310.

FIGURE 5.13: Plane configuration, streamline patterns. Page 311.

FIGURE 5.14: Axisymmetric configuration, streamline patterns. Page 311.

FIGURE 5.15: Plane discharge, strength of the recirculation cell. Page 312.

FIGURE 5.16: Round jet RST prediction, the influence of the inlet shear stress profile on the centreline velocity decay. Page 312.

FIGURE 5.17: Round jet $V_{\emptyset}$=Ø.512 m/s, D=12.44 cm, H/D=4. Velocity profiles across the tank. Page 313.

FIGURE 5.18: Round jet, turbulence anisotropy along the axis of symmetry and beneath the surface. Page 313.

FIGURE 6.1 : Vertical buoyant jet in a shallow tank. Flow configuration and solution domain. Page 314.

FIGURE 6.2 : Vertical buoyant jet (Fd=5, H/D=1.6). Surface excess temperature and transverse temperature profiles. Page 315.

FIGURE 6.3 : Vertical buoyant jet (Fd=4, H/D=1Ø). RSFT and k-ϵ predictions. Centreline temperature. Page 316.

FIGURE 6.4 : Sketch of the experimental apparatus of Pryputniewicz and Bowley (1975). Solution domain. Page 316.

FIGURE 6.5 : Grid independence checks (Fd=4, H/D=1Ø). Page 317.

FIGURE 6.6 : Evolution of the solution (Fd=4, H/D=1Ø). Pages 317 and 318.

FIGURE 6.7 : Centreline velocity H/D=1Ø and Fd=2,4,8. Page 318.

FIGURE 6.8 : Centreline excess temperature H/D=1Ø and Fd=2,4,8. Page 319.

FIGURE 6.9 : Centreline velocity and excess temperature H/D=1Ø and Fd=2,4,8. Predictions of the integral analysis of Jirka et al. Page 32Ø.

FIGURE 6.1Ø: Temperature profiles close to the axis of symmetry, H/D=1Ø, Fd=2. Page 321.

FIGURE 6.11: Surface excess temperature, H/D=1Ø and Fd=2,4,8. Page 322.

FIGURE 6.12: Stability map of Jirka and Lee (1981). Axisymmetric geometry. Location of the predicted configurations. Page 323.

FIGURE 6.13: Solution domain for the buoyant vertical discharge in shallow water. Steady-state solutions. Page 323.

FIGURE 6.14: Evolution of the solution for the case H/D=11.1, Fd=46. Page 324.

FIGURE 6.15: Evolution of the solution for the case H/D=11.1, Fd=11Ø. Page 324.

FIGURE 6.16: Evolution of the temperature field for the case H/D=11.1, Fd=46. Page 325.

FIGURE 6.17: Predicted streamline patterns for four discharge Froude numbers: Fd=2Ø,46,66,11Ø with H/D=11.1. Steady-state solution approach. Page 326.

FIGURE 6.18: Predicted surface temperature for four discharge Froude numbers Fd=2Ø,46,66,11Ø with H/D=11.1. Steady-state solution approach. Page 327.

FIGURE 6.19: Predicted temperature profiles for four discharge Froude numbers Fd=2Ø,46,66,11Ø with H/D=11.1. Steady-state solution approach. Page 328.

FIGURE 6.2Ø: Predicted visible interface ($\Delta T/\Delta T_{Ø}$=3%) for four discharge Froude numbers Fd=2Ø,46,66,11Ø with H/D=11.1, Steady-state solution approach. Page 329.

FIGURE 6.21: Comparison of temperature field predictions with the experimental data H/D=11.1, Fd=46. Temperature profiles and visible interface. Page 33Ø.

FIGURE 6.22: Solution domain for the buoyant vertical jet in shallow water. True transient solution. Page 331.

FIGURE 6.23: Vertical buoyant jet in shallow water - stable form. Transient solution. Sketch of the predicted evolution of the flow. Page 331.

FIGURE 6.24: Stable discharge H/D=11.1, Fd=46, transient solution. Streamline pattern and location of the visible interface. Page 332.

FIGURE 6.25: H/D=11.1, Fd=46. Transient solution. Reattachment length as a function of time. Page 333.

FIGURE 6.26: H/D=11.1, Fd=46. A) Evolution of the predicted stream function profile at two radial locations. B) The influence of the tank length on the near-field temperature predictions. Page 334.

FIGURE 6.27: Steady-state approach calculations for the geometry H/D=2.2, D=2.54 cm. Streamline

patterns and temperature contours for Fd=8 and 10.4. Page 335.

FIGURE 6.28: Stable configuration Fd=8, H/D=2.2. Temperature field predictions. Page 336.

FIGURE 6.29: Stable discharge Fd=2.2, Fd=8, transient solution. Streamlines and temperature contours. Page 337.

FIGURE 6.30: Unstable discharge, H/D=10, Fd=205, transient solution. Streamlines and visible interface. Page 337.

FIGURE 6.31: Unstable plane discharge H/D=190.6, Fd=80. Streamlines and temperature contours. Page 338.

FIGURE 6.32: H/D=190.6, Fd=80. Evolution of the solution: Location of the reattachment point and total circulation in the tank. Page 339.

FIGURE 6.33: Unstable discharge H/D=190.6, Fd=80. Temperature field predictions. Page 340.

FIGURE 6.35: Unstable discharge, sketch . Mixed water re-entrainment. Page 340.

FIGURE 6.35: Stable discharge. Sketch. Dye-trace interface shape observed in the experiments. Page 340.

FIGURE A1.1: Coordinate system. Page 341.

FIGURE A2.1: Scalar variable control volume. Page 342.

FIGURE A2.2: Plane channel with a symmetric contraction, flow configuration and solution domain. Page 342.

FIGURE A2.3: Streamline pattern at low Reynolds numbers, Re=1,10. Page 342.

FIGURE A2.4: Axial velocity profiles at two Reynolds numbers, Re=10, 500. Page 343.

FIGURE A2.5: Streamline pattern at high Reynolds numbers, Re=333, 500. Page 343.

FIGURE A2.6: Size of the corner eddy, QUICK and HYBRID predictions for a 42*40 grid. Page 344.

FIGURE A2.7: Grid independence study, size of the corner eddy. Page 344.

FIGURE A2.8: One-dimensional convection-diffusion of a conserved scalar. Wiggles in numerical predictions, Quick and UD. Page 345.

FIGURE A2.9: Wiggles in QUICK solutions. Page 345.

FIGURE A2.1Ø: U-velocity control volume. Page 346.

FIGURE A2.11: Retardation of convergence due to QUICK numerical problems. The mixed QUICK-Upwind scheme. Page 346.

FIGURE A3.1: Horizontal convection with stable stratification. Page 347.

FIGURE A3.2: Horizontal convection with stable stratification, coupled equations, diverging iteration path. Page 347.

FIGURE A3.3: Local simultaneous solution of the vertical momemtum and temperature equations. Control volumes involved. Page 347.

FIGURE A3.4: Simultaneous solution of momentum and temperature equations. The Newton-Raphson method. Page 348.

FIGURE A3.5: The buoyancy driven square cavity laminar flow. Solution domain and boundary conditions. Page 348.

FIGURE A3.6: Convergence rate of buoyant and non-buoyant solutions. Page 349.

FIGURE A3.7: Mixing layer Fd=2.3. Static under-relaxation $r_U=r_V=Ø.15$. Convergence rate. Page 349.

FIGURE A3.8: Mixing layer, Fd=2.3. Evolution of the solution over a large number of iterations. Page 35Ø.

FIGURE A3.9: Mixing layer, Fd=2.3. Local Continuity error distribution. Page 351.

NOMENCLATURE

1) Governing Partial Differential equations

B : Mean buoyancy $B=\Delta\rho/\rho_a$

b : Buoyancy fluctuations

$\overline{b^2}$: Variance of buoyancy fluctuations

c_1, c_2, c_3 : Pressure-strain model constants (RSFT)

c_1', c_2' : Constants of the wall or free surface corrections of the pressure-strain model (RSFT)

c_{1T}, c_{2T}, c_{3T} : Pressure-buoyancy gradient correlation model constants (RSFT)

c_{1T}' : Constant of the wall or free surface correction of the pressure-buoyancy gradient model (RSFT)

c_w : Wall effects function proportionality constant

c_{ϵ_1}, c_{ϵ_2} : ϵ equation constants (RSFT or k-ϵ)

c_s, c_s', c_{TT}, c_ϵ : Diffusion constants in $\overline{u_i u_j}$, $\overline{u_i b}$, ϵ and $\overline{b^2}$ PDE's (RSFT)

c_μ : Constant shear stress ratio $|\overline{uv}|/k$ in near-wall local equilibrium turbulence

D_{bb} : Diffusion terms in the PDE for $\overline{b^2}$ (RSFT)

D_{ib} : Diffusion terms in the PDE for $\overline{u_i b}$ (RSFT)

D_{ij} : Diffusion terms in the PDE for $\overline{u_i u_j}$ (RSFT)

D_ϵ : Diffusion terms in the PDE for ϵ (RSFT)

E : Wall roughness parameter

f : The wall or free surface effects correction function f

G : Buoyancy production/destruction of k

G_{ib} : Buoyancy production/destruction of $\overline{u_i b}$

G_{ij} : Buoyancy production/destruction of $\overline{u_i u_j}$

g_i : Acceleration of gravity vector (g_1, g_2, g_3)

k : Turbulence kinetic energy

l : Large scale eddies, length scale

P : Static pressure minus the hydrostatic pressure at a reference density

P : In turbulence equations, the stress - mean rate of strain production of k

P_{bb} : The scalar flux - mean buoyancy gradient production of b^2

P_{ib} : The mean - field production of $\overline{u_i b}$

P_{ij} : The stress - mean rate of strain production of $\overline{u_i u_j}$

p : Pressure fluctuations

R_T : ratio of the decay time scale characterizing the scalar fluctuations to that characterizing the velocity fluctuations (RSFT)

R_t : Turbulence Reynolds number

T : Mean temperature

t : time, also used as the time scale of the large scale eddies and for temperature fluctuations

U_i : Mean velocity component in the x_i direction ($U_1=U, U_2=V, U_3=W$)

u_i : U_i velocity fluctuations

$\tilde{u}$: velocity scale for the large scale eddies

u_T : skin friction velocity

$\overline{u_i b}$: Turbulent scalar flux

$\overline{u_i^2}$: Normal Reynolds stress

$\overline{u_i u_j}$: Reynolds stresses in general

x_i : Cartesian coordinate directions ($x_1=x, x_2=y, x_3=z$)

x_i^+ : Non-dimensionalized distance from a wall vertical to the direction x_i , $x_i^+ = x_i * u_T/\nu$

x_n : Distance from a wall or a free surface denoted by n

β : densimetric expansion coefficient

β_{av} : Average densimetric expansion coefficient between the maximum and minimum temperatures occuring in the flow-domain

Δx_i : Grid spatial increment in the i direction

δ_{ij} : The Kronecker delta function

ϵ : The dissipation rate of k

ϵ_{bb} : The dissipation rate of $\overline{b^2}$

ϵ_{ib} : The dissipation rate of $\overline{u_i b}$

ϵ_{ij} : The dissipation rate of $\overline{u_i u_j}$

η : Kolmogorov eddies length scale

κ : Von-Karman wall constant

ν : Molecular kinematic viscosity

ν_t : Turbulent kinematic viscosity (k-ϵ)

Π_{ib} : The pressure-buoyancy gradient correlation

Π_{ij} : The pressure-strain correlation

ρ : Fluid density

ρ_a : Ambient fluid density

σ_B : Molecular diffusion Prandtl number

σ_T : Turbulent diffusion Prandtl number, scalar variables

σ_k : Turbulent diffusion Prandtl number for k (k-ϵ)

σ_ϵ : Turbulent diffusion Prandtl number for ϵ (k-ϵ)

τ : Kolmogorov eddies time scale

2) Discretisation and Linearization of PDE's

AP : Centre-node coefficient of the finite difference algebraic equations resulting from the discretisation and linearization of each flow PDE

AL : Left-node value coefficient in the finite difference equation (similarly AN, AS, AR)

ALL : Left-left node value coefficient in the finite difference equation (similarly ANN, ASS, ARR). Associated with QUICK discretisation

CS : Convective sensitivity of a discretisation scheme

Gr : Grashof number of the flow

Pc : Cell Peclet number

Pc_x, Pc_y : Cell Peclet numbers at a node in the x and y direction of the co-ordinate system respectively

$r'_F(x,y)$: Spatially varying under-relaxation factor resulting from the false transient solution method in buoyant flow calculations

Su : Source term in the finite difference equation

ϵ_T : Local perturbation of the temperature field of a converged buoyant flow solution

$[A]$: The finite difference coefficient matrix

$[\Phi]^n$: The variable Φ values in a matrix form at the n^{th} iteration of an iterative solution

3)Buoyant and Non-Buoyant vertical jet in shallow water

Cu : Nominal Courant number at the discharge $Cu=V_\emptyset * \Delta t/D$. Transient solutions of the buoyant discharge

D : Jet width or diameter at the discharge

E : Dimensionless specific energy flux of the configuration $(D, H/D, V_\emptyset)$

F : Discharge Froude number

Fd : Discharge densimetric Froude number

g : Acceleration of gravity

H : Submergence depth

L : Tank length in the transient calculations of the buoyant discharge

M : Dimensionless specific momentum flux

$\dot{m}_\emptyset$: Flowrate at the discharge

$\dot{m}_C$: Entrained ambient water flowrate, buoyant discharge

$\dot{m}_D$: Large scale diluting circulation, buoyant discharge

$\dot{m}_e$: Ambient water entrainment rate $(=d\dot{m}/dy)$ by a vertical buoyant jet

$\dot{m}_R$: Near-field recirculation flowrate, buoyant discharge

$\dot{m}_{TOT}$: Total circulation induced in the tank by the jet, buoyant discharge

P : Static pressure

P_{surf} : Static pressure on the rigid lid

$P_{surf,\infty}$: Static pressure on the rigid lid at the outflow of the solution domain

$\dot{q}_{\emptyset}$: Convective heat flux at the discharge, buoyant jet

$\dot{q}(x)$: Convective heat flux through a vertical level (or cylindrical surface) at a distance x from the plane (or axis) of symmetry, buoyant jet

Re : Reynolds number at the discharge

T : Temperature

$T_{\emptyset}$: Discharge temperature

T_A : Ambient temperature

T_C : Centreline temperature

T_S : Surface temperature

$t_{\emptyset}$: Period of time elapsed before the visible interface had reached the outflow of the tank

U_S : Surface velocity

$V_{\emptyset}$: Discharge velocity

V_C : Centreline velocity

Xr : Reattachment lenght

α : Entrainment constant

ΔH_C : Centreline surface elevation

$\Delta H(x)$: Surface elevation

Δt : Time increment in transient solutions

ΔT : Temperature in excess of the ambient temperature

$\Delta \rho$: Density deficiency from the ambient density

4) Buoyant surface layer

$B_{\emptyset}$: Mean buoyancy at the discharge

D : Jet width at the discharge

E	: Cross-sectional entrainment coefficient
Fd	: Densimetric Froude number at the discharge
$\dot{Q}_e$	: Ambient water entrained by the layer
$\overline{Ri}$	: Cross-sectional Richardson number
$U_\emptyset$	: Velocity at the discharge
Um	: Characteristic cross-sectional velocity scale
$\Delta\rho_\emptyset$	: density deficiency at the discharge
ρ_a	: ambient density

CHAPTER 1

INTRODUCTION

CHAPTER 1 : INTRODUCTION

Stably stratified flows, in wich the fluid density decreases in the vertical direction, occur in several flow problems of practical interest. Cooling tower and chimney plume dispersion in the lower layers of the earth's atmosphere, flame spread near the ceiling of room fires and waste or warm water discharges into natural water bodies are but a few examples. In many of these flows the density variations combine with gravity to produce body force effects which can crucially influence the fluid dynamic behaviour. These buoyancy effects are similar in many of the applications mentioned above, but they are amongst the least understood of buoyant flow phenomena. The present work examines one of the problem areas mentioned above (water discharge into a stagnant water body) and studies the way in which the stable stratification influences the flow and how this may be simulated in mathematical models of these phenomena. A brief introduction into the background of the particular practical application studied is first provided.

1.1. Vertical buoyant discharges in environmental shallow water bodies

A commonly used practice for the disposal of condenser waste heat resulting from steam electric power generation, is to discharge the condenser waste water into a large environmental water body. The power plants are therefore conveniently located near the coast or near a large river.

The cooling water is withdrawn from the water body, passed once through the condensers, and pumped back to the receiving body. Economical considerations favour this approach instead of the disposal of the condenser heat by means of cooling towers commonly used in large inland power plants.

A large temperature rise of the condenser water reduces the average temperature difference between the condensing steam and cooling water and consequently decreases the efficiency of the heat transfer process; larger heat transfer surface is then required and the cost of the condenser is increased. A low temperature rise increases the efficiency of the condenser but a higher cooling water flowrate is then required which results in larger pipes and an increased pumping power requirement. Both the installation and operating costs of the cooling system are higher in such a case. The choice of the optimum temperature rise is finally defined by a cost/benefit analysis.

Apart from these condenser-based considerations, environmental factors can also define a maximum permissible temperature rise. An increase of environmental water temperature results in a reduction of its free oxygen solubility (see e.g. Nemerow, 1978). The potential of the water to face biological oxygen demand for aerobic degradation processes is thereby reduced. This situation is aggravated by the fact that many near-coast regions and rivers are already heavily loaded by urban or industrial effluents which increase very strongly the biological oxygen demand of the river. Furthermore, a substantial increase of

the river water temperature may affect the whole ecology of the river or estuary since it may destroy a whole series of temperature sensitive species and favour the growth of other temperature tolerant ones. It is therefore usually considered desirable that the disposed water should be thoroughly mixed and should not cause an excessive rise of the average temperature of the receiving body. It is, further, obvious that the estimation of the environmental impact of the discharge requires reliable methods for the prediction of the hydrodynamic and temperature fields resulting from such a discharge.

One additional aspect underlines the need for a good understanding of the effects associated with warm water discharges. It has been observed that in water bodies influenced by tidal motions, due to buoyancy effects the discharge water forms a floating layer around the discharge. This layer is transported by the tide and may influence the water temperature at the location where the cooling water is withdrawn. The result is a reduction of the power plant efficiency and a substantial increase in operating costs. This "short circuit" between discharge and intake sites must therefore be prevented by suitable design.

In recent years high velocity injection schemes such as multiple port diffusers have increasingly been used as effective mixing devices to diffuse the excess heat rapidly within a small area (for a review of the subject see Jirka, (1982)). However, many once-through condenser cooling systems currently in operation involve, essentially, a single port discharging vertically. The Littlebrook

power station on the Thames estuary and the San Onofre nuclear plant in California are two cases in point. The main operating parameters of these plants are shown in table 1.1 taken from Lee and Jirka, (1981). From the Reynolds numbers given it is clear that the flow in question is turbulent; the densimetric Froude numbers Fd:

$$Fd = \frac{V_\emptyset}{\sqrt{\frac{\Delta\rho}{\rho_a} g D}}$$

characterizing the ratio of inertia to buoyancy forces, are also sufficiently low that the buoyancy forces are likely to be important in determining the flow development close to the discharge. Frequently these discharges are located in waters only a few port diameters deep. Significant surface and bottom interactions may then dominate the mixing characteristics of such depth-restricted discharges. It is this type of discharge which forms the basis for the present study.

Table 1.1. Summary of operating parameters for two plant sites.

Plant site	San Onofre	Littlebrook
Condenser Flow (m^3/s)	25.2	19.0
Port diameter D (m)	4.3	3.5
Submergence depth ratio	1.1	0.9-1.7
Discharge velocity $V_\emptyset$ (m/s)	1.74	1.98
ΔT degrees °C	10.00	11.65
Reynolds number $Re = V_\emptyset D/\nu$	8.10^6	$6.9\ 10^6$
Froude number Fd	7.0	7.9

1.2. The aspect of the problem dealt with here

A vertical buoyant discharge near the bottom of a shallow receiving body of large horizontal extent is, in general, a three-dimensional time-dependent problem. Three-dimensionality is introduced mainly by the background velocity field of the receiving body (e.g. the main stream velocity of a river or the tidal motion which create a jet-in-crossflow type of flow). The geometry of the discharge may also itself not be exactly two-dimensional. The main river velocity or the near coast currents vary with time and thus make the problem time-dependent. However, in this study it was considered appropriate to examine initially the more fundamental case of a single, steady-state two-dimensional vertical buoyant discharge into a stagnant shallow water body of infinite horizontal extent. The main simplification introduced thereby is the decoupling of the flow induced by the discharge from the background velocity field. The flow is dominated by the interaction between the momentum and buoyancy of the jet alone with the stagnant ambient. It is important to stress that this simplification does not idealize in any way the physics of the stable stratification effects of most concern here, but merely reduces the dimensionality of the problem. It is therefore clear that the results of the present study are relevant also to the full blown practical case.

Previous work

The following sections contain a review of previous work on vertical two-dimensional buoyant and non-buoyant jets in a stagnant shallow water body of infinite horizontal extent. The literature abounds with experimental and theoretical investigations of buoyant and non-buoyant jets in infinite surroundings (for a detailed review see Chen and Rodi, (1980)). This work, though relevant to the present project, will not be discussed here, rather attention is concentrated on shallow water discharges. As will emerge from what follows, several topics such as the behaviour of buoyant surface layers are also important for the above flow. For clarity, the work on these aspects of the problem is reviewed later where it may be more closely associated with the contributions from the present study to these subsidiary topics.

1.3. Non-buoyant 2-D vertical jet in shallow water

A typical flow configuration for a plane vertical jet in shallow water is shown in figure 1.1. Initially the jet spreads like a submerged turbulent jet entraining fluid from the ambient; as the free surface is approached the jet is deflected and eventually forms another jet-like flow moving away from the symmetry plane along the water surface, also entraining ambient fluid. The sudden reduction of the vertical velocity near the surface results in an increase of the pressure in this area and consequently in an elevation of the surface near the plane of symmetry. The combined result of jet deflection and entrainment processes is to set

up a recirculating motion in the ambient as indicated by the arrows in figure 1.1. Further downstream the flow reattaches and continues to develop until a parallel flow is established far downstream. A similar flow pattern occurs in the axisymmetric configuration.

The described flow pattern is valid for a given geometry when the discharge velocity is sufficiently low. At high discharge velocities the jet may entirely penetrate the surface and a significantly different flow pattern may be observed (see figure 1.2 taken from Liong (1971) who studied this configuration experimentally). Such a case does not occur in practical shallow discharges and it will not be further examined.

Dimensional analysis shows that the flow can be described by three dimensionless groups (Hunt and Hsu, 1965)

.The Reynolds number of the flow : $Re = \frac{V_\emptyset \, D}{\nu}$

.The normalized submergence depth : H/D

.The discharge Froude number : $F = \frac{V_\emptyset}{\sqrt{g\, D}}$

Other frequently used product groups are:

.The dimensionless specific momentum flux of the jet :

(i=Ø for plane jets and 1 for round jets)

$$M = \frac{D\, V_\emptyset^2}{g\, H^2} \left(\frac{D}{H}\right)^i$$

.The dimensionless specific energy flux of the jet:

$$E = \frac{D\, V_\emptyset^3}{g^{1.5}\, H^{2.5}} \left(\frac{D}{H}\right)^i$$

For turbulent flows the Reynolds number dependence is not usually significant and various authors use either F, M or E to characterize the flow.

1.3.1. Experimental work

The flow for plane and round discharges has been studied experimentally by Muraoka and Murota (1967). The plane jet experiments were conducted in a 6 m long by 1 m high tank of .3 m width. The submergence ratio was varied between 3.6 and 2Ø.6 and the discharge Froude number between Ø.3 and 1.27. Only mean hydrodynamic variables were measured. Measurements were presented for the vertical velocity close to the plane of symmetry, for the horizontal velocity near the surface and close to the symmetry plane and for the surface shape. No information is available about the downstream development of the flow, the shape of the separation streamline or for the reattachment point. Practically speaking the sole interest of this study was in the hydrodynamic field near the symmetry plane.

The symmetry plane velocity decay measurements were compared with the self-similar decay rate ($\sim y^{-1/2}$) and it was found that, for the larger submergence depths studied, the velocity does decay self-similarly except for a region close to the surface where the velocity decays rapidly to zero. In the self-similar part of the jet-flow the normalized data compared satisfactorily with the Tollmien solution for the self-similar jet. The same agreement with the Tollmien

solution was observed for the horizontal velocity profiles, but not close to the plane of symmetry.

The experimental apparatus used for the round discharge was a cubic tank of one meter side with the discharge located at the centre of the base of the tank. The submergence ratio was varied between 1.6 and 8.8 and the discharge Froude number between Ø.3 and 1.3. The same quantities as for the plane jet were measured; again the main interest was in the region near the axis of symmetry. This work was the only published work discovered containing measurements of the hydrodynamics of a bottom vertical discharge in shallow water. Hunt and Hsu (1965) did however study the surface shape above a vertical round water jet; their experimental apparatus was a cylindrical tank with a diameter of 1Ø4 cm and a depth of 168 cm. The tank was equipped with a wave absorbing beach to minimize the interaction of reflected waves with the surface shape induced by the jet. A vertical pipe of adjustable height was located at the axis of the tank. Nozzles of varying diameter were fitted at the top of the pipe. By varying the height of the pipe, the distance of the nozzle from the free surface (H) could be changed. In this way (and also by using different nozzle diameters (D)) a wide range of submergence depths H/D were examined. The configuration was not an exact simulation of a shallow water discharge since even though the H/D ratios studied included small values (i.e. 1,4,9,16 and 25) the depth of the tank was large in relation to the distance of the nozzle from the surface. Given the scarsity of non-buoyant round jet shallow discharge data however, it

does represent a useful source of information. The non-dimensionalized data for the surface shape collapsed onto a unique curve for a wide range of configurations (H/D,F). The centreline surface elevation ($\Delta H_c/H$) was also given as a function of the nondimensional momentum flux of the jet at various submergence depths. Finally, Hunt and Hsu examined the hypothesis that the centreline displacement of the free surface may be approximated by the velocity head ($V_c^2/2g$) of the same jet issuing in a infinite water body at distance $H+\Delta H_c$ from the discharge. They evaluated V_c from the relation given in the pioneering work of Albertson (1950):

$$V_c = 6.2 \frac{D V_\emptyset}{H + \frac{V_c^2}{2g}}$$

derived from the conservation of momentum principle applied to a jet considered as a pure source of momentum. Only for the higher submergence ratios examined (16 and 25) was the surface elevation found to be in good agreement with the last equation.

Finally , Jirka and Harleman (1979), in the introduction of their paper on the instability and mixing of a vertical plane buoyant jet (see below), gave their description of the non-buoyant case. They did not perform experiments on the non-buoyant jet but referred to the previously mentioned experimental work of Muraoka and a study of Iamandi and Rouse (1969) which, however, bore closer resemblance to a driven cavity type of flow where instead of a moving wall a jet discharge was used. For this reason the postulated flow pattern of the non-buoyant case suggested by Jirka and

Harleman (containing multiple counter-rotating cells, see Figure 1.3) is unlikely to occur in a true vertical non-buoyant shallow discharge unless the high initial momentum effects shown in Figure 1.2 intrude; as mentioned above this is not relevant to the practical case and such multiple cells were not observed by Muraoka et al. Using dimensional arguments and relevant experimental information Jirka and Harleman estimated the length of the recirculation zone and the recirculating flowrate. The main line of their analysis is as follows: The jet after impingement and deflection on the surface spreads horizontally like a fully developed jet. The spreading rate of such a jet is Ø.2Ø and the total jet width therefore becomes equal to half the water depth at a distance from the symmetry plane equal to x=Ø.5H/Ø.2=2.5H. It is assumed that the horizontal jet entrains ambient water for this distance and downstream of this point water is de-entrained from the jet to sustain the recirculating cell. The volume flowrate per unit of jet length ($\dot{q}$) for a line momentum jet is given, according to the analysis of Morton, Taylor and Turner (1956), by the relation $\dot{q}=(2\alpha\dot{m}x)^{1/2}$ where α is an entrainment coefficient with a value of about Ø.Ø7 (assuming Gaussian similarity profiles) and $\dot{m}$ is the specific momentum flowrate per unit length. Hence for an entrainment distance of order 2.5H the circulation in the cell is of the order $\dot{q}=Ø.6(\dot{m}H)^{1/2}$.

1.3.2. Previous numerical predictions

The plane jet in shallow water was calculated

numerically by McGuirk and Rodi (1977). In this work turbulence was modelled by means of the standard k-ϵ model and the numerical solution procedure used the standard Hybrid discretisation scheme for the convection terms. The free surface boundary was treated as a plane of symmetry coinciding with the undisturbed water level (a 'rigid lid' approximation). The geometric configuration was kept constant (H/D=6.15, D=4 cm, plane jet) while the discharge velocity was varied. The influence of the location of the outflow boundary on the hydrodynamic field near the symmetry plane was studied and it was found necessary to locate the outflow at least 1Ø water depths removed from the symmetry plane. A rigid lid assumption results in the prediction of a static pressure variation along the surface; this variation was converted into an equivalent deviation $\Delta H(x)$ from the undisturbed water level using the approximation of negligible vertical acceleration near the surface which results in:

$$\Delta H(x) = \frac{P_{surf}(x) - P_{surf,\infty}}{g\,\rho}$$

where $P_{surf,\infty}$ is the predicted static pressure at the surface at the outflow location. The predictions for the normalized surface elevation ($\Delta H_c/H$) at the symmetry plane plotted against the non-dimensional jet energy flux E compared satisfactorily with the data of Muraoka and Murota quoted earlier. Predictions for the symmetry plane velocity decay, the surface shape and the streamline pattern were presented for one of the configurations calculated. The predictions of the symmetry plane velocity decay compare

satisfactorily with the data of Muraoka and Murota while the surface shape was predicted qualitatively rather than quantitatively. Only one recirculation cell was predicted and the flow tended to be horizontal downstream of the reattachment. The predicted reattachment length was equal to 5.3H, significantly larger than the value 2H suggested by Jirka et al.

1.4. Buoyant vertical 2-D jet in shallow water

The buoyant vertical 2-D jet in shallow water has been studied experimentally and analytically by Jirka and Harleman (1979) (plane jet) and by Lee and Jirka (1981) (round jet). The experimental data available consist of flow-visualization photographs and temperature measurements. Velocity field measurements have not so far been made. Thus, flow patterns had to be inferred from the flow visualization photographs and from the temperature measurements. The derivation of a flow pattern from this type of experimental data is more a matter of interpretation and judgement rather than a direct translation of the data as it would be if extensive velocity measurements were available. In the next section the data of Jirka et al will be presented together with their interpretation of the flow; their analytical integral model will also be briefly presented in one of the following sections.

1.4.1. Description of the flow and previous experimental work

The possible evolution of a buoyant discharge depends for a given geometry on an additional dimensionless parameter to those mentioned above which describes the relation between the momentum and buoyancy of the jet:

$$Fd = \frac{V_{\emptyset}}{\sqrt{\frac{\Delta\rho}{\rho_a} g D}}$$

Fd is usually referred to as a densimetric Froude number. We shall first describe the flow pattern when Fd is relatively low i.e. the buoyancy flux of the jet is significant in relation to its momentum flux. In figure 1.4 (case 1) taken from Lee and Jirka (1981) temperature profiles are given for an axisymmetric configuration with a submergence depth H/D=11.1 and a densimetric Froude number Fd=46. During the experiment the discharge water was previously mixed with a neutral dye and photographs were taken of the visualized flow. In the same figure the location of the dyed water / clear water interface is shown together with measured temperature profiles. The following observations can be made:

1) At the downstream part of the flow the visible interface remains practically horizontal.

2) The temperature data show that the surface temperature (excess above the ambient) is substantially lower than the initial discharge temperature excess ($\Delta T_s/\Delta T_{\emptyset} \leq \emptyset.2$) indicating that vigorous mixing of the discharged water with the ambient fluid has taken place.

3) In the downstream part of the flow the surface

temperature remains more or less constant, (slight reduction) indicating a very low level of mixing.

4) Also, over the downstream part of the flow, the excess heat is not diffused all over the water depth but from a point just below the visible interface the water has the initial ambient temperature.

The following conclusions were made on the basis of these observations:

1) For the downstream part of the flow a two layer structure explains the observations. A mixed warm water surface layer is moving downstream while a submerged ambient water layer is moving upstream; the mixing between the two layers being rather insignificant.

2) Intense mixing between the discharged jet and the upstream moving ambient water takes place close to the axis of symmetry.

Close to the axis of symmetry the vertical jet is expected initially to develop unaffected by the existence of the free surface driven by its initial momentum and buoyancy acceleration. The development of the jet is associated with intense entrainment of ambient fluid having, in the case examined, the initial ambient temperature. Therefore, as the surface is approached the peak temperature of the jet continuously decreases. Near the surface the vertical velocity rapidly decays to zero and a horizontal jet is formed in a similar way as in the isothermal flow. This jet deflection is associated with an intensification of turbulent activity and mixing which results in a further continuous reduction of the surface temperature close to the

axis of symmetry. In both the previously mentioned works, Jirka and Harleman (1979) and Lee and Jirka (1981), continuous curves of the surface temperature are ,unfortunately, not presented and the above mentioned strong reduction of the surface temperature cannot be clearly seen in the temperature profiles shown in figure 1.4 close to the axis of symmetry. This reduction is however clear in the work of Pryputniewicz et al (1975) which is to be discussed below.

The evolution of horizontal buoyant surface layers such as the one formed after the deflection near the surface is obviously important to the present flow and has been extensively studied by Ellison and Turner (1959), Wilkinson and Wood (1971) and Chu and Baddour (1984). These works are examined in detail later, but a summary of their observations is appropriate here. Depending on upstream and downstream conditions the flow in such surface layers initially develops as a surface buoyant jet entraining ambient fluid. Subsequently the flow exhibits a rapid increase in depth in the form of an internal hydraulic jump (also called density jump). This increase in layer depth is also accompanied by the formation of an elongated recirculation cell beneath the layer.

This type of flow development was suggested by Jirka, Lee and Harleman to occur also in the vertical buoyant discharge and this is supported by the shape of the visible interface and temperature data shown in figure 1.4. In case 1 the interface deepens slightly at first while further downstream a strong increase of the interface depth occurs

supporting the hypothesis of the formation of a density jump. This sudden increase of the interface depth is more emphatically shown in case 2 of figure 1.4 corresponding to H/D=2.2 and Fd=8.

On the basis of this analysis Jirka et al conceptually divided the flow into five interacting regions:

.A vertical jet region

.A surface impingement region.

.A horizontal buoyant surface jet region

.An internal density jump, and

.A stratified counter-flow region.

The cases 1 and 2 of Figure 1.4 examined so far are characterized by the fact that the ambient temperature fluid does reach the discharge and is entrained by the discharged jet. It is obvious that this feature is important in the dilution of the discharge and in the overall decrease of water temperatures. For such a configuration Jirka et al used the term stable.

When, for the same geometry and discharge velocity, the densimetric Froude number of the discharge is increased the temperature field and the location of the visible interface are substantially altered in relation to the stable configuration. Such a case corresponding to a submergence depth H/D=10 and a densimetric Froude number of 205 is shown in figure 1.4 case 3; also in figure 1.5 for a plane discharge corresponding to H/D=192 and Fd=80. The main differences in relation to the stable configuration are:

1) In the near-field region of the flow an increased water

temperature is observed over the whole water depth.

2) The visible interface of the flow is attached to the bottom of the tank.

It is obvious that in this case the discharge entrains water of temperature higher than the ambient temperature i.e. previously discharged water is re-entrained. For such a configuration Jirka et al used the term unstable.

Jirka et al comment on the unstable form of the flow as follows: " Under high momentum, low buoyancy shallow water conditions the energy input by the buoyant jet into the receiving body may be so strong that the buoyancy contained in the discharge is not sufficient to establish a stable stratified flow. Recirculation cells are set up near the jet efflux leading to heat re-entrainment into the discharge and thus to an impairment of mixing capacity " see figure 1.6 (quotation and figure from Lee and Jirka, (1981)). Obviously this flow pattern is suggested in contradistinction with the flow pattern of the stable configuration. The formation of recirculating cells is shown by these authors (figure 1.6) for the unstable configuration while not for the stable configuration. It is not clear if Jirka et al suggest for the stable configuration an internal hydraulic jump region occuring without a recirculation cell (roller) or if they consider the role of the cell less important in the stable configuration in relation to the unstable where the recirculating cell plays a significant role in the transport of heat down to the bottom of the tank. This uncertainty is undoubtedly due to the lack of detailed velocity data.

1.4.2. Stability analysis of Jirka, Lee and Harleman (1979)

Jirka, Lee and Harleman developed an integral mathematical model of the vertical buoyant 2-D jet in shallow water. They demonstrated that the model predicts satisfactorily the change from stable to unstable form as described in the previous section. For a given submergence depth (H/D) it allows the calculation of a critical discharge Froude number beyond which the configuration is unstable. In the following paragraphs the main assumptions of the model and the flow structure built into the model are briefly presented.

The flow is conceptually divided into five interacting parts as described in the previous section. Each part is separately examined and the solutions are matched at the boundaries. The vertical buoyant jet is calculated on the basis of the conservation of momentum and thermal energy, using the assumptions of Gaussian profiles, of hydrostatic pressure distribution and of a linear spreading rate. The surface impingement region is calculated on the basis of conservation of mass and thermal energy and a pre-specified loss of total head over this region. The surface jet is calculated exactly as the vertical jet (omitting the buoyancy induced radial pressure gradient) with the length of this region being defined empirically from the visible interface data (Ø.6H). This procedure leads to the calculation of the peak velocity, temperature and of the layer width before the jump; also of the cold layer flowrate and width.

The hydraulic jump is assumed to be a two layer stratified counterflow without any diffusive interaction between the layers. The governing equations are the conservation laws for each layer and the geometric constraint of constant water depth. The slope at the interface is taken from the experiments (1:4) and the single remaining unknown is the location of the downstream end of the jump. The final outcome of the analysis is the calculation of the downstream conjugate layer depths. The configuration is considered stable when the downstream conjugate depth (h_1') of the upper layer lies in the physically feasible range $\emptyset < h_1' < H$ and, at the same time, the solution shows a reduction of the specific energy of the system across the jump.

However, for high discharge densimetric Froude numbers such a solution does not exist. The non-existence of a solution is interpreted by Jirka et al as a hydrodynamically unstable situation. Under these high momentum conditions, the buoyancy contained in the upper layer flow is not sufficient to establish stable conjugate downstream conditions, leading to a breakdown of the stratified flow and heat re-entrainment into the buoyant jet region. Although, as stated above, the final model can predict the stable/unstable boundary, much empirical input from the authors' own experiments has gone into the calibration of the model, and some dubious unjustified assumptions were made (e.g. the neglect of pressure gradient effects in the surface jet region does not seem justified, particularly at low submergence depths).

1.4.3. Related experimental work

Closely related to the above topic is the experimental work of Pryputniewicz and Bowley (1975) who studied a vertical buoyant round jet discharged close to the surface of a semi-infinite water body (i.e. once again not exactly a shallow discharge). The experimental apparatus was a cylindrical tank of 2.40 m diameter and 1.50 m deep. The jet nozzle was fitted at the top of an adjustable height pipe located at the axis of symmetry of the tank, which was equipped with an overflow weir. A strong cold water supply from the bottom ensured steady state conditions and constant ambient temperature by forcing the entrained ambient water out of the tank. Experimental data were presented for the centreline and surface excess temperature and the temperature profiles close to the axis of symmetry. The very limited temperature data provided by Jirka et al did not allow a safe validation of the mathematical model and, therefore, the data of Pryputniewicz assumed crucial significance in terms of validation in spite of the fact that the configuration tested was not an exact shallow discharge.

1.4.4. Previous numerical predictions

Only a single example of an attempt to simulate the buoyant vertical shallow water discharge has been published ,Trent et al (1973). The turbulence model employed in this

work was an algebraically specified eddy viscosity model with different eddy-viscosity values fixed for different flow regions. Prandtl's free shear layer model together with a buoyancy correction was used for the vertical and horizontal jet regions. For combinations of discharge Froude numbers and submergence depths (Fd,H/D) for which an internal hydraulic jump should occur according to the analysis of Lee and Jirka, Trent et al did not predict such a jump. It is difficult ,however, to judge if Trent's rather crude turbulence modelling was sufficiently accurate to predict the main features of the flow. Trent (198Ø) reports that he also conducted tank experiments but never observed an internal hydraulic jump situation.

1.5. Assesment : objectives and strategy of present contribution

From the foregoing discussion, the following facts emerge:

a) although a substantial amount of experimental data has been obtained for the vertical buoyant shallow discharge problem and this enabled a picture of the flow behaviour to emerge, details of the exact nature of the flow patterns and the role played by the kind of recirculation cell observed in the non-buoyant case are unclear.

b) The only mathematical model capable of predicting practically important information about these flows (e.g. whether the flow is "stable" or "unstable") is based very heavily on the available experimental data and is not

sufficiently fundamental to enable the questions concerning the velocity field details to be assessed. The lack of a fundamental base for the mathematical model does not inspire confidence in its ability to carry over to situations closer to the real problem (e.g. with time-varying cross-flow velocity in the ambient) without significant further experimentation.

c) The alternative, more fundamentally based, modelling approaches have so far had limited application in the type of flows under consideration. Only a limited number of non-buoyant configurations have been studied in the previous work of McGuirk and Rodi (1977). Also, in the previous buoyant jet predictions of Trent et al the question of the stability of the discharge was not specifically addressed ; furthermore , it is difficult to judge whether Trent's rather coarse turbulence treatment was capable of predicting the main features of the flow. This lack of applications to the buoyant problem may be associated with known difficulties in applying this kind of numerical technique to strongly buoyant flows which introduce significant numerical stability problems (see e.g. Leschziner, 1979).

It is therefore the objective of the present work to adopt the computational fluid mechanics approach and develop this to the stage where it can succesfully calculate the experimental data on vertical 2-D buoyant jets in shallow water. It is clear however that several subsidiary tasks must be accomplished before the ultimate problem may be predicted; these may be grouped under the headings of numerical, physical and validation and are outlined below.

1) Numerical

Two problems fall under this heading. The first has already been mentioned and concerns the numerical instabilities produced by the presence of buoyancy. Some method must be found for satisfactorily handling these if the strongly buoyant "stable" type of flow is to be predicted. The second concerns numerical accuracy. As will be described later, the kind of Hybrid differencing approximation used for example in the calculations of McGuirk and Rodi (1977) is now well known to lead to so called numerical diffusion problems (see e.g. Leonard 1979) and require excessively fine grids in recirculating flow problems to achieve accurate solutions. Since the ultimate aim is to apply the developed technique in three dimensional flows, every effort must be made at an early stage to introduce a more accurate method for discretisation of the convection terms. This is paticularly so considering the proposals below concerning the type of turbulence model to be used.

2) Physical

As already mentioned, in the previous non-buoyant calculations the standard two-equation (k-ϵ) scalar eddy viscosity model was used; the version of this model suitable for strongly buoyant flows has been considerably less tested and validated. Furthermore, the recirculating nature and the strong buoyancy influence imply that the so-called Reynolds stress scalar flux transport closures (to be described in

chapter 2) may be necessary. A second task therefore is to choose and demonstrate adequate performance of the turbulence model in firstly non-buoyant recirculating flows and then in flows with strong stable stratification effects.

3) Validation

The task just mentioned is one of validation of the turbulence model against data relevant to the present problem. It seems sensible to use the phenomenological distinction produced from the experiments to test the model against available experimental data for identifiable sub-sets of the final problem such as i) the surface buoyant jet, ii)the internal density or hydraulic jump, iii) the isothermal vertical discharge in shallow water and, iv) the vertical buoyant jet impinging on a free surface.

The strategy thus proposed will undoubtedly lead to a better physical understanding of the phenomena associated with vertical buoyant 2-D discharges and will increase confidence in the ability and accuracy of the finally developed mathematical model to predict the 2-D vertical buoyant jet in shallow water.

1.6. Outline of the thesis

The thesis consists of seven chapters of which this is the first. Chapter 2 outlines the mathematical model used for the various tasks listed above, i.e. the governing Partial Differential Equations (PDE's) for the mean hydrodynamic and scalar variable fields and the modelled

PDE's for the turbulence quantities. In the same chapter the reduction of the governing PDE's to finite difference form is briefly presented with emphasis on the two numerical tasks discussed above. In chapter 3 the performance of the two turbulence closures mentioned above is tested in a series of isothermal recirculating flows. Chapters 4 and 5 deal respectively with the buoyant surface layer and the isothermal 2-D vertical jet in shallow water. The main task of the project, the calculation of the vertical 2-D buoyant discharge in shallow water is then presented in chapter 6. Finally, in chapter 7 a summary is made of the work performed, conclusions are drawn and suggestions are made for future work. Background work which does not fit well into the main body of the thesis is presented in Appendices. In Appendix 1 the full set of PDE's governing the phenomena studied are presented in an expanded form for the case of plane and axisymmetric recirculating flows. Appendices 2 and 3 deal with details of the numerical problems studied i.e. with the higher order convection discretisation method and with the buoyancy related numerical instability.

CHAPTER 2

THE MATHEMATICAL MODEL

CHAPTER 2 : THE MATHEMATICAL MODEL

The present chapter describes a mathematical model for the two-dimensional turbulent recirculating flows of interest here. Some aspects of the numerical solution of the model equations are also dealt with.

In sections 2.1 and 2.2 the underlying approach to the problem of modelling turbulent flows is presented. This approach leads to a system of Partial Differential Equations (PDE's) defining the mean and turbulence quantities describing the flow. The resulting system of governing PDE's is presented in a cartesian tensor notation in these sections. The solution of this system requires specification of boundary conditions for all the unknown variables. Certain types of boundaries are common in all flows examined in this thesis and the corresponding "problem independent" boundary conditions are described in section 2.3. Finally, in section 2.4 the two particular aspects of the numerical solution of the governing PDE's mentioned in chapter 1 are discussed. In subsection 2.4.1 the method adopted to improve the accuracy of the convection term discretisation is presented. Sub-section 2.4.2 deals with the buoyancy related instability problem. Chapter 2 is complemented by three appendices: A1, A2 and A3. In appendix A1 the governing PDE's are given in a detailed form for two dimensional plane and axisymmetric flows. Appendices A2 and A3 deal respectively, in more detail, with the quadratic interpolation scheme chosen to improve the convection accuracy and with the buoyancy related numerical instability problem.

2.1. Mean flow equations.

The PDE's which define the hydrodynamic and scalar variable fields of any flow are the expressions in differential form of the conservation laws of mass, momentum, thermal energy and species concentration. Mass conservation is expressed by the continuity equation, momentum conservation by the Navier-Stokes equations and energy or species conservation by the relevant scalar transport equations. This system of PDE's is, in principle, sufficient for the description of any flow be it laminar, turbulent, two or three-dimensional, steady or unsteady. For the complex type of flows of interest in this thesis, the system of governing PDE's can rarely be solved analytically. Recourse must be made to numerical solution procedures using finite difference or finite element methods.

If the previously mentioned fundamental formulation of the governing PDE's is adopted, the numerical solution must be able to resolve the whole range of eddies (length and time scales) characterizing a turbulent flow. Tennekes and Lumley (1972) have shown, based on dimensional arguments that the ratio of the Kolmogorov microscales (i.e. the smallest scales present) to the large scale eddies are given by the relations:

$$\text{length scales:} \quad \frac{\eta}{l} = R_t^{-3/4}$$

$$\text{time scales:} \quad \frac{\tau}{t} = R_t^{-1/2}$$

where R_t is a turbulence Reynolds number based on the characteristics of the large scale eddies:

$$R_t = \frac{\tilde{u}\, l}{\nu}$$

R_t values of order of 1000 occur in practical turbulent flows resulting in the following order of magnitude estimates:

length scales: $O(\frac{\eta}{l}) = 5.6\ E\text{-}3$

time scales: $O(\frac{\tau}{t}) = 3.1\ E\text{-}2$

From these estimates the characteristics of the numerical grid and time step required for calculation can be derived. The grid must be three-dimensional with a spatial increment Δx_i equal to a fraction of the small eddies. The large eddies (l) scale with the dimensions of the flow (L_i); therefore the increment Δx_i must be of the order $O(L_i/1000)$ resulting in a grid having 1000 nodes in each direction (Rodi,1980). Also, the time increment must be a fraction of the smaller time scales resulting in a time step of the order of 1/100 of the mean flow time scale, which may be a small fraction of the flow duration required e.g. for the derivation of time-averaged values in steady-state flows. Thus, the numerical solution of the fundamental formulation leads to a requirement of very large computational capacities exceeding by far the capabilities of current computers both in terms of storage and processing speed.

Such a resolution is not required if instead of solving for the instantaneous values of the dependent variables, PDE's are solved for their time -or ensemble- averaged values (hereafter jointly referred to as mean values). In such a case the influence of the fluctuating turbulent motions on the mean field is taken into account through the appearance in the PDE's of extra turbulence terms. All instantaneous quantities are decomposed into a mean (F) and

a fluctuating component (f) i.e. F(t)=F+f(t). Substitution of these decompositions into the conservation laws and averaging yields the PDE's governing the mean flow quantities (for details see Hinze (1959)). For incompressible flows these equations can be expressed in cartesian tensor notation as:
(upper case symbols represent mean quantities and lower case fluctuations; an overbar represents the averaging operation).

Continuity equation: $$\frac{\partial U_i}{\partial x_i} = \emptyset$$

Momentum equations:

$$\frac{\partial U_i}{\partial t} + U_j \frac{\partial U_i}{\partial x_j} = -\frac{1}{\rho_a}\frac{\partial P}{\partial x_i} + \frac{\partial}{\partial x_j}\left(\nu \frac{\partial U_i}{\partial x_j} - \overline{u_i u_j} \right) - g_i B$$

$$\text{where : } B = -\frac{\overline{\rho} - \rho_a}{\rho_a}$$

Mean buoyancy equation:

$$\frac{\partial B}{\partial t} + U_i \frac{\partial B}{\partial x_i} = \frac{\partial}{\partial x_i}\left(\frac{\nu}{\sigma_B} \frac{\partial B}{\partial x_i} - \overline{u_i b} \right)$$

In these equations P is the mean static pressure minus the hydrostatic pressure at the ambient density ρ_a. Use has been made of the Boussinesq approximation so that the influence of the variable density appears only through the gravity term.

In the flows studied in this thesis the buoyancy is induced by temperature or salt concentration differences in a water body. For salinity induced buoyancy a linear relationship holds between the instantaneous density and

concentration differences:

$$B \propto \Delta\rho = \rho_a - \rho \propto c - c_a$$

For temperature induced buoyancy, density differences are related to temperature differences via:

$$\Delta\rho = -\int_{T_a}^{T} \beta\, \rho_a\, dT = -\overline{\beta_{av}}\, \rho_a\, (T - T_a)$$

where $\overline{\beta_{av}}$ is an average densimetric expansion coefficient. For the relatively small differences as typically found in warm water discharges, $\overline{\beta_{av}}$ can be considered constant and, again, a linear relationship holds between the instantaneous density and temperature. Thus, the mean buoyancy equation quoted above can be derived from the salt concentration or from the energy equation respectively.

The above equations, although derived from a closed system of equations, no longer form a closed system since the averaging process has introduced unknown correlations between fluctuating velocities ($\overline{u_i u_j}$) and between velocity and scalar fluctuations ($\overline{u_i b}$). Physically these correlations (multiplied by the density ρ_a) represent the transport of momentum and heat -or mass- due to the fluctuating motion. Thus, $-\rho_a \overline{u_i u_j}$ is the averaged flux of x_i momemtum in the x_j direction, it is usually viewed as exerting an additional stress on the fluid and is therefore called a turbulent or Reynolds stress. Also $-\rho_a \overline{u_i b}$ is the averaged transport of B in the x_i direction and is therefore a turbulent mass or heat flux. The previous system of equations can be solved if the unknown correlations $\overline{u_i u_j}$ and $\overline{u_i b}$ are determined in some way. The determination of these correlations constitutes the turbulence closure problem.

2.2. The turbulence closure problem

Several review articles have appeared which summarize the various possible routes for handling the turbulence closure problem and describe the state of the art in the various methods (Bradshow, Cebeci and Whitelaw (1981), Reynolds and Cebeci (1976), etc)

More closely related to the present work is the review of Rodi (1980) who presented an extensive account of the performance of various turbulence models in the prediction of several flows occuring in hydraulic and environmental applications (similar to the flows of interest here). A series of turbulence models of increasing sophistication were examined and classified in four categories:

i) The zero-equation models. These relatively simple models do not involve transport equations for turbulence quantities. They employ the eddy viscosity concept which is specified either directly from experiments or by relating its value to the mean velocity and buoyancy distribution.

ii) The one-equation models. These models employ one transport equation for a characteristic velocity scale (e.g. $k^{1/2}$, $|uv|^{1/2}$). They use the eddy viscosity concept which is estimated from this velocity scale and from an algebraically specified length scale.

iii) The two-equation models. These models employ an eddy viscosity based on characteristic velocity and length scales which are specified by the solution of two modelled transport equations.

iv) The stress/flux transport equation models. These models do not use an eddy viscosity. Modelled transport equations are solved for all turbulent stresses and scalar fluxes.

Comparisons of the performance of models belonging in these categories showed that the most promising are the two-equation and transport equation or second moment closures. In contrast to the first categories, the application of the models belonging in the last two categories does not require any empirical information (other than the boundary conditions) in addition to the information used in the derivation of the model constants. The above review showed that these models performed satisfactorily in a series of complex buoyant and non-buoyant flows with or without recirculation, without alterations of the model constants. Therefore the last two categories are only considered in the present work though they are by no means the only possible methods. In what follows these two model types are described further.

The first category of turbulence models considered makes use of the Boussinesq eddy viscosity concept. This assumes that by analogy with the treatment of viscous stresses in laminar flows, the turbulent stresses $\overline{u_i u_j}$ are linearly related to the mean velocity gradients. For general flow situations this concept may be expressed as:

$$-\overline{u_i u_j} = \nu_t \left(\frac{\partial U_i}{\partial x_j} + \frac{\partial U_j}{\partial x_i} \right) - \frac{2}{3} \delta_{ij} k$$

ν_t is the turbulent or eddy viscosity which, in contrast to the molecular viscosity, is not a fluid property but

depends strongly on the state of turbulence. From dimensional analysis arguments (Launder and Spalding (1972)) the eddy viscosity may be considered proportional to a velocity scale characterizing the fluctuating motion and a typical length scale of this motion. Several suggestions have been made to define the characteristic velocity and length scales of which the best tested and most successfully used (in complex flows) is the k-ϵ model. In this model the characterizing velocity is assumed to be proportional to $k^{1/2}$ (a velocity scale for the large-scale turbulent motion). The characteristic length scale is assumed to be, by dimensional arguments (see Tennekes and Lumley (1972)), proportional to $k^{3/2}/\epsilon$ where ϵ is the viscous dissipation of the turbulence energy. The k-ϵ closure requires the determination of k and ϵ fields throughout the flow domain. This is achieved by the solution of two modelled transport equations for k and ϵ. The development of the modelled form of these equations, the assumptions contained therein and the derivation of the empirical constants in the model is described in detail by Launder and Spalding (1974). In the present text only the final modelled form of the equations constituting the k-ϵ approach will be given.

The second category of turbulence models is based on the solution of transport equations for the turbulent stresses and scalar fluxes. Two basic disadvantages of eddy viscosity models are:

i) The assumption of an isotropic eddy viscosity or diffusivity for all the Reynolds stresses and fluxes.

Experimental evidence (Webster, 1964) suggests that for flows with strong directional influence on the turbulence field, as for example strongly buoyant or curved flows, the assumption of an isotropic eddy viscosity, or of a constant and isotropic Prandtl number are not realistic.

ii) In eddy viscosity models, transport effects i.e. convection and diffusion on the individual turbulent stresses and scalar fluxes are only indirectly taken into account through the solution of transport equations for the quantities defining the eddy viscosity. However it is believed that in complex flows the local values of the stresses and fluxes could be strongly influenced by such transport effects.

In order to allow for the different development of the various Reynolds stresses (representing various velocity scales in complex flows) and to account properly for their transport, turbulence models have been developed which employ transport equations for each individual stress and flux. Exact transport equations for $\overline{u_i u_j}$ can be derived from the Navier Stokes equations, but these equations contain turbulence correlations of the next higher order. Therefore closure of the equations cannot be achieved by resorting to equations of higher and higher order. Instead a turbulence model must be introduced which approximates the correlations of a certain order in terms of lower order correlations and mean flow quantities. It should be emphasized that the derivation of the exact equations automatically introduces terms accounting for buoyancy effects in the development of each stress or flux.

Once again several possible models at this transport equation or second moment closure level have been proposed (see Rodi (1980)). The development of the model described below is presented in detail in the papers by Launder, Reece and Rodi (1975), Launder (1975) and Gibson and Launder (1978). This model will be referred to in this thesis as the RSFT model (Reynolds stress/flux transport model). Again in the context of this brief presentation only the final modelled form of the transport equations will be given in subsection 2.2.2.

Finally it should be noted that the versions of the models presented in subsections 2.2.1 and 2.2.2 are suitable for high turbulence Reynolds number (R_t) flows. As discussed below low Reynolds number versions of these models have been presented but are not considered here on the assumption of high R_t numbers in the flows considered.

2.2.1. The k-ϵ model

The form of the k-ϵ model appropriate for buoyant flows is usually referred to as the buoyancy extended k-ϵ model. This version of the model has been less extensively used and validated than the standard k-ϵ model. The set of equations constituting the model is:

$$\nu_t = c_\mu \frac{k^2}{\epsilon}$$

$$-\overline{u_i u_j} = \nu_t \left(\frac{\partial U_i}{\partial x_j} + \frac{\partial U_j}{\partial x_i} \right) - \frac{2}{3} \delta_{ij} k \qquad -\overline{u_i b} = \frac{\nu_t}{\sigma_T} \frac{\partial B}{\partial x_i}$$

Modelled k equation

$$\frac{\partial k}{\partial t} + U_i \frac{\partial k}{\partial x_i} = \frac{\partial}{\partial x_i}\left(\frac{\nu_t}{\sigma_k} \frac{\partial k}{\partial x_i}\right) + P + G - \varepsilon$$

where P is the stress production and G is the buoyancy production/destruction of k, i.e. G can be either a positive or a negative term depending on the nature of the stratification.

$$P = -\overline{u_i u_j} \frac{\partial U_i}{\partial x_j} = \nu_t \left(\frac{\partial U_i}{\partial x_j} + \frac{\partial U_j}{\partial x_i}\right) \frac{\partial U_i}{\partial x_j}$$

$$G = -g_i \overline{u_i b} = \frac{\nu_t}{\sigma_T} g_i \frac{\partial B}{\partial x_i}$$

Modelled ϵ equation

$$\frac{\partial \varepsilon}{\partial t} + U_i \frac{\partial \varepsilon}{\partial x_i} = \frac{\partial}{\partial x_i}\left(\frac{\nu_t}{\sigma_\varepsilon} \frac{\partial \varepsilon}{\partial x_i}\right) + c_{\varepsilon_1} \frac{\varepsilon}{k} P - c_{\varepsilon_2} \frac{\varepsilon^2}{k}$$

In this form of the dissipation equation only the stress production of k (P) is included in the source term while the destruction/production of k by buoyancy (G) is not taken into account. This form of the ϵ equation has mainly been used in the buoyant flow calculations reported in the literature (see e.g. Gibson and Launder (1976), McGuirk and Rodi (1979), Markatos (1984)). Rodi (1980) suggested a different formulation for the production of ϵ which is equivalent to a partial inclusion of G in the production of ϵ. This subject is further discussed in chapter 4 in the light of the present predictions.

The set of empirical constants appearing in the modelled equations is given in table 2.1. Experimental data suggest

that the turbulent Prandtl number σ_T has a value near Ø.9 in near wall flows, Ø.5 in plane jets and Ø.7 in round jets (Rodi, 198Ø).

TABLE 2.1 : Values of constants used in the k-ε model.

c_μ	c_{ε_1}	c_{ε_2}	σ_k	σ_ε	σ_T
0.09	1.44	1.92	1.0	1.3	0.5-0.9

2.2.2. The RSFT model

The RSFT closure requires the solution of transport equations for the Reynolds stresses $\overline{u_i u_j}$, the turbulent fluxes $\overline{u_i b}$, the energy dissipation rate ϵ and for the variance of the scalar fluctuations $\overline{b^2}$. Thus for a two-dimensional problem equations are solved for $\overline{u^2}, \overline{v^2}, \overline{w^2}, \overline{uv}, \epsilon, \overline{ub}, \overline{vb}$ and $\overline{b^2}$ i.e. a total of eight transport equations instead of the two equations solved in the k-ε eddy viscosity approach. The equations are modelled as follows (details may be found in the references quoted above):

a. The modelled $\overline{u_i u_j}$ equation.

$$\frac{\partial \overline{u_i u_j}}{\partial t} + U_\ell \frac{\partial \overline{u_i u_j}}{\partial x_\ell} = D_{ij} + P_{ij} + G_{ij} + \Pi_{ij} - \varepsilon_{ij}$$

. P_{ij} is the stress production of $\overline{u_i u_j}$: $P_{ij} = - \overline{u_i u_\ell} \frac{\partial U_j}{\partial x_\ell} - \overline{u_j u_\ell} \frac{\partial U_i}{\partial x_\ell}$

. G_{ij} is the buoyancy source term : $G_{ij} = - (g_i \overline{u_j b} + g_j \overline{u_i b})$

.At high Reynolds numbers (R_t) the turbulence is assumed locally isotropic and the same amount of energy is dissipated in each energy component $\overline{u_i^2}$, furthermore the dissipation correlation ϵ_{ij} is zero for $i \neq j$ when local isotropy prevails. Therefore the dissipation term ϵ_{ij} appearing in each stress transport equation can be written as:

$$\varepsilon_{ij} = \frac{2}{3} \delta_{ij} \varepsilon$$

.The turbulent transport term D_{ij} is modelled by a gradient type assumption:

$$D_{ij} = c_s \frac{\partial}{\partial x_\ell} \left(\frac{k}{\varepsilon} \overline{u_\kappa u_\ell} \frac{\partial \overline{u_i u_j}}{\partial x_\kappa} \right)$$

.A most important term is the pressure-strain correlation which has the exact form:

$$\Pi_{ij} = \overline{\frac{p}{\rho_a} \left(\frac{\partial u_i}{\partial x_j} + \frac{\partial u_j}{\partial x_i} \right)}$$

It can be shown by eliminating the pressure fluctuation p via a Poisson equation (Launder, 1975) that three processes contribute to the pressure – strain correlation Π_{ij}, one being due to the interaction of fluctuating velocities only $\Pi_{ij,1}$, one arising from the interaction of the mean strain rate with fluctuating velocities $\Pi_{ij,2}$ and one due to the interaction of density and velocity fluctuations $\Pi_{ij,3}$, thus:

$$\Pi_{ij} = \Pi_{ij,1} + \Pi_{ij,2} + \Pi_{ij,3}$$

The three contributions are modelled as follows:

$$\Pi_{ij,1} = - c_1 \frac{\varepsilon}{k} \left(\overline{u_i u_j} - \frac{2}{3} \delta_{ij} k \right)$$

$$\Pi_{ij,2} = -c_2 \left(P_{ij} - \frac{2}{3}\delta_{ij} P \right) \qquad \text{where } P = -\overline{u_i u_j} \frac{\partial U_i}{\partial x_j}$$

$$\Pi_{ij,3} = -c_3 \left(G_{ij} - \frac{2}{3}\delta_{ij} G \right) \qquad \text{where } G = -g_i \overline{u_i b}$$

For the second contribution $\Pi_{ij,2}$ Launder et al (1975) also suggested an alternative more complex form. The previous relation for $\Pi_{ij,2}$ is a simplification of the more complex formulation, where only the dominant term is retained. (Launder et al (1975), Rodi (1980), Rodi and Gibson (1981)). When the model has been applied to buoyant flows, the simpler form of $\Pi_{ij,2}$ has usually been used and the buoyancy term $\Pi_{ij,3}$ was modelled similarly (Launder (1975), Gibson and Launder (1976) and (1978), McGuirk and Rodi (1979)). The simpler form of $\Pi_{ij,2}$ was used in all the applications presented in this thesis.

Wall and free surface effects on Π_{ij}

In local equilibrium shear layers where convection and turbulent diffusion terms are absent the ratios of the individual stresses $\overline{u_i u_j}$ to k are determined solely by the pressure strain model. Experiments have shown that these ratios are significantly different in shear layers near to and remote from walls: in near-wall turbulence the level of stress normal to the wall surface is damped while that parallel to the main flow is enhanced relative to a free shear flow. The pressure-strain model presented so far does not produce these differences because it does not account for any wall effects. These effects can be introduced by a wall correction to the pressure-strain model as described by Gibson and Launder (1978) who extended the previous work of

Shir (1973):

$$\Pi'_{ij,1} = c'_1 \frac{\varepsilon}{k} \left(\overline{u_n^2}\,\delta_{ij} - \frac{3}{2}\overline{u_n u_i}\,\delta_{nj} - \frac{3}{2}\overline{u_n u_j}\,\delta_{ni} \right) f\left(L/x_n \right)$$

$$\Pi'_{ij,2} = c'_2 \left(\Pi_{nn,2}\,\delta_{ij} - \frac{3}{2}\Pi_{ni,2}\,\delta_{nj} - \frac{3}{2}\Pi_{nj,2}\,\delta_{ni} \right) f\left(L/x_n \right)$$

These expressions are valid if the wall is aligned with the coordinate system; n denotes the direction normal to the wall; x_n is the distance from the wall and L is the length scale of turbulence ($\sim k^{3/2}/\epsilon$). The role of the function f is to reduce the influence of the corrections away from the wall.

A third correction $\Pi'_{ij,3}$ was initially suggested by Gibson and Launder (1978) for the buoyancy term of the pressure-strain correlation. They comment that this term appeared to exercise little influence in the prediction of stratified wall flows. Also in the absence of definite information validating the influence of this term they decided to set $\Pi'_{ij,3}$ equal to zero. In the absence of any further information the same practice was applied in the present work.

Although very little is known about the effect of a free surface on the turbulence structure in a water body, limited experimental evidence sugests free surface effects similar to the wall effects described above. The data of Nakagawa et al (1975) for an open channel flow showed that close to the surface the normal stress component vertical to the surface is damped whereas the streamwise component is enhanced. Also the data of Chu and Baddour (1984) for the buoyant surface jet showed that close to the discharge, before the intrusion

of buoyancy effects, the surface jet spreads like a neutral wall jet. Therefore in the present work, the previous wall corrections were also used as "free surface" corrections in order to account for the effects of a free surface on the turbulence structure. A similar practice was applied by Hossain (1980) in his open-channel and surface jet calculations in the context of an algebraic approximation of the RSFT model (Gibson and Launder, (1976)).

b. The modelled ϵ equation

The modelled dissipation equation is similar in form to the ϵ equation in the k-ϵ model except for the diffusion term which is modelled as follows:

$$D_\epsilon = c_\epsilon \frac{\partial}{\partial x_i} \left(\frac{k}{\epsilon} \overline{u_i u_\kappa} \frac{\partial \epsilon}{\partial x_\kappa} \right)$$

c. The modelled $\overline{u_i b}$ equation

$$\frac{\partial \overline{u_i b}}{\partial t} + U_j \frac{\partial \overline{u_i b}}{\partial x_j} = D_{ib} + P_{ib} + G_{ib} + \Pi_{ib} - \varepsilon_{ib}$$

.P_{ib} is the mean field production:

$$P_{ib} = - \overline{u_i u_j} \frac{\partial B}{\partial x_j} - \overline{u_j b} \frac{\partial U_i}{\partial x_j}$$

.G_{ib} is the buoyancy production/destruction: $G_{ib} = - g_i \overline{b^2}$

.ϵ_{ib} is the viscous dissipation: $\varepsilon_{ib} \propto \overline{\frac{\partial u_i}{\partial x_\ell} \frac{\partial b}{\partial x_\ell}}$

which, on the assumption of locally isotropic turbulence, is identically equal to zero.

The remaining two terms D_{ib} and Π_{ib} are modelled as follows:

.Diffusion is modelled by a gradient type assumption:

$$D_{ib} = c_s' \frac{\partial}{\partial x_\ell} \left(\frac{k}{\varepsilon} \overline{u_\kappa u_\ell} \frac{\partial \overline{u_i b}}{\partial x_\kappa} \right)$$

.The pressure-buoyancy gradient correlation:

$$\Pi_{ib} = \overline{\frac{p}{\rho_a} \frac{\partial b}{\partial x_i}}$$

As in the case of the pressure-strain correlation, it can be shown with the aid of a Poisson equation for the fluctuating pressure that three physical processes contribute to the correlation Π_{ib}, namely the interaction of velocity and temperature fluctuations $\Pi_{ib,1}$, an interaction between fluctuating quantities and the mean strain field $\Pi_{ib,2}$ and a contribution due to the buoyancy forces $\Pi_{ib,3}$. For the first part Launder (1975) adopted the proposal of Monin:

$$\Pi_{ib,1} = -c_{1T} \frac{\varepsilon}{k} \overline{u_i b}$$

by analogy with the pressure strain model, Launder (1975) proposed that the second and third part of Π_{ib} should be proportional to the production due to the mean strain and buoyancy respectively i.e.:

$$\Pi_{ib,2} = c_{2T} \overline{u_\ell b} \frac{\partial U_i}{\partial x_\ell}$$

$$\Pi_{ib,3} = c_{3T} g_i \overline{b^2}$$

Wall and free-surface effects on Π_{ib}

Gibson and Launder (1978) assumed that the presence of a wall has an effect also on the pressure-scalar gradient correlation; analogous to the wall correction for the pressure-strain term they proposed:

$$\Pi'_{ib,1} = -c'_{1T} \frac{\varepsilon}{k} \overline{u_n b}\, \delta_{in}\, f(\, L/x_n\,)$$

Similar corrections were introduced for $\Pi_{ib,2}$ and $\Pi_{ib,3}$ but they were found of no importance in the prediction of stratified wall flows and were eventually set equal to zero. In the absence of any further information this practice was also followed in the present work.

One reason for introducing the above correction is that, without it, the experimentally found difference between the turbulent Prandtl number near walls (=Ø.9) and in free flows (Ø.5-Ø.7) cannot be predicted. In the present work the previous wall corrections are used as free surface corrections also.

d. The modelled $\overline{b^2}$ equation.

$$\frac{\partial \overline{b^2}}{\partial t} + U_i \frac{\partial \overline{b^2}}{\partial x_i} = D_{bb} + P_{bb} - \varepsilon_{bb}$$

where P_{bb} is the mean field production: $P_{bb} = -2\overline{u_i b} \frac{\partial B}{\partial x_i}$

The modelled terms are:

.Diffusion: $$D_{bb} = c_{TT} \frac{\partial}{\partial x_j} \left(\frac{k}{\varepsilon} \overline{u_j u_\ell} \frac{\partial \overline{b^2}}{\partial x_\ell} \right)$$

.The dissipation of the variance of the scalar fluctuations

is estimated from the assumption (Launder, (1975)) that the ratio of the characteristic decay times for the turbulent scalar and velocity fields is constant so that:

$$\varepsilon_{bb} = \frac{1}{R_T} \frac{\overline{b^2}}{k} \varepsilon$$

CONSTANTS

The set of empirical constants appearing in the modelled equations are given in table 2.2. The values recommended by Gibson and Launder (1978) have been used.

TABLE 2.2 : Values of constants in the RSFT model.

Π_{ij}			Π'_{ij}		Π_{ib}			Π'_{ib}
c_1	c_2	c_3	c'_1	c'_2	c_{1T}	c_{2T}	c_{3T}	c'_{1T}
1.80	0.60	0.50	0.50	0.30	3.00	0.33	0.33	0.50

ε		ε_{bb}	Diffusion constants			
$c_{\varepsilon 1}$	$c_{\varepsilon 2}$	R_T	c_s	c_ε	c'_s	c_{TT}
1.44	1.92	0.80	0.24	0.15	0.22	0.22

2.3. Boundary conditions

The transport equations for the mean field variables given in section 2.1 together with the turbulence model equations given in section 2.2 form a closed system of equations which can be solved numerically if sufficient boundary conditions for all variables are provided. A limited number of physical or conceptual boundaries confine

the solution domain of the flows examined here; namely: walls, a free surface, a plane or axis of symmetry, inflow and outflow boundaries. The treatment of the first three types of boundaries is common to all the turbulent flows examined while the last two are problem dependent. The purpose of this section is to describe the "problem independent" boundary conditions.

In all the calculated flows the walls, the free surface and the plane or axis of symmetry are aligned with one of the directions of the coordinate system. In the following relations the walls, free surface, plane or axis of symmetry are assumed to coincide with or be parallel to the direction x_1 of the coordinate system.

Plane or axis of symmetry

$$F = 0 \quad \text{for} \quad F \equiv U_2 \, , \, \overline{u_1 u_2} \, , \, \overline{u_2 b}$$

$$\frac{\partial F}{\partial x_2} = 0 \quad \text{for} \quad F \equiv U_1 \, , \, B \, , \, k \, , \, \varepsilon \, , \, \overline{u_i^2} \, , \, \overline{u_1 b} \, , \, \overline{b^2}$$

Free surface

The previous set of conditions was also applied for the free surface boundary. In all the flows examined the free surface was treated as a symmetry plane coinciding with the level of the undisturbed surface. This is a modelling assumption since, in reality, in all free-surface flows the surface is distorted. The influence of this modelling assumption on the predictions will be examined in chapter 5 dealing with the vertical non-buoyant jet in shallow water for which a considerable distortion occurs close to the axis

of the discharge.

Walls

When the boundary conditions are specified right at the wall the equations have to be integrated through the so called viscous sub-layer existing close to a solid surface (Tennekes and Lumley (1972)). This is undesirable for two reasons. Firstly, very steep velocity gradients prevail in the viscous sublayer so that for proper resolution many grid points have to be placed in the layer; secondly, viscous effects are important in this layer so that the high Reynolds number turbulence models presented above are not applicable. Low Reynolds number versions of the models have been developed. Jones and Launder (1973) presented a low Reynolds number version of the two equation model and Hanjalic and Launder (1976) presented a low Reynolds number version of the transport equation model. However, the problem of exorbitant computational expense required for the resolution of the near wall region remains and becomes even worse when the low Reynolds number versions are used. Integration through the viscous sublayer is avoided by means of the "wall function" method based on the fact that semi-empirical laws are available that connect the wall conditions (e.g. wall shear stress) to the dependent variables just outside the viscous-sublayer. These laws (Tennekes and Lumley (1972)) are valid for a limited region close to the wall defined by:

$$30 < x_2^+ < 100 \qquad \text{where} \quad x_2^+ = x_2 \, u_T / \nu \qquad \text{and} \quad u_T = \sqrt{\frac{\tau_w}{\rho}}$$

u_T being the friction velocity. For this region:

i) The turbulence is assumed in local equilibrium: $P=\epsilon$

ii) The turbulent shear stress is constant and approximately equal to the wall shear stress: $|\overline{uv}|_{x_2^+} = u_T^2$.

iii) The ratio $|\overline{uv}|/k$ is a common constant, experiments suggest that:

$$|\overline{uv}| / k = 0.3 \ (= \sqrt{c_\mu}\ )$$

iv) The velocity parallel to the wall is given by the log-law:

$$\frac{U_1}{u_T} = \frac{1}{\kappa} \ln(x_2^+ E) \quad \text{or} \quad \frac{\partial U_1}{\partial x_2} = \frac{u_T}{\kappa\ x_2}$$

where κ is the Von-Karman constant (=Ø.42) and E is a roughness parameter; E=9 for hydraulically smooth walls.

The above set of relations provide the basis for the specification of the wall boundary conditions. The first grid points must be placed in the range $3Ø<x_2^+<1ØØ$.

The set of related boundary conditions are:

Production of k. At the first node close to the wall:

$$P = \left| \overline{uv} \frac{\partial U}{\partial y} \right| = \frac{u_T^3}{\kappa\ x_2} \rightarrow P = \frac{c_\mu^{3/4}\ k^{3/2}}{\kappa\ \ x_2}$$

this relation is used for the source term of the turbulence energy equation at the near-wall nodes rather than the discretised version of the normal expression for P.

Dissipation rate . The value of the dissipation rate close to the wall is estimated directly from the local equilibrium assumption $P=\epsilon$:

$$\epsilon = \frac{c_\mu^{3/4}\ k^{3/2}}{\kappa\ \ \ x_2}$$

this value is fixed at the near-wall node and the relevant transport equation is not solved at these nodes.

Wall shear stress. The wall shear stress used in the integration of the x_1 momentum equation close to the wall is estimated from the relation:

$$|\overline{uv}|_{wall} = k\, c_\mu^{\frac{1}{2}}$$

where k is the calculated turbulence energy at the grid node closest to the wall.

As far as the temperature or species concentration are concerned the walls are assumed adiabatic to heat or mass.

Therefore, together with the above wall function conditions the full set of the wall boundary conditions are:

$$F = 0 \text{ for } F = U_1 \,,\, U_2 \,,\, \overline{u_2 b}$$

$$\frac{\partial F}{\partial x_2} = 0 \quad \text{for} \quad F = B \,,\, k \,,\, \overline{u_i u_j} \,,\, \overline{u_1 b} \,,\, \overline{b^2} \,,\, \varepsilon \,.$$

for the first node close to the wall:

$$P = \varepsilon = \frac{k^{3/2}\, c_\mu^{3/4}}{\kappa\, x_2} \quad \text{and} \quad |\overline{uv}|_{wall} = k\, c_\mu^{\frac{1}{2}}$$

2.4. Numerical solution of the governing PDE's

The system of governing PDE's together with the boundary conditions were solved numerically by a finite difference method. The basis of the computational algorithm is the well established SIMPLE algorithm of Patankar and Spalding (1972). The analytical derivation of SIMPLE the structure of the algorithm and information about the discretisation

practices which lead to the set of algebraic equations replacing the PDE's can be found in detail in Patankar (1980). Only remarks are included here on the modifications to the "standard" computational algorithm found necessary or beneficial for the present flow problems.

As already briefly mentioned in the previous chapter two areas of the numerical algorithm required some considerable attention. The first was the need to improve the numerical accuracy of the convection term discretisation. The standard practice (the Hybrid method, see Patankar (1980)) is only first order accurate and has associated with it a truncation error which is of a numerical or false diffusion type. Previous works (e.g. Leonard et al (1978), McGuirk et al (1981)) had shown that the numerical diffusion problem may substantially affect the accuracy of a solution. The problem may be alleviated by increased grid resolution though, because of its first order accuracy, the standard method is slow to respond to grid refinement. The detrimental efects of numerical diffusion are, obviously, particularly undesirable when intercomparisons of various physical diffusion approximations (i.e. turbulence models) are carried out.

In the present work the possibilities of using fine grids were limited since, due to the buoyancy instability discussed below the computations required unusually high numbers of iterations and the grids used should be as economical as possible. Furthermore, since a considerable part of the present work consists of comparisons of the performance of the two turbulence closures presented above,

it was considered essential to address the discretisation accuracy problem. From the several alternatives aiming to improve the convection term treatment the method chosen and successfully applied in this work is the third order accurate quadratic interpolation scheme of Leonard (1979) (hereafter called the QUICK method). This subject is dealt with in subsection 2.4.1.

The second area of the numerical algorithm requiring attention was the treatment of the buoyancy related numerical instability problem. This subject is dealt with in subsection 2.4.2. Finally, in subsection 2.4.3 a few remarks are made on the incorporation of the RSFT model into the computer code.

2.4.1. The QUICK discretisation

Increasing evidence in the literature (Leonard et al (1978), Han et al (1981), Pollard et al (1982)) suggests that the third order accurate quadratic discretisation scheme of Leonard (1979), widely known now as QUICK, is an appealing alternative to the commonly used Hybrid scheme. The existing evidence shows that QUICK offers substantial possibilities for the removal of the numerical diffusion problem associated with Upwind Differencing. It was thus decided that this discretisation would be employed in the current work. The work carried out concerning QUICK is reported in some detail in Appendix A2. The following discussion is a resumé of some of the points raised there.

Historically, one of the main problems encountered when

numerical solutions of the flow transport equations were first attempted, was the discretisation of the convective terms in the transport equations. The most obvious choise is the use of a second order accurate Central Differencing (CD) approximation. However the use of CD in calculations where convection processes locally dominate diffusion results in negative coefficients in the discretised algebraic linear equations. The negative coefficients may result in:

.an unrealistic oscillatory pattern of the solution i.e. waves or wiggles around the correct solution.

.divergence as a physical consequence of the oscillatory pattern of the solution of one of the variables (e.g. negative k or ϵ values).

.numerical divergence when an iterative solution of the linearized equations is employed, as e.g. a point-by-point or line-by-line iterative method.

This last form of numerical instability can be removed by manipulation of the coefficients aiming to ensure diagonal dominance of the coefficient matrix. The other ,more inherent, convergence problems were removed , when instead of CD, Upwind Differencing (UD) was used for the convection terms. In UD the truncation error (TE) involved in the derivation of the discretised equations is of the order of the grid spacing Δx_i while in CD the TE is of the order of Δx_i^2 . It can be shown (see e.g. Leonard, 1979) that the use of UD is equivalent to the addition of a spatially varying artificial or numerical viscosity to the physical viscosity of the fluid. The detrimental effects of this false numerical diffusion on the numerical predictions

have been clearly demonstrated in cases where comparisons were possible between UD and higher order -or analytical solutions (see e.g. Leonard et al (1978)).

Even though UD was ,and still is, extensively used in practical calculations the discretisation problem has remained the weak point of the algorithm. It has been increasingly realized that the cost of the unconditional stability of UD was a strong reduction in the accuracy of the solution.

The Quadratic Interpolation scheme of Leonard (1979) offers a substantial improvement in relation to CD both in terms of accuracy and numerical stability. The truncation error involved in the derivation of the discretised equation is of the order Δx_i^3 and the numerical stability of the solution is significantly improved in relation to CD. Practically ,increased stability means that solutions are possible where previously divergence occured and that the amplitude of oscillations or wiggles is reduced.

The existing evidence in the literature and the experience from the application of QUICK during this project suggest that the stability characteristics of QUICK allow the use of the new scheme over a wide range of flows of practical importance. However the stability of QUICK is not unconditional; convergence problems associated with wiggles in the variable fields were experienced in some of the QUICK calculations reported in this thesis. Such calculations are for example all the RST calculations for which the cell Peclet numbers are high due to the explicit treatment of turbulent diffusion (the definition and importance of the

cell Peclet number in this context is described in Appendix A2). For these cases a compromise had to be made between the desired higher accuracy of QUICK and the need to obtain converged solutions. One possible course for the removal of the convergence problems is again a direct or indirect introduction of artificial or numerical viscosities aiming to reduce the cell Peclet numbers and to damp artificially the wiggles in the variable fields. In this project this was done by the introduction of a mixed QUICK-Upwind scheme shifting from QUICK to UD on the basis of the local cell Peclet number. In Hybrid the shift from CD to UD is performed at the critical Peclet number where the CD coefficients become negative (i.e. Pc=2 for a uniform grid). In the present QUICK-UD scheme the shift from QUICK to UD is performed when the local cell Peclet number exceeds a prescribed local limiting value. In most of the applications convergence was possible at values of the limiting Peclet numbers significantly higher than the critical value where QUICK coefficients become negative (i.e. Pc=8/3 for a uniform grid). For the flows where the mixed scheme had to be used convergence was possible for values of the limiting cell Peclet numbers typically in the order of 1000 to 10000, which should be compared with the previously mentioned value of 2 for Hybrid. Details on the way the mixed scheme was applied for each of the calculations will be given in the relevant Chapters of the thesis.

Concluding, it should be emphasized that in the limited number of flows where the mixed scheme had to be applied the shift QUICK-Upwind always took place at very high cell

Peclet numbers. It will be demonstrated that for these cases QUICK could still be used over the great majority of the solution domain and that the numerical diffusion problem had still been considerably alleviated.

2.4.2. The buoyancy related instability

An additional coupling between the vertical momentum equation and the temperature (or species concentration) equation occurs in buoyant flow calculations through the buoyancy term appearing in the momentum equation. This buoyancy coupling causes severe numerical instability problems when the common sequential solution algorithm is applied in buoyant flow calculations. The buoyancy related numerical instability problem can be experienced in the following ways:

.Strong under-relaxation of the momentum equations is required to avoid numerical divergence in the early stages of an iterative solution. Also a correct (as far as possible) initialization of the variable fields is far more important compared with non-buoyant calculations, in order to avoid early numerical divergence.

.If the under-relaxation of the momentum equations is not sufficiently strong the cumulative errors in the solution of the variables are initially reduced to a certain limit which, however, cannot be made smaller by further iterations. Successive iterations result in oscillations of the cumulative errors around the previously mentioned limit and not in a further reduction. At this stage the

hydrodynamic and mean buoyancy fields do not change substantially over a large number of iterations; however at each node the variables change slightly following an irregular small amplitude oscillation.

The work carried out during this project related to the buoyancy induced numerical instability is reported in some detail in Appendix A3. In the following paragraphs some of the points discussed in the Appendix are briefly presented.

The source of the buoyancy related instability was located as the sequential solution of the coupled momentum and mean buoyancy equations. Depending on the local conditions at each node and in particular on the strength of the horizontal convection and on the buoyancy gradient (local Reynolds and Grashof numbers) the successive separate solution of the coupled equations does not always lead to a solution of the system which these equations constitute; furthermore it may result in unstable growth of errors from iteration to iteration and subsequently to numerical divergence. The unstable error growth mechanism was demonstrated by perturbing the solution of a stably-stratified horizontal convection and by examining under what conditions a sequential solution of the finite difference equations may either damp the original perturbation or result in unstable error growth. From this study a stability condition was developed for this particular case relating the Reynolds number of the flow and the grid spacing to a maximum Grashof number of the flow beyond which stable sequential solution is not possible.

The buoyancy related unstable error growth was removed

in the numerical prediction of the previously mentioned stably-stratified horizontal convection when instead of the common sequential solution algorithm a modified algorithm was used solving the coupled equations locally but simultaneously. The simultaneous solution algorithm was unconditionally stable at any Grashof number for the flow examined while the sequential solutions diverged when the Grashof number of the flow exceeded the analytically derived stability condition.

The simultaneous solution algorithm was however subsequently shown to be unsuitable for practical buoyant calculations due to an extremely low convergence rate. Point-by-point algorithms using simultaneous adjustments of the variables are well-known for their very slow convergence (Roberts (1972), Crossley (1975)) and are not in use for practical calculations of flows with strong body forces (buoyant or swirling).

The remaining solution to the buoyancy related instability problem is strong under-relaxation of the sequential solution of the coupled equations. As was previously mentioned strong under-relaxation is in any case required to avoid numerical divergence in the first stages of solution and in order to achieve an acceptable level of overall errors in the solution. The small amplitude oscillations of the variable fields mentioned above and the difficulty in continuously reducing the cumulative errors of the solution were studied. They were related to local instabilities of the coupled equations which did not result in unstable error growth due to the correcting action of the

pressure correction equation and to the strong under-relaxation.

In certain strongly buoyant flows examined in this project the usually employed static under-relaxation did not result in acceptable levels of overall errors. (The term static under-relaxation is defined in Appendix A3). In these cases a false-transient solution of the momentum equations allowed a more satisfactory level of overall errors (Markatos et al (1982), (1984)). By an appropriate choice of a false time step the alteration of the variables from iteration to iteration can be controlled. The turbulence quantities and the mean buoyancy equations were solved in their steady state form; further, to accelerate the physically slow evolution of the mean buoyancy field in stably stratified buoyant flows the mean buoyancy equation was not under-relaxed at all. It was found beneficial, from the overall errors point of view, to solve the pressure correction equation more accurately at each iteration compared with non-buoyant applications of SIMPLE. Convergence in a steady state situation was assumed when the overall errors were sufficiently low and the variable fields did not substantially change over a large number of iterations. This meant that the solution had to be monitored by plotting the evolution of several critical parameters; the computation was stopped when these parameters reached asymptotic values. Examples are given in Chapter 6 where the false-transient method was widely used. Using the above techniques, satisfactory performance was achieved in all the buoyant flows studied here.

2.4.3. The incorporation of the RSFT model in the computer code

Although the incorporation of the RST model into the computer code used in this project was a rather straightforward operation a few points are worthwhile mentioning.

The locations where the turbulent shear stress and the turbulent fluxes are stored in the finite-difference mesh are shown in figure 2.1. The turbulent shear stress was stored at the mid point of the cell formed from the pressure nodes, as suggested by Pope and Whitelaw (1976). This location does not require any interpolation for the estimation of the shear stress gradients appearing in the momentum equations. Pope and Whitelaw report that they found this double staggering of the shrear stress necessary for stability reasons. The turbulent scalar flux $\overline{u_i b}$ was stored for similar reasons at the staggered point where the mean velocity U_i is stored in the basic mesh (see Patankar (1980)). Again this location does not require any interpolation for the estimation of the turbulent flux gradients appearing in the transport equation of B. When the turbulent fluxes were not staggered, strong wiggles were observed in the mean buoyancy field. Finally, in the RSFT calculation turbulent diffusion is treated explicitly i.e. the Reynolds stress and scalar flux gradients are incorporated in the source terms of the relevant transport equations.

This concludes the description of the mathematical model used in this thesis; further information which was deemed not to fit well into the description given here has been relegated to the appendices A1, A2 and A3. In appendix A2 the first test of the computer code incorporating the new convection discretisation is presented via the prediction of a laminar recirculating flow. The flow was calculated also with the standard Hybrid method and the merits of the higher order scheme could be clearly demonstrated. The following chapter presents further tests of the computer code including, in addition, the second moment closure.

CHAPTER 3

A STUDY OF THE PERFORMANCE OF THE RST MODEL IN TWO NON-BUOYANT RECIRCULATING FLOWS

CHAPTER 3 : A STUDY ON THE PERFORMANCE OF THE RST MODEL IN TWO NON-BUOYANT RECIRCULATING FLOWS

3.1. Introduction

The second moment turbulence closure presented in Chapter 2 has been tested mainly in turbulent flows of a boundary layer nature without recirculation. Very limited evidence exists in the literature about the performance of the model in complex recirculating flows in relation to the more commonly used first moment closures such as the k-ϵ model. Several reasons can be mentioned for the very limited application, so far, of the RST model in such flows. The model was, and still is, under development and researchers have tended to apply the RST closure in relatively simple boundary layer flows for which: i) detailed experimental data concerning the turbulence characteristics can be more easily obtained and ii) special effects on the turbulence structure can be emphasized and studied separately. Such effects are for example the influence of stable stratification on a surface buoyant jet (to be given special attention in the next chapter), the influence of streamline curvature, the effect of a free surface or a wall on the turbulence structure etc. Even the simplest recirculating flows combine several such effects and obviously their prediction requires some confidence about the extent to which the RST model is able to predict the simpler comprising phenomena.

The detailed experimental study of turbulent

recirculating flows is also a rather recent development. During the last decade or so, systematic investigations of turbulent recirculating flows have been carried out and relevant publications have started to appear more frequently in the literature. Several of such works have dealt with relatively simple internal 2-D recirculating flows such as the flow after a step in a plane channel studied by Kim et al (1978) (more recently by Pronchick et al (1983)), the flow in a pipe with a symmetric disc blockage studied by Taylor et al (1984), the flow in a pipe with a sudden expansion by Khezzar et al (1985) etc. It is obvious that the prediction of such relatively simple, 2-D recirculating flows is the next stage for the testing of higher order turbulence closures after their initial testing in boundary layer-like flows.

On the numerical prediction side, the possibilities of using more advanced turbulence models in such complex flows highlighted the problem of the numerical accuracy of the predictions. The use and intercomparison of various alternative models for turbulent diffusion requires the reduction as far as possible of "numerical diffusivities" which can distort to a large and uncertain extent the physics of the flow. This was one of the reasons for the recent intensification of research into more accurate convection discretisation schemes in relation to the commonly used Hybrid or Upwind differencing schemes. This is also the reason, as stated earlier, for the adoption in this work of a third order accurate convection discretisation scheme.

The work presented in this chapter is a comparison of the performance of the standard k-ϵ and RST model in the prediction of two non-buoyant 2-D recirculating flows. This represents the final stage in the development of the computer codes used for the calculations presented in this thesis and served the following purposes:

i) To test the correct incorporation of the transport equation model into the computer code. The code incorporating the RSFT model was to be used in a series of buoyant and non-buoyant recirculating flows for which very limited experimental data and previous predictions were available to validate the current numerical predictions. It was considered therefore necessary to check the RST code in the prediction of recirculating flows for which detailed experimental data and previous predictions were available.

ii) The second purpose of the current work was to study the performance of the quadratic discretisation scheme in conjuction with the two turbulence closures. The code incorporating QUICK had already been tested in the prediction of a laminar recirculating flow (Appendix A2). However in this flow the maximum cell Peclet numbers were of the order of 1Ø whereas in the turbulent flows examined in this thesis the cell Peclet numbers were significantly higher (typically of the order of $1Ø^2$ for k-ϵ predictions and $1Ø^4$ for RST predictions). As mentioned in the previous chapter the convergence problems caused by the negative coefficients of the quadratic scheme are increased in high cell Peclet number solutions. The study of this aspect of the numerical algorithm was the second purpose of the

present work and it was during this work that the mixed QUICK-Upwind scheme was introduced.

It is obvious that both purposes are served by the model intercomparisons presented in this chapter. Concluding this introductory section it should be pointed out that the main interest of the present work was in obtaining numerically accurate and correct applications of the turbulence closures presented in chapter 2. A thorough investigation and computational experimentation aiming to improve model performance was outside the scope of this work.

The flows considered

The only published work where systematic comparisons were carried out between the standard k-ϵ model and the RST model of Launder et al in the prediction of recirculating flows is the work of Pope and Whitelaw (1976). In this work near-wake axisymmetric flows, with or without recirculation, were calculated by both models, using the same grid and set of boundary conditions, and the results were compared with the experimental data. However, the validity of these model comparisons was undermined by the following factors. The discretisation of the convective terms in the transport equations was carried out by means of the standard Hybrid scheme and the numerical predictions were performed with rather coarse grids (26*26 nodes). McGuirk et al (1985) who calculated a similar flow (the flow behind a symmetric disc blockage in a pipe) showed that substantially finer grids (55*50 for the k-ϵ predictions) are required to prove true

grid independence; as the grid was refined further details of the flow were revealed which could not be detected with the coarser grids giving a false impression of grid-independence. Furthermore, detailed experimental data were not available about the conditions at the inlet of the solution domain and the results proved very sensitive to these conditions. Changes in the inlet conditions (transverse velocity,k,ϵ) affected the predictions far more than the turbulence models tested, reducing the validity of the comparison with the experimental data.

Effort was made to avoid the previous drawbacks in the present work. Special attention was given to both the numerical accuracy of the predictions and to the specification of the correct conditions at the inlet of the flow domain.

The flows chosen to test model performance were:

1) The flow in a plane channel with a one-sided downstream facing step. This flow was one of the test cases (No Ø421) used for the comparison of turbulent flow prediction procedures in the recent Stanford conference on complex turbulent flows (1982). The detailed data of Kim et al (1978) were used for the validation of the predictions and for the specification of the inlet conditions. The more recent detailed LDA data of Pronchick et al (1983) -not available initially- were also used for additional experimental information about the flow.

2) The flow in a pipe with a symmetric disc blockage. This

flow has been studied experimentally by Taylor and Whitelaw (1984); detailed LDA data are available. The flow was previously predicted by : McGuirk, Taylor and Whitelaw (1981) (k-ϵ model) and by McGuirk and Taylor (1985) (RST model of Launder et al). The more complex form of the pressure-strain correlation was used in this latter work. The convective terms of the transport equations were discretised by means of the standard Hybrid scheme. Very fine grids were used for the predictions (55*50, k-ϵ; 80*50 RST) selectively refined on the basis of the distribution of estimated numerical errors (McGuirk et al 1985). Both of these previous sets of predictions made this flow ideal not only for a turbulence model comparison, but also for the testing of the current computer program, the main aim of the present chapter.

In the following section the performance of the quadratic scheme and the numerical accuracy of the current predictions are discussed in some detail.

3.2. Computational details, boundary conditions and numerical tests

Step flow. The physical boundaries and dimensions of the flow domain are shown in figure 3.1a. The solution domain began at the expansion cross-section as shown by the dashed lines in the same figure; the length of the domain being equal to 18.4 step heights (H). The problem dependent boundary conditions were as follows. At the inlet the experimental data were used for the definition of the

velocity, turbulence energy and shear stress profiles. The local equilibrium near wall turbulence relationships were used to evaluate the dissipation rate:

$$\varepsilon = k^{3/2} / (c_w \Delta y) \quad , \quad c_w = \kappa \, c_\mu^{-0.75}$$

where Δy is the distance from the respective walls. The normal stresses were defined from the relation $\overline{u^2}:\overline{v^2}:\overline{w^2}$=Ø.96,Ø.52,Ø.52 representing average values of the turbulence anisotropy in a plane channel (Laufer (195Ø)). At the downstream boundary a zero normal gradient condition was assumed for all the variables.

For the k-ϵ predictions four meshes of increasing resolution were used to check grid independence with (21*21),(31*31),(41*41) and (61*61) nodes. In the main flow direction the grid was uniformly expanding with an expansion ratio of 1.15 for the coarser grid decreasing to 1.Ø5 for the finest. In the vertical direction the grid was slightly more concentrated in the lower part of the domain for better resolution in the shear layer and recirculation regions. The number of iterations required for convergence and the corresponding computing times are given in table 3.1. For the RST predictions three meshes were used with (21*21), (31*31) and (41*41) nodes. The grids were exactly the same as for the k-ϵ calculations and the number of iterations and computing times are given in table 3.1.

Table 3.1: Number of iterations and CPU time (AMDAHL V8) for the step problem.

Grid	Turbulence model	Iterations	CPU time in min
21*21	k-ϵ	289	1.32

31*31	k-ϵ	449	4.27
41*41	k-ϵ	636	11.48
61*61	k-ϵ	753	30.14
21*21	RST	284	2.15
31*31	RST	662	10.88
41*41	RST	800	21.07

Convergence problems were encountered in both k-ϵ and RST calculations associated with the negative coefficients of QUICK. These problems are discussed in some detail in section A2.4 of Appendix A2, dealing with QUICK, and therefore are only briefly presented here. The flow is characterized by the existence of an extensive "potential" throughflow region with insignificant turbulence levels. The turbulence quantities thus display steep gradients at the boundary separating the developing shear layer from this potential flow core. This situation is typical for the generation of artificial oscillations or wiggles in the predicted profiles due to the negative finite difference coefficients of QUICK. Small positive and negative values of k, $\overline{u_i^2}$ and ϵ occur at the edge of the layer resulting in practically arbitrary diffusivities ($\sim k^2/\epsilon$, $\sim k\,\overline{u_i^2}/\epsilon$) which inhibited convergence. These problems were removed when the mixed QUICK-Upwind scheme was used for the discretisation of the horizontal convection terms of the turbulence equations. The limiting cell Peclet number for which the shift QUICK-Upwind occured was 10^3 for the RST predictions and 5.10^3 for the k-ϵ predictions. Upwind discretisation took place only over a narrow band within the potential core as

shown, for the finer grid, in figure 3.2a.

For the k-ϵ predictions the momentum equations were discretised with the quadratic scheme while for the RST predictions the spatial oscillations interfered with the solution of the momentum equations also. The problems associated with the negative coefficients of QUICK were exacerbated in the RST calculations; this was to be expected since in the RST algorithm the turbulent diffusion is included in the source terms of the momentum equations and only molecular diffusivities appear in the finite difference coefficients. This results in higher cell Peclet numbers and an increased tendency for large negative coefficients all over the solution domain. In the RST calculations the mixed scheme had to be applied for the discretisation of the horizontal convection term of the momentum equations also with a limiting cell Peclet number of 10^4. The region of the solution domain where Upwind differencing was applied is shown in figure 3.2b. For the flow in question, the vertical velocities were in general lower than the horizontal and consequently the vertical convection terms were discretised using QUICK all over the domain.

Results of the grid-dependence checks are shown in figure 3.3 for the k-ϵ predictions and in figure 3.4 for the RST predictions. The parameters chosen for plotting in figures 3.3 and 3.4 were the transverse velocity at the step level and the maximum cross-sectional value of the turbulence energy and shear stress (for the RST predictions). The quantities were normalized by the velocity in the potential core $U_\emptyset$ at the expansion cross-section.

These parameters were found to be the most sensitive to grid resolution. As shown in these figures negligible changes in predictions were observed beyond the (31*31) level. The demonstrated grid independence allowed a safe comparison between the two turbulence closures since the predictions are clearly free of numerical errors.

Finally, for the transport equation predictions two versions of the model were tested, in the first (Model IIa) the influence of the walls on the turbulence structure was ignored and in the second (Model IIb) the wall corrections of the modelled pressure strain correlation were taken into account as described in chapter 2. A linear relationship was assumed for the wall effects function f:

$$f = \frac{k^{3/2}}{c_w \Delta y \ \varepsilon}$$

The proportionality constant c_w is chosen to give an f value of unity in local equilibrium near wall turbulence. (This value of f was assumed by Gibson and Launder (1978) in the derivation of the wall correction constants c_1' and c_2'). It was shown in chapter 2 that for such a case the dissipation rate is estimated from the relationship:

$$\varepsilon = \frac{k^{3/2} \ c_\mu^{3/4}}{\kappa \ \Delta y}$$

Combining the last two relations we have close to the wall:

$$f = \frac{\kappa}{c_w c_\mu^{3/4}} = 1 \rightarrow c_w = \frac{\kappa}{c_\mu^{3/4}}$$

The exact definition of f is shown in figure 3.5. The upper wall does not influence the turbulence structure in

the shear layer due to the existence of the turbulence free potential core in between. The influence of the step wall was considered of minor importance and was not taken into account in the definition of f.

The disc blockage pipe flow. The physical boundaries and dimensions of the flow domain for this case are shown in figure 3.1b. The solution domain started at the downstream facing side of the disc as shown by the dashed lines in the same figure. The length of the domain was equal to 12 disc radii (Rd). The problem dependent boundary conditions were as follows. At the inlet the experimental data were used for the definition of the axial and transverse velocity profiles. A uniform turbulence energy profile was assumed at a level indicated in the experiments reported by Taylor and Whitelaw (1984) i.e. $\emptyset.\emptyset5*U_{\emptyset}^2$ where $U_{\emptyset}$ is the bulk velocity at the disc cross-section. For the dissipation rate a uniform value based on a length scale equal to the annulus width was used. The normal stresses were defined from the relation $\overline{u^2}:\overline{v^2}:\overline{w^2}=\emptyset.96,\emptyset.52,\emptyset.52$ and the shear stress was defined from the relation $|\overline{uv}|/k=\emptyset.3\emptyset$. At the outflow boundary a zero normal gradient condition was assumed for all variables.

For the k-ϵ calculations the quadratic differencing scheme gave no problems and could be used everywhere for all variables while for the RST calculations the mixed QUICK-Upwind scheme had to be applied for the discretisation of the horizontal convection terms in the momentum equations for a zone close to the pipe wall -figure 3.2c. The

corresponding limiting cell Peclet number had the value of 10^4. To check grid independence four meshes of increasing resolution were used for the k-ϵ calculation with (24*29), (34*38), (41*49) and (42*50) nodes. For the three first meshes the grid was uniformly expanding in the main flow direction, with an expansion ratio of 1.1; in the radial direction the grid was slightly concentrated in the region of the disc tip. The parameters chosen to check grid dependence were the axial velocity and turbulence energy at the axis of symmetry, figure 3.6. As shown in this figure negligible changes occured as the grid was refined so that it could be justifiably assumed that grid independence had already been achieved. However previous experience from the prediction of the flow (McGuirk et al 1981) had shown that the results were very sensitive to the grid spacing in the main flow direction close to the disc for two reasons:

i) the experimental data show considerable transverse velocities at the disc cross-section and the simulation of the evolution of the slope of the separation streamline in this region required very fine grids. ii) steep axial velocity gradients occur close to the wall within the recirculation bubble which result in an intense production of k. In the previous calculations of McGuirk et al (1985) very fine grids were required to resolve these details of the flow ((55*50) for k-ϵ and (80*50) for RST). For these meshes the grid lines were particularly concentrated close to the disc tip in both directions and close to the stagnation point in the axial direction. A fourth k-ϵ calculation was carried out to resolve these details of the

flow. The grid had (42*5Ø) nodes and was constructed on the basis of the (24*29) grid with additional nodes placed in the previously mentioned regions (i.e. disc tip and stagnation point -figure 3.7). The predictions for the centreline velocity remained the same (figure 3.6) but some changes (+8%) occured in the predicted centreline turbulence energy. Further comparisons showed that the changes were everywhere of the order of 2% for the velocity field and 8% for the turbulence energy. Thus, even though the gradual "uniform" refinement of the grid showed all signs of grid indepedence, the selective refinement produced changes from the previous solutions. However, the relatively small changes observed led to the acceptance of the previously described level of accuracy for the predictions in question (42*5Ø grid). For the RST prediction the same (42*5Ø) selectively refined grid was used. The number of iterations and CPU time required for the disc flow calculations are given in table 3.2.

TABLE 3.2: Number of iterations and CPU time (AMDAHL V8) for the disc problem.

Grid	Turbulence model	Iterations	CPU time min
24*29	k-ϵ	435	2.5
34*38	k-ϵ	663	7.29
41*49	k-ϵ	719	12.85
42*5Ø	k-ϵ	1ØØØ	18.79
42*5Ø	RST	135Ø	4Ø.59

3.3. Results and discussion

3.3.1. Step flow

The two versions of the transport equation model gave very similar mean velocity field results. The differences between Model IIa and IIb predictions normalized by the potential core velocity ($U_\emptyset$) were of the order of 1%. Therefore, in the corresponding figures only model IIa results are plotted though model IIb results would lie very close.

a. Recirculation zone

Figure 3.8a shows the k-ϵ predictions for the separation streamline and the locus of zero axial velocity location; figure 3.8b shows the same parameters for the RST model IIa. Both calculations predict a reattachment distance of 6.3 step heights, an underprediction of 10% from the measured value of 6.7H. The k-ϵ prediction is in the upper end of the range reported for the standard k-ϵ model at the Stanford Conference (5.3H-6.7H) and is in good agreement with the value obtained by Hackman et al (1984) (=6.2H) who used a different (curvilinear orthogonal) mesh system and a different convection discretisation (skewed upwind differencing). Although the RST model predicts a similar bubble length, significanly closer agreement is observed for the velocity reversal locus and for the fuller shape of the bubble at its downstream end. Only after five step heights from the expansion do noticeable differences with the

measured data occur.

b. Velocity profiles

RST and k-ϵ predictions for the axial velocity are compared with the data in figures 3.9a to 3.9e for five cross-sections located before, close to and after the reattachment point. The k-ϵ predictions for the backflow region show a too peaked shape with the maximum velocity occuring close to the wall. The same shape can be observed in the k-ϵ predictions presented in the Stanford conference proceedings and by Hackman et al (1984). In contrast, both measurements and RST predictions show a much flatter shape within the backflow region. Although the absolute level of the negative velocity is substantially smaller in the RST predictions than in the data, the shape of the profile in this region and the gradient in the shear layer are much better represented. It should be pointed out that the peaky k-ϵ prediction cannot be attributed exclusively to the use of log-law functions as these were also used in the RST calculations. The flatter velocity profile predicted by RST is associated with a more accurate prediction of the shear stress profile close to the step (see discussion below).

At further distances downstream, the RST predictions are always closer to the data in terms of shape. However, at the furthest downstream locations the momentum deficit in the redeveloping boundary layer is substantially larger in both predictions than in the measurements. A question arises here however on the mass flowrate in the channel corresponding to the measured velocities. From figures 3.9d and e, it can be

seen that at these locations the flowrate is apparantly larger in the experiment than in the calculations (which certainly conserve mass at all cross-sections of the solution domain). This feature is also to be seen in the comparisons shown by Mansour et al (1983) and by Hackman et al (1984) where the area under the predicted velocity curves is clearly less than under the measured data. It is possible that side-wall boundary layer growth in the experiment caused acceleration in the centre plane of the channel. One further point should be made with reference to the RST predictions for the furthest downstream velocity profiles. These profiles clearly display a point of inflection close to the lower wall and a probable two layer nature of the boundary layer. This is not present in the k-ϵ predictions, or in the data included in figure 3.9, but is to be observed in the more recent LDA data reported by Pronchick and Kline (1983) (figure 3.1Ø). This is a further indication that the RST model represents the shape of the velocity profile better than k-ϵ, even in the redeveloping boundary layer part of the flow.

c. Static pressure coefficient

Figure 3.11 completes the comparisons of the mean quantities by showing the prediction of the static pressure coefficient on the step-side wall. A substantial improvement in the predictions is brought about by the use of RST. As for the RST predictions for the axial velocity the agreement is good before reattachment but starts to deteriorate close to the reattachment region.

d. Turbulence kinetic energy and Reynolds stresses

Comparisons of both model predictions with measurements for the turbulence kinetic energy are shown in figures 3.12 and 3.13. Figure 3.12 shows the longitudinal development of the cross-sectional maximum of the turbulence energy. The predictions obtained using both versions of the transport equation model are shown in figure 3.12; only small differences can be observed (of the order of 3%) occuring mainly downstream of the reattachment point. The k-ϵ and RST predictions practically coincide after the reattachment point though relatively small differences (<10%) can be observed before reattachment. Both models predict a too rapid increase of the turbulence energy and a too rapid decay after a peak value is reached. As a result, close to the step, the cross-sectional maximum of k is significantly overpredicted whereas in the downstream part of the domain it is underpredicted by 50% of the experimental values. The peak turbulence energy value ,k_{max} (all over the domain) occurs at the cross-section x=4.3H (k-ϵ), x=4.6H (RST) and x=8.5H (experiment); the numerical value of k_{max} is $k_{max}/U_{\emptyset}^2$=4.15% (k-ϵ), 3.8% (RST) and 4.1% experiment. It is clear from this that both models predict incorrectly the development of the turbulence energy and that the transport equation model did not bring about improvements in this respect.

The discrepancies between data and predictions mentioned above are reflected in the turbulence energy profile comparisons shown in figure 3.13a to d. The shape of the

profile is generally well predicted but the quantitative comparisons are not satisfactory. Two noticeable improvements can however be observed in the RST predictions. The first concerns the shape close to the step (shown in figure 3.13a) where the peaky pattern observed in the experiments was reproduced by RST, whereas k-ϵ showed a too diffused shape. The second concerns the gradual reduction of k at the border of the mixing layer and the potential core displayed by the data. RST reproduced this feature of the profile whereas k-ϵ showed a too steep reduction of k in this area.

In figures 3.14a to d the pedictions of the axial normal stress $\overline{u^2}$ are compared with the data. Expectedly the transport equation model predicts the axial stress profiles significantly better than the eddy viscosity model, both in terms of shape and values. However, the incorrect prediction of the maximum cross-sectional k mentioned above is reflected in these profiles also resulting in poor quantitative agreement. Model IIb predicts a further enhancement of the axial normal stress at the expense of the vertical component which is damped in the near wall region.

Shear stress profiles are shown in figure 3.15. The observations made for the turbulence energy profiles hold for the shear stress component also. Close to the step RST predicts (as for k and $\overline{u^2}$) a peaky $\overline{uv}$ profile in relation to the fuller shape predicted by k-ϵ. The lower RST $\overline{uv}$ values cause the better prediction of the velocity profile in the backflow region.

Finally, figure 3.16 shows the model IIa predictions for

the longitudinal development of the maximum cross-sectional values of $\overline{u^2}$, $\overline{v^2}$, $\overline{w^2}$ and k together with the corresponding experimental data for $\overline{u^2}$, $\overline{v^2}$ and k. Measurements for $\overline{w^2}$ were not made and k was derived on the assumption: $\overline{w^2}=\overline{v^2}$. The predictions for the cross-sectional maximum values of $\overline{v^2}$ and $\overline{w^2}$ show relatively small differences between the two stresses (<10%); hence, at least on the basis of the predictions, the previous approximation is a reasonable one and would result in an overestimation of measured k of the order of 3% only. As for the turbulence kinetic energy, the cross-sectional maximum values of the normal stresses initially increase too rapidly and subsequently decay too rapidly. Consequently close to the step the stresses are overpredicted whereas at the downstream part of the domain they are underpredicted by 50% of the experimental values. The relative size of the stresses $\overline{u^2}:\overline{v^2}:\overline{w^2}$ is only qualitatively predicted. It is clear from figure 3.16 that the axial component is in general overpredicted and assumes values close to the turbulence energy values whereas in the experiments the axial component was always significantly smaller than k. Model IIb predictions were even worse in this respect. Both data and predictions show that downstream from the location where the peak k and $\overline{u^2}$ values occur the relative size of the stresses $\overline{u^2}:\overline{v^2}$ is decreased showing a tendency towards isotropy. In the experiment the ratio $\overline{u^2}:\overline{v^2}$ is decreased from 1.56 to 1.26 within 7 step heights whereas in the predictions $\overline{u^2}:\overline{v^2}$ is reduced from 1.81 to 1.67 within 11 step heights. Therefore, though the model contains return to isotropy mechanisms (through the pressure-strain model)

their impact is far less vigorous than the experimental data suggest.

Concluding this discussion of the prediction of turbulence quantities, it is clear that though both models (and particularly RST) predict correctly all the observed qualitative trends the quantitative agreement is rather poor.

3.3.2. Disc flow

Mean velocity

An analogous comparison of separation streamlines and velocity reversal lines for the disc flow problem is presented in figure 3.17a for the k-ϵ model and 3.17b for RST model. In comparison with the measured free stagnation point location (3.5*Rd) k-ϵ underpredicts the bubble length slightly (3.28*Rd) and the RST model overpredicts this length by a greater margin (4.5*Rd). As in the plane flow case the prediction of the locus of zero axial velocity is improved by the RST model. Improvements in the shape of the velocity profile in the backflow region similar to the plane flow were also observed, figure 3.18. In the downstream wake flow axial velocity profiles are similar for the two models in that both show a too large deficit in velocity at the centreline. This can be discerned in figure 3.19 which represents the development of the centreline velocity. Good agreement is obtained between the present k-ϵ prediction and that of McGuirk et al (1981). The transport equation predictions of McGuirk and Taylor (1985), who used the more

complex form of the pressure-strain correlation model, are also included in figure 3.19; relatively small differences with the present RST predictions result. The major improvement brought about by the RST model is a better prediction of the location of the peak backflow velocity, although the level is still under-predicted by 25%. The slow rate of recovery in the wake region was attributed by McGuirk et al (1981) to the use in the k-ϵ predictions of a constant c_μ value associated with local equilibrium, a condition not obeyed in the wake region. In figure 3.19 it is clear that the slow rate of recovery is present in the RST calculations as well. It is probable then that the cause is in the large underprediction of the levels of turbulence energy in the vicinity of the free stagnation point. This underprediction was observed in the k-ϵ predictions and has not been improved at all by moving to an RST model as discussed in the following paragraphs.

Turbulence kinetic energy - Reynolds tresses

The turbulence kinetic energy predictions show errors of the order of 50% of the experimental values. In figure 3.20 k profiles are shown at two axial locations before and after the free stagnation point. The better agreement of k-ϵ with the data in the first profile is coincidental as it can be seen in figure 3.21 where the centreline turbulence energy is shown. The downstream k profiles in figure 3.20 are, for both models, wrong both in terms of values and shape.

It was speculated by McGuirk et al (1981) that the k-ϵ

deficiancy in the turbulence energy predictions could be caused by the model's inability to represent the normal stress-normal strain production terms properly:

$$P = \underbrace{-\overline{uv}\left(\frac{\partial U}{\partial r}+\frac{\partial V}{\partial x}\right)}_{\text{Shear stress Production}} + \underbrace{\left(\overline{v^2}-\overline{u^2}\right)\frac{\partial U}{\partial x}-\overline{w^2}\frac{V}{r}+\overline{v^2}\frac{V}{r}}_{\text{Normal stress Production}}$$

This feature still remains in the RST calculations as shown by the distribution of the two contributions to the production of k from shear and normal stress terms in the profile drawn in figure 3.22 at an axial location near reattachment. Although positive values of the normal stress term are obtained near the axis they represent only about 1Ø% of the maximum shear stress production. Estimates made from the measurements of this flow reported by Taylor and Whitelaw (1984) show that the maximum values should be of the same order, so that even in the RST calculations the normal stress production is too small by an order of magnitude. As can be seen from the form of the terms in the previous expression this can come about because of a significant error in the prediction of the differences between the normal stresses or of the velocity gradients (or of both). Figure 3.23 addresses the question of prediction of the anisotropy levels by plotting the ratios of the individual normal stresses to k for the centreline (along which the $\partial U/\partial x$ predictions are not disastrously in error, figure 3.19). Surprisingly the k-ϵ predictions shown in figure 3.23 lie in closer agreement with the data than the RST predictions.

In the k-ϵ predictions the normal stresses are

calculated from the eddy viscosity relation:

$$\frac{\overline{u_i^2}}{k} = \frac{2}{3} - 2\, c_\mu \frac{k}{\epsilon} \frac{\partial U_i}{\partial x_i}$$

Along the centreline, the velocity gradients are at least qualitatively correctly predicted; their local values dominate the levels of the individual stresses in the k-ϵ prediction resulting in a qualitatively correct partitioning of the stresses along the centreline (it seems also that the predicted time scale k/ϵ at least does not adversely affect this result).

The turbulence anisotropy for the RST predictions was examined along the separation streamline. Initially at the more or less horizontal part of the shear layer the axial component is correctly predicted to be larger than the transverse component ($\overline{u^2}=1.7\overline{v^2}$). As the flow approaches the stagnation point , the $\overline{v^2}$ component is gradually increased giving a value at the stagnation point of $\overline{v^2}=1.\emptyset 5\overline{u^2}$. This trend is certainly in the right direction, but is much too weak as the experiment indicates a ratio of $\overline{v^2}=2.66\overline{u^2}$. As the fluid is recirculated within the bubble the RST model correctly predicts the reversal of the relative size of the stresses but since the "initial" condition at the stagnation point is wrong the inadequate separation is reflected all along the bubble length.

Multiple factors affect the RST prediction of normal stresses at the stagnation point so that further speculation as to which of the modelled terms of the Reynolds stress transport equations is responsible for the deficiencies

would be unfounded without further analysis and computational experimentation. As previously mentioned, such a task was considered to be out of the main scope of the present work. However it is clear that improvement in the major deficiencies of the RST predictions i.e. the slow velocity recovery after the stagnation point and the severe underprediction of the turbulence energy at the vicinity of the stagnation point cannot be achieved until the turbulence anisotropy in this region is correctly predicted.

3.4. Summary

The main conclusions drawn from the present work may be summarised as follows:

I) The numerical accuracy checks for the step flow showed that the quadratic differencing scheme gave grid independent results with a reasonable size mesh. The disc flow numerical checks emphasized the importance of a selective grid refinement.

II) The RST predictions for both flows showed noticeable improvements in the shape of the velocity profiles in the backflow region compared with the eddy viscosity calculations.

III) The near reattachment region was clearly identified as the problem region whether it was onto a wall or a free stagnation point as in the disc flow. In the axisymmetric case particularly the problem seems to be associated with the inability of the RST model to predict and sustain the large anisotropy levels observed in the measurements. Until

this is achieved neither the large underprediction of the turbulence energy nor the discrepancies in the rate of redevelopment of the momentum deficit region can be reduced.

As was mentioned above the aim of the work reported in this chapter was to test the computer code incorporating the new discretisation scheme and the transport equation model in the prediction of two-dimensional recirculating flows. With this task succesfully accomplished the developed code was applied to buoyant and non buoyant recirculating flows more closely related with the final task of this project. The first application concerns the internal hydraulic jump flow presented in the following chapter.

CHAPTER 4

THE PREDICTION OF THE BUOYANT SURFACE LAYER

CHAPTER 4 : THE PREDICTION OF THE BUOYANT SURFACE LAYER

The present Chapter deals with the prediction of a two-dimensional buoyant surface layer. The review in Chapter 1 emphasized that such a layer is an important component of the vertical buoyant jet in shallow water after impingement. Its prediction, therefore, forms a necessary intermediate stage both in terms of model development and understanding of the physical phenomena involved. The plane layer has been the subject of the great majority of the previous experimental and analytical work. Limited experimental evidence for the axisymmetric buoyant surface jet (Anwar, 1972) suggests a behaviour similar to the one observed in the plane jet experiments of Ellison and Turner (1959) and Chu and Baddour (1984) which are discussed below. Previous published works on the radial hydraulic jump are not available. A brief integral analysis of the subject was presented by Lee and Jirka (1981) in the context of their study of the round vertical buoyant discharge in shallow water.

The work reported in this Chapter concerns the plane layer since -as indicated above- only for this case were reliable data available for the validation of the predictions. The radial buoyant surface layer is examined in Chapter 6 in the context of the vertical buoyant discharge in shallow water.

The present Chapter is divided into four sections with appropriate subsections. Section 4.1 introduces the observed physical nature of this flow. The two possible evolutions,

i.e. the entraining surface jet and the internal hydraulic jump are distinguished and previous experimental and predictive works are reviewed. Section 4.2 deals with the prediction of the surface jet, followed by section 4.3 on the prediction of the internal hydraulic jump. The Chapter concludes with a summary of major findings.

4.1. Physical phenomena occuring in buoyant surface layers

Buoyancy forces play a significant role in the development of a surface layer both in terms of creating excess hydrostatic pressure forces, which (in the case of a three-dimensional layer) drive rapid spreading of the layer in the horizontal plane, and because of the strong turbulence damping action due to the stably stratified nature of the warm floating layer. The entrainment into the surface layer is strongly influenced by this latter phenomenon. It is the simulation of this aspect which is studied in the present Chapter using various turbulence models.

A comprehensive experimental investigation of a two-dimensional plane buoyant surface layer has been published recently by Chu and Baddour (1984). The original, often-quoted data of Ellison and Turner (1959), however, laid the foundation for the phenomenon of stably stratified reduction of turbulent entrainment. The experiments of Chu and Baddour, complemented by an earlier study (1975) were conducted using fresh water discharging over saline water in an experimental arrangement sketched in figure 4.1. These

authors and other studies (Wilkinson 1971, Stefan 1970) have shown that this type of flow can develop in two ways for any given conditions (mean velocity, mean density deficiency, depth of flow) at the discharge, as long as these conditions correspond to a supercritical flow; i.e. a discharge densimetric Froude number greater than unity, viz:

$$Fd = \frac{U_{\emptyset}}{\sqrt{\frac{\Delta\rho_{\emptyset}}{\rho_a} g D}} > 1$$

Which of the two possible states of the flow occurs depends on the details of the downstream control provided by a combination of (i) the amount ($\dot{Q}e$) of make-up water supplied to compensate for the entrainment into the surface jet, and (ii) the depth of the flow (h) at the exit from the test section dictated by the location of the skimmer. The provision of make-up water is an essential improvement in the experiments of Chu and Baddour over the system used by Ellison and Turner and is necessary to enable a steady flow situation to be achieved.

The first possibility for the layer behaviour is the so-called maximum or fully entraining jet. The jet thickness grows gradually (as expected in a turbulent shear layer) over the whole test section, although the rate of growth diminishes rapidly as the flow develops due to the stable stratification effects mentioned above. This situation occurs when the skimmer is lowered to allow the downstream depth of the layer to be that achieved when entrainment is permitted to take place until it dies out completely. Under these conditions there is no effective downstream control

(the make-up water is there only to ensure a steady state). An integral analysis may be performed (Wilkinson (1971) and Baddour and Chu (1975)). This indicates that -in contrast to the isothermal surface jet- the total volume flow in the layer cannot increase continuously but a maximum value exists -for any set of initial conditions- beyond which any further entrainment is incompatible with the integral constraints of the flow (i.e. salinity and momentum conservation). The exact values of the maximum flowrate and the corresponding layer Froude number depend on assumptions made for the shapes of velocity and density deficiency profiles within the layer. The integral analysis imposes only conservation of momentum and density deficiency constraints on the flow and takes no account of the details of the entrainment mechanism or how the stratification influences this. It is therefore possible that in strongly buoyant situations turbulence may collapse and entrainment cease at a Froude number higher than the minimum value imposed by the integral constraints. The critical downstream values in a fully entraining layer and the distance over which they are achieved form a suitable and specific test for the ability of a turbulence model to predict accurately the stably-stratified damping phenomenon. Hossain (1980), and Gibson and Launder (1976) have made calculations of this type of flow and have both adopted an algebraic Reynolds stress/scalar flux level of closure, reproducing the entrainment damping phenomenon well. These calculations were, however, performed before the detailed profile data of Chu and Baddour were available to test model performance.

The second flow condition observed to be possible is that the gradual growth of the jet is terminated by a rapid increase in depth accompanied by the appearance of a recirculating flow zone commonly referred to as a roller region. This second possible state is categorized as an internal hydraulic jump to emphasize that it is the equivalent in this smoothly varying density flow of the well known free-surface hydraulic jump. This condition occurs when the skimmer downstream is raised above the position where it first meets the critical depth defined above under fully entraining conditions. The extra resistance introduced into the flow by the downstream control requires a depth of flow greater than that which can be achieved by entrainment i.e. a subcritical flow immediately prior to the skimmer. As in the free-surface case the transition from supercritical to subcritical state can only be achieved by the appearance of an energy dissipating roller which effects the required increase in layer depth. Experimental evidence for this kind of behaviour was reported by Wilkinson (1971) and Stefan (1970) and by Baddour and Chu (1975) for the present geometry; measurements show that entrainment takes place predominantly in the region before the roller. The amount of entrainment is fixed by the downstream control and once more the turbulence model will dictate the distance from the discharge to the toe of the hydraulic jump. The recirculating nature of this second kind of flow behaviour necessitates the use of computationally more complex forms of the governing equations.

The internal hydraulic jump studied by Wilkinson (1971)

has been calculated previously by Leschziner (1979); again a form of the algebraic stress/flux model was chosen. The difficulty of applying the complete algebraic model equations in this recirculating flow encouraged the use of an approximate form of the model. The algebraic equations were used only for the shear stress and the transverse scalar flux and were derived on the assumption of a boundary layer-like nature of the flow. This assumption allows the derivation of explicit algebraic relations for the shear stress and transverse flux but cannot be theoretically justified in the recirculating part of the flow. The normal stresses and the axial flux were calculated from the normal k-ϵ eddy viscosity. Good qualitative behaviour was observed in these calculations; the predictions compared satisfactorily with the limited amount of data available i.e. the post-jump layer depth, Froude number and flowrate. The shape of the velocity and mean buoyancy profiles were reproduced though detailed comparisons were not possible due to the lack of data. Also the predictions for the length of the entraining and recirculating parts of the flow could not be validated for the same reason.

In the following parts of the Chapter the two possible evolutions of the flow are examined separately.

4.2. The prediction of the fully entraining buoyant surface jet

The experimental data of Chu and Baddour (1984) for the fully entraining jet show that the mean velocity profile

can be approximated by a Gaussian curve and the mean buoyancy profile by a linear relationship; also that the two profiles have the same thickness. These two characteristics clearly differentiate the buoyant surface jet from the neutral jet which is known to have an approximately Gaussian scalar profile wider than the velocity profile (see e.g. the compilation of experimental data for neutral jets by Gibson and Launder (1976)).

The linear profile of the buoyancy is rather surprising. Since there is no mass transfer across the free surface, the vertical buoyancy gradient should be zero at the free surface at least for a thickness relevant to the molecular diffusion length scale. However, the molecular diffusion length scale is very small to contradict a linear profile up to very close to the surface. It is shown below that the almost linear buoyancy profile could not be predicted by the buoyancy extended k-ϵ model. Thus, it was decided that a stress-flux transport model should also be tested in order to allow the buoyancy and free surface effects to be taken into account more accurately. The various models used are described in the next section.

4.2.1. The mathematical model

The governing Partial Differential Equations and the set of transport equations constituting the turbulence closures tested in this work were presented in Chapter 2. In the following paragraphs additional information is provided for their application to this particular problem.

i. For the current calculations advantage was taken of the boundary layer-like nature of the flow. The changes in the velocity, buoyancy, etc fields are far more important in the transverse (y) than in the longitudinal direction. In such a case the longitudinal diffusion can be ignored on order of magnitude arguments. Furthermore, taking into account the nearly horizontal character of the flow, and hence the relatively insignificant vertical acceleration, the lateral momentum equation was approximated by a hydrostatic pressure distribution :

$$-\frac{d\,P}{d\,y} + \rho_a\ g\ B = 0$$

Taking into account that for $y \to -\infty$ (figure 4.1) the fluid is undisturbed and hence the streamwise derivative of the pressure is zero, the streamwise pressure gradient within the layer was expressed as:

$$\frac{d\,P}{d\,x} = \frac{d}{dx} \int_{-\infty}^{y} \rho_a\ g\ B\ dy$$

ii. The turbulence models tested are the buoyancy extended $k-\epsilon$ model and the Reynolds stress flux transport model of Launder et al (1975); the models will be referred to as Model I and Model II respectively. Two versions of the latter model were tested: In the first, (Model IIa) the free surface is consistently treated as a plane of symmetry assuming that it does not affect, in any way, the turbulence structure. In the second version (Model IIb) the free surface corrections were added to the pressure-strain and pressure-buoyancy gradient correlations in the way described

in Chapter 2. The free surface effects function (f) was defined as a linear function of the ratio of the turbulence length scale ($\simeq k^{3/2}/\epsilon$) to the distance from the free surface n :

$$f = \frac{k^{3/2}}{c_w\, n\, \epsilon} \qquad , \; c_w = \frac{\kappa}{c_\mu^{0.75}}$$

the proportionality constant c_w was chosen so that the function f takes on a value of unity in local equilibrium near-wall turbulence. In Model I the turbulent Prandtl number had the near-wall average value σ_T=Ø.9.

iii. In the form of the dissipation equation finally adopted the buoyancy destruction term appearing in the $\overline{v^2}$ or k equations was not included in the production term of ϵ. Rodi (198Ø) recommends the inclusion of a buoyancy term in the dissipation production as follows:

$$P_\varepsilon = c_{\varepsilon_1} \frac{\varepsilon}{k} (P + G) (1 + c_{\varepsilon_3} Ri)$$

where for the present flow $P = - \overline{uv} \frac{\partial U}{\partial y}$, $G = g\, \overline{vb}$ and $Ri = - \frac{G}{P+G}$

$$\text{thus} \quad P_\varepsilon = c_{\varepsilon_1} \frac{\varepsilon}{k} (P + (1 - c_{\varepsilon_3}) G) \quad \text{with} \quad c_{\varepsilon_3} = 0.80$$

$$\text{or} \quad P_\varepsilon = c_{\varepsilon_1} \frac{\varepsilon}{k} (P + \alpha G) \qquad \text{with } \alpha = 0.2$$

i.e. Rodi's suggestion is equivalent to a partial inclusion of the destruction by buoyancy in the production of the dissipation. In order to investigate this proposition the following production term for ϵ was assumed:

$$P_\varepsilon = c_{\varepsilon_1} \frac{\varepsilon}{k} (P + \alpha G) \qquad \text{with } 0 \leqslant \alpha \leqslant 1$$

A parametric study was carried out varying α from zero to unity in the calculation of a buoyant surface jet with a discharge Froude number of 12. The recommended value of

c_{ϵ_3} =Ø.8 (α=Ø.2) gave almost identical results with α=Ø. The variation of the jet width and decay of surface velocity with α is rather insignificant, figure 4.2. This lack of sensitivity is in contrast to the results of Rodi(1979) for the horizontal jet. This is probably due to the use of the transport equations for the turbulent stresses and fluxes and the different treatment of the near surface effects. In view of these results all further calculations were performed omitting buoyancy destruction terms in the ϵ equation.

iv. The use of an algebraic stress/scalar flux version of Model II was examined in the present work, but was abandoned for the following reasons. The local equilibrium version of the algebraic model was not appropriate for the present case since near the free-surface (whose influence is crucial) this approximation does not hold. The version of the algebraic model used by Gibson and Launder (1976) (which approximates the transport terms using algebraic relations) also caused difficulties in the present flow. Negative values of the transverse normal stress $\overline{v^2}$ were predicted near the surface when the near surface damping correction involving the function f was introduced. Similar difficulties were reported by Hossain (198Ø) ,and since as shown below, the use of the additional damping correction is essential to reproduce the measured behaviour, the algebraic approximation was abandoned in favour of the transport equation approach which gave no problems in this respect.

4.2.2. Computational details

The set of governing Partial Differential Equations are parabolic in nature and were solved by means of the Patankar-Spalding procedure (1970) encoded in the GENMIX computer program. Following the practice adopted for the elliptic stress-flux computer code (described in Chapter 2) the shear stress and the transverse scalar flux were calculated at the mid-node points instead of the usually employed main node storage. The pressure gradient dP/dx was calculated from the discretised version of the equation:

$$\left(\frac{d\,P}{d\,x}\right)_y = \frac{d}{dx}\int_{-\infty}^{y} \rho_a\, g\, B\, dy$$

already given above. The calculation of velocities at each station requires the knowledge of the axial pressure gradient which depends on the as yet unknown distribution of the buoyancy B at the same station. To avoid this shortcoming the pressure gradient at each node was defined on the basis of the calculated profiles of buoyancy at the two previous upstream stations and extrapolated to the station under calculation. This extrapolation imposes limitations on the forward marching step of the integration in order to ensure the conformity of the velocity and buoyancy profiles with the integral constraint of momentum conservation.

As far as boundary conditions are concerned, uniform $U, B, k, \epsilon, \overline{u_i^2}$ and $\overline{u_i b}$ profiles were prescribed at the inlet. The homogeneous shear layer anisotropy ratios defined the normal stresses. A linear shear stress profile was assumed

with a maximum value $|\overline{uv}|/k = 0.3$. Zero values of $\overline{ub}$ and $\overline{vb}$ were accepted in the absence of any relevant information. The inlet values of k and ϵ had a clear but not deciding influence on the results particularly close to the discharge. Plausible values were chosen for k and ϵ (e.g. $\sqrt{k}/U_0 = 5\%$) and were tested and altered in preliminary runs to ensure that they reproduced the experimental spreading of the jet and mass flux close to the discharge. At the entraining boundary the fluid was assumed quiescent with zero buoyancy and zero turbulence quantities. The free surface was treated as a plane of symmetry for all variables except for $\overline{uv}$ and $\overline{vb}$ where zero values were prescribed.

The numerical grid had thirty six nodes across the layer for the surface jet calculations and forty six nodes for the mixing layer calculations to be reported below. The marching step of the integration was gradually increased from 0.01% to 1% of the layer half velocity width. For this mesh configuration the results were practically grid-independent. Several checks were made to ensure this; the results were the same in predictions having 26, 36 and 46 nodes across the layer. Also the forward step was halved with insignificant influence on the results. For both values of the axial stepsize overall momentum and salinity constraints were fully satisfied. The calculations were performed on an AMDAHL V8 computer and required approximately 2 minutes of CPU time.

4.2.3. Results and discussion

The experiments of Chu and Baddour were examined and the data which best satisfied overall momentum and salinity flux conservation were chosen as the first test for model comparisons, figure 4.3. The discharge Froude number for this case was 12. The test conditions are shown in table 4.1.

TABLE 4.1 : Test conditions of the fully entraining layer experiments.

	surf. jet	mixing-layer
Velocity at the exit $U_{\emptyset}$ (m/s)	0.232	0.145
Depth at the exit D (cm)	0.777	2.010
$\Delta\rho_{\emptyset}/\rho_a$ %	0.50	2.1
Froude number at the exit F_d	12.	2.3

Figure 4.4 shows the performance of the three models on the basis of the downstream development of surface velocity and buoyancy , the increase of the velocity profile half width and the total flow in the surface layer. The buoyancy extended k-ϵ model overpredicted the growth of the jet and consequently resulted in too rapid decay of the surface values. In general the transport equation Model IIa performed better but only marginally so in the case of the surface buoyancy for reasons related to the shape of the mean buoyancy profile which are discussed below. The variant (b) of model II which accounted for damping of the transverse component at the free surface was able to simulate all four parameters plotted in figure 4.4 well and was the only model capable of predicting the density

deficiency accurately in the far downstream region. That this model adequately simulates the stably stratified damping of turbulence is demonstrated in figure 4.5 where an entrainment coefficient versus Richardson number curve predicted by the three models is compared with the data given by Chu and Baddour, and Ellison and Turner. The definition of the parameters used in figure 4.5 is:

$$U_m = \frac{\int_{-\infty}^{n} U^2 \, dy}{\int_{-\infty}^{n} U \, dy}, \quad \overline{Ri} = \frac{\int_{-\infty}^{n} U B g \, dy}{U_m^3}, \quad E = \frac{1}{U_m} \frac{d}{dx} \left(\int_{-\infty}^{n} U \, dy \right)$$

where n represents the free surface. The transition from the neutral state to the critical Richardson number where turbulence collapses is qualitatively simulated by all models though clearly more satisfactorily by model IIb. The k-ϵ $E=f(\overline{Ri})$ curve lies out of the envelope of the experimental data and underpredicts the stable stratification turbulence damping. The model IIb calculation was advanced until entrainment had practically ceased; the corresponding critical Richardson number value was Ø.667.

Axial velocity profiles at two downstream stations are shown in figure 4.6 plotted in non-normalized form (when normalized in the usual way the experiments and all model predictions lie close to a Gaussian profile); Model I predictions are not shown, they lie a little furher from the data than model IIa. Once more the IIb model has produced a significant shift towards the data, although at the furthest downstream station an overprediction of entrainment is still evident as implied in figure 4.4d. It is in the comparison

with the scalar profiles that the real improvement brought about in model IIb can be most clearly seen. Figure 4.7 shows the surprising feature observed in Chu and Baddour's experiment (and also by other authors e.g. Wilkinson (1971)) namely the departure from Gaussian shapes in the mean scalar profiles, which display an almost linear variation. Only model IIb is capable of reproducing this behaviour, all other models give a quite different shape which, because of the requirement to conserve salinity, is the major cause of the underprediction of the surface values noted above. The reason for the improvement in Model IIb is related to the effect of the surface correction on the predicted transverse stress ratio $\overline{v^2}/k$. When no correction is used (model IIa) values in the order of Ø.5 for this ratio are obtained in the near surface region decreasing as the overall Richardson number increases with downstream distance, figure 4.8. In Model IIb, however, the transverse normal stress is significantly supressed particularly close to the free surface where very low $\overline{v^2}/k$ values are predicted (as low as Ø.Ø5 for the higher Richardson numbers). The free surface effects function f is plotted for two stations in figure 4.9. A self-similar shape is practically established with high values close to the surface (f≈1Ø) rapidly decreasing to small values (Ø.3) over the larger part of the layer width. One consequence of this is that the predicted value for the turbulent Prandtl number defined by:

$$\sigma_T = \frac{\overline{uv} \,/\, \frac{\partial U}{\partial y}}{\overline{vb} \,/\, \frac{\partial B}{\partial y}}$$

takes on values in the near surface region as high as 3.2 where the combined effects of surface damping and stable-stratification are strongest, figure 4.10. The value of σ_T deeper in the layer is about half this value and it is this strong variation in Prandtl number which enables the linear profile shape to be recovered. As a consequence of this behaviour it was also noted that the predicted half-widths obtained from the velocity and scalar profiles, figure 4.11, were about equal in Model IIb whereas in Models I and IIa the velocity half width was always narrower than the scalar width (a factor of 0.7-0.8); the data confirm the correctness of the IIb predictions.

One further case without downstream control was considered to examine the influence of initial Froude number. If Fd is much lower than the case considered above then buoyancy effects intrude more quickly and entrainment effectively ceases before the mixing layer at the edge of the jet spreads to the surface i.e. a buoyant mixing layer is formed. Chu and Baddour examined a jet with an initial Fd value of 2.3 and observed just this behaviour. The test conditions are given in Table 4.1.

In this case the free surface effects are not so important and the two versions of the transport equation model gave very similar results. Furthermore, models I and II agree closely for this flow; figure 4.12 shows comparisons of Model I and II predictions with measured transverse profiles. Although it is noticeable that the transport equation model predicts the buoyancy profile

slightly better, both models show a too diffused shape. In figures 4.13 and 4.14 the Model II predictions for the velocity and mean buoyancy profiles are compared with the experimental data at several axial locations. The predictions for the mean velocity compare very well with the experimental data. At the last downstream location, however, the agreement deteriorates. At this location the data for the longitudinal development suggest that the layer contracts and the corresponding flowrate is lower than the flowrate at the previous station. In the predictions the flowrate tends to an asymptotic value. The prediction of the mean buoyancy is not equally satisfactory. The experimental data suggest that as the flow develops the buoyancy profile is steeper and significantly less diffused than the velocity profile. Such a trend is not observed in the predictions where the scalar diffusion is clearly overpredicted.

Figure 4.15 presents comparison with the downstream development of the maximum value of the axial normal stress; the trend is well predicted although the values in the close to discharge region are overpredicted. This probably indicates that the assumed value of the axial stress at the discharge was higher than in the experiment. Figure 4.16 shows that not only the peak values are well represented but also the profile shape.

The variance of the buoyancy fluctuations $\overline{b^2}$ is not so well predicted ,figure 4.17. This is consistent with the under-prediction of the mean buoyancy gradient since, in the calculation the levels of $\overline{b^2}$ depend on the mean buoyancy gradient:

$$\overline{b^2} \propto \overline{vb}\,\frac{\partial B}{\partial y} \propto \left(\frac{\partial B}{\partial y}\right)^2$$

Finally, the boundaries and the centreline of the layer based on the velocity and buoyancy profiles are given in figure 4.18. The velocity based boundaries and centreline are predicted satisfactorily reflecting the good agreement with the velocity data. The buoyancy based centreline is further from the data reflecting the underprediction of the mean buoyancy gradient referred above.

Conclusions concerning the application of the mathematical and turbulence model to the fully entraining surface layer are drawn in section 4.4 following the presentation of the predictions for the internal hydraulic jump.

4.3. The prediction of the internal hydraulic jump

The data of Baddour and Chu (1975) relevant to the internal hydraulic jump situation were used for the assesment of the predictions; the following data are given for each of the cases examined:

i. The discharge conditions i.e. the layer depth, the flowrate and density deficiency at the discharge.

ii. The downstream conditions i.e. the entrainment flowrate and the visual layer depth after the hydraulic jump.

iii. The interface of the layer obtained by flow visualization.

(velocity and mean buoyancy data are not available.)

Two of these tests were predicted by the buoyancy extended k-ϵ model; the test conditions are given in table 4.2. The predictions were qualitatively satisfactory but some quantitative discrepancies were observed in the prediction of the extent of the entraining region and also on the location of the roller region. Since the discrepancies could be due to an underprediction by the k-ϵ model, of the stable stratification turbulence damping -as observed in the previous section- one of the tests was also predicted by a transport equation model.

The mathematical model and the turbulence closures were described in Chapter 2 and further details for the current application were given in section 4.2. Again, the buoyancy extended k-ϵ model is referred to as Model I and the RSFT equation model employing the free surface corrections is labelled Model IIb.

TABLE 4.2 : Test conditions of the internal hydraulic jump experiments.

	EXP 1	EXP 2
Flowrate at the discharge (kg/s)	2.0889	2.0889
Depth at the discharge (cm)	1.079	0.904
Froude number F_d	4.9	6.39
Entrained flowrate (kg/s)	0.737	0.737
Max visual depth of the layer (cm)	7.15	8.69
$\Delta\rho_\phi / \rho_a$ %	1.476	1.476

4.3.1. Computational details

i.Numerical Instability Problems

The governing Partial Differential Equations are elliptic in nature and were solved by means of the k-ϵ and

RSFT elliptic computer codes developed during this project.

Strong under-relaxation was required to control the buoyancy related instability; the false transient approach described in Appendix A3 was used in both the k-ϵ and RSFT calculations. The buoyancy related instability problems were exacerbated in the RSFT calculation. In this case the relegation of all stress and scalar flux gradients to the source terms and the use of only molecular diffusion coefficients increases both the cell Peclet and Grashof numbers of the solution aggravating the numerical instability associated with the buoyancy coupling (high Grashof numbers) and with the negative coefficients of QUICK (high Peclet numbers). Convergence could only be achieved using the RSFT model when the turbulent diffusion terms in the momentum and mean buoyancy equations were re-written as follows:

$$\text{e.g. } \frac{\partial}{\partial x}(-\overline{u\phi}) = \underbrace{\frac{\partial}{\partial x}\left(\nu_t^* \frac{\partial \Phi}{\partial x}\right)}_{A} + \underbrace{\left[\frac{\partial}{\partial x}(-\overline{u\phi}) - \frac{\partial}{\partial x}\left(\nu_t^* \frac{\partial \Phi}{\partial x}\right)\right]}_{B}, \quad \nu_t^* = c_\mu k^2/\varepsilon$$

A: included in the finite difference coefficients.

B: modified source term.

The introduction of the artificial eddy viscosities ν_t^* had a stabilizing influence (by reducing the cell Grashof and Peclet numbers) but did not affect the solution since when convergence was achieved the same terms were added and subtracted leaving the stress-flux gradients as calculated from the RSFT model.

Wiggles associated with the quadratic differencing of

the equations were observed in the transverse profiles of the mean buoyancy, k, ϵ, $\overline{u_i^2}$ and $\overline{b^2}$ close to the discharge where strong transverse convection exists due to the entrainment. The mixed QUICK-Upwind scheme had to be used in this region for the above variables. Instead of using the practice of a limiting cell Peclet number, presented in Appendix A2, the use of Upwind Differencing at the entraining edge region only was specified independently of the cell Peclet numbers to avoid unnecessary use of Upwind in other parts of the flow where the cell Peclet numbers were high (e.g. at the post-jump edge of the layer) but QUICK did not give oscillation problems. The RSFT computer code developed during the present work uses QUICK or Upwind differencing on the basis of the local cell Peclet numbers (Pc_x, Pc_y) and a specified maximum cell Peclet number where the shift QUICK-Upwind occurs. This procedure was modified for the present predictions as follows. The area of the domain where wiggles occured when QUICK was used was identified during preliminary runs as the entrainment zone before the roller region. For this area only Upwind differencing was used for the equations for B, k, ϵ, $\overline{u_i^2}$ and $\overline{b^2}$, independently of the local cell Peclet numbers, whereas for the rest of the domain QUICK was used by setting the limiting max. value of the cell Peclet number equal to a very large number.

ii.Boundary conditions

The experimental apparatus (figure 4.1) was simulated as shown in figure 4.19. The problem dependent boundary conditions are as follows. At the fresh water inlet uniform

horizontal velocity and mean buoyancy profiles were assumed with values corresponding to the experimental data ; uniform k and ϵ profiles were also prescribed with values similar to those adopted for the surface jet calculations. The homogeneous shear layer anisotropy ratios were again used for the estimation of the normal stresses and a linear shear stress profile was assumed with a maximum value of $|\overline{uv}|/k = 0.30$. In the absence of any relevant information zero values were assumed for the scalar fluxes and the variance of the scalar fluctuations. At the saline water (bottom) inlet a uniform horizontal velocity profile corresponding to the experimental flowrate was prescribed together with a zero mean buoyancy profile. All the turbulence quantities at the saline water inlet were assumed zero in analogy with the "quiescent" entraining boundary of the entraining jet calculations. In the experiments the downstream skimmer was placed at the edge of the layer; similarly, in the calculations the outlet depth was set equal to the experimental downstream layer depth and a uniform exit horizontal velocity profile was prescribed. Zero normal gradient was assumed at the outlet for all the remaining variables.

iii. Grid and CPU times

For all the calculations the numerical grid had 31 nodes in the horizontal and 28 nodes in the vertical direction. The large number of iterations required for convergence and the increase of the transport equations to be solved from six in model I to 12 in model II result in computationally

very expensive calculations. Grid refinement calculations were, therefore, restricted by this factor. Grid resolution of 31*28 nodes was considered satisfactory for the following reason: the previously examined fully entraining jet with Fd=12 was recalculated by the elliptic k-ϵ code on the 31*28 grid by adjusting the boundary conditions to correspond to no effective downstream control. The elliptic and parabolic code predictions were very close indicating satisfactory numerical accuracy of the elliptic solution (figure 4.20). The computations were carried out on an AMDAHL V8 machine. About 1800 iterations and 15 minutes of CPU time were required for the k-ϵ calculations and 2000 iterations and 35 minutes of CPU time for the transport model calculations.

4.3.2. Results and discussion

i. k-ϵ predictions

The case of an initial Froude number of 4.9 was predicted first. The predicted streamline pattern is shown in figure 4.21 and the characteristics of the jump are clearly distinguishable. The majority of entrainment into the surface layer takes place before the formation of the roller (about 94% of the supplied saline water). The reverse flow zone characterized by the roller can also be identified. The streamlines after the roller remain horizontal and the post-jump depth of the layer (identified by the locus of the zero forward velocity points) was predicted to be 7.3 cm compared to a measured value of 7.15 cm. The fixed depth of the outlet of 7.15 cm should not have

influenced this result since the outlet channel was located far downstream of the roller region. Typical profiles in the post-jump region, figure 4.22, indicated almost uniform buoyancy profiles and Gaussian-like velocity profiles in agreement with the findings of Wilkinson and Wood (1971).

For the larger Fd case the jump should be located nearer the discharge; the predictions for this case -Fd value of 6.39- are given in figure 4.23A. Once more the post-jump depth was well reproduced, both calculations and experiments giving 8.7 cm. The upstream shift of the toe of the roller has been simulated by the predictions, but quantitatively some discrepancies appear in comparison with measurements. For the case of Fd=4.9, figure 4.21, the entrainment zone was predicted to be 6.2 cm long, whereas in the experiment the corresponding value was 11.2 cm; the same comparison for the case of Fd=6.39, figure 4.23A, was 3.6 cm (predicted) and 2.5 cm (measured). (It is obvious from figures 4.21 and 4.23A that the values of the entraining length suggested by the experimenters and obtained purely from dye trace photographs are more qualitative indications of the length of the entraining region rather than exactly defined measurements). Further discrepancies appear when the experimentally deduced location of the interface is examined in figures 4.21 and 4.23A; the predicted streamline patterns are clearly not compatible with the location of the visual boundary of the layer in the experiments, particularly in the roller region.

Finally, to demonstrate that the amount of make-up water does indeed act in the predictions as the downstream

control, the case of Fd=6.39 was repeated but with a much larger entrainment water supply, leaving all other parameters the same. Figure 4.23B shows the resulting streamline pattern near the discharge; the roller region has effectively been removed far downstream and out of the solution domain and the case of a fully entraining surface jet has been recovered.

ii) Model IIb predictions

The observed discrepancies between the k-ϵ predictions and the measurements concerning the entraining length and the location of the roller could be due to an underprediction of the stable stratification turbulence damping in the entraining region. This would result in an over-estimation of the ability of the surface jet to entrain the fixed saline water supply and hence in the prediction of a shorter length for the entraining part of the flow. In the entraining jet calculations the ability of Model IIb to adequately simulate the stable stratification turbulence damping has been demonstrated. It was therefore inferred that if the discrepancies in the Model I predictions were indeed due to inaccurate simulation of the turbulence damping, improvements could be expected if Model IIb was used. Hence the case Fd=4.9 ,for which the discrepancies between predictions and measurements were larger, was recalculated using Model IIb.

The predicted limiting streamline around the calculated roller region is shown in figure 4.24 together with the k-ϵ

predictions. As illustrated in figure 4.21 the limiting streamline is the first identifiable open streamline which surrounds the roller. The predicted streamline pattern is now perfectly compatible with the experimental data for the visual boundary of the layer. The entraining region, the roller and the downstream layer depth are all in good agreement with the experimental data. The entraining length is now 14.4 cm compared to the 11.2 cm value suggested by the experiments.

Figure 4.25 shows predictions for the mean buoyancy at several axial locations for both models I and IIb. Close to the discharge, Model IIb predicts a steeper and significantly less diffused buoyancy profile; as a consequence the almost uniform buoyancy values across the layer are established gradually and further downstream. Assuming that the visible boundary of the layer corresponds to a dye concentration equal to 20% of the concentration at the discharge, we may locate a predicted boundary of the layer implied by the mean buoyancy predictions. The exact percentage used for the derivation of the implied interface does not affect significantly its location since as can be seen in figure 4.25 the profiles are in general very steep at the interface. In figure 4.25 it can be observed that Model IIb shows a substantial shift towards the data, in particular close to the discharge.

In the k-ϵ predictions, the buoyancy profile of the layer after the roller is wider than the layer depth defined by the zero forward velocity points; the k-ϵ predictions suggest that immediately beneath the downstream moving layer

a zone of practically stagnant water exists where the sudden decrease of salinity occurs. In the Model IIb predictions, the separation between the zero velocity and zero buoyancy layer width is substantially reduced. The Model IIb predictions also show, in the region after the roller, a less steep interface of the buoyancy profile in relation to the Model I predictions. This difference may be due to the transverse diffusion of the vertical flux in the transport equation model. Though the less steep interface of the Model IIb predictions seems to contradict the evidence from the work of Wilkinson and Wood (1971), no conclusions can be drawn until more detailed experimental data are available.

Finally, in figure 4.26 the predicted anisotropy ratios $\overline{u_i^2}/k$ and the implied vertical Prandtl number $\sigma_{T,y}$ are given across the layer at a location downstream of the roller. As expected the vertical component $\overline{v^2}/k$ is damped close to the free surface, due to the free surface effects, and close to the layer edge due to the destruction by buoyancy. Similarly, the implied turbulent Prandtl number has its maximum values close to the surface and to the interface. It is undoubtedly the case that the more correct simulation of these parameters provided by the RSFT model has caused the significant improvement in the streamline and mean buoyancy predictions.

4.4. Conclusions

From the previous discussion the following conclusions can be drawn on the abilily of the mathematical and

turbulence models tested to predict the two-dimensional buoyant surface layer.

1) The mathematical model and all turbulence models tested are able to predict qualitatively the two-dimensional buoyant surface layer. The influence of the buoyancy term and downstream control on the momentum equations, in the case of the internal hydraulic jump, and the stably stratified turbulence damping in both the entraining jet and the internal jump are qualitatively simulated and the main features of the flows can be reproduced.

2) The simulation of the damping influence of the free surface on the vertical normal stress and scalar flux was shown to be very important for the prediction of the stable stratified turbulence damping and for good quantitative agreement with the experimental data. Best agreement with the data was obtained using the Reynolds stress-flux transport model where the free surface effects on the turbulence structure were taken into account. The same model performed slightly better than the buoyancy extended k-ϵ model when the free surface was treated purely as a plane of symmetry.

3) The level of agreement for both the surface layer and, the internal hydraulic jump have shown that both of these components of the flow field, found in the verical shallow discharge, (and in other types of discharge it should be stressed) can be adequately simulated.

CHAPTER 5

THE PREDICTION OF THE VERTICAL 2-D NON-BUOYANT DISCHARGE IN SHALLOW WATER

CHAPTER 5 : THE PREDICTION OF THE VERTICAL 2-D NON-BUOYANT DISCHARGE IN SHALLOW WATER

So far in this thesis, the buoyant flows considered have been sub-components, in a phenomenological sense, of the final problem of this project, the vertical buoyant discharge in shallow water. In this chapter attention is turned to the "full" problem, in a fluid dynamics sense, but for the moment the buoyancy effects are neglected. As explained in the introduction the work reported in this chapter forms a further intermediate stage in the gradual build-up of physical understanding and turbulence model testing towards the final task of the project.

The present chapter deals therefore with the two-dimensional vertical non-buoyant discharge in shallow water; both plane and axisymmetric cases are examined. The data from the experimental work of Muraoka and Murota (1967), presented in Chapter 1, were used for the validation of the predictions. The bulk of the calculations were carried out using the standard k-ϵ model. Although the k-ϵ predictions compare satisfactorily with the data one of the axisymmetric configurations was recalculated using the RST model of Launder et al in order to compare model performance.

The present chapter consists of three sections; in the first information is given about the computations i.e. boundary conditions, grid etc; in the second the k-ϵ predictions are presented and discussed and in the third the k-ϵ and transport equation predictions are compared for one axisymmetric case. The chapter concludes with a summary.

5.1. Computational details

Solution domain and boundary conditions

The solution domain for the plane configuration is shown in figure 5.1a. The problem dependent boundary conditions are as follows. At the discharge uniform profiles were prescribed for the vertical velocity and the turbulence kinetic energy and dissipation rate. In the absence of experimental data for the turbulence, a turbulence energy level of Ø.5% of the mean energy and a length scale equal to half the discharge width were assumed for the estimation of k and ϵ at the inlet. The inlet k and ϵ values had a small but not deciding influence on the near field results; in particular, the velocity decay rate was affected in configurations with large submergence depth ratio (H/D). The influence of the assumed inlet turbulence intensity on the symmetry plane velocity decay is shown in figure 5.2 for a plane discharge ($V_{\emptyset}$=Ø.6 m/s, D=4 cm, H/D= 15). Similar tests concerning the assumed value of the dissipation rate at the inlet were carried out for the deeper discharges examined. The turbulence length scale was given values of Ø.3D, Ø.5D, Ø.7D while the turbulence energy was kept constant at a level equal to Ø.5% of the mean energy. Effects similar to those shown in figure 5.2 were observed. The lower the dissipation rate the higher the initial effective viscosity and consequently the stronger the velocity decay close to the discharge. For the deeper discharges the proper choice of the inlet turbulence level and length scale was confirmed by several checks aiming to reproduce the experimental

velocity decay close to the discharge. In all cases examined the previously mentioned combination of turbulence energy (Ø.5% of $V_{Ø}^2$) and length scale (Ø.5D) reproduced satisfactory the observed initial velocity decay rate, and results shown are for these values. At the downstream end of the solution domain a zero normal gradient was assumed for all the variables. McGuirk and Rodi (1977) report that in order to eliminate the influence of the location of the downstream boundary on the near-field predictions the boundary had to be located ten water depths from the symmetry plane. The same practice was used in the present work; this subject is further discussed in section 5.2.

The experiments for the round discharge were carried out in a cubic tank (1*1*1 m) with the discharge located at the center of the tank bottom. No information is given by Muraoka and Murota (1967) about the method adopted in the experiment to maintain a constant average water level in the tank. In the predictions the experimental apparatus was approximated by an axisymmetric tank with an "overflow" outlet, figure 5.1b. At the overflow-outlet of the solution domain a fixed uniform horizontal velocity profile was assumed together with a zero normal gradient condition for the rest of the variables. For the transport equation calculation the inlet normal stresses were defined from the homogeneous shear layer anisotropy ratios. Three different forms of the shear stress profile at the inlet were tested: a)a linear profile with a maximum wall values of $|\overline{uv}|/k=Ø.3Ø$ corresponding to a fully developed pipe flow b) a uniform profile with a value equal to $|\overline{uv}|/k=Ø.3Ø$ and a zero shear

stress profile. The influence of the assumed profile on the results is discussed in section 5.3. The uncertainty about the experimental downstream control and the three-dimensional character of the flow in the experiment, due to the cubic geometry of the tank, imply that comparisons between the data and the (2-D) predictions may be considered reliable only close to the axis of symmetry where the influence of the jet is undoubtedly dominant.

Grid

The bulk of the plane configuration calculations were carried out with a non-uniform grid having 37 nodes in the horizontal direction and 25 nodes in the vertical direction. In the vertical direction the grid was uniform except close to the surface region where additional nodes were placed. Increased resolution in this area was required in order to achieve grid independent surface shape predictions. In the horizontal direction the grid was more concentrated close to the plane of symmetry, intermediate along the recirculation eddy and coarser after the reattachment (figure 5.3a). The maximum resolution of the grid was in the region close to the symmetry plane and close to the surface where experimental data were available for comparisons. The influence of the grid spacing on the predicted separation streamline and on the surface shape is shown in figure 5.3 (the surface shape is derived from the pressure predictions as described in section 5.2). From figure 5.3 it can be seen that the 37*25 grid ensures satisfactory resolution giving practically grid-independent results in the near field

region and sufficient accuracy in the far field region.

The bulk of the axisymmetric configurations were calculated with a grid having 30 nodes in each direction. The grid was more concentrated close to the axis of symmetry and the free surface. To check possible grid dependence of the results one of the configurations (V_0=0.512 m/s, D=12.44 cm, H/D=4) was recalculated with a finer (45*45) grid. Both calculations gave practically the same vertical and horizontal velocity profiles. Indicative of the practically grid independent results are:

1) the predicted value of the total circulation induced in the tank, figure 5.14, was equal to 6.038*$\dot{m}_0$ (30*30 grid) and 6.197*$\dot{m}_0$ (45*45 grid) where $\dot{m}_0$ is the flowrate at the discharge i.e. a 2.6% difference, and

2) the predicted surface elevation at the axis of symmetry was 0.96 cm (30*30 grid) and 0.98 cm (45*45 grid) i.e. a difference of only 2%.

The transport equation calculations were carried out with the same 30*30 grid and the results are compared with the 30*30 k-ϵ results.

The computations were carried out on an AMDAHL V8 machine; the 30*30 k-ϵ calculations required 400 iterations and 3.15 minutes of CPU time and the transport equation (30*30) calculation required 510 iterations and 6.50 minutes of CPU time.

Finally, for the calculations reported in this Chapter the Quadratic Differencing scheme (QUICK) did not give problems. The shift from QUICK to Upwind Differencing at high cell Peclet numbers, described in Chapter 2, was found

unnecessary for this particular flow, presumably because of the absence of significant "non-turbulent" regions within the solution domain.

5.2. k-ϵ results and discussion

Centreline velocity decay

In figure 5.4 the predictions of the symmetry plane velocity decay are compared with the experimental data for four plane configurations of increasing submergence depth ratio (H/D= 5,10,15,20). The agreement with the data is satisfactory for all the cases examined. For the larger submergence depths the three distinct regions of the velocity decay curve identified by Muraoka and Murota (1967) (namely the potential core region, the self-similarity region ($V_c \sim 1/\sqrt{y}$) and the rapid decay close to the surface) can also be observed in the predictions. Close to the symmetry plane the flow is jet-like in character and it is known that the standard k-ϵ model predicts satisfactorily the plane jet so this level of agreement is perhaps to be expected. In figure 5.5 the k-ϵ predictions of the centreline velocity decay are compared with the data for three axisymmetric configurations of increasing submergence depth ratio (H/D=3,4,6), (data for deeper discharges were not available). The agreement is again satisfactory for all cases. It is known that the k-ϵ model overpredicts the spreading of the self-similar round jet, (Rodi 1980); however the low submergence depths examined mean that pressure gradient effects dominate and this does not allow

this aspect of the k-ϵ model to affect the results.

Vertical velocity profiles

In figure 5.6 the predicted vertical velocity profiles close to the axis of symmetry are compared with the experimental data for a shallow axisymmetric discharge ($V_{\emptyset}$=Ø.512 m/s, D=12.44 cm, H/D=4) for which detailed data were available. Very good agreement can be observed at all stations except the last two close to the surface where the velocities are significantly underpredicted. At least partially responsible for the underprediction of the velocity at the last two stations is the treatment of the free surface as a symmetry plane coinciding with the undisturbed water level (the rigid lid assumption). In the calculations the distance betwen the last station and the undisturbed surface is 1.6 cm while in the experiments the surface is elevated at the axis of symmetry by 1.4 cm and the distance between the last station and the elevated surface is now 3 cm. Therefore in the experiments the centreline velocity had to decay to zero within 3 cm from the last station whereas in the calculations the decay to zero is taking place within 1.6 cm, resulting in an underprediction of the vertical velocities at the last two stations. However, it is clear that the detrimental effects of the rigid lid assumption on the prediction of the vertical velocities are confined to the close-to-surface region (i.e. y/H>9Ø%). In figure 5.7a the predicted vertical velocity profiles close to the symmetry plane are compared with the data for a plane discharge with a relatively high

submergence depth ratio ($V_{\emptyset}$=Ø.6 m/s, D=4 cm, H/D= 2Ø). The agreement is again satisfactory except for the last station close to the surface where the velocities are once more underpredicted. In the same figure comparisons are given for a shallow discharge with ($V_{\emptyset}$=Ø.4 m/s, D=4 cm, H/D=6). For this case the peak velocities and the velocities close to the plane of symmetry are well predicted but the velocities at the edge of the jet are underpredicted indicating that the recirculation implied by the data is stronger than the predicted. The discrepancies could be slightly reduced (dashed curve in figure 5.7b) when the inlet turbulence was substantially increased ($k/V_{\emptyset}^2$=2.5%) at the expense, however, of the agreement close to the symmetry plane. The small changes observed indicate that the discrepancies between data and predictions cannot be attributed to the assumed boundary conditions for turbulence quantities at the discharge.

Horizontal velocity profiles

In figure 5.8 horizontal velocity profiles close to the surface are compared with the data for the two previous plane configurations i.e. $V_{\emptyset}$=Ø.6 m/s, D=4 cm, H/D=2Ø and $V_{\emptyset}$=Ø.4 m/s, D=4 cm, H/D=6. In both cases the surface velocities are well predicted. The shape and the development of the profiles are also satisfactorily predicted although the horizontal velocities away from the surface are underpredicted , particularly in the shallower discharge, indicating again an underprediction of the recirculation. In figure 5.9 the horizontal velocity predictions are compared

with the data for the previously examined axisymmetric shallow discharge ($V_{\emptyset}$ = Ø.512 m/s, D=12.44 cm, H/D=4). The agreement for the stations close to the axis of symmetry is satisfactory implying that the bend over phase of the flow is well simulated; at the last downstream station, however, the agreement deteriorates. The discrepancies between data and predictions for the horizontal velocity can also be observed in figure 5.11 showing the surface velocity evolution. The agreement is good close to the axis of symmetry (r/L<Ø.25), the maximum value is well predicted but further downstream the predictions show a too rapid decay of the surface velocity. The discrepancies in question could indicate a deterioration of model performance in this region; however, the very limited amount of data available, the uncertainties concerning the character of the experimental flow mentioned in section 5.1 and the good agreement of the velocity predictions close to the axis of symmetry do not allow any safe conclusions on this matter. Furher experimental data and predictions are required for a safe validation of the model in the downstream region of the axisymmetric flow.

Surface elevation

The rigid lid assumption results in a pressure variation along the "free-surface". Following the practice of McGuirk and Rodi (1977) the pressure variation was converted to an equivalent deviation from the undisturbed water level as follows:

$$\Delta H(x) = \frac{P_{surf}(x) - P_{surf,\infty}}{\rho g}$$

where $P_{surf,\infty}$ is the static pressure at the surface at the grid node furthest removed from the symmetry plane or axis.

The predicted symmetry plane surface elevation non-dimensionilized by the submergence depth ($\Delta H_c/H$) was plotted against the non-dimensionilized energy flux (E) of the jet (figure 5.10a) together with the corresponding experimental data. The normalized symmetry plane surface elevation can be expressed as a function of the dimensionless groups given in chapter 1; on the assumption of high Reynolds numbers at the discharge this leads to a functional relationship:

$$\Delta H_c/H = F(H/D, E)$$

Thus the symmetry plane surface elevation depends in general on both the submergence depth and the energy flux of the configuration. Consequently the experimental data (or the predictions) plotted in figure 5.10 should not necessarily collapse to a unique curve since they correspond to different submergence depths (H/D) varying from 3 to 20. Comparisons between data and predictions should be made for each configuration separately as shown by the dashed lines in this figure. Reasonable agreement with the data can be observed, the predicted values being in general lower than the experimental. Four of the configurations shown correspond to the same jet (V_0=0.6 m/s, D=4 cm) discharging at four different depths of the channel: H/D=5.5, 8.2, 10 and 15. It is clear that the agreement deteriorates at the lower submergence depths indicating probably a deterioration of the accuracy of the rigid lid assumption

for such depths where the surface distortion is more pronounced in relation to the channel depth. The remaining data support this proposition though it is not possible to draw soundly based conclusions on this subject without further experimental and predictive work.

In figure 5.10b the predicted surface shape is compared with the data for three plane configurations of increasing submergence depth ratio (V_0=0.6 m/s, D=4 cm, H/D=10,15,20). Close to the plane of symmetry the surface shape is reasonably well predicted but further downstream the predictions show a significant surface depression which was not observed in the experiments.

The experimental data for the centreline surface elevation were examined for three axisymmetric configurations (V_0=0.512 m/s, D=12.44 cm, H/D=2.31, 3 and 4); it was found that in all cases the measured centreline elevation exceeded its maximum bound given by the dynamic head at the discharge (by 21% for H/D=2.31 to 4% for H/D=4). This incorrect behaviour was not observed in the plane jet data or in the predictions for the round discharge where the surface elevation was always lower than the dynamic head at the discharge (varying from 95% for H/D of 2.31 to 75% for H/D=4). These observations undermine the validity of comparisons between predicted and observed surface shape for the axisymmetric case. For completness however figure 5.12 presents such a comparison for the previously examined axisymmetric configuration (V_0=0.512 m/s, D=12.44 cm, H/D=4). As mentioned before, the experimental centreline elevation for this case exceeds by 4% the dynamic head at

the discharge. Again the calculations show an underprediction of the centreline value and a depression of the free surface which was not observed in the experiments.

Stream line pattern, recirculation strength

The predicted streamline patterns for a series of plane and axisymmetric configurations are shown in figures 5.13 and 5.14. Figure 5.13 shows the streamline pattern in the near field region (X/H<5) for three plane configurations ($V_{\emptyset}$=Ø.26 m/s, D=4 cm, H/D=5), ($V_{\emptyset}$=Ø.6 m/s, D=4cm, H/D=1Ø and 2Ø). Figure 5.14a shows the streamline pattern for the experimental confined axisymmetric configuration ($V_{\emptyset}$=Ø.512 m/s, D=12.44 cm, H/D=4); and figure 5.14b shows the streamline pattern for an unconfined round discharge corresponding to the same $V_{\emptyset}$, D and H/D values.

In order to investigate the streamline pattern several configurations were predicted, both plane and axisymmetric, with submergence depth ratios (H/D) varying between 2.2 and 2Ø. In all cases the reattachment length Xr when scaled with the water depth H was found to be practically independent of the H/D value and fell in the range Xr/H = 3.6-3.9 and 3.9-4.1 for plane and axisymmetric configurations respectively. Invariably only one recirculation cell was predicted. As mentioned in chapter 1 Jirka and Harleman (1979) suggested that the flow can be considered as a series of counter-rotating cells as shown schematically in figure 1.3. Such a situation was not observed in the present predictions where a practically horizontal flow was established soon after reattachment. In the predictions the

downstream boundary was placed ten water depths downstream of the discharge and a zero normal gradient boundary condition was applied. In order to investigate the influence of the downstream boundary on the predicted streamline pattern, computations were repeated with the boundary located twenty water depths downstream. The configurations considered were the following: a plane discharge of $V_{\emptyset}$=Ø.6 m/s, D=4 cm and H/D=1Ø and an axisymmetric discharge $V_{\emptyset}$=Ø.29 m/s, D=2.54 cm, H/D=2.2. The same streamline pattern was predicted with a single eddy. No significant alterations in surface shape and velocity predictions were observed.

Further checks were carried out in order to investigate the influence of the nature of the downstream boundary on the predicted streamline pattern. In the predictions presented so far, a zero normal gradient $\partial U/\partial x=\emptyset$ was assumed at the downstream boundary. If continuity is taken into account, it can be seen that this assumption is equivalent to $\partial V/\partial y=\emptyset$ or to $V(y)=\emptyset$ all over the outflow since $V=\emptyset$ at the bottom and the free surface. Therefore the zero normal gradient condition dictates a horizontal flow at the end of the domain and this could possibly inhibit a multiple eddy evolution, as postulated by Jirka and Harleman. In order to investigate this possibility the axisymmetric configuration ($V_{\emptyset}$=Ø.29 m/s, D=2.54 cm, H/D=2.2) was recalculated assuming an overflow outlet similar to the one shown in figure 5.1b which enforces a streamline curvature close to the outflow. The boundary was located 1Ø water depths from the discharge; the streamline pattern remained practically unaffected and a single eddy was again predicted.

Jirka and Harleman based their proposition on the experimental works of Iamandi and Rouse (1974), which was presented in chapter 1, and on the work of Pan and Acrivos (1967) concerning the laminar flow in a rectangular cavity with a sliding wall. In the latter flow at large cavity aspect ratios a multiple counter-rotating cell structure was indeed observed. This flow however is significantly different from the present flow since in this case the horizontal surface jet (which dominates the shallow discharge) is not present. In conclusion, the present numerical predictions and the predictions of McGuirk and Rodi (1977) and Trent (1973) do not support the proposition of Jirka and Harleman about the downstream development of the flow. Further experimental work is required to confirm the numerical predictions.

As mentioned in chapter 1 Jirka and Harleman estimated the plane configuration recirculation from the relation:

$$\Psi_{max} = 0.6 \; (\dot{q} H)^{\frac{1}{2}}$$

where $2\dot{q}$ is the initial jet momentum. From this relationship it can be furher derived that:

$$\Psi_{max} = 0.848 \; (H/D)^{\frac{1}{2}} \; \dot{m}_{\emptyset}$$

where $2\dot{m}_{\emptyset}$ is the mass flux at the discharge. In this derivation it has been assumed that the surface jet momentum flux is equal to the momentum flux at the discharge. It can be shown, on the basis of the impingement region integral analysis of Lee and Jirka (1981), that this assumption provides an order of magnitude estimate of the surface jet momentum flux but in general overpredicts its value. Therefore, it should be expected that the last relation

would overpredict the circulation but still provide a reasonable estimate. This can indeed be seen in figure 5.15 where the previous relation is compared with the numerical predictions. The agreement is close vindicating the dimensional analysis of these authors on the basis of the horizontal jet development. Their estimate for the length of the recirculation cell, however, Xr=2H is not in agreement with the present findings. According to their analysis the "entraining length" of the surface jet is of the order 2.5H. Furthermore it is argued that since the "flow reversal zone" has a characteristic radius of Ø.5H the eddy must have a length of order 2H i.e. the flow reversal zone radius is subtracted from the "entraining length". However the flow reversal is a part of the eddy and hence its length should be added, rather than subtracted, to the entraining length to give a length of the eddy equal to 3H. Given the slope of the separation streamline close to reattachment a more reasonable estimate of the eddy size -on the basis of the analysis of Jirka et al - should be 3.5H which is close to the present predictions.

5.3. Transport equation results and discussion

The previously examined axisymmetric configuration ($V_{Ø}$=Ø.512 m/s, D=12.44 cm, H/D=4) was recalculated using the transport equation model presented in chapter 2. Two versions of the model were again examined. In the first the free surface was consistently treated as a plane of symmetry (Model IIa) and in the second the free surface corrections

were added to the pressure-strain correlation in the way described in Chapter 2 (Model IIb). The free surface effects function f was defined as described in chapter 4 for the surface layer calculations. The two versions of the transport equation model gave very similar mean velocity field results. The differences between Model IIa and IIb predictions normalized by the discharge velocity ($V_\emptyset$) were of the order of 1%. Therefore, in the corresponding figures only model IIa results are plotted though model IIb results would lie very close.

The Model IIa predictions for the centreline velocity decay are shown in figure 5.16. The results were sensitive to the assumed shear stress profile at the discharge. In order to reproduce the slight increase of the vertical velocity close to the discharge which was observed in the experiments, a zero shear stress profile had to be assumed at the inlet. When a fully developed pipe flow linear shear stress profile was used the predictions were close to the experimental data but the observed slight increase was not reproduced. The predictions were also worse, in this respect, when a uniform shear stress profile was assumed. The assumption of a zero shear stress profile is equivalent to the implied initial condition for the shear stress in the k-ϵ calculations. The slight increase of the velocity observed in the experiment is characteristic of the development of the mixing layer formed between the core of the jet and main flow and, in particular, of the rate that the layer spreads inwards. A slight increase of the potential core velocity was also observed at the edge of the

mixing layer formed in the sudden expansion in a plane channel flow examined in chapter 3. The vertical velocity profile predictions are shown in figure 5.6 together with the k-ϵ predictions. The agreement with the experimental data is again satisfactory. Close to the axis of symmetry the two models gave very similar results though the k-ϵ model gave in general higher velocities at the edges of the jet reflecting a stronger circulation in the tank. Though not readily apparent from figure 5.6 k-ϵ predicts a value of the induced circulation equal to $6.\emptyset 38\dot{m}_{\emptyset}$ (where $\dot{m}_{\emptyset}$ is the flowrate at the discharge) whereas model IIa predicts a circulation equal to $4.265\dot{m}_{\emptyset}$ (the corresponding value with model IIb is slightly lower i.e. $4.25\dot{m}_{\emptyset}$). Differences between the k-ϵ and model IIa predictions can be observed in the horizontal velocity comparisons shown in figure 5.9; the k-ϵ predictions show higher surface velocities and imply a stronger circulation. However, the limited experimental data (no measurements were made in the region where the model predictions differ) together with the uncertainties about the experimental set-up mentioned above do not allow further speculation. The transport equation predictions for the surface shape -figure 5.12- are close to the k-ϵ predictions.

The different predictions of the two models for the induced circulation can be clearly seen in figure 5.17 where vertical and horizontal velocity profiles are given across the tank. As for the mean velocity predictions of the recirculating flows examined in Chapter 3 the k-ϵ and transport equation model gave very similar results outside

the recirculation zone but significantly different results within it.

An interesting feature of the transport equation calculations is the turbulence anisotropy predicted by the two versions of the model. In figure 5.18 the anisotropy ratios $\overline{u^2}/k$ and $\overline{v^2}/k$ are plotted along the axis of symmetry and along the first grid-line beneath the free surface. On the axis of symmetry model IIa initially predicts a slight tendency towards isotropy while close to the surface a strong enhancement of the vertical component occurs due to the strong vertical velocity gradient $\partial V/\partial y$. After the jet deflection by the free surface a predominantly horizontal flow is established resulting in a gradual increase of the horizontal component and a reduction of the vertical component. The model IIb predictions show the expected suppression of the vertical component in the downstream region of the flow. However on the axis of symmetry the free surface corrections result in a further enhancement of the vertical component. This unexpected result can be explained if the surface correction action is examined for this particular case. The form of the corrections derived from the general formulation given in chapter 2 are, for the vertical component:

$$\Pi'_{22,1} + \Pi'_{22,2} = -2\, c'_1\, f\, \frac{\varepsilon}{k}\, \overline{v^2} + 2\, c'_2\, c_2\, f\, \left(P_{22} - \frac{2}{3} P \right)$$

where P_{22} and P are the $\overline{v^2}$ and k production respectively. The model was introduced by Gibson and Launder (1978) in order to reproduce the damping of the vertical component in horizontal boundary layer like flows close to a wall. For

such a case $P_{22} = \emptyset$ and both contributions are negative resulting in the suppression of the vertical component. For the present application the surface impingement region is characterized by intense production of $\overline{v^2}$ due to steep vertical velocity gradients ($\partial V/\partial y$) occuring close to the surface. Thus the second contribution of the free surface correction (Π'_{22}) was found to be positive and dominant resulting in an enhancement rather than a reduction of the stress component normal to the free surface. It should be pointed out that both contributions are multiplied by the value of the surface effects function f and any definition of f (with positive values) would have qualitatively the same effects. Although experimental data are not available to confirm conclusions it cannot be easily perceived how in a real impinging jet situation the free surface may lead to an enhancement of the component normal to the surface. The present findings cast doubt on the universality of the free surface corrections as described in chapter 2. Once more, further experimental evidence is required to confirm these preliminary findings.

5.4. Conclusions

The following conclusions concern 2-D non-buoyant discharges in shallow waters characterized by a relatively low discharge velocity and surface distortion:

1) The rigid lid assumption for the free surface did not adversely affect the predictions except for a small region close to the jet impingement. The rigid lid assumption even

allowed the estimation of a surface shape which was found to be in reasonable agreement with the experimental data.

2) The infinite horizontal extent flow was found to contain only one recirculating cell in contrast to the proposition of Jirka and Harleman (1979) for a series of eddies.

3) The experimental data confirm that both the standard $k-\epsilon$ and the transport equation model predict satisfactorily the velocity field in the vertical and horizontal jet regions and the surface shape. The models gave different results in the recirculation region but no data are available to validate these findings.

4) The application of the free surface correction for the pressure—strain correlation in the transport equation calculation led to the prediction of unrealistic turbulence anisotropy ratios in the jet impingement region.

5) The flow-field of the non-buoyant version of the 2-D vertical discharge in shallow water is certainly predicted sufficiently well by both models to encourage extension to the buoyant version of this flow.

CHAPTER 6

THE PREDICTION OF THE VERTICAL BUOYANT JET IN SHALLOW WATER

CHAPTER 6 : THE PREDICTION OF THE VERTICAL BUOYANT JET IN SHALLOW WATER

This chapter combines information acquired in the previous two chapters and deals with the final task of this thesis, the prediction of the vertical buoyant jet in a shallow water body of infinite horizontal extent. The work on this subject is reported in sections 6.3 to 6.9. Predictions for four of the configurations examined by Jirka, Lee and Harleman (1979,1981) are presented and compared with experimental data. On the basis of these predictions a model of the flow is proposed and compared with the model of Jirka et al presented in chapter 1. Due to numerical problems and time limitations the second moment closure tested in the previous chapters could not be applied to the present problem; the reasons for this are explained in the first section. In section 6.2 the buoyancy extended k-ϵ model, used for the final calculations as well, is first tested on the buoyant vertical jet experiments of Pryputniewicz and Bowley (1975) for which more detailed data were available to study the turbulence model performance.

6.1. The performance of the RSFT model in confined vertical buoyant jet flows

The RSFT computer program used for the internal hydraulic jump calculations presented in chapter 4 was further tested in a series of confined vertical buoyant jet flows.

In all flows examined in this chapter the buoyancy is induced by temperature differences in a water body. Therefore, in order to facilitate comparisons with experimental data, the results are presented in terms of temperature differences instead of the mean buoyancy form used in chapter 4. The formulation presented in chapter 2 was retained based, as mentioned there, on the assumption of a constant densimetric expansion coefficient.

The first flow considered and the solution domain used for the predictions are shown in figure 6.1. A vertical round buoyant jet is discharged from the centre of the bottom of a shallow cylindrical tank. A strong cold water flowrate is supplied at the bottom periphery. The surface level is maintained constant by withdrawing (from the top periphery of the tank) a flowrate equal to the flowrate entering the tank. The characteristics of the discharged jet were D=12.5 cm, H/D=1.6, $V_{\emptyset}$=Ø.2 m/s and Fd=5 where Fd is the densimetric Froude number of the discharge defined in chapter 1. The cold water flowrate was equal to five times the jet flowrate.

The problem dependent boundary conditions were as follows. At the discharge the conditions were defined as described in chapter 5 for the axisymmetric RST calculations together with a uniform temperature profile and zero $\overline{ut}$, $\overline{vt}$ and $\overline{t^2}$ values. At the bottom inlet uniform horizontal velocity and "ambient" temperature profiles were prescribed together with zero values for the turbulence quantities. At the outlet of the tank a uniform horizontal velocity profile

conserving mass was assumed together with a zero normal gradient condition for the remaining variables.

The aim of this calculation was to check the computer program in a situation resembling the flows examined in the present chapter. For this purpose grid independence was not essential and a rather coarse numerical grid having 21 nodes in each direction was used; the grid was uniform in both directions. Furthermore, in order to eliminate the retardation of convergence associated with the buoyancy related numerical instability, the buoyancy term in the vertical momentum equation was omitted but was still retained in the turbulence equations. The steady-state form of all equations was solved. The elimination of the momentum/buoyancy coupling allowed fast convergence in 200 iterations requiring 2.6 minutes of CPU time on an AMDAHL V8 computer.

In the present predictions the surface was consistently treated as a symmetry plane and the free surface corrections of the pressure-strain and pressure-buoyancy gradient correlations were not taken into account. The temperature field was calculated in two ways: the first was a consistent application of the RSFT closure. In the second the full set of equations constituting the RSFT closure were solved; however, instead of using the calculated turbulent fluxes for the diffusion terms in the mean temperature equation these terms were modelled using the k-ϵ eddy diffusivity concept (the k and ϵ values were obtained from the transport model). The purpose of this was to provide a check of the RSFT predictions in this purely numerical exercise. The two

methods gave similar temperature field results (figure 6.2) the full RSFT predictions giving slightly more diffused profiles. Plausible values were predicted for both the mean and turbulence quantities and the solution did not present any numerical problems.

The second series of checks concerned the same geometry but the parameters of the flow were more closely related with the vertical buoyant jet experiments of Pryputniewicz and Bowley (1975) presented in the following section. The characteristics of the jet were: D=1.Ø8 cm, H/D=1Ø, Fd=4. The diameter of the tank was Ø.6 m and again the cold water flowrate was set equal to five times the discharge flowrate. The grid had 28*2Ø nodes and was more concentrated close to the surface and to the axis of symmetry.

Three calculations were carried out: In the first the buoyancy terms were omitted in all equations, in the second the buoyancy terms were included only in the momentum equations and in the third the buoyancy was taken into account in all equations. In the latter calculation the temperature field was defined in two ways as described above for the previous test case.

The predictions for the centreline temperature are shown in figure 6.3. The shape of the centreline temperature decay is physically realistic for the non-buoyant case (curve A) and for the case where the buoyancy term was taken into account in the vertical momemtum equation only (curve B). When buoyancy was introduced in the turbulence equations the predictions showed an unrealistic increase of the temperature close to the surface (curve C). The peak close

to the surface was not present when the temperature field was calculated using the eddy diffusivity concept for the estimation of the diffusion terms in the temperature equation (curve D).

The temperature peak close to the surface predicted by RSFT indicates that in this region the scalar flux gradients appearing in the source term of the temperature equation have a positive source effect leading to the unexpected temperature rise. Such a behaviour was not observed in the previous shallow discharge (H/D=1.6) where, however, it was found that the convection terms dominated the temperature field evolution in the problematic area and probably did not allow diffusion related errors to influence the solution.

Further RSFT calculations were carried out simulating one of the confined vertical buoyant jet flows studied by Pryputniewicz and Bowley (1975) (H/D=10, Fd=4). In these calculations the grid had 35*38 nodes and was particularly concentrated close to the surface and to the axis of symmetry in order to increase the numerical accuracy in the problematic area of the flow. The same behaviour was observed; the peaking was again removed when the buoyancy terms in the turbulence equations were set to zero. This fact indicates that the area of the model requiring particular attention is the buoyancy coupling of the turbulence equations.

From these preliminary studies it became clear that the understanding and removal of the problem required a systematic investigation of the RSFT model performance in this particular flow. The successful applications of the RSFT computer code reported in chapters 4 and 5 and in this

section (when the buoyancy was not taken into account) encourage the view that the problem is not caused by erroneous discretisation practices or by (so far undetected) programming errors. Therefore, attention should be directed to the performance of the turbulence model in the present flow and in particular to:

.the predicted scalar flux gradients all over the domain in order to identify the problematic areas.

.the level of the predicted scalar fluxes and mean square scalar fluctuations and to the modelled terms in the transport equations which affect the level of these correlations.

A useful starting point for such an investigation would be to use a converged k-ϵ solution of the problem in order to calculate the stresses and fluxes using the RSFT model and compare their values and gradients with predictions based on the eddy viscosity-diffusivity concept.

Time limitations did not allow such an investigation during the current work; because of the unrealistic behaviour reported above it was felt premature before removing this problem to apply the RSFT model to the experimental situation of shallow buoyant discharges. This forced the decision to abandon the use of the RSFT closure in the final problem calculations. Therefore in contrast to the other studies reported in this thesis the following predictions were carried out using the buoyancy extended k-ϵ closure only.

6.2. The prediction of the vertical buoyant jet experiments of Pryputniewicz and Bowley (1975)

In the following sections it will become clear that only a limited amount of data from the buoyant jet experiments of Jirka et al (1979) are available for comparisons. This, together with the difficulties in simulating the exact experimental situation, also to be discussed below, did not allow a complete validation of the mathematical model and turbulence simulation for the vertical buoyant jet in shallow water. In order to examine more closely the performance of the model in a confined vertical buoyant jet situation, the experiments of Pryputniewicz and Bowley (1975) were simulated.

The experimental apparatus used by these authors is shown schematically in figure 6.4a; it consists of a large cylindrical tank of 2.4 m diameter and 1.5 m in depth. A jet nozzle was fitted at the top of an adjustable height pipe located on the axis of symmetry of the tank, which was further equipped at the top with an overflow weir. A strong cold water supply from the bottom of the tank ensured steady state conditions and constant ambient temperature by forcing the entrained water out of the tank. Data for two submergence depths (H/D=1Ø and 4Ø) were presented for a series of discharge densimetric Froude numbers Fd=1 to 5Ø. Temperature measurements were obtained for the centreline and surface excess temperature and for a few temperature profiles close to the axis of symmetry for the case (Fd=2, H/D=1Ø). It is obvious that this experimental situation is

different from the shallow discharge problem since the bottom depth is very large in relation to the submergence depth.

The experimental apparatus was represented in the calculations as shown in figure 6.4b. For computational economy reasons the simulated tank had a diameter of 1 m and a depth of Ø.5 m and was significantly smaller than in the experiment. Numerical checks, however, using an even smaller tank (diameter of Ø.7 m and depth of Ø.35 m) showed exactly the same temperature field results. The lower submergence depth (H/D=1Ø) experiments were simulated for three discharge Froude numbers Fd=2,4 and 8. The experimental cold water flowrate was not reported and had to be estimated using the measured temperature data and an overall heat balance for the tank. On the assumption of a uniform temperature across the layer at the outflow, the cold water flowrate was estimated from the relation:

$$(\dot{m}_C + \dot{m}_\emptyset) \Delta T_S = \dot{m}_\emptyset \Delta T_\emptyset \rightarrow \frac{\dot{m}_C}{\dot{m}_\emptyset} = \frac{\Delta T_\emptyset}{\Delta T_S} - 1$$

where $\dot{m}_C$ and $\dot{m}_\emptyset$ are the cold water and discharge flowrates respectively. ΔT_S and $\Delta T_\emptyset$ are the temperatures at the outflow and the discharge in excess of the cold water temperature.

The problem dependent boundary conditions were as follows. Uniform velocity and temperature profiles were prescribed at the jet nozzle corresponding to the experimental flowrate and temperature at the discharge. In the absence of experimental data for the turbulence a turbulence energy level of Ø.5% of the mean energy and a

length scale equal to half the discharge diameter were assumed for the estimation of -uniform- k and ϵ values at the discharge. The inlet k and ϵ values had a small but not deciding influence on the results. This is shown in figure 6.8a where the centreline temperature decay for the case (H/D=1Ø, Fd=2) is given for three levels of the inlet turbulence intensity : $k/V_{\emptyset}^2$= Ø, Ø.5, 3.Ø %. At the bottom inlet a uniform horizontal velocity profile was assumed corresponding to the estimated cold water flowrate; the temperature was taken from the experiments and zero values were assumed for k and ϵ . At the outflow boundary a uniform exit velocity profile conserving mass was assumed together with a zero normal gradient condition for the rest of the variables.

The computations were carried out with a grid having (35*38) nodes. This level of grid resolution was obtained from grid dependence checks for the case (H/D=1Ø, Fd=4) shown in figure 6.5. Three grids of increasing resolution were used in these checks having (25*25), (3Ø*32) and (35*38) nodes. The parameters checked were the centreline (T_C^*) and surface (T_S^*) excess temperatures normalized as follows:

$$T_C^* = \frac{T_C - T_A}{T_{\emptyset} - T_A} \qquad T_S^* = \frac{T_S - T_A}{T_{\emptyset} - T_A}$$

where T_C, T_S, $T_{\emptyset}$, T_A are respectively the centreline, surface, discharge and ambient temperatures. Negligible changes can be observed between the (3Ø*32) and (35*38) levels and even the coarsest grid results were very close. The grid was significantly more concentrated close to the axis of symmetry and to the free surface and these were the

sensitive areas where the extra nodes were introduced. The strongly buoyant character of the flow required heavy under-relaxation of the momentum equations in the form of the false transient approach described in Chapter 2. About 1800 iterations were required to obtain a steady state situation. The evolution of the solution for the case H/D=10, Fd=4 is shown in figures 6.6 a,b and c. The temperature field did not substantially change over the last 1000 iterations but small changes of the velocity field can be observed -figure 6.6c. The computations required 32 minutes of CPU time on an AMDAHL V8 computer. Finally, for these and the rest of the calculations reported in this chapter the quadratic differencing scheme did not produce significant problems. Overshoots and undershoots were observed in the temperature field particularly at the edges of the jet close to the discharge resulting in temperatures higher than the discharge temperature (+2%) or lower than the ambient temperature (-3%) Temperatures exceeding the discharge temperature or below the ambient temperature were not taken into account in the estimation of the buoyancy terms in the momentum and k equations but no actual clipping of the mean temperature was performed.

We begin the presentation of the results with the predictions of the centreline velocity. Velocity data are not available for comparisons but it is interesting to demonstrate the influence of the buoyancy acceleration on the centreline velocity development, figure 6.7. For the larger Froude number (Fd=8) the centreline velocity curve is

similar to those presented for isothermal flows showing a continuous decay. As the Froude number is decreased the buoyancy accelerates the flow and for the case Fd=2 the centreline velocity reaches a maximum value equal to $1.5*V_{\emptyset}$ ($V_{\emptyset}$ is the velocity at the discharge) before it starts to decay. Predictions for the centreline excess temperature T_C^* are compared with the data in figure 6.8. The agreement is very good for the two larger Froude numbers (4 and 8), whereas for the lower Froude number Fd=2 the centreline temperatures are overpredicted by 10%. For this latter case, better agreement with the predictions -close to the surface- could be obtained with significantly higher values of turbulence at the inlet ($k/V_{\emptyset}^2 =$ 3%) but then the initial decay was overpredicted (figure 6.8a).

Lee and Jirka (1981) derived relations for the centreline velocity and excess temperature of a vertical buoyant jet discharging in an infinite water body. These relations form a part of the integral analysis of these authors for the vertical buoyant discharge in shallow water and were used for the calculation of the vertical jet region of the shallow discharge. The assumptions made for the derivation of these relations were briefly presented in chapter 1, it should be pointed out however, that in this analysis it is assumed that the vertical buoyant jet region is not influenced in any way by the existence of the free surface. The centreline velocity and excess temperature predicted by these relationships were plotted (for $y/D<10$) in figure 6.9a for the three cases considered here (Fd=2,4,8). The acceleration of the jet shown in this figure

is far more pronounced than in the numerical predictions though the qualitative trends are the same. Comparisons with the temperature data (figure 6.9b) are meaningful only away from the free surface (in the region y/H<Ø.8 according to the analysis of Lee and Jirka (1981)). It can be seen that both the length of the potential core and the decay rate of the centreline excess temperature are overpredicted though the qualitative trends are correct. It is clear from figure 6.9 that the performance of the present numerical solution is far more satisfactory than the integral analysis.

Both data and predictions show that the lower the Froude number the lower the centreline temperatures indicating more vigorous mixing at lower Froude numbers. This trend can be explained if the influence of the buoyancy on the jet evolution is taken into account. The ambient fluid entrainment is sometimes related to the centreline velocity of the jet by a relationship of the form:

$$\dot{m}_e = \frac{d\dot{m}}{dy} = 2\pi\ \alpha\ b\ V_C$$

where $\dot{m}_e$ is the entrainment, $\dot{m}$ is the mass flux within the jet, b is the nominal jet width, V_C is the centreline velocity and α is an entrainment coefficient. Experimental evidence (Lee and Jirka, 1981) suggests that for self-similar round jets and plumes α assumes values of Ø.Ø57 and Ø.Ø85 respectively. In the present predictions α does not have to be specified, being defined by the turbulence model. The previous relation shows that the strong acceleration of the flow occuring at the lower Froude numbers is associated with an intensification of entrainment

and hence with a more rapid decay of the centreline temperature. A second factor contributing to the same effect is the influence of the unstable stratification, occuring close to the axis of symmetry, on the turbulence energy equation. In this region the buoyancy contribution in the balance of k is positive:

$$\frac{\partial T}{\partial y} < 0 \quad \text{and} \quad G = - g \frac{\nu_t}{\sigma_T} \frac{\partial T}{\partial y} > 0$$

The lower the Froude number the higher the buoyancy generation (G) in relation to the mean rate of strain production. The higher turbulence intensity predicted for the lower Froude numbers results in more intense entrainment and mixing and hence in lower centreline temperatures. That these factors contribute separately to the intensificaton of entrainment is shown in figure 6.3 where centreline excess temperature (RSFT) predictions are given for a shallow discharge (H/D=1Ø, Fd=4). As discussed in the previous section these predictions were obtained when:

.the buoyancy terms were omitted in both the momentum and turbulence equations (curve A)

.the buoyancy was omitted in the turbulence equations (curve B)

.the buoyancy terms were retained in all equations (curve C or D)

in agreement with the previous rationale the magnitude of the centreline temperatures is reduced in the order (A)-(B)-(C).

As far as the centreline velocity development is concerned, the buoyancy effects influence this in two ways:

Firstly through the gravitational term in the vertical momentum equation which tends to accelerate the flow. Secondly through the gravitational term in the turbulence energy equation which tends to increase the level of turbulence energy or shear stress at the edge of the jet and consequently to decelerate the flow. It is obvious from figure 6.7 that for the lower Fd case, where both influences are relatively stronger, the accelerating influence is dominant.

Comparisons with the few experimental temperature profiles are shown in figure 6.10. Reasonable agreement can be observed though it seems that diffusion is underpredicted. Surface excess temperature (T_s^*) comparisons are shown in figure 6.11. At some distance from the axis of symmetry (r/D>5) good agreement with the data can be observed -particularly if the approximate derivation of the cold water flowrate is taken into account-. Close to the axis of symmetry both data and predictions show a rapid decay of the surface temperature associated with:

i) the intense mixing occuring in the surface impingement region,

ii) the continuing entrainment of ambient water.

As the stably stratified temperature profile is gradually established steep stabilizing buoyancy gradients occur at the edges of the warm water layer (figure 6.6b) resulting in a continuous reduction of entrainment and consequently insignificant temperature changes. It is therefore obvious that the predictions are more sensitive to the accuracy of the turbulence model in the region (r/D<5)

where entrainment and diffusion dominate the evolution of the temperature field and less sensitive in the downstream region where the strong stable stratification damps the turbulence at the edges of the layer leading to a cessation of entrainment. It is consistent with this rationale that the maximum deviations from the data occur in the region $r/D<5$; however reasonable agreement can still be observed in this region.

The surface temperature data complete the comparisons with the experimental data available. On the basis of these comparisons it is clear that the buoyancy extended k-ϵ model performed satisfactorily in this flow. This conclusion, together with the observed performance of the model for the buoyant surface jet, the internal hydraulic jump and the shallow isothermal discharge encouraged optimistic expectations for the prediction of the more complex vertical buoyant discharge in shallow water, where these phenomena occur in a combined form.

The remainder of the chapter deals with the prediction of the buoyant vertical jet in shallow water. The experimental data used for the validation of the predictions were those of Jirka and Harleman (1979) and Lee and Jirka (1981). The presentation of this work requires first some discussion of the approach adopted for the simulation of the experimemts.

6.3. The simulation of the experimental situation

In the experiments of Jirka, Harleman and Lee

(1979,1981) a round or plane vertical buoyant jet was discharged from the bottom of a large water tank. The surface level of the tank was kept constant by means of overflow weirs, in the round jet experiments, or by withdrawing an ambient water flowrate equal to the discharged flowrate in the plane jet experiments. It is obvious that with this experimental set-up a truly steady state situation cannot be achieved given that the majority of the mixed warm water remains in the tank increasing continuously its heat content. However, the capacity of the tanks used was so large in relation to the discharge flowrate that a quasi-steady state situation could be established for a period of time, sufficiently long to allow temperature measurements and flow visualization to take place. Lee and Jirka (1981) report that in order to ensure that "...some kind of quasi-steady state situation was reached in the experiments a surface temperature scan was always taken at the end of the experiment. In all runs the temperature recordings of the last surface scan in the near field were very close to those of the first few scans...". It is clear therefore that both experimental situations (plane and axisymmetric) were time dependent, characterized by a quasi-steady period during which the temperature field did not change substantially (at least in the near-field) and the same qualitative characteristics of the flow prevailed.

An exact simulation of these experiments would therefore require , firstly, the simulation of the experimental tank as closely as possible (in a 2-D form for the present

calculations) as a pre-requisite for the proper representation of the experimental quasi-steady state. Secondly, the transient character of the flow must be accepted starting the calculation from a still, ambient temperature water condition and continuing the solution in real time until an acceptably low rate of change of the variables was established.

This type of approach could be followed only partially in the present work since the consistent transient simulation of the experiments presented, for the following reasons, very severe computational difficulties. The achievement of true transient solutions (i.e. fully converged at each time step - without inner iterations and recalculation of the coefficients-) required very small time steps dictated by the relatively high velocities at the discharge and the strongly buoyant (and hence numerically unstable) character of the flow. Small time steps result in a very slow evolution of the solution in the far-field region where the velocities are literally orders of magnitude lower than the velocity at the discharge. This problem was exacerbated in the case of round jet experiments by the axisymmetric character of the flow leading to a diffusing effect on the far-field velocities. Thus, if the true dimensions of the experimental tank were used the achievement of a quasi-steady state would -as demonstrated in the following sections- lead to exorbitant computer run-times. Hence, in the true transient solutions reported in the following sections a substantially smaller tank had to be adopted to allow a quasi-steady state situation to be

reached in reasonable computing times.

The reduction of the tank size had the following consequences. The continuation of the solution is only meaningful until the stage where the warm floating layer has reached the end of the simulated tank and starts to be recirculated towards the discharge. This, for the axisymmetric configurations represented a period of time of the order of 3 minutes which is substantially lower (due to the reduced tank size) than the typical duration of the round jet experiments (20 minutes). Consequently, it is possible that the full effects of the very slow transverse diffusion could not materialize to the extent that they did in the experiments. There is also the possibility that the location of the downstream boundary -typically ten water depths from the discharge- may have affected the results.

Because of these reservations and the exceedingly high computing times required for the transient calculations another approach was initially adopted. The experimental data suggest that in the downstream region of the flow a nearly horizontal stratified counterflow is established (this is indeed one of the sub-regions in the model of the flow suggested by Jirka and Harleman). On the basis of the experimental temperature data the cold ambient water flowrate can be calculated from an overall heat balance. Assuming a uniform temperature across the warm layer the cold-ambient water flowrate ($\dot{m}_c$) can be estimated from the relation:

$$\frac{\dot{m}_c}{\dot{m}_\emptyset} = \frac{\Delta T_\emptyset}{\Delta T_s} - 1$$

where $\dot{m}_{\phi}$ is the discharge flowrate and ΔT_s and ΔT_{ϕ} are the downstream surface and discharge excess temperatures respectively.The uniform temperature profile assumption is a reasonable approximation as can be seen from the experimental downstream temperature profiles (figure 1.4) and the corresponding predictions (figure 6.19). Futhermore, the interface between the two layers can be approximated from the location of the experimental dye trace interface. Therefore, although velocity data are not available, an approximate horizontal velocity profile can be worked out for the downstream region of the flow together with the assumption of zero vertical velocities . Fixing the downstream velocities a steady state calculation can now be performed. The major draw-back of this approach is that the amount of ambient water entrained is fixed from the experiment biasing the predictions. This practice is similar to the one adopted in the internal hydraulic jump calculations. However, in this case the length of the entraining region and the location of the toe of the jump provided a powerful check on the correct simulation of the entrainment process. Such information was not available for the present problem. This type of fixed outflow condition was used for some of the calculations reported in section 6.5.

To relax the above mentioned disadvantage of fixing the entrainment, the following practice was also adopted for a series of predictions. The outflow boundary conditions were initially fixed as previously described and the solution was

significantly advanced to establish realistic variable fields all over the domain. At this stage the downstream boundary condition was altered -as described in detail in the next section- in order to allow the exit profile to vary and conform to the upstream conditions and the turbulence model. This practice required very strong under-relaxation and affected significantly the convergence rate but did allow the entrained water quantity to be an outcome of the calculation rather than an input.

The steady state approach predictions allowed the demonstration of the dominance of the upstream conditions (H/D, Fd) on the evolution of the flow as also postulated by Jirka and Harleman. However, the quantitative comparisons were not satisfactory and transient solutions were subsequently carried out.

In the following sections a series of stable and unstable configurations are considered and a conceptual model of the flow is gradually built-up. In the final section the model of Jirka et al is discussed in the light of the present findings.

6.4. Axisymmetric discharge H/D=11.1

The first series of calculations concern an axisymmetric discharge of D=1.27 cm and H/D=11.1 for which the discharge Froude number was varied. For this geometry and a discharge Froude number of 46 experimental data are available for the temperature field and the location of the visible interface;

the configuration is stable in the way described in chapter 1 i.e. warm-mixed water is not re-entrained. In the predictions the discharge and ambient water temperatures were as for the experiment; the discharge velocity was given the experimental value and was also varied resulting in four discharge Froude numbers: Fd=20,46,66 and 110. The location of these configurations on the stability map of Jirka and Harleman is shown in figure 6.12. The first value is well within the stable region, the last well in the unstable and the two intermediate values are close to the stability line (one on the stable and one on the unstable side).

The steady state approach with a free outflow boundary (entrainment flow not fixed) was initially adopted for these calculations. The downstream surface temperature data for this configuration (H/D=11.1, Fd=46) suggest that the entrained cold water flowrate was approximately 10 times the discharge flowrate. For all cases predicted it was initially assumed that the cold water flowrate was ten times the discharge flowrate. A horizontal outflow velocity profile was worked out to satisfy continuity with a zero value at the depth of the experimental interface taken from the case Fd=46. The profile consisted of two uniform value parts (positive in the upper region and negative in the lower region) with a smoothing parabolic curve in between, figure 6.13. Zero vertical velocities were assumed across the outflow, which was located 8 water depths from the axis of symmetry. The remaining outflow boundary conditions were as follows. For the temperature the ambient value was prescribed for the in-flowing part of the profile and a zero

normal gradient condition was applied for the out-flowing part. For k and ϵ zero values were adopted for the inflow stream and zero normal gradient for the out-flow. At the discharge the conditions were defined as for the calculations reported in section 6.2.

Close to 1000 iterations were initially carried out to allow the establishment of realistic flow and buoyancy fields. Strong under-relaxation in the form of a false-transient solution was required to overcome the buoyancy related instability. At this stage the downstream boundary condition for the horizontal velocity was changed as follows. The continuity equation was applied locally at each grid node; the horizontal velocities were, at each iteration, set equal to the value of the node immediately before the outflow appropriately normalized by the ratio of the corresponding radii. The vertical velocity was kept at zero (when the vertical velocity was also allowed to vary the solution consistently diverged). From this point the solution was constantly monitored until a steady state situation was approached.

The evolution of the solution for the experimental case (H/D=11.1 and Fd=46) is shown in figures 6.14 and 6.16. In figure 6.14 three critical parameters are plotted i.e. the in-coming cold water flowrate, the stream function value at a characteristic location in the middle of the solution domain and the downstream surface temperature. After 4.900 iterations the last two parameters tend to asymptotic values while the cold water flowrate is still changing slightly. The temperature field, figure 6.16, did not change

significantly over a very large number of iterations. The same trends can be observed in figure 6.15 for the case H/D=11.1, Fd=11Ø where close to asymptotic values have been established.

In general 49ØØ-6ØØØ iterations were required to confirm a steady state situation. The grid in these calculations had 37 nodes in the horizontal direction and 31 nodes in the vertical direction; the computations required 8Ø minutes of CPU time (AMDAHL V8). These large computing times did not allow grid independence checks to be performed, but calculations of recirculating flows reported earlier encourage the view that this mesh is sufficiently fine.

The predicted steamline patters are shown, for the four cases, in figure 6.17. The following observations can be made on this figure:

1) In the downstream part of the solution domain (r/H>5) a horizontal stratified counterflow is established. As shown by the streamlines and the temperature profiles a mixed floating layer is moving towards the outflow whereas an ambient temperature layer is moving towards the discharge. The amount of ambient water ($\dot{m}_c$) entrained by the discharge decreases as the Froude number of the discharge is increased.

2) Closer to the discharge a recirculation cell is formed for Fd=46,66 and 11Ø separating the cold and warm water layer. The maximum value of the stream function ($\dot{m}_{TOT}$) shown in figure 6.17 quantifies the total circulation induced in the tank by the discharge. The total circulation consists of

two parts:

i.A large scale circulation where ambient water is approaching and mixes with the discharge and eventually forms the mixed warm layer which moves towards the outflow. The flowrate of the mixed layer is $\dot{m}_D=\dot{m}_\emptyset+\dot{m}_C$ where $\dot{m}_\emptyset$ is the discharge flowrate.

ii. A closed, near-field recirculation where re-entrainment occurs. The amount of re-entrained or recirculated water $\dot{m}_R$ is $\dot{m}_R=\dot{m}_{TOT}-\dot{m}_\emptyset-\dot{m}_C$.

The partition of the total circulation induced in the tank into large scale diluting circulation and recirculating components is shown in table 6.1.

TABLE 6.1

Fd	Total circulation $\dot{m}_{TOT}$ / $\dot{m}_\emptyset$	Recirculation $\dot{m}_R$ / $\dot{m}_\emptyset$	Large scale circulation. $\dot{m}_D$ / $\dot{m}_\emptyset$
110	18.1	11.4	6.7
66	18.4	7.2	11.2
46	19.5	6.4	13.1
20	23.0	0.0	23.0

From table 6.1 and figure 6.17 it can be observed that both the strength ($\dot{m}_R$) and the size of the recirculation cell increase as the Froude number is increased.

3) For all Fd values considered the streamline patterns are similar in the close to the discharge region (r/H<3); differences are observed mainly in the region r/H>3 concerning the extent and the strength of the cell. For example for Fd=11Ø the streamline $1Ø\dot{m}_\emptyset$ is closed whereas for Fd=66,4Ø and 2Ø the same streamline is open indicating the reduction of the recirculation strength and size. As Fd is

decreased the strength of the buoyancy forces increases and a new balance is established between buoyancy and inertial and viscous forces. The new balance affects the streamline patterns particularly in the region r/H>3 leading to a gradual reduction of strength and extent of the recirculation cell until it finally disappears for Fd=2Ø. The distinction between the large scale diluting circulation ($\dot{m}_D$) and the near field re-entraining recirculation ($\dot{m}_R$) is crucial for the explanation of the temperature field predictions.

Predictions of the surface temperature are shown in figure 6.18. In agreement with the experimental data a practically constant surface temperature is established over the downstream part of the flow. As the Froude number is increased the large scale diluting circulation is decreased resulting in higher surface temperatures.

Temperature profiles are shown for several radial locations in figure 6.19. For the lower Froude numbers Fd=2Ø and 46 it can be seen that the temperature profile width is always smaller than the tank depth and consequently cold ambient water does reach the discharge. Thus the configurations Fd=2Ø and 46 are predicted to be stable in the terminology of Lee anf Jirka (1981). As mentioned above these configurations lie on the stable side of the stability map of the previous authors (figure 6.12). For the higher Fd value studied (Fd=11Ø) the profiles are diffused down to the bottom of the tank for the stations r/H=Ø.36, 1 and 2 while at the last downstream station the two layer structure can be observed. Cold ambient water does not reach the discharge

and consequently the configuration is predicted to be unstable, in agreement with the integral analysis prediction (figure 6.12). An intermediate situation is predicted for Fd=66. For this case the temperature profile close to the discharge is diffused across the tank but water with temperature very close to the ambient temperature is still reaching the discharge. For this case Jirka et al used the term submerged jump (see figure 1.4, case 2).

The shape of the temperature profiles shown in figure 6.19 can be explained if the predicted streamline patterns are taken into account. The higher the Froude number the lower the dilution of the discharge and consequently the higher the peak temperatures of the profiles. Furthermore, as the Froude number is increased the size and strength of the near-field recirculation increases resulting in wider profiles due to downwards convection of mixed water. For r/H=2 the profiles show a characteristic flatness beneath the surface layer which reflects the convective mixing associated with the near field recirculation.

In order to simulate the experimental visual observations of the flow it was assumed that the visible interface corresponded to an excess temperature (or similarly dye concentration) of 3% of the temperature excess at the discharge. This percentage was deduced from the location of the experimental visible interface in relation to the measured temperature profiles (figure 1.4). The predictions are shown in figure 6.20. As the Froude number is increased the predicted visible layer depth increases until for, the unstable case Fd=110, the interface is

attached to the bottom. Figure 6.2Ø provides an indication from the numerical predictions of the visual manifestation of the transition from stable to unstable forms as observed during the experiments.

In figure 6.21 the temperature field predictions are compared with the experimental data for the case H/D=11.1 and Fd=46. The comparisons of the temperature profiles and location of the implied visible interface are not satisfactory. In the first two radial locations the surface temperature is significantly overpredicted indicating also significant differences in the velocity field (implied by the conservation of thermal energy). Even though -at this stage- conclusions cannot be safely drawn the width and shape of the experimental temperature profiles and the visible interface data suggest that in the experiment either the recirculation cell did not exist at all or it was of a far more limited transverse extent and closer to the surface than the predictions imply.

In order to investigate the serious quantitative discrepancies between data and predictions a true transient solution of the problem was eventually adopted. Only the experimental configuration H/D=11.1 and Fd=46 was recalculated. The solution domain adopted for this calculation is shown in figure 6.22. A uniform velocity profile conserving mass was assumed at the outflow together with a zero normal gradient condition for the remaining variables. Two calculations were carried out; in the first the outflow boundary was located 1Ø water depths from the

axis of symmetry and in the second 2Ø water depths.

To obtain a solution converged at each time step (without inner iterations and recalculation of the coefficients) a time increment Δt corresponding to a nominal Courant number $Cu=V_{\emptyset}*\Delta t/D=\emptyset.16$ had to be adopted. As mentioned in section 6.3 the solution was continued until the stage when the warm floating layer had reached the end of the simulated tank and started to recirculate towards the discharge. This required 136.8 seconds from the moment the discharge was "switched-on" or 68400 time steps. For the rather coarse grid adopted (29*21 nodes) the computations required 7.7 hours of CPU time on an AMDAHL V8 computer.

In order to investigate possible effects of the location of the outflow on the results a larger tank was considered in the second calculation with the outflow located 2Ø water depths from the axis of symmetry. The grid had (42*21) nodes, the solution was advanced for 36000 time steps with the same Courant number at the discharge.

The smaller tank predictions will be discussed first. In the initial stages of the solution the flow-pattern is similar to the axisymmetric isothermal discharge. The initial condition of zero turbulence energy all over the domain results, at the first stages of the solution, in a reattachment length of Xr=2.8H i.e. a value smaller than the value Xr≈4H reported in the previous chapter for axisymmetric configurations. However, as soon as the temperature field is convected into the surface jet region the reattachment point starts to move downstream and the

recirculation cell becomes more elongated until it finally covers the whole solution domain. The flow-pattern evolution is presented schematically in figure 6.23. As the higher temperature fluid is convected up to the surface region, the buoyancy forces overcome inertial and viscous forces (which cause downward streamline curvature) and fluid which was previously recirculated in the near field region begins to move in practically horizontal trajectories setting up the large scale circulation shown in figures 6.23 and 6.24. The reattachment length as a function of time is shown in figure 6.25. The normalizing time $t_{\emptyset}$ used in the last two figures is the time required for the predicted visible interface ($\Delta T/\Delta T_{\emptyset}$=3%) to reach the outflow of the solution domain.

The large scale circulation covering the whole domain is established at $t/t_{\emptyset}$=Ø.5 i.e. considerably before the temperature is convected to the downstream end of the domain. The streamline pattern shown in figure 6.24 corresponds to the time $t/t_{\emptyset}$=1. After the large scale circulation has been established ($t/t_{\emptyset}$=Ø.5) only small changes were observed in the velocity field. In figure 6.26a the stream function was plotted for two radial locations and for three different stages of the solution; slight changes can be observed but for the downstream station only. It is obvious therefore that the velocity field reached a quasi-steady state situation soon after the large scale circulation was established.

Furthermore, it is clear from figure 6.24 that the temperature field had also reached a quasi-steady state situation in the region of the discharge which is not

immediately affected by the outflow. During the whole duration of the solution the temperature field in the near-field region remained unchanged as can be seen from the locus of points where $\Delta T/\Delta T_{\emptyset}$=3% (visible interface) and $\Delta T/\Delta T_{\emptyset}$=1% plotted in figure 6.24 for two stages of the solution ($t/t_{\emptyset}$=0.81 and 1.15).

The main difference between the flow-pattern predicted by the steady state approach (figure 6.17-Fd=46) and the transient predictions is that in the latter case the near-field recirculation cell does not appear; this brought about significant improvements in the temperature field predictions. Comparisons with the data are shown in figure 6.21. The quality of the predictions has been substantially improved but the quantitative comparisons are still imperfect. Initially the surface temperature is overpredicted whereas in the downstream region the predictions show a more diffused profile in relation to the data. This overprediction of diffusion is probably a manifestation of the deficiancies of the buoyancy extended k-ϵ model discussed in chapter 4. The model tends to underpredict the stable stratification turbulence damping and is not able to account for the influence of the free surface on the turbulence structure. These two factors result, for the situation shown in figure 6.21a, in an overprediction of transverse diffusion. The implied visible interface though better predicted still does not exactly reproduce the observed shape.

Finally, for the larger tank (L/H=20) the transient solutions showed practically identical results with the

corresponding smaller tank (L/H=1Ø) results. At the stage where the larger tank calculation was stopped ($t/t_{\emptyset}$=Ø.55) the reattachment point was located 11 water depths downstream from the axis of symmetry. Temperature profiles obtained for the two tank lengths are shown for $t/t_{\emptyset}$= Ø.55 in figure 6.26b and can hardly be distinguished. Hence the reservation mentioned in section 6.3 concerning the influence of the tank length on the near-field results does not seem to be justified.

6.5. A stable shallow axisymmetric discharge (H/D=2.2, Fd=8)

The second series of calculations deal with a second experimentally examined axisymmetric discharge D=2.54 cm, H/D= 2.2, Fd=8. This submergence depth and Froude number combination is much closer to those occuring in practice (see chapter 1, table 1.1). The steady state approach with a fixed outflow velocity profile was initially adopted. In order to minimize the influence of the downstream boundary on the near field predictions this was located sixteen water depths from the axis of symmetry. The downstream boundary velocity profile was again worked out on the basis of information derived from the experimental temperature and interface data in the way described in the previous section and was kept constant throughout the solution. The fixed outflow conditions allowed faster convergence; 3ØØØ iterations were required for the establishment of a steady state solution with a grid having 31 nodes in each direction. The computations required 34 minutes of CPU time (AMDAHL V8).

The predicted streamline pattern -figure 6.27b- is similar to the steady state approach predictions for the previous configuration; it consists of a near field entraining region, a recirculating cell separating the warm and ambient water layer and a horizontal stratified counterflow in the far-field region. Comparisons of the temperature field predictions with the data are shown in figure 6.28. Across the near-field recirculation, the temperature profiles are spread over the larger portion of the tank depth. Closer to the wall however, low temperatures are predicted ($\Delta T/\Delta T_{\emptyset} < 3\%$) and water of temperature close to the ambient temperature is still reaching the discharge. A similar situation was observed in the experiment and the term "submerged jump" was used by Lee and Jirka for the configuration in question. The quantitative comparisons were again not satisfactory; as a consequence of the predicted near-field recirculation the predicted temperature profiles are wider than the experimental and the values are in general overpredicted. As for the previously examined stable configuration the experimental profile shape and width suggest that in the experiment either the cell did not exist or it was of far more limited transverse extent and closer to the surface than the predictions imply.

In order to demonstrate the importance of the discharge Froude number on the predicted flow pattern another steady state calculation was carried out for which the geometry, the ambient water entrainment and the discharge and ambient water temperatures were as for the experimental case but the discharge velocity was increased to give an Fd value of 10.4

(an increase of 30%). The new configuration (H/D=2.2, Fd=10.4) lies on the unstable side of the Lee and Jirka stability map (figure 6.12). This increase of the discharge Froude number changed critically the balance between buoyant and inertial and viscous forces giving a reattached recirculation close to the discharge, figure 6.27a. In the steady state calculations reported in the previous section it was demonstrated that as the discharge Froude number is increased the strength and size of the recirculation cell increases whereas the ambient water entrainment decreases. The present situation can be considered as a limit of this process; the near-field recirculation is attached onto the bottom covering the whole depth of the tank and the discharged jet does not entrain ambient water al all. The closed recirculation cell is fully mixed and the discharge temperature prevails all over the cell (figure 6.27c). Further downstream the buoyancy forces force the warm layer afloat and the strong buoyancy gradients at the edges of the layer damp the turbulence resulting in slow mixing of the warm and cold water. (Practically speaking the surface temperature is equal to the discharge temperature for r/H<10).

In order to investigate the discrepancies between the steady state predictions and the data a transient solution of the experimemtal configuration (H/D=2.2, Fd=8) was also carried out. Again a tank smaller than in the experiment was assumed (L/H=10); the grid had 29*21 nodes, the nominal Courant number -$Cu=V_0 * \Delta t/D$- had a value of 0.05; 15000 time steps were calculated and the computation required 1.8 hours

of CPU time (AMDAHL V8).

The evolution of the solution is similar to the one described in the previous transient solution; as the buoyancy field is convected the reattachment point moves towards the downstream end of the domain resulting in the large scale circulation shown in figure 6.29. The streamline pattern in this figure corresponds to the time $t/t_{\emptyset}$=1.34 ($t_{\emptyset}$ is the time elapsed before the isotherm $\Delta T/\Delta T_{\emptyset}$=1Ø% reached the outflow). Soon after the large scale circulation was established the streamline pattern reached its quasi-steady state. In the same figure it can be observed that the temperature field had also reached a quasi-steady state in the region of the flow not immediately affected by the downstream end of the domain.

The predicted streamline pattern, figure 6.29, does not show a near-field recirculation. However the stream function has a local maximum in the near-field region (figure 6.29) though the rather coarse grid used did not allow the resolution of a corresponding closed recirculation of limited extent. The non-existence of significant near-field recirculation produced a substantial shift of the temperature field predictions towards the data (figure 6.2Ø); the width and shape of the temperature profile is correctly predicted but the surface temperatures are still in error by 2Ø%. The locus of the points where $\Delta T/\Delta T_{\emptyset}$=1Ø% -figure 6.29- reproduces qualitatively the shape of the experimental visible interface. (Comparison between the experimental and predicted interface is not meaningful in this case since in the experiment the interface given does

not correlate consistently with the temperature data i.e. it does not correspond to a locus of given temperature excess ,figure 1.4).

From the steady state predictions it can be concluded that the treatment of the downstream boundary associated with the steady state approach affects significantly and adversely the temperature field predictions. The transient solution predictions and the data show that the assumed horizontal velocity profile with zero vertical velocities at the downstream end of the domain are not unrealistic assumptions. However the enforcement of the horizontal character of the flow by the boundary condition and ,probably, the inability to specify the local pressure gradients forced the inner streamlines to close and form the near field recirculation affecting considerably the temperature field predictions.

The steady-state predictions did prove sensitive to the variation of the discharge Froude number and the correct qualitative behaviour was predicted, however, the quantitative comparisons were rather descouraging and it was therefore decided that subsequent calculations for the unstable configuration should be carried out with the transient approach only.

The transient solution predictions for the two stable configurations previously examined support the following generalizations concerning the nature of the flow in its stable form. A large circulation is induced in the shallow water body by the buoyant discharge. The discharge Froude

number must be sufficiently low to prevent reattachment onto the lower wall and establish the nearly horizontal flow pattern. A two layer structure is then established and the typical (for isothermal flows) near-field recirculation disappears. The strength of the large scale circulation depends on the submergence depth ratio H/D (the possible dependence on the discharge Froude number will be discussed in one of the following sections). The surface temperatures (for the stable form) depend on the induced circulation and consequently the lower the submergence depth ratio the higher the surface temperatures. The experimentally observed shape of the visible interface for the stable configuration is compatible with the suggested flow pattern and was reproduced in the predictions by the shape of the isotherms.

6.6. An unstable axisymmetric discharge (H/D=10, Fd=205)

A third experimentally examined configuration was considered next D=0.635 cm, H/D=10 and Fd=205. The configuration is unstable (see figure 1.4, case 3) and the experimental data show that the visible interface was attached to the bottom of the tank. The data show that, relating to the stable form, the temperature field is significantly more diffused in the near-field region. In the downstream region a horizontal counterflow is again established. The temperature data suggest that though mixing with the ambient water occurs the amount of ambient water entrainment is significantly reduced in relation to the stable discharge.

In the predictions the outflow of the tank was located 11.5 water depths from the axis of symmetry. The nominal Courant number had a value of Ø.269. The solution was advanced for 56ØØ time steps and the computations required 6.7 hours of CPU time (AMDAHL V8) for a 3Ø*21 grid.

The predictions for the streamline pattern and the implied visible interface ($\Delta T/\Delta T_{Ø}$=3%) are shown in figure 6.3Ø . In contrast to the previous stable configuration predictions the implied visible interface is indeed attached to the bottom of the tank. The time $t_{Ø}$ elapsed before the attachment of the interface was used for the normalizations shown in figure 6.3Øb.

As in the previously examined configurations, during the early stages of the solution the flow-pattern is similar to the isothermal discharge flow-pattern. As the temperature is convected into the surface layer the reattachment point again moves downstream until the large scale circulation covers the whole solution domain as shown in figure 6.3Øa. The different behaviour of the unstable discharge can be explained if the streamline pattern of the developed large circulation shown in figure 6.3Øa is compared with the streamline pattern of the previously examined stable discharge (H/D=11.1, Fd=46) shown in figure 6.24a. In both cases the buoyancy forces are strong enough to remove the reattachment to the downstream end of the domain and establish the large scale circulation. However, in the stable configuration the buoyancy forces are also sufficiently strong to establish a practically horizontal flow of the warm layer and eliminate completely the

near-field recirculation. As a consequence mixed water is not re-entrained in the near-field region and ambient water penetrates right up to the discharge. In the unstable configuration the buoyancy forces are not sufficiently strong to effect the same evolution. The near-field recirculation remains and mixed water is re-entrained close to the discharge. As a consequence of the mixed water re-entrainment, high excess temperatures are found over the entire tank depth and the visible interface is attached to the tank bottom. Furthermore, the re-entrainment of already mixed water leads to the higher surface temperatures observed for the unstable configurations in the experiments.

The effects of the near-field recirculation are clear in figure 6.30b where the evolution of the predicted visible interface ($\Delta T/\Delta T_{\emptyset}=3\%$) is shown for three stages of the solution. The interface quickly attaches itself to the bottom of the tank and the temperature profile is diffused all over the tank depth in the near-field region. It is obvious that the experimentally observed increased surface temperatures, for the unstable configuration in question, could be reproduced in the predictions if the solution was advanced in terms of real time sufficiently long to allow the warm-entrained water to be convected within the recirculation zone and eventually to be re-entrained by the vertical jet. However the time step imposed by the convergence criteria was very small in relation to the time scales of the flow development so that a quasi-steady state situation could not be achieved in feasible computing times. The solution was terminated at the stage shown in figure

6.30; comparisons with the temperature data are meaningless since the temperature field was far away from a quasi-steady state situation even in the near-field region where the temperatures were continuously increasing due to re-entrainment of mixed water.

In order to overcome the problem of the very slow downstream evolution of the solution which is partially associated with the axisymmetric geometry, it was decided to continue the study of the unstable configuration in its plane form where it was expected that this problem would be alleviated.

6.7. A plane unstable discharge (H/D=190.6, Fd=80)

A plane unstable configuration was therefore considered next: D=0.32 cm, H/D=190.6, Fd=80 (the configuration is not a shallow discharge, however only for this case were detailed temperature data available (Jirka and Harleman (1979)).

In the predictions the outflow of the tank was located 10 water depths from the symmetry plane. In the experiment the channel had the same length but was connected with a very large water reservoir ensuring that the warm entrained water was not recirculated from the end of the channel. The nominal Courant number had a value of 1.625, the grid had 40*21 nodes, the solution was advanced for 57225 time steps and the computations required 9.23 hours of CPU time (AMDAHL V8). In the predictions the solution was advanced for 7.7 minutes of real time and this should be compared with a

period of 1Ø minutes required in the experiment for the establishment of a quasi-steady state situation within the channel.

Again, initially the flow pattern is similar to the isothermal one, but as buoyancy forces intrude the reattachment point gradually moves downstream until the large scale circulation, common in all configurations examined so far, is established all along the solution domain (figure 6.31a). The location of the reattachment point as a function of time is shown in figure 6.32a. The normalization time $t_{\emptyset}$ used in figures 6.31 and 6.32 is the time elapsed before the predicted visible interface ($\Delta T/\Delta T_{\emptyset}$=3%) reached the outlet of the tank.

During the whole duration of the solution, and even during the period of the large scale circulation development, the total circulation induced in the tank ($\dot{m}_{TOT}$) and the location of the point where the stream function has its maximum remain -after an initial development stage- more or less constant, figure 6.32a. The stream function reaches a maximum value of $\dot{m}_{TOT}/\dot{m}_{\emptyset}$=1Ø.3 which compares satisfactorily with the previous estimate for plane isothermal configurations:

$$\dot{m}_{TOT} / \dot{m}_{\emptyset} = 0.848 \ (H/D)^{\frac{1}{2}}$$

giving in this case a value of 11.68. As the temperature field is convected the stable stratification damps the turbulence, and hence the entraining capacity of the surface jet, and the $\dot{m}_{TOT}/\dot{m}_{\emptyset}$ value is slightly but continuously reduced to a value of 9.3. Thus the normalized total

circulation ($\dot{m}_{TOT}/\dot{m}_{\emptyset}$) depends, as was shown for the non-buoyant discharge, on the submergence depth (H/D) and, in addition, on the strength of the stable stratification across the surface layer which is related with the discharge densimetric Froude number ($-Fd^{-1}$).

The predicted streamline pattern for the time $t/t_{\emptyset}=1.17$ (5.25 minutes) is shown in figure 6.31a; the distinction between the near-field recirculation ($4\dot{m}_{\emptyset}$) and the large scale diluting circulation ($5.5\dot{m}_{\emptyset}$) is clear . The predicted strength of the large scale circulation ($5.5\dot{m}_{\emptyset}$) is in agreement with the reported experimental dilution of the discharge ($5.3\dot{m}_{\emptyset}$). The existence of a near-field recirculation results in the convection of the temperature field across the tank, consequently the implied visible interface is attached to the bottom in the near-field region i.e. an unstable configuration in the terminology of Jirka et al.

In figure 6.31b where the surface temperature and the implied visible interface are given for three stages of the solution $t/t_{\emptyset}=1.07$, 1.32 and 1.49 it can be seen that a practically quasi-steady situation was established for the region not immediately affected by the outlet ($x/H<6$). To further check the establishment of a quasi-steady state situation the heat flux across the channel was evaluated along the domain at ($t/t_{\emptyset}=1.324$) from the equation:

$$\dot{q}(x) = c_P \int_0^H U\,(T-T_A)\,dy$$

where T_A is the ambient temperature. The resulting heat flux $\dot{q}(x)$ normalized by the heat flux at the discharge $\dot{q}_{\emptyset}$

was plotted in figure 6.32b. If a true steady-state situation has been established, the downstream region temperature gradients dT/dx and, consequently,the longitudinal diffusive flux should be negligible giving a ratio $\dot{q}(x)/\dot{q}_{\emptyset}$ close to unity in this region. In figure 6.32b it can be seen that such a situation has not been established since the circulation close to the outlet results in a transverse heat convection continuously increasing the heat content of the tank. However for x/H<6 the quasi-steady state was approached making comparisons with the experimental data meaningful in this region. The predicted temperature profiles for x/H<6 are compared with the data in figure 6.33 for $t/t_{\emptyset}$=1.324 (profiles for $t/t_{\emptyset}$=1.492 practically coincide). It should be taken into account that for the last station (x/H=6) $\dot{q}(x)/\dot{q}_{\emptyset}$=Ø.91 and therefore an error of the order of 1Ø% should be expected anyway. Qualitatively the comparisons are satisfactory; for all stations the profile shape and width are correctly predicted. For the stations x/H=2,3 and 6 the quantitative comparison is satisfactory whereas at the two first stations (x/H=Ø.26,1) the data show a substantially more diffused shape. The surface temperature is correctly predicted at all stations.

6.8. A model of the flow based on the predictions; comparisons with the model of Jirka et al

In the present section a conceptual model of the 2-D vertical buoyant discharge in shallow water, based on the

predictions, will be presented. It is assumed that a vertical 2-D jet (plane or round) is discharged in an initially stagnant water tank of large horizontal extent. As in the predictions the surface level is maintained constant. When the discharged water has a temperature equal to the tank water temperature ($Fd \to \infty$) the isothermal discharge flow pattern will be established consisting of a single attached recirculating eddy in the near-field region and of a practically horizontal outward directed flow in the far-field region.

If, for the same discharge velocity, the discharge temperature is significantly higher than the water tank temperature the buoyancy forces affect substantially the evolution of the flow. Initially the flow pattern is similar to the isothermal flow. However, as soon as the thermal energy is convected into the surface jet region the increased temperatures result in a new balance between buoyant, inertial and viscous forces which tends to keep the warm surface layer afloat. As a consequence the reattachment point moves further downstream; if the discharge Froude number is sufficiently small the reattachment point gradually reaches the outlet wall of the tank. A large circulation is thus established all along the tank consisting in its larger part of a practically horizontal stratified counterflow. However, a closed recirculation cell still exists in the near-field region between the downstream moving surface buoyant layer and an upstream moving mixed water layer (see e.g. figure 6.31a). The extent of the recirculating cell depends on the discharge Froude number;

the smaller the Fd value the smaller the extent of the cell. Below a certain Fd value no near-field recirculation exists.

The total circulation induced in the tank (maximum value of the stream function) depends -as was shown for the isothermal discharge- on the submergence depth ratio (H/D) and, in addition, on the discharge Froude number. The lower the Fd the stronger the turbulence damping at the edge of the surface layer and consequently the lower the entrainment. The total circulation can be conceptually divided in two parts; the first is the near-field closed (re-entraining) recirculation which does not contribute to the dilution of the discharge and the second is the large scale circulation which dilutes the discharge. The near-field recirculation causes re-entrainment of already mixed water. Heat is convected within the near-field recirculation and ambient temperature water does not reach the discharge (figure 6.34). It is obvious that for such a configuration if dye were injected for sufficient time at the discharge it would give a visible interface attached to the bottom in the near-field i.e. an ustable configuration in the terminology of Jirka et al.

As already mentioned, for the case of very low discharge Froude numbers the predictions showed that the near-field closed recirculation disappears altogether and only the large scale circulation all along the tank exists. In such a case ambient temperature water reaches the discharge and the surface temperatures are substantially reduced in relation to the unstable form of the flow. The visible interface observed in the experiments (i.e. sudden deepening close to

the discharge and gradual reduction further downstream) is compatible with this flow pattern as was demonstrated from the implied visible interface in the two stable configurations predicted.

The experimentally observed visible interface (stable discharge) can be divided into two regions (figure 6.35). In the first near-field region ($r/H<3$) the visible layer depth increases with the distance from the discharge. In the second further downstream region the depth decreases until it reaches an asymptotic value in the far-field stratified counter-flow. The suggested model explains the observed shape of the interface as a product of the combination of turbulent diffusion between the counter-flowing layers and the buoyancy term in the momentum equation. In the far-field region the stable stratification damps turbulence at the interface of the layers, consequently insignificant diffusion occurs and the visible depth remains more or less constant. As we move closer to the discharge turbulent diffusion is more intense and dye is diffused into the upper part of the ambient water layer giving the visual impression of a decreasing surface layer width as the distance from the discharge is increased (figure 6.35). The shape of the interface in the first near-field region (region I in figure 6.35) can be explained if the entrainment process is taken into account. In this region the observed increasing depth of the interface with distance from the discharge is a product of dye diffusion between the surface jet and co-flowing newly entrained ambient water.

It should be emphasized that in this suggested model of

the flow the transition from stable to unstable forms is not an abrupt qualitative change of the flow pattern but a continuous change reflecting the decreasing influence of the buoyancy forces.

Qualitatively the suggested interpretation of the unstable form is similar to the one presented by Jirka et al (1979,1981). In the model of Jirka et al the transition to the unstable mode is predicted when the influence of buoyancy forces is reduced resulting in impossible post-jump situations which do not exhibit the energy dissipative nature of the internal jump, Jirka and Harleman (1979). In such a case the flow is interpreted by Jirka and Harleman "...as consisting of a recirculation cell in the near-field with repeated entrainment of mixed water in the buoyant jet. This would lead to a continuous build-up of species-concentration and buoyancy in the near-field. It is assumed therefore that a steady-state limit of this build-up is reached when the "stabilizing" buoyancy force has increased sufficiently to drive the counterflow system in balance with opposing inertial and viscous forces." -quotation from Jirka and Harleman, 1979-. It is clear that the interpretation of the unstable form by Jirka et al is similar to the one previously suggested (present predictions), though the mathematical model of Jirka et al is not able to predict any quantitative details of the unstable form.

For the stable form the main differences between the suggested conceptual model and the model of Jirka et al are:

i) the assumption of Jirka et al that an internal hydraulic jump occurs after an initial surface jet development, and ii) the assumption of Jirka et al that the visible (or temperature) interface of the flow more or less coincides with the zero horizontal velocity interface over a large part of the flow i.e. in the jump and counterflow regions.

The latter assumption is crucial in the analysis of Jirka et al. Only with this assumption can the observed increase of the visible layer depth close to the discharge be interpreted as a sudden increase of the velocity width of the layer i.e. as the roller region of an internal hydraulic jump. The present predictions contradict this assumption and the predicted visible layer depth by no means coincides in the near-field region with the velocity width of the layer. In the model suggested here the heat diffusion between the counterflowing layers plays a crucial role in explaining the observed behaviour.

The surface layer development suggested by Jirka et al for the stable form is similar to the one described for the internal hydraulic jump predictions (chapter 4). For this jump type of flow entrainment takes place only in the initial ante-jump region; along the roller and in the post-jump layer entrainment is insignificant. The steep stabilizing buoyancy gradients at the edge of the post-jump layer destroy the turbulence locally and no diffusive turbulent interaction exists between the surface layer and the supporting non-buoyant fluid. Therefore if the interpretation of the data by Jirka et al is correct the turbulence model used for the present predictions must very

severely underpredict the stable stratification turbulence damping. From the buoyant calculations reported in chapter 4 and other related works a reasonable performance of the buoyancy extended k-ϵ model has been established which does not support this speculation.

Even thought the suggested model offers a unified explanation of all the forms observed stable, unstable and intermediate its validity cannot be confirmed except by further experimental work. A critical test would be the measurement of both temperature and velocity near-fields in all forms of the flow which could clarify the question of the occurence, or not, of an internal hydraulic jump and the question of heat transfer by diffusion between the two layers in the near-field region.

6.9. Summary

The presentation of the prediction of the vertical buoyant jet in shallow water is concluded with a summary of some important aspects of the work and of its major findings.

1) In the experiments the flow is time dependent characterized by a long quasi-steady situation. The exact simulation of the experimental situation could be accomodated by the numerical solution procedure, but this was hampered by the exceedingly high computing times required for the calculations. Smaller tank sizes had to be assumed in the predictions resulting in a significantly shorter duration of the quasi-steady period of the flow

relating to the experimental duration. It had been established that the assumed tank length (1ØH) did not influence the near-field results but some uncertainty remains concerning the extent to which diffusion effects were allowed to materialize.

2) Steady state solutions were performed based on the assumption of a practically horizontal counter-flow in the downstream region with a fixed velocity profile at the downstream boundary based on the temperature and visible interface data. In these solutions the dominance of the discharge Froude number on the evolution of the flow for a given geometry has been demonstrated but the downstream boundary condition affected adversely the results, giving in all cases a near-field recirculation cell and a too diffused temperature field.

3)The transient solution calculations were based on rather coarse grids and grid-independence was not studied. Grid independence checks were not performed due to exceedingly high computational times.

4)Given the drawbacks mentioned in paragraphs 1 and 3 the transient solutions predicted satisfactorily the flow both in qualitative terms (stable, unstable and "intermediate" forms) and in quantitative terms (temperature field predictions).

5) The predictions allowed the proposition of a conceptual model of the flow where all possible evolutions of the flow can be interpreted as departures from the isothermal flow pattern to an extent depending on the strength of the buoyancy forces quantified by the discharge Froude number.

6) The model was compared with the previous proposal of Jirka et al (1981). The viewpoint of these workers for the unstable form is practically identical with the present proposition. For the stable form the propositions are different. The main differences are: 1) the suggestion of an internal hydraulic jump by Jirka et al which was not observed in the present work and 2) the extent to which transverse diffusion of heat takes place between the two layers in the near-field. Further experimental work where both velocity and temperature measurements should be performed is necessary to resolve this controversy.

7) The second moment closure which was applied in all other works reported in this thesis was not applied in this work. It has been demonstrated in chapter 4 that improvement of the prediction of the stable stratification turbulence damping can be achieved by the RSFT model. It is expected that the application of this model in the present flow would be equally beneficial. Further work is however necessary to investigate the problems reported in the first section of this chapter.

CHAPTER 7

ACHIEVEMENTS, CONCLUSIONS AND SUGGESTIONS FOR FUTURE WORK

CHAPTER 7 : ACHIEVEMENTS, CONCLUSIONS AND SUGGESTIONS FOR FUTURE WORK

This chapter summarizes the work performed during this project, outlines the main findings and contributions of the present thesis and puts forward some recommendations for future work. Summaries and conclusions concerning each part of the present work were presented in the relevant chapters of this thesis. In this chapter the previous conclusions are conbined and generalized where appropriate.

7.1. Outline of the work, achievements and conclusions

As explained in chapter 1 the nature of the work presented in this thesis required improvements in two regions of the standard finite difference numerical algorithm solving the set of PDE's governing 2-D buoyant or non-buoyant turbulent flows. The first was the improvement of the convection term discretisation accuracy. To this end the third order accurate quadratic differencing scheme of Leonard (1979) was incorporated into the standard computational algorithm and used throughout this project. The performance of the new scheme was compared with the standard Hybrid scheme in the prediction of a laminar recirculating flow. It was demonstrated that the performance of the standard Hybrid method deteriorated seriously as the cell Peclet numbers of the solution were increased; the quadratic scheme responded faster to the refinement of the numerical grid and grid independence was achieved with grids

significantly coarser than those required by the standard Hybrid method for the same purpose. In all the calculations presented in this thesis, for which grid-dependence and numerical accuracy were examined, the quadratic differencing scheme resulted in grid independent solutions with reasonable size meshes. (In this context the term reasonable relates to the storage and processing capacity of present day computers and to the requirements of the standard Hybrid method to achieve the same effect). However, numerical stability is not unconditional with the new scheme. Due to problems associated with negative finite difference coefficients resulting from QUICK, convergence was retarded or completely inhibited in some of the flows examined in this thesis, for which steep gradients occur in areas of strong convection. This problem was overcome by the introduction, for the problematic flows, of the mixed QUICK-Upwind scheme. Though not generally guaranteed, it was demonstrated, that for the flows where this method had to be applied, the mixed scheme allowed quadratic differencing to take place in all the areas of the flows which were important from the numerical diffusion point of view. Thus, even for the problematic flows the benefits of the partial application of QUICK allowed grid-independent results to be achieved with reasonable grids. The experience gained from the application of the new scheme during this project supports the conclusion that QUICK offers possibilities for a successful alternative to the standard Hybrid method for practical calculations though further improvements of the instability treatment are necessary.

The second region of the standard computational algorithm where improvements were necessary concerned the buoyancy related numerical instability . It has been clearly demonstrated that the source of instability lies in the sequential solution of the coupled momentum and mean buoyancy equations. The instability problem was eliminated when a modified algorithm, solving locally but simultaneously the coupled equations, was introduced. However, the modified algorithm did not represent a viable proposition due to extremely slow convergence rates. The buoyancy related instability problem was overcome by the use of strong under-relaxation of the coupled equations. The false transient solution method presented in chapter 2, and in more detail in Appendix A3, allowed convergence to be achieved for all the cases examined in this thesis whereas convergence was not always possible when the standard (even very strong) static under-relaxation method was applied. The strength of the buoyancy forces in the flows examined in this thesis was similar (or even stronger) to that occuring in practical environmental water discharges and this allows confidence about the ability of the false transient method to guarantee solutions for real environmental buoyant flow problems.

A further objective accomplished during the current work was the testing and comparison of the standard or buoyancy extended k-ϵ model with the RSFT equation model of Launder et al (1975). Conclusions from these comparisons were

presented in the relevant chapters of the thesis. The following points summarize the experience gained from this work.

1) The predictions for the two internal non-buoyant recirculating flows reported in chapter 3 showed that the transport equation model gave more realistic velocity profiles in the recirculation region as a result of more accurate predictions for the turbulence energy and shear stress distribution within the recirculation cell. Substantial differences between the velocity field predictions by the two models within the recirculation zone were also observed for the confined non-buoyant vertical jet flow reported in chapter 5. However experimental data were not available to allow conclusions to be drawn for this case. For the internal flows presented in chapter 3 the transport equation model reproduced the experimentally observed trends of the turbulence quantities but the quantitative agreement was still rather poor.

2) Though both models predicted satisfactorily the 2-D buoyant surface layer the RSFT model brought in substantial improvements both in qualitative and quantitative terms. The main reason for the superior performance of the RSFT model was its ability to account for the influence of the free surface on the turbulence structure through free surface corrections to the pressure-strain and pressure-buoyancy gradient correlations.

3) Unfortunately, the application of the free surface corrections to the confined vertical non-buoyant jet flow gave rather problematic results. As explained in some detail

in chapter 5 the free surface corrections lead to an enhancement of the stress component normal to the free surface (in the surface impingement region) whereas the aim of the introduction of these corrections is to model the damping influence of a free surface on the velocity fluctuations normal to the surface. Though experimental data are not available to confirm conclusions, these preliminary findings cast doubt on the universality of the free surface corrections as presented in chapter 2.

4) The application of the RSFT model to the vertical buoyant jet flow impinging on a free surface gave an unrealistic increase of temperature close to the free surface. The problem was located as the buoyancy coupling of the turbulence equations. Time limitations did not allow a thorough investigation of the problem and forced the decision to abandon the application of the RSFT closure to the final task of this project.

The main objective of the present work was the prediction of the vertical buoyant jet in a shallow water body of infinite horizontal extent using the techniques of computational fluid dynamics. The strategy adopted towards the fullfilment of this task was determined on the basis of the findings of the previous work of Jirka, Lee and Harleman. The model of the flow suggested by these authors assumes that the flow may be considered as a combination and interaction of several simpler buoyant flow phenomena. The strategy adopted during this project was to examine and demonstrate the ability of the computational fluid dynamics

approach to predict these simpler phenomena before dealing with the final problem where these phenomena were expected to occur in a combined form. To this end the following 2-D flows were calculated: the buoyant surface jet, the internal hydraulic jump, the vertical buoyant jet impinging on the free surface of a semi-infinite water body and the vertical non-buoyant discharge in shallow water. It has been demonstrated that these flows can be correctly predicted; the observed behaviour was reproduced in all cases and the predictions were quantitatively validated by extensive comparisons with experimental data.

After the accomplishment of this task the final problem was dealt with. The predictions demonstrated the dominance, for a given geometry, of the discharge densimetric Froude number on the evolution of the flow. The two forms of the flow termed as stable and unstable by Jirka et al were reproduced. Promising agreement with the temperature and visible interface data was demonstrated but only when the exact nature of the experimental process was simulated by performing transient calculations. A conceptual model of the flow was suggested based on the present predictions which offers a unified explanation of all the forms of the flow observed (stable, unstable and intermediate) as departures from the non-buoyant flow pattern to an extent depending on the strength of the buoyancy forces. The differences between this model and the one suggested by Jirka et al were identified; they mainly concern the stable form and in particular, the occurence or not of an internal hydraulic jump which was not observed in the present predictions but

whose appearance is crucial to the model proposed by Jirka et al. Finally, it was pointed out that safe conclusions concerning which of the two models describes the flow correctly cannot be drawn unless more detailed data concerning the temperature and mean velocity fields become available.

7.2. Suggestions for future work

On the basis of the experience gained during this work the following suggestions for future work can be made.

A. Further experimental work is suggested for the vertical 2-D buoyant discharge in shallow water where both mean velocity and temperature measurements should be carried out. Critical from the model validation point of view would be the determination, during the quasi-steady state period, of the surface layer width on the basis of the zero axial velocity location and the relation of this width with the temperature profile width. This test would resolve the problem of the interpretation of the visible interface and of the occurence (or not) of an internal hydraulic jump. Beneficial for the validation of the proposed model would be the acceptance of the transient character of the phenomenon (in its 2-D form) and the measurement of the evolution of at least some aspects of the temperature and velocity fields (as for example the evolution of the surface temperatures, of the location of the visible interface, etc).

B. It is clear from the series of flows examined in chapters 4,5 and 6 that the techniques employed during the present work allowed satisfactory predictions for a series of buoyant and non-buoyant flows closely related to the flows occuring in environmental buoyant discharges. The demonstrated agreement with experiments encourages optimistic expectations for the application of these methods to practical problems. An obvious extension of the present work would be the prediction of a vertical buoyant jet in a cross-flow of shallow water depth. It is quite probable that although such a flow is three-dimensional, certain of the difficulties encountered in the prediction of the two-dimensional discharge would be alleviated. For example, the prediction of the two-dimensional configuration proved to be extremely expensive from a computational point of view due to the transient character of the flow. The vertical buoyant discharge in a cross-flow of constant back-ground velocity is a steady-state phenomenon and its prediction would not require a true transient solution as for the two-dimensional case. Therefore, it is quite probable that although the suggested flow is three-dimensional, the computational expense of its prediction could be reduced in relation to the present calculations. Furthermore, the simulation of such an experimental situation could be easier since the far-field boundary location and specification is less problematic and uncertainties like those concerning the duration of the flow in the present predictions, in relation to the real experimental duration, would be eliminated.

C. The numerical instability problems associated with the negative coefficients of QUICK were exacerbated in the transport equation predictions. As discussed in the part of chapter 4 dealing with the RSFT prediction of the internal hydraulic jump, it was found necessary, in order to achieve stability, to manipulate the momentum and mean buoyancy equations by the introduction of artificial diffusion terms expressed via strain terms and some conveniently defined eddy viscosity. In a paper published during the writing of this thesis Huang and Leschziner (1985) reported a more consistent practice aiming towards the stabilization of the numerical solution by the introduction of similar diffusion terms which result from an appropriate re-writing of the normal stress transport equations. The development and testing of similar practices would improve the stability of QUICK-RSFT solutions to the superior level experienced in the QUICK-(k-ϵ) calculations.

D. In the present work the influence of a free surface on the turbulence structure was tentatively modelled by the assumption of free surface corrections for the pressure strain model similar to those suggested by Gibson and Launder (1978) for the modelling of solid wall influence. This assumption performed satisfactorily for the buoyant surface jet and the internal hydraulic jump where the free surface corrections improved very substantially the predictions in relation to both the eddy viscosity model and to the RSFT model when the influence of the free surface was ignored. However the application of the corrections in a

similar way in the case of a non-buoyant jet impinging on a free surface lead to an enhancement of the normal stress component vertical to the surface. Though experimental data are not available to confirm conclusions it is difficult to comprehend such a paradoxical behaviour. The influence of the free surface on the turbulence structure has been so far the subject of very limited theoretical and experimental investigation. Further work on this subject is obviously required to establish a more soundly based treatment of the free surface influence.

E. Finally, the RSFT model of Launder et al resulted in significant improvements of the prediction of most of the flows examined in this thesis. However, the application of the model in the case of a vertical buoyant jet impinging on a free surface lead to an unrealistic temperature rise close to the surface. The problem region was identified on the buoyancy coupling of the turbulence equations. Further study is required to investigate this behaviour before the improvements observed in other flows can be realized in the case of vertical buoyant jets in shallow water, leading (hopefully) to even better predictions of the temperature field.

APPENDIX A1

THE SET OF GOVERNING PARTIAL DIFFERENTIAL EQUATIONS

APPENDIX A1. THE SET OF GOVERNING PARTIAL DIFFERENTIAL EQUATIONS

In the present Appendix the set of Partial Differential Equations governing the mean hydrodynamic and scalar variable fields for the flows considered in earlier chapters is presented together with the set of transport equations constituting the two turbulence closures tested. The form appropriate for turbulent buoyant flows is chosen; the co-ordinate system and the gravity vector direction are shown in figure A1.1. For axisymmetric flows the axis of symmetry coincides with the y direction of the co-ordinate system. The upper boundary of the solution domain ($y = y_S$) is assumed to correspond to a free surface and the appropriate corrections have been added to the pressure-strain and pressure-buoyancy gradient correlations in the transport equation turbulence model. The fluid is assumed incompressible; the Boussinesq approximation was adopted and the influence of the variable density appears only in the gravitational terms.

Usually the set of modelled transport equations constituting the turbulence closures are presented for a Cartesian system and in tensor notation (as in Chapter 2). Such a presentation of the buoyancy extended k-ϵ model and of the transport equation model of Launder et al (1975) is given by Rodi (1980). The additional terms appropriate for axisymmetric flows are given by Pope and Whitelaw (1975) and by Bryant and Humphrey (1976).

In the form presented here the equations are appropriate to both two-dimensional plane and axisymmetric flows; the terms in curly brackets are to be included only for cylindrical-polar co-ordinates.

Furthermore, in all equations presented:

$$r \equiv \begin{cases} 1 & \text{for cartesian co-ordinates} \\ x & \text{for cylindrical-polar co-ordinates} \end{cases}$$

Since some of the calculations reported earlier were obtained using the transient form of the equations, the unsteady version of the equations is used below.

1. THE MEAN VARIABLE EQUATIONS

Continuity equation:

$$\frac{1}{r}\frac{\partial}{\partial x}(rU) + \frac{\partial}{\partial y}(V) = 0$$

Momentum equations:

$$\frac{\partial U}{\partial t} + \frac{1}{r}\frac{\partial}{\partial x}(rU^2) + \frac{\partial}{\partial y}(VU) = D_{MU} - \frac{1}{r}\frac{\partial}{\partial x}(r\overline{u^2}) - \frac{\partial}{\partial y}(\overline{uv}) - \frac{1}{\rho_a}\frac{\partial P}{\partial x} + \{\frac{\overline{w^2}}{r}\}$$

$$\frac{\partial V}{\partial t} + \frac{1}{r}\frac{\partial}{\partial x}(rUV) + \frac{\partial}{\partial y}(V^2) = D_{MV} - \frac{1}{r}\frac{\partial}{\partial x}(r\overline{uv}) - \frac{\partial}{\partial y}(\overline{v^2}) - \frac{1}{\rho_a}\frac{\partial P}{\partial y} + gB$$

In these equations the pressure P is the mean static pressure minus the hydrostatic pressure at a reference density ρ_a. The mean buoyancy B is defined from the equation:

$$B = -\frac{\overline{\rho} - \rho_a}{\rho_a}$$

where ρ_a is (for the flows considered here) the maximum density occuring in the domain. All the upper case symbols and overbars represent mean (time- or ensemble averaged) values and the lower case symbols represent fluctuations. The molecular diffusion terms D_{MU}, D_{MV} are given by the expressions:

$$D_{MU} = \frac{1}{r}\frac{\partial}{\partial x}\left[2\nu r \frac{\partial U}{\partial x} \right] + \frac{\partial}{\partial y}\left[\nu \left(\frac{\partial U}{\partial y} + \frac{\partial V}{\partial x}\right)\right] - \left\{ 2\nu \frac{U}{r^2} \right\}$$

$$D_{MV} = \frac{1}{r}\frac{\partial}{\partial x}\left[\nu r \left(\frac{\partial U}{\partial y} + \frac{\partial V}{\partial x}\right)\right] + \frac{\partial}{\partial y}\left[2\nu \frac{\partial V}{\partial y} \right]$$

where ν is the kinematic molecular viscosity (assumed constant)

Mean Buoyancy Equation

$$\frac{\partial B}{\partial t} + \frac{1}{r}\frac{\partial}{\partial x}(rUB) + \frac{\partial}{\partial y}(VB) = \frac{1}{r}\frac{\partial}{\partial x}\left[r \frac{\nu}{\sigma_B}\frac{\partial B}{\partial x} - r\,\overline{ub} \right] + \frac{\partial}{\partial y}\left[\frac{\nu}{\sigma_B}\frac{\partial B}{\partial y} - \overline{vb} \right]$$

in this equation the molecular Prandtl/Schmidt number σ_B is also assumed constant.

2. THE BUOYANCY EXTENDED k-ϵ MODEL

The Reynolds stresses and scalar fluxes are given by the equations:

$$\overline{u^2} = \frac{2}{3}k - 2\nu_t \frac{\partial U}{\partial x}$$

$$\overline{v^2} = \frac{2}{3}k - 2\nu_t \frac{\partial V}{\partial y}$$

$$\overline{w^2} = \frac{2}{3}k - \left\{ 2\nu_t \frac{U}{r} \right\}$$

$$\overline{uv} = -\nu_t \left[\frac{\partial U}{\partial y} + \frac{\partial V}{\partial x} \right]$$

$$\overline{ub} = -\frac{\nu_t}{\sigma_T}\frac{\partial B}{\partial x}$$

$$\overline{vb} = -\frac{\nu_t}{\sigma_T}\frac{\partial B}{\partial y}$$

where ν_t is the eddy viscosity defined from the equations:

$$\nu_t = C_\mu \frac{k^2}{\epsilon}$$

$$\frac{\partial k}{\partial t} + \frac{1}{r}\frac{\partial}{\partial x}(rUk) + \frac{\partial}{\partial y}(Vk) = \frac{1}{r}\frac{\partial}{\partial x}(r\frac{\nu_t}{\sigma_k}\frac{\partial k}{\partial x}) + \frac{\partial}{\partial y}(\frac{\nu_t}{\sigma_k}\frac{\partial k}{\partial y}) + P + G - \epsilon$$

$$\frac{\partial \epsilon}{\partial t} + \frac{1}{r}\frac{\partial}{\partial x}(rU\epsilon) + \frac{\partial}{\partial y}(V\epsilon) = \frac{1}{r}\frac{\partial}{\partial x}(r\frac{\nu_t}{\sigma_\epsilon}\frac{\partial \epsilon}{\partial x}) + \frac{\partial}{\partial y}(\frac{\nu_t}{\sigma_\epsilon}\frac{\partial \epsilon}{\partial y}) + C_{\epsilon_1}\frac{\epsilon}{k}P - C_{\epsilon_2}\frac{\epsilon^2}{k}$$

where:

$$P = \nu_t\left[2\left[\left[\frac{\partial U}{\partial x}\right]^2 + \left[\frac{\partial V}{\partial y}\right]^2\right] + \left[\frac{\partial U}{\partial y} + \frac{\partial V}{\partial x}\right]^2\right] + \left\{2\nu_t\frac{U^2}{r^2}\right\}$$

$$G = -g\frac{\nu_t}{\sigma_T}\frac{\partial B}{\partial y}$$

and σ_T is the turbulent Prandtl/Schmidt number for scalar turbulent transport.

3. THE TRANSPORT EQUATION MODEL

Reynolds stresses

$$\frac{\partial \overline{u^2}}{\partial t} + \frac{1}{r}\frac{\partial}{\partial x}(rU\overline{u^2}) + \frac{\partial}{\partial y}(V\overline{u^2}) = D_{11} + P_{11} + G_{11} + \Pi_{11} - \frac{2}{3}\epsilon + \{AT_{11}\}$$

$$\frac{\partial \overline{v^2}}{\partial t} + \frac{1}{r}\frac{\partial}{\partial x}(rU\overline{v^2}) + \frac{\partial}{\partial y}(V\overline{v^2}) = D_{22} + P_{22} + G_{22} + \Pi_{22} - \frac{2}{3}\epsilon + \{AT_{22}\}$$

$$\frac{\partial \overline{w^2}}{\partial t} + \frac{1}{r}\frac{\partial}{\partial x}(rU\overline{w^2}) + \frac{\partial}{\partial y}(V\overline{w^2}) = D_{33} + P_{33} + G_{33} + \Pi_{33} - \frac{2}{3}\epsilon + \{AT_{33}\}$$

$$\frac{\partial \overline{uv}}{\partial t} + \frac{1}{r}\frac{\partial}{\partial x}(rU\overline{uv}) + \frac{\partial}{\partial y}(V\overline{uv}) = D_{12} + P_{12} + G_{12} + \Pi_{12} + \{AT_{12}\}$$

The diffusion terms D_{ij} are given by the equation:

$$D_{ij} = C_s \left[\frac{1}{r} \frac{\partial}{\partial x} \frac{rk}{\epsilon} \left(\overline{u^2} \frac{\partial \overline{u_i u_j}}{\partial x} + \overline{uv} \frac{\partial \overline{u_i u_j}}{\partial y} \right) + \right.$$

$$\left. \frac{\partial}{\partial y} \frac{k}{\epsilon} \left(\overline{v^2} \frac{\partial \overline{u_i u_j}}{\partial y} + \overline{uv} \frac{\partial \overline{u_i u_j}}{\partial x} \right) \right]$$

The mean strain production terms are:

$$P_{11} = -2\left(\overline{u^2} \frac{\partial U}{\partial x} + \overline{uv} \frac{\partial U}{\partial y} \right)$$

$$P_{22} = -2\left(\overline{v^2} \frac{\partial V}{\partial y} + \overline{uv} \frac{\partial V}{\partial x} \right)$$

$$P_{33} = \left\{ -2 \overline{w^2} \frac{U}{r} \right\}$$

$$P_{12} = -\left[\overline{v^2} \frac{\partial U}{\partial y} + \overline{u^2} \frac{\partial V}{\partial x} - \left\{ \overline{uv} \frac{U}{r} \right\} \right]$$

The buoyancy production terms are:

$$G_{11} = 0$$

$$G_{22} = 2g \overline{vb}$$

$$G_{33} = 0$$

$$G_{12} = g \overline{ub}$$

The pressure-strain correlation terms Π_{ij} are given by the expressions:

$$\Pi_{11} = -C_1 \frac{\epsilon}{k} \left(\overline{u^2} - \frac{2}{3} k \right) + C_1' \frac{\epsilon}{k} f \overline{v^2}$$

$$- C_2 \left(P_{11} - \frac{2}{3} P \right) \quad - C_2 C_2' f \left(P_{22} - \frac{2}{3} P \right)$$

continued/

$$- C_3(G_{11} - \frac{2}{3} G)$$

$$\Pi_{22} = - C_1 \frac{\epsilon}{k} (\overline{v^2} - \frac{2}{3} k) - 2C_1' \frac{\epsilon}{k} f \overline{v^2}$$

$$- C_2(P_{22} - \frac{2}{3} P) + 2C_2C_2' f(P_{22} - \frac{2}{3} P)$$

$$- C_3(G_{22} - \frac{2}{3} G)$$

$$\Pi_{33} = - C_1 \frac{\epsilon}{k} (\overline{w^2} - \frac{2}{3} k) + C_1' \frac{\epsilon}{k} f \overline{v^2}$$

$$- C_2(P_{33} - \frac{2}{3} P) - C_2C_2' f(P_{22} - \frac{2}{3} P)$$

$$- C_3(G_{33} - \frac{2}{3} G)$$

$$\Pi_{12} = - C_1 \frac{\epsilon}{k} \overline{uv} - \frac{3}{2} C_1' \frac{\epsilon}{k} f \overline{uv}$$

$$- C_2 P_{12} + \frac{3}{2} C_2C_2' f P_{12}$$

$$- C_3 G_{12}$$

In the previous expressions P is the mean strain production of k and G is the buoyancy production or destruction of k.

$$P = - \overline{uv} \left[\frac{\partial U}{\partial y} + \frac{\partial V}{\partial x} \right] - \overline{u^2} \frac{\partial U}{\partial x} - \overline{v^2} \frac{\partial V}{\partial y} - \left\{ \overline{w^2} \frac{U}{r} \right\}$$

$$G = g \overline{vb}$$

f is the free surface (or wall) effects function.

$$f = \begin{cases} 0 \text{ when no such effects are present} \\ \dfrac{k^{3/2}}{C_w \epsilon \eta} \end{cases}$$

η is the distance from the free surface (or wall) at the point considered and $C_w = \kappa/C_\mu^{0.75}$ where κ is the Von Karman constant.

The additional terms $\{AT_{ij}\}$ - for cylindrical co-ordinates only - are given by the equations:

$$\{AT_{11}\} = - \left[2 \frac{C_s k \overline{w^2}}{\epsilon} \frac{(\overline{u^2} - \overline{w^2})}{r^2} \right]$$

$$\{AT_{22}\} = 0$$

$$\{AT_{33}\} = \left[2 \frac{C_s k \overline{w^2}}{\epsilon} \frac{(\overline{u^2} - \overline{w^2})}{r^2} \right]$$

$$\{AT_{12}\} = - \frac{C_s k \overline{w^2}}{\epsilon} \frac{\overline{uv}}{r^2}$$

Scalar fluxes

$$\frac{\partial \overline{ub}}{\partial t} + \frac{1}{r} \frac{\partial}{\partial x} (rU\overline{ub}) + \frac{\partial}{\partial y}(V\overline{ub}) = D_{1b} + P_{1b} + G_{1b} + \Pi_{1b} + \{AT_{1b}\}$$

$$\frac{\partial \overline{vb}}{\partial t} + \frac{1}{r} \frac{\partial}{\partial x} (rU\overline{vb}) + \frac{\partial}{\partial y}(V\overline{vb}) = D_{2b} + P_{2b} + G_{2b} + \Pi_{2b} + \{AT_{2b}\}$$

The diffusion terms D_{ib} are given by the equation:

$$D_{ib} = C_s' \left[\frac{1}{r} \frac{\partial}{\partial x} \frac{rk}{\epsilon} \left(\overline{u^2} \frac{\partial \overline{u_i b}}{\partial x} + \overline{uv} \frac{\partial \overline{u_i b}}{\partial y} \right) + \right.$$

$$\left. \frac{\partial}{\partial y} \frac{k}{\epsilon} \left(\overline{v^2} \frac{\partial \overline{u_i b}}{\partial y} + \overline{uv} \frac{\partial \overline{u_i b}}{\partial x} \right) \right]$$

The production terms P_{ib} and G_{ib} are:

$$P_{1b} = - \overline{u^2} \frac{\partial B}{\partial x} - \overline{uv} \frac{\partial B}{\partial y} - \overline{ub} \frac{\partial U}{\partial x} - \overline{vb} \frac{\partial U}{\partial y}$$

$$P_{2b} = - \overline{uv} \frac{\partial B}{\partial x} - \overline{v^2} \frac{\partial B}{\partial y} - \overline{ub} \frac{\partial V}{\partial x} - \overline{vb} \frac{\partial V}{\partial y}$$

$$G_{1b} = 0$$

$$G_{2b} = g\,\overline{b^2}$$

The pressure-buoyancy gradient correlation is given by the expressions:

$$\Pi_{1b} = - C_{1T}\,\frac{\epsilon}{k}\,\overline{ub} + C_{2T}\,(\overline{ub}\,\frac{\partial U}{\partial x} + \overline{vb}\,\frac{\partial U}{\partial y})$$

$$\Pi_{2b} = - C_{1T}\,\frac{\epsilon}{k}\,\overline{vb} - C'_{1T}\,\frac{\epsilon}{k}\,f\,\overline{vb} + C_{2T}\,(\overline{ub}\,\frac{\partial V}{\partial x} + \overline{vb}\,\frac{\partial V}{\partial y})$$

$$- C_{3T}\,g\,\overline{b^2}$$

(f is the free surface effects function.)

The additional terms $\{AT_{ib}\}$ - for cylindrical co-ordinates only - are:

$$\{AT_{1b}\} = - C'_s\,\frac{k}{\epsilon}\,\frac{\overline{w^2}}{r^2}\,\overline{ub}$$

$$\{AT_{2b}\} = 0$$

<u>The dissipation rate equation</u>

$$\frac{\partial \epsilon}{\partial t} + \frac{1}{r}\,\frac{\partial}{\partial x}\,(rU\epsilon) + \frac{\partial}{\partial y}\,(V\epsilon) = D_\epsilon + C_{\epsilon_1}\,\frac{\epsilon}{k}\,P - C_{\epsilon_2}\,\frac{\epsilon^2}{k}$$

P is the mean strain production of k, and:

$$D_\epsilon = C_\epsilon\left[\,\frac{1}{r}\,\frac{\partial}{\partial x}\,\frac{rk}{\epsilon}\,(\overline{u^2}\,\frac{\partial \epsilon}{\partial x} + \overline{uv}\,\frac{\partial \epsilon}{\partial y}) + \frac{\partial}{\partial y}\,\frac{k}{\epsilon}\,(\overline{v^2}\,\frac{\partial \epsilon}{\partial y} + \overline{uv}\,\frac{\partial \epsilon}{\partial x})\right]$$

<u>The scalar fluctuations variance equation</u>

$$\frac{\partial \overline{b^2}}{\partial t} + \frac{1}{r}\,\frac{\partial}{\partial x}\,(r\overline{Ub^2}) + \frac{\partial}{\partial y}\,(\overline{Vb^2}) = D_{bb} + P_{bb} - \epsilon_{bb}$$

$$D_{bb} = C_{TT}\left[\frac{1}{r}\frac{\partial}{\partial x}\frac{rk}{\epsilon}\left(\overline{u^2}\frac{\partial\overline{b^2}}{\partial x} + \overline{uv}\frac{\partial\overline{b^2}}{\partial y}\right) + \frac{\partial}{\partial y}\frac{k}{\epsilon}\left(\overline{v^2}\frac{\partial\overline{b^2}}{\partial y} + \overline{uv}\frac{\partial\overline{b^2}}{\partial x}\right)\right]$$

$$P_{bb} = -2\left(\overline{ub}\frac{\partial B}{\partial x} + \overline{vb}\frac{\partial B}{\partial y}\right)$$

The dissipation rate of the variance of the scalar fluctuations is estimated from the relation:

$$\epsilon_{bb} = \frac{1}{R_T}\frac{\overline{b^2}}{k}\epsilon$$

A local equilibrium approximation of the $\overline{b^2}$ equation was used for the surface jet calculations reported in Chapter 4. Neglecting transport (convection and diffusion) and transient terms, results in:-

$$P_{bb} - \epsilon_{bb} = 0$$

$$\text{or} \quad -2\left(\overline{ub}\frac{\partial B}{\partial x} + \overline{vb}\frac{\partial B}{\partial y}\right) - \frac{1}{R_T}\frac{\overline{b^2}}{k}\epsilon = 0$$

$$\text{i.e.} \qquad \overline{b^2} = -2R_T\frac{k}{\epsilon}\left(\overline{ub}\frac{\partial B}{\partial x} + \overline{vb}\frac{\partial B}{\partial y}\right)$$

The constants appearing in the modelled transport equations of the two turbulence models described here were given in Chapter 2.

APPENDIX A2

THE QUICK DISCRETISATION SCHEME

APPENDIX A2 : THE QUICK DISCRETISATION SCHEME

Increasing evidence in the literature shows that the third order accurate discretisation scheme of Leonard (1979), widely known now as QUICK, is an appealing and successful alternative to the commonly used HYBRID scheme (Patankar,1980) for the discretisation of the convection terms in flow transport equations. The existing evidence reviewed below suggests that QUICK offers substantial possibilities for the removal of the numerical diffusion problem associated with upwind differencing. It was thus decided that the QUICK discretisation would be employed in the current work. Since emphasis was to be placed in the current predictions on turbulence model performance it was deemed essential that numerical diffusion should be reduced as much as possible. It is also the case that improved performance of the numerical scheme was generally to be expected since grid indepence ought to be achieved with the new technique on considerably coarser meshes.

In his first two papers Leonard (1979) introduced the new scheme, examined analytically its stability and accuracy and showed that for simple one-dimensional situations stable and accurate solutions were possible with QUICK, in contrast to Central and Upwind differencing methods. In another paper Leonard, Leschziner and McGuirk (1978) derived the QUICK formulation for 2-D situations and gave comparisons between QUICK and HYBRID in the calculation of recirculating flows; substantial reduction of numerical diffusion was

demonstrated. Han, Humphrey and Launder (1981) and Pollard and Su (1982) predicted a series of laminar and turbulent flows using both QUICK and Hybrid; both groups concluded that QUICK showed a substantial improvement in numerical accuracy in relation to HYBRID. Both groups also reported convergence problems at high cell Peclet numbers and suggested reformulations of the finite difference equations aiming to ensure diagonal dominance of the coefficient matrix. Han et al also reported that strong under-relaxation, in the form of a false transient approach, was required to ensure convergence in turbulent flow calculations; both these points are addressed further below.

The present appendix A2 consists of four sections. In the first QUICK is mathematically described. This is followed by a description of the method used in the current work to ensure diagonal dominance, section A2.2. In section A2.3 comparisons are presented between QUICK and HYBRID for the calculation of the laminar flow in a plane channel with a symmetric contraction; this problem was chosen to test the incorporation of the QUICK method in the computer program. In section A2.4 the problem of wiggles in the variable fields is discussed; the effects on convergence are demonstrated and a mixed QUICK-UPWIND scheme is introduced.

A2.1 : A mathematical definition of QUICK

The various discretisation schemes mentioned above are basically different finite-difference approximations of the convection terms in the flow transport equations. Assume

that the transport equation for a scalar variable F is to be discretised with reference to a uniform Cartesian grid and that the x-direction convection is locally from left to right, Figure A2.1. The estimation of the discretised x-convection term usually adopted (Patankar, 1980) is as follows:

$$\frac{\partial(UF)}{\partial x} = \frac{(U_r)\ F_r - (U_l)\ F_l}{\Delta x} \qquad (1)$$

this requires the knowledge of the values of F (F_r, F_l) at the walls of the control volume shown in figure A2.1 (the velocities U_r and U_l are stored at those locations and require no further approximation). Mathematically the value of F_r can be found by a Taylor series expansion between points P and r:

$$F_r = F_I + F'_I \frac{\Delta x}{2} + \frac{1}{2} F''_I \frac{(\Delta x)^2}{4} + \frac{1}{6} F'''_I \frac{(\Delta x)^3}{8} + O(\Delta x^4) \qquad (2)$$

(I indicates the y grid-line index for point P)

In Upwind Differencing it is assumed that $F_r = F_I$, the truncation error involved is of the order of Δx and identically equal to zero when F has a constant value between points P ad R.

The value of the derivative F'_I can be estimated by means of a forward Taylor expansion between points P and R and solution for F'_I :

$$F'_I = \frac{F_{I+1} - F_I}{\Delta x} - \frac{1}{2} F''_I \Delta x - \frac{1}{6} F'''_I (\Delta x)^2 + O(\Delta x^3) \qquad (3)$$

Substitution of F'_I in (2) by means of equation (3) gives:

$$F_r = \frac{F_I + F_{I+1}}{2} - \frac{1}{8} F''_I (\Delta x)^2 - \frac{1}{16} F'''_I (\Delta x)^3 + O(\Delta x^4) \qquad (4)$$

In Central Differencing it is assumed that $Fr=(F_I+F_{I+1})/2$, the truncation error involved is in the order of Δx^2 and is equal to zero when F is a linear function between points P and R.

The value of the second derivative F''_I can be similarly estimated:

$$F''_I = \frac{F_{I+1} + F_{I-1} - 2F_I}{\Delta x^2} - \frac{1}{12} F_I^{IV} (\Delta x)^2 + O(\Delta x^4) \qquad (5)$$

Substitution of F''_I in equation (4) by means of (5) gives:

$$F_r = \frac{F_I + F_{I+1}}{2} - \frac{1}{8}(F_{I+1} + F_{I-1} - 2F_I) + O(\Delta x^3) \qquad (6)$$

Similarly, if instead of the forward expansion previously used, backwards expansion were used i.e. from point R to r and from R to P, it can be shown that:

$$F_r = \frac{F_I + F_{I+1}}{2} - \frac{1}{8}(F_{I+2} + F_I - 2F_{I+1}) + O(\Delta x^3) \qquad (7)$$

In QUICK Differencing the terms $O(\Delta x^3)$ are omitted, the truncation error involved is thus of order Δx^3 and equal to zero when F is a parabola through the points L,P and R (or P,R and RR). Equation (6) is used when convection is from left to right and equation (7) is used when the convection is in the opposite direction. Thus QUICK interpolation is defined by:

$$F_r = \frac{F_I + F_{I+1}}{2} - \frac{1}{8}(F_{I+1} + F_{I-1} - 2F_I) =$$

$$= -\frac{1}{8}F_{I-1} + \frac{3}{4}F_I + \frac{3}{8}F_{I+1} \quad , \text{ when } U_r > 0 \qquad (8a)$$

$$F_r = \frac{F_I + F_{I+1}}{2} - \frac{1}{8}\left(F_{I+2} + F_I - 2\,F_{I+1} \right) =$$

$$= \frac{3}{8}F_I + \frac{3}{4}F_{I+1} - \frac{1}{8}F_{I+2} \quad , \text{ when } U_r < 0 \qquad (8b)$$

It is obvious from equations (8) that the interfacial value F_r can be calculated from a parabola fitted through the interpolation points (hence the acronym: QUICK = QUadratic Interpolation for Convective Kinematics). It is also obvious from equations (8) that QUICK is a conservative scheme i.e. $F_l(I+1)=F_r(I)$. When the grid is non-uniform the values of the coefficients in equations (8) depend on the geometry of the grid. If, in 2-D problems, second order terms are retained (i.e. of the order Δx^2, Δy^2, $\Delta x \Delta y$), the interfacial values, say in the x direction, depend also on the lateral curvature Fyy of the F(x,y) surface which is approximated locally by a second order interpolation surface. Leonard et al (1978) suggest that the influence of the lateral curvature is negligible and that it can be neglected with very little loss of accuracy. The same practice was followed in the present work.

Leonard (1979) examined QUICK in terms of the convective sensitivity of the scheme defined as :

$$CS = \frac{\partial(\text{INFLUX})}{\partial F_P} \qquad (9)$$

where INFLUX is the nett convective influx per unit volume

into a control volume. From the last equation it can be seen that CS shows the tendency of the scheme to alter the influx subsequent on a change of the value of F_P in the control volume. The analysis of Leonard is restricted to one-dimensional flows. He showed (for a uniform grid) that Central Differencing has a neutral sensitivity (CS=Ø) while QUICK exhibits a stable behaviour since CS<Ø i.e. an erroneous increase in F_P ($\Delta F_P > Ø$) would result in a negative and thus stabilizing change of the influx. Thus, the addition of the curvature terms in the estimation of the interfacial values apart from its contribution to higher accuracy, has a stabilizing effect on the numerical solution.

It is known that all higher order convection discretisation methods (where the interfacial values of F depend on both upstream and downstream values of F) may result , when convection dominates diffusion locally , in negative coefficients of the finite difference equations derived from the discretisation of the corresponding transport equation (see e.g. Patankar (1980), Roache (1982)). This is also the case for the third order accurate quadratic method. Imagine a one-dimensional convection-diffusion problem for a scalar F. The transport equation describing this phenomenon is:

$$U \frac{dF}{dx} = \Gamma \frac{d^2F}{dx^2} + Su \qquad (\text{ U and } \Gamma \text{ are constants })$$

(where Su is a possible source-sink term).

Discretisation of the last equation using QUICK for the convection term results in a linear equation relating the

value Fp with the values of F at two points upstream and two points downstream of the point P.

$$AP\ F_P = ALL\ F_{LL} + AL\ F_L + AR\ F_R + ARR\ F_{RR} + Su_P$$

assuming $U>0$ - Figure A2.1 - and a constant diffusion coefficient Γ it can be shown that:

$$ALL = -\frac{\Gamma}{\Delta x^2}\frac{Pc}{8}\ ,\quad AL = \frac{\Gamma}{\Delta x^2}\left(1+\frac{7Pc}{8}\right)\ ,\quad AR = \frac{\Gamma}{\Delta x^2}\left(1-\frac{3Pc}{8}\right)$$

$$ARR = 0\ ,\quad AP = \frac{\Gamma}{\Delta x^2}\left(2+\frac{3Pc}{8}\right)$$

where Pc is the cell Peclet number: $Pc = U\Delta x/\Gamma$

From the last relationship it can be seen that: 1) The downstream coefficient AR assumes negative values when the cell Peclet number is larger that 8/3, and 2) $|AP| < |ALL| + |AL| + |AR| + |ARR|$ i.e. the coefficient matrix is not diagonally dominant. These two points influence substantially the numerical realisation of the solution and are further discussed in the following sections.

In this brief presentation QUICK was introduced with reference to the discretisation of a scalar variable transport equation. The discretisation of the convective terms of the momentum equations is the same in principle, but the staggering of the grid for each velocity component has to be taken into account in the calculation of the interpolation coefficients. The same applies for the remaining "staggered" variables $\overline{ub}$, $\overline{vb}$ and $\overline{uv}$.

A2.2. The treatment of negative coefficients in QUICK

The negative coefficients of the QUICK method give rise to problems when QUICK is incorporated into a computational algorithm solving the system of linear equations (derived

from the discretisation and linearization of each PDE) by methods other than a direct inversion of the coefficient matrix. The direct inversion methods are usually avoided since they have been shown to be expensive both in terms of core-store and run time for the sparce matrices typically occuring in fluid dynamics problems (for a discussion of the reasons why direct matrix inversion is unsuitable for iterative methods see Patankar ,198Ø). The algorithm used in this project employs a repeated (i.e. iterative) line-by-line solution with alternating direction (Patankar, 198Ø). Convergence of such an iterative procedure is guaranteed if the coefficient matrix is diagonally dominant (the Scarborough criterion ,Patankar 198Ø),

$$\sum_i |A_i| / |A_p| \leq 1 \ , \ i = L \ , \ N \text{ etc}$$

which is a sufficient but not necessary condition.

This relation is in general not satisfied when QUICK discretisation is applied due to the existence of negative coefficients. For example in the previously examined one-dimensional convection/diffusion problem for Pc>8/3 :

$$\frac{\Sigma|A_i|}{|A_p|} = \frac{11Pc/8}{3Pc/8 + 2} > 1 \quad \text{and for } Pc \rightarrow \infty : \frac{\Sigma|A_i|}{|A_p|} = \frac{11}{3}$$

For the first of the present applications of the computer program containing QUICK (in the calculation of the laminar flow in a plane channel with a symmetric contraction) no provisions were taken for the negative coefficients; a nine node finite-difference star was adopted relating the centre-node value of the variable with the values at the four neighbouring nodes in each co-ordinate

direction. The original solution algorithm was modified so that instead of a tri-diagonal line-by-line Gaussian elimination a penta-diagonal line-by-line Gaussian elimination was introduced to perform the elimination of the exterior coefficients (e.g. ALL, ARR etc). At the lower Reynolds numbers examined the convergence rate was satisfactory even at Reynolds numbers where, in certain regions of the solution domain, the downstream coefficients were negative. At higher Reynolds number of the flow the solution diverged. This was undoubtedly related to the negative coefficients as the problem was removed when provisions were taken to ensure unconditional diagonal dominance of the coefficient matrix. This was achieved by a decomposition of the discretised-linearized transport equation with regard to the negative coefficients. For example if in a 2-D situation the coefficients AR, AN were negative the linearized equation would be reformed as follows:

$$\left(\sum_i A_i\right) F_P = \sum_i (A_i F_i) + Su_P \quad \text{and say } AR < 0 \text{ , } AN < 0$$

reformulation :

$$\underbrace{\left(\sum_i A_i - AR - AN\right)}_{\text{New center node coefficient}} F_P = \sum_{i \neq AR \atop AN} (A_i F_i) + \underbrace{Su_P + AR\,(F_R - F_P) + AN\,(F_N - F_P)}_{\text{New source term}}$$

Furthermore, since the larger negative interior coefficients were treated explicitly, the same practice was applied to the negative exterior coefficients (ALL, ARR etc); their contributions were always added to the source term thus ensuring unconditional diagonal dominance. With

this reformulation the divergence problems associated with the lack of diagonal dominance of the original formulation were removed. Other forms of decomposition were tried, for example an implicit treatment of the diffusion part of the negative coefficients, adding only the negative convective contribution to the source terms. At large cell Peclet numbers, common in practical turbulent flows, all such alternatives had a convergence rate similar to the previous simpler decomposition which was finally adopted.

A2.3. The laminar flow in a plane channel with a symmetric contraction

The aims of the work reported in this section were:

1) To test the modified computer program (after the changes required for the incorporation of QUICK) for a recirculating flow problem.

2) To compare the performance of QUICK and HYBRID in the calculation of a laminar recirculating flow for which an accurate solution was available in the literature.

The problem selected was the laminar flow in a plane channel with a symmetric contraction, see Figure A2.2. The flow had previously been calculated numerically by Dennis and Smith (1980) for a wide range of Reynolds numbers (for a definition of the Reynolds number (Re) see Figure A2.2). Solutions were reported for each Reynolds number and for five different uniform grids of increasing resolution -from 11*11 to 81*81 grid nodes. Dennis and Smith solved the Vorticity-Stream function form of the Navier-Stokes

equations using a second order accurate stable discretisation scheme i.e. central differencing with some technique for achieving iterative stability. The method involves local series expansion approximations introducing , partially, higher order stabilizing terms ; this procedure is described in detail by Dennis and Smith (1980).

In the current work the flow was calculated for a range of Reynolds numbers (Re: 1, 10, 50, 100, 333, 500).
Four series of calculations were carried out:
i) employing the standard Hybrid method and a 42*40 non-uniform grid concentrated in the region of the contraction,
ii)employing QUICK and the same 42*40 grid,
iii) employing Hybrid and a 56*60 non-uniform grid being 50% more concentrated than the 42*40 grid close to the contraction,
iv) employing QUICK and the same 56*60 grid.

42*40 Grid Results : For Re=1 and 10 the two schemes gave almost identical results. For these Reynolds numbers the cell Peclet numbers (Pc_x,Pc_y) in the part of the solution domain where the flow changes rapidly were less than two. In such a case Hybrid is equivalent to Central Differencing. Furthermore at low Reynolds numbers the convective terms are not so influential and the accuracy of the discretisation used for these terms is less significant. The streamlines calculated by both schemes coincide and cannot be distinguished in the accuracy of the plots, see figure A2.3. The U velocity profiles given in Figure A2.4A for Re=10 are almost identical; also the predicted upstream recirculation

cells have the same shape, size and circulation.

For Re>5Ø the two schemes gave significantly different results. For Re>5Ø the cell Peclet numbers in the part of the solution domain where the flow changes rapidly are, in the majority of cells, higher than two; Hybrid is now therefore equivalent to Upwind Differencing. Further, for the higher Reynolds numbers the correct modelling of convection becomes very important. The effects of numerical diffusion are clear in the U velocity profiles shown in Figure A2.4B for a Reynolds number of 5ØØ. Hybrid tends to reduce the curvature and give more smoothly changing profiles. As a result the gradients of the streamlines predicted by Hybrid change more evenly and the fluid is shown to move in less steep trajectories, figures A2.5A and A2.5B. It can be shown (Patankar, 198Ø) that the detrimental effects of the numerical diffusion are maximized when the slope of the streamlines is 45 degrees in relation to the co-ordinate directions and minimized when the flow is parallel to one of the co-ordinate directions. Consistently the predicted streamline patterns are significantly different in the area of the flow where the streamlines are oblique to the grid directions and particularly where the slope of the streamlines is near 45 degrees. The predictions of both schemes for the size of the upstream recirculation zone are plotted in figure A2.6. In the same figure the results of Dennis and Smith for a 41*41 grid are given for comparison. The agreement between the results of Dennis and Smith and the present QUICK predictions is remarkable especially for the higher Reynolds numbers. Hybrid

overpredicts the size of the recirculation zone, especially its length.

Grid independence study. The result of a grid independence study for the upstream recirculation zone are shown in figure A2.7, where the 56*60 grid results are compared with the 42*40 results and with the results of Dennis and Smith for an 81*81 grid.

QUICK gave practically the same results for both the 42*40 and 56*60 grid. Hybrid gave significantly different results for each grid. Even for the finer grid Hybrid clearly overpredicted the size of the eddy. The agreement between the results obtained by QUICK -56*60- grid and the results of Dennis and Smith for the 81*81 grid is again remarkable.

From this discussion it can be concluded that the Quadratic method performed -for this particular problem- much better than Hybrid for Re>50. QUICK gave more accurate results and grid independence was achieved with coarser grids. The Computing time and the Computer memory requirements were practically the same for both schemes though slightly higher for QUICK (+10%), but since a significantly finer grid would be required by the Hybrid scheme to achieve the same level of grid independence, the QUICK technique has led to significant savings in both memory and run time.

A2.4. Wiggles in QUICK predictions. "Remedial" measures.

The previously described treatment of the negative

coefficients aims to ensure diagonal dominance of the coefficient matrix in order to remove the possibility of numerical divergence of the iterative solution. This is a different problem from the one dealt with in this section, namely the problem of wiggles or oscillatory patterns in the numerical solution of the linearized algebraic equations associated with higher order treatments of the convection terms (Patankar (1980), Roache (1982)). The problem can be clearly demonstrated by the numerical solution of the transport equation for a conserved (i.e. zero source term) scalar variable F in a one dimensional problem with constant velocity (U) and diffusivity (Γ) where F is forced to have two different values F_L and F_R between two points L and R a distance L apart. The analytical solution of the transport equation is:

$$\frac{F_L - F(x)}{F_L - F_R} = \frac{\exp(P_\emptyset \; x/L) - 1}{\exp(P_\emptyset) - 1}$$

where $P_\emptyset$ is an overall Peclet number $P_\emptyset = U\ L/\Gamma$.

The transport equation for this problem was discretised using both Central and Quadratic differencing and the resulting system of linear equations was solved by Gaussian elimination of the tridiagonal or pentadiagonal coefficient matrix involved. Solutions were obtained for an overall Peclet number $P_\emptyset$=100 and four cell Peclet numbers Pc:10,5,2.5 and 1. The solutions are shown in figures A2.8A (QUICK) and A2.8B (Central Differencing) together with the analytical solution. The numerical solution for the finer grid (Pc=1) practically coincided with the analytical solution while the rest of the grids examined (Pc=10,5,2.5)

gave oscillatory solutions. The wave length of the oscillations is twice the grid increment and the amplitude of oscillations is larger for the coarser grids. It can be further observed that the amplitude of the oscillations grows much more rapidly for Central Differencing than for QUICK, underlining the additional numerical stability mentioned earlier. The generation of these wiggles is a direct result of the discretisation of the transport equation at cell Peclet numbers which result in negative coefficients (Pc>2 in CD and Pc>8/3 for QUICK). The form of the discretised F transport equation for QUICK is:

$$\left(2 + \frac{3Pc}{8} \right) F_I = \left(1 - \frac{3Pc}{8} \right) F_{I+1} + \left(1 + \frac{7Pc}{8} \right) F_{I-1} - \frac{Pc}{8} F_{I-2} \qquad (10)$$

In figure A2.8 it can be seen from the analytical solution that for the coarsest grid examined (Pc=1Ø) and for the last node before the downstream boundary we have:

$$F_{I+1} \simeq F_R \ , \quad F_{I-1} \simeq F_{I-2} \simeq F_L$$

Substitution of these values in equation (10) results in an overestimation of F_I in relation to the correct value $F_I = F_L$:

$$\varepsilon_I = \frac{F_I - F_L}{F_L - F_R} = \frac{3Pc - 8}{3Pc + 16} = 47.82\ \%$$

i.e. even though the correct values for the neighbouring nodes were used, the discretisation process results in an erroneous F_I value. This process then spreads upstream giving the oscillatory patterns shown in figures A2.8A and A2.8B. Finally from the previous discretised equation it can also be seen that the generation of wiggles is associated

with steep gradients in the F field, if for example $dF/dx|_R = 0$ and $F_{I+1} = F_{I-1} = F_{I-2}$ then discretisation errors would be zero.

Oscillatory QUICK solutions were observed in most of the two dimensional flows examined in this project in areas combining high cell Peclet numbers and steep gradients of the variable field. Two typical examples of oscillatory solutions are shown in figures A2.9A and A2.9B. Figure A2.9A concerns the calculation of the laminar flow in a plane channel with a symmetric contraction at a Reynolds number of 100 with a coarse grid of 16*16 nodes. The component of the velocity vertical to the main stream direction is shown ,at a plane close to the symmetry plane, for the QUICK and Hybrid solutions and for the QUICK solution with a 42*40 grid. For the coarse grid QUICK gave an oscillatory pattern around the correct solution and the velocity assumed negative and unrealistic values resulting in an oscillatory streamline pattern before the contraction. Grid refinement in this case removed the oscillations.

Figure A2.9B concerns the calculation of the turbulent flow in a plane channel with a downstream facing step reported in Chapter 3. In this case steep gradients of turbulence quantities ($k, \epsilon, \overline{u_i^2}$) occur between the main throughflow and the shear layer. For example, the form of turbulence kinetic energy profile predicted, when all transport equations were discretised using QUICK, is shown in figure A2.9B. In fact the oscillations had a spatially two-dimensional pattern; small values of k with alternating sign were also observed in the main flow direction within

the potential core. Other turbulence quantities which should be positive by definition (e.g. ϵ) behave similarly. Close to the throughflow region both k and ϵ assumed an unrealistic oscillatory pattern which for the nodes where both k and ϵ were positive gave essentially arbitrarily high values for the eddy viscosity while for the nodes where k or ϵ were negative (an unphysical situation) the eddy viscosity was set equal to zero. Thus within the potential core the turbulent viscosity varied between zero and values 3 to 4 orders of magnitude higher than the values occuring even in the turbulent part of the flow. This strongly oscillatory eddy viscosity pattern interferred with the solution of the momentum and continuity equations and inhibited convergence. The same adverse effects on convergence were observed when wiggles were present in the velocity field.

Another category of convergence problems associated with negative coefficients was observed in the Reynolds Stress Transport calculations reported in Chapter 3. In RST calculations the cell Peclet numbers are particularly high due to the explicit treatment of turbulent diffusion (i.e. the cell Peclet numbers are estimated using the molecular viscosity). In certain flows convergence was retarded and continuity and other errors remained high in areas of the flow where wiggles in the velocity and other fields could not be directly observed. An example is the area in the neighbourhood of a separation streamline, figure A2.1Ø. It was observed that in certain cases the mass flux at the vertical faces of a control volume containing the separation streamline could have opposite outwards directions as shown

in figure A2.1Ø resulting in the following negative coefficients:

AL<Ø, AR<Ø , AS<Ø , (AN>Ø).

A possible explanation for the observed retardation or even inhibition of convergence for such a case could be as follows. The negative coefficients (AR,AL,AS) are treated as described in section A2.2 and the center node coefficient of the reformulated momentum equation would be set equal to AN (AP=AN). This value of AP is used in the construction of the pressure correction equation (see e.g. Patankar, 198Ø). It is clear that the simplified momentum equation used for the construction of the pressure correction equation has a very weak resemblance with the full discretised momentum equation for the node considered. This could result in local incompatibilities between the changes in the velocities associated with the pressure correction procedure and the evolution of the velocity field during the iterative solution of the momentum equations. The problem was alleviated when stronger under-relaxation of the momentum equations was applied.

For the type of problems discussed above a compromise had to be made between the desired higher accuracy of QUICK and the need to obtain converged solutions for the flows in question. This was achieved by the introduction - for these flows - of a mixed discretisation scheme employing QUICK for lower cell Peclet numbers and Upwind in areas of high cell Peclet numbers where problems associated with negative coefficients occured. The QUICK-UPWIND scheme can be considered as an equivalent to Hybrid; Hybrid shifts from CD

to Upwind on the basis of the local cell Peclet number. In Hybrid the shift CD-Upwind is perfomed at the critical Peclet number where the CD downstream coefficients become negative (i.e. Pc=2 for uniform grids). In the current QUICK-Upwind mixed scheme the shift QUICK-Upwind is performed when the local Peclet number exceeds a prescribed local limiting value Pc,max(x,y). In most of the cases where the mixed scheme had to be applied convergence was possible for values of the limiting Peclet numbers in the order of 10^4 compared with a value in the order of 2 for Hybrid.

The mixed QUICK-Upwind scheme was applied in the present calculations as follows: At first the limiting values of the cell Peclet numbers were set equal to a very large number so that a first attempt was made solving all equations using QUICK. The evolution of the solution was observed; if convergence problems were present the limiting Peclet numbers were reduced for the appropriate transport equation and for the region of the flow where the problems occurred, thus allowing a partial upwind discretisation. Further interventions of this kind were performed ,if necessary, until convergence was achieved. An example of this practice is given in figure A2.11 showing the convergence rate for the k-ϵ calculation of the turbulent flow in a plane channel with a one-sided step for a coarse 21*21 grid. It can be seen that when all equations were solved with QUICK convergence could not be achieved and this was traced to the previously mentioned spatial oscillations in the k and ϵ fields. The limiting Peclet number was reduced for the k and ϵ equations (i.e. QUICK was still retained in the momentum

equations) until the problem was removed. The problem was less pronounced for the finer grids studied (31*31,41*41 and 61*61). As already mentioned in Chapter 3 for the finest grid (61*61) Upwind discretisation had to be applied only in a narrow band within the non-turbulent potential core shown in figure 3.2. The shift QUICK-Upwind was applied as follows:

.the momentum equations were discretised using QUICK all over the solution domain.
.For the k and ϵ equations upwind discretisation was applied over a narrow band within the potential core and only for the main flow direction. The corresponding value of the limiting cell Peclet number was 5000.

It is therefore clear that the shift QUICK-Upwind allowed convergence to be achieved while the third order accurate scheme was applied in all important parts of the flow.

Particular information for the way in which the quadratic method was applied for each of the predicted flows has been given in the relevant Chapters of the thesis. The following conclusions summarize the experience gained from the application of the quadratic scheme in this project.
.In most of the predictions using the eddy viscosity concept the application of QUICK did not give rise to convergence problems. In certain cases, only minor remedial measures were required. Examples are the omission of negative values of k or ϵ at the edges of a jet in shallow water (close to the discharge) or the omission of obvious temperature over-shoots and under-shoots, occuring in the same area in

the estimation of the buoyancy terms in the momentum or k equation. The problems were exacerbated in the prediction of flows including areas of very low turbulence as e.g. the previously mentioned channel flow or the edges of a strongly buoyant surface layer. In such cases the mixed scheme had to be applied for positive-definite quantities (i.e. k, ϵ , B).

In the Reynolds stress flux transport predictions the convergence problems were more serious and the mixed QUICK-Upwind scheme had to be used more extensively and for all equations. However even for these cases the shift QUICK-Upwind was found necessary only at very high cell Peclet numbers typically of the order of 10^4 in relation to a value of 2 for HYBRID. As was shown in Chapter 3 even for such cases QUICK was applied in the most important parts of the flows concerned.

APPENDIX A3

THE BUOYANCY RELATED INSTABILITY PROBLEM

APPENDIX A3 : THE BUOYANCY RELATED INSTABILITY PROBLEM

This Appendix deals with the buoyancy related numerical instability problem which was referred to briefly in Chapter 2. The sequential numerical solution of the momentum and temperature or concentration equations which is usually adopted, may result in unstable error growth and divergence or in a severe retardation of convergence due to the coupling between the equations introduced via the buoyancy term. This mechanism is illustrated in section A3.1 where an analytical study of the unstable error growth is presented for a stably stratified convection problem. Section A3.2 presents the main features of an algorithm which solves locally and simultaneously the coupled momentum and temperature equations and attempts therefore to remedy the above problem. Section A3.3 discusses the application of this algorithm in two buoyant flows.

The work reported in sections A3.2 and A3.3 is based on the previous work of Crossley (1975). Crossley examined the buoyancy related instability problem in the stream function-vorticity formulation of the governing equations. He located the source of instability in the coupling of the vorticity and temperature equations and devised an algorithm solving locally and simultaneously all the governing equations (vorticity, stream-function and temperature in laminar flows of interest in this work). He also applied this algorithm successfully to a stratified convection problem and to the buoyancy driven cavity flow. The work reported in sections A3.2 and A3.3 may be considered as more

or less a "translation" of Crossley's work to the primitive variable (U,V,P) formulation used in this project.

Section A3.4 deals with another manifestation of the buoyancy related instability problem concerning small amplitude persistent oscillations in the variable fields. Finally, section A3.5 is a presentation of the practice adopted in this project to relax the instability problem and to achieve satisfactory levels of convergence in the calculation of buoyant flows.

A3.1. Analytical study of unstable error growth

The purpose of this section is to show how the sequential iterative solution of the buoyancy coupled momentum and temperature (or concentration) equations can lead to unstable error growth. The mechanism for unstable error growth is illustrated by perturbing a hydrodynamic and temperature field which initially satisfies the conservation equations exactly. One such solution, convenient for the present purposes, is the uniform horizontal flow of a fluid with a stable linear density stratification which was studied numerically by Crossley (1975). The solution domain and the boundary conditions of this problem are shown in figure A3.1. The temperature increases linearly with y and the viscosity of the fluid is assumed constant. We assume that the temperature field is perturbed by an amount ϵ_0 in the middle of two nodes P and S, figure A3.1. In a real situation the velocity and temperature at the horizontal boundaries could be affected by a strong local perturbation

of the temperature field; however in the following analysis we assume that the velocity and the temperature of the lower and upper boundaries remain constant. We aim to examine under what circumstances the commonly used sequential numerical solution algorithm damps the perturbation and reestablishes the correct solution and under what circumstances the perturbation results in an unstable error growth.

It is not possible to follow analytically the exact sequence of operations when a sequential algorithm is used for this problem. However, it is possible to examine analytically the solution of the lateral momentum and temperature equations in the vicinity of the perturbation. The following assumptions also had to be made to make the analysis of the problem tractable:

.The iterative procedure is assumed to be of the simplest point by point Jacobi type viz

$$[\ \Phi\ ]^{n+1} = [\ A\ ] * [\ \Phi\ ]^{n}$$

i.e. the variables are updated using all the variable values from the previous iteration $[\Phi]^{n}$. We are mainly interested in the first iteration so $[\Phi]^{n}$ is the exact solution with the temperature perturbation at the midpoint of PS.

.The PDE's for the momentum and temperature are discretised using upwind differencing for the convective terms and central differencing for the diffusive terms. Any other more realistic discretisation scheme could be used but the analytical treatment becomes significantly more cumbersome.

When the lateral momentum equation is first solved the temperature perturbation ϵ_0 would generate locally an upward

velocity due to the excess gravitational force. If the temperature equation is subsequently solved at points P and S the lateral convection would transport colder fluid between points P and S and an average temperature $\overline{Tp}=\emptyset.5*(Tp+Ts)$ lower than for the exact solution would occur. The second solution of the lateral velocity equation would now generate a downward velocity bringing warmer fluid from point P towards S. An oscillatory pattern is thus established when the vertical momentum and temperature equations are solved sequentially. We are interested to see if this oscillation is converging -stable error growth- or diverging -unstable error growth.

The lateral velocity Vp for the node P can be expressed as linear function of the average temperature $\overline{Tp}=\emptyset.5*(Tp+Ts)$. Also from the solution of the energy equation we can express the average temperature $\overline{Tp}$ as a non-linear function of the velocity between points P and S. The derivations are straight-forward but lengthy and only the final expressions are given here. For the moment assume that the steady state form of the equations is solved and that the equations are not under-relaxed al all, this analysis then leads to the following conditions:

$$V = \frac{Gr\ \varepsilon_T}{L(\ Re + 4L\ )} \qquad \text{and} \quad \varepsilon_T = \frac{\pm 1}{2L}\,\frac{|V|}{|V| + Re + \frac{4L}{\sigma_T}} \qquad \begin{matrix} + \text{ when } V>0 \\ - \text{ when } V<0 \end{matrix}$$

the following definitions and normalizations have been made:

.Re is the Reynolds number of the flow: $Re = \frac{H\ U_0}{\nu}$

.V is a non-dimensionalized lateral velocity Vp: $V = \frac{H\ V_P}{\nu}$

.Gr is a Grashof number of the flow:

$$Gr = \frac{H^3\ \beta\ g\ (\ T_T - T_B\ )}{\nu^2} \qquad \text{where} \quad \beta = -\frac{1}{\rho}\ \frac{\Delta\rho}{\Delta T} \text{ assumed constant.}$$

. ϵ_T is the normalized average temperature between points P and S in excess or deficit from the correct solution:

$$\varepsilon_T = \frac{(\ \overline{T_P}\ ) - (\ \overline{T_P})_{correct}}{T_T - T_B}$$

and L+1 is the number of nodes in each grid-direction and σ_T is the (constant) Prandtl number of the fluid.

The relations for V and ϵ_T are plotted in figure A3.2. The first solution of the momentum equation gives a positive (upwards) velocity V1 due to the temperature perturbation $\epsilon_0 > \emptyset$. The first sequential solution of the temperature equation gives a temperature deficit ϵ_1. We are interested in the growth or damping of the initial error ϵ_0. Successive substitutions between the previous equations for V and ϵ_T give:

$$\text{(say : } a = \frac{Gr}{L(Re+4L)}\ ,\ b = Re + \frac{4L}{\sigma_T}\ ,\ c = 1/(2L)\ )$$

$$\left|\frac{\varepsilon_1}{\varepsilon_0}\right| = \frac{ac}{b+a\varepsilon_0} \qquad \text{and} \qquad \left|\frac{\varepsilon_1}{\varepsilon_0}\right|_{\varepsilon_0 \to 0} = \frac{ac}{b}$$

$$\left|\frac{\varepsilon_2}{\varepsilon_0}\right| = \frac{a^2\ c^2}{b^2 + \varepsilon_0\,(ab+ca^2)} \qquad \text{and} \left|\frac{\varepsilon_2}{\varepsilon_0}\right|_{\varepsilon_0 \to 0} = \left(\frac{ac}{b}\right)^2 \text{ etc}$$

The error growth is stable when :

$$\left|\frac{\varepsilon_1}{\varepsilon_0}\right| < 1 \ , \ \left|\frac{\varepsilon_2}{\varepsilon_0}\right| < 1 \quad \text{for} \quad \varepsilon_0 \to 0$$

Both conditions are satisfied when : $ac/b < 1$ or

$$G_r < 2L^2 \ (\ Re+4L \ ) \ (\ Re+4L/\sigma_T \ )$$

This last relation is the condition for a stable error behaviour; it highlights the main parameters which define the stability of a sequential solution of the problem examined. The main parameters are the Reynolds number and the Grashof number (which define the flow), and the resolution of the grid (L) which is a feature of the numerical procedure. For a given grid density (L) stable solutions are possible at higher Grashof numbers when the Reynolds number of the flow is higher. Also a given flow (Gr,Re) can have stable solution if the grid is adequately refined. These trends were verified in the numerical solution of the problem.

It is obvious that the previous stability analysis is oversimplified. It deals mainly with one iteration in the vicinity of the perturbation; also the changes of the horizontal velocity and pressure brought in to ensure continuity satisfaction are not taken into account al all. In practice the imposition of the continuity constraint affects the sequential solution of the equations by preventing an arbitrary growth of the vertical velocity and thus increases stability.

Stability through under-relaxation

A commonly used approach to improve stability in the

sequential solution of buoyant flows is a strong under-relaxation of the coupled equations. In the following text the term static under-relaxation will be used for the case where a common under-relaxation factor r_ϕ is used for all nodes of the domain i.e.

$$\Phi_i^{n+1} = r_\phi \Phi_i^{n+1} + (1 - r_\phi) \Phi_i^n \qquad 0 < r_\phi < 1$$

The previous analysis was repeated assuming that the equations were statically under-relaxed. The resulting stability condition is:

$$Gr < \frac{1}{r_V r_T} 2L^2 \ (Re+4L) \ (Re+4L/\sigma_T)$$

where r_V and r_T are the under-relaxation factors of the lateral momentum, and temperature equations respectively. Thus for every flow configuration (Re,Gr) and for a given grid (L) stable solutions are possible if under-relaxation is adequately strong.

Transient solutions

The stability condition when a transient approach is adopted (i.e. unsteady terms are added to all transport equations and a fully implicit time-marching procedure is adopted for the numerical solution) is given by the expression:

$$Gr < 2L^2 \ (Re+4L+\frac{1}{L \ \Delta t_0}) \ (Re+\frac{4L}{\sigma_T}+\frac{1}{L \ \Delta t_0})$$

The time step is normalized by a time scale of the flow:

$$\Delta t_{scale} = \frac{H^2}{\nu} \quad \text{and} \quad \Delta t_0 = \frac{\Delta t_{real}}{\Delta t_{scale}}$$

Again, for a given flow (Re,Gr) and grid (L), stable

solutions are possible when the time step Δt_{real} is sufficiently small.

A3.2. Simultaneous solution of the momentum and temperature equation

The previous analysis located the source of unstable error growth as the sequential solution of the coupled vertical momentum and temperature equations. This source of instability could be eliminated if the equations were solved exactly at each iteration.

The previous analysis demonstrated that the sequential separated solution of the coupled equations does not always give a true solution of the system of equations, and furthermore, may lead to an increase of errors at each iteration. However, the system does have an exact bounded solution. The problem is that for cases where the stability condition is not satisfied, the correct solution cannot be reached by successive separate solutions. The simultaneous solution of the discretised momentum and temperature equations all over the solution domain or even along a line of the grid, is unpractical since the coupling of the equations is non-linear. However exact-simultaneous solution is possible locally. Following a practice similar to the one devised by Crossley (1975) the momentum and temperature equations were solved simultaneously as follows.

The lateral momentum equation at each node P, figure A3.3, was solved together with the energy equation at points P and S. The finite difference lateral momentum equation for point

P reads:

$$AP_P^V V_P = \sum_{N,S..} A_i^V V_i - \left(\frac{\Delta P}{\Delta y}\right)_P + \beta\rho g \left(\overline{T_P} - T_{ref}\right) \quad , \quad \overline{T_P} = (T_P+T_S)/2$$

The neighbouring velocities Vi and the pressure gradient are considered constant and Vp is expressed as a function of the average temperature $\overline{Tp}$:

$$A = \frac{\sum_{N,S..} A_i^V V_i - \left(\frac{\Delta P}{\Delta y}\right)_P}{AP_P^V} \quad , \quad B = \beta\rho g / AP_P^V \quad , \quad \underline{V_P = A+B\,\overline{T_P}} \qquad (1)$$

The temperature equation for points P and S reads:

$$AP_P^T T_P = \sum_{i\neq S} A_i^T T_i + AS_P^T(V_P)\, T_S \qquad (2)$$

$$AP_S^T T_S = \sum_{i\neq N} A_i^T T_i + AN_S^T(V_P)\, T_P \qquad (3)$$

Temperatures Tp and Ts are determined from equations (2) and (3) as functions of the uknown velocity Vp:

$$T_P = F_P(V_P) \quad , \quad T_S = F_S(V_P) \quad \text{and hence} \quad \overline{T_P} = F(V_P) \qquad (4)$$

The last equation is not determined analytically but is defined numerically during the solution procedure. The form of the momentum and temperature equations (1) and (4) is shown for a stably stratified flow in figure A3.4. For the slopes of the energy and momentum equations shown in figure A3.4 a sequential solution would diverge (iteration path rstxyw); a Newton-Raphson method is used instead. The temperature equation is approximated by chords of the $\overline{Tp}$=F(Vp) curve as follows:

1) Assuming that the "initial" temperature $\overline{Tp}$ has the value Tp_o the momentum equation (1) is solved and the velocity Vp has the value Vp_1.

2) The corresponding temperature $\overline{Tp_1}$ =F(Vp_1) is evaluated

from equations (2) and (3), point $A(Tp_1, Vp_1)$.

3) Steps 1 and 2 are repeated in order to locate another point $B_1(Tp_2, Vp_2)$ on the temperature equation curve.

4) At this stage the temperature equation is approximated analytically by a chord of the correct curve, defined by the previously located points A and B1:

$$\frac{V_P - V_{P2}}{V_{P1} - V_{P2}} = \frac{T_P - T_{P2}}{T_{P1} - T_{P2}} \qquad (5)$$

A first approximation of the correct solution is found from the system of equations (1) and (5) , $SL1(Tp_3, Vp_3)$.

5) The temperature Tp_4 corresponding to $Vp_4 = Vp_3$ is evaluated from equations (2) and (3) and another point of the temperature curve $B_2(Tp_4, Vp_4)$ is defined.

6) At this stage the accuracy of the approximative solution (Tp_3, Vp_3) is examined by checking the quantity:

$$Q = B(T_{P4} - T_{P3})$$

if Q is not sufficiently small in relation to Vp_3 the procedure is repeated from step 4 using the new point B_2 of the $\overline{Tp}=F(Vp)$ curve instead of the point B_1.

After convergence of the Newton-Raphson procedure is achieved the whole process is repeated for the next pair of nodes P and N.

During this stage the temperature at the node P will be readjusted. The solution is convergent when from iteration to iteration the readjustments become smaller and smaller.

The common sequential solution algorithm was modified in order to incorporate the simultaneous V-T solution procedure

described above; the remaining equations are solved as usual. The modified algorithm was tested in the buoyant flows discussed in the next section.

A3.3. Application of the simultaneous solution algorithm

i.The stratified convection problem

As mentioned in section A3.1 the initial field values satisfied exactly the conservation laws except for the temperature perturbation. The initial field values were:

.A uniform horizontal velocity all over the domain.

.A linear temperature profile. The energy equation for this flow is simply:

$$\frac{\partial}{\partial y}\left(\frac{\nu}{\sigma_T} \frac{\partial T}{\partial y} \right) = 0$$

which is satisfied by a linear temperature profile.

.The initial pressure field was defined from the lateral momentum equation which for the flow considered has the simple form:

$$-\frac{\partial P}{\partial y} + \beta\rho g \left(T-T_B \right) = 0 \rightarrow P(y) = P(0) + \beta\rho g \left(T_T - T_B \right) \frac{y^2}{2}$$

The temperature was perturbed at the centre of the domain by a small amount ϵ_0 =5% of Tp (figure A3.1).The grid used had 7 nodes in each direction.

The flow was calculated by both the sequential and simultaneous solution algorithms. For the sequential solution the Reynolds number of the flow was given the values 1 and 1ØØ; the Grashof number of the flow was increased by orders of magnitude until the solution

diverged. The equations were solved in their steady state form without under-relaxation. Information about the calculations is given in table A3.1.

Application of the previously developed stability condition for the current grid spacing (L=6) and Reynolds numbers studied (Re=1 and 100) gave the following stability limits for the Grashof number of the flow:

$$(r_V = r_T = 1 \ , \ \sigma_T = 1)$$

$$Re = 1 \qquad G_r < 4.5\ 10^4$$

$$Re = 100 \qquad G_r < 1.1\ 10^6$$

From table A3.1 it can be seen that the stability criterion is in agreement with the value of the Grashof number where the solutions diverged. Also the stabilizing influence of the horizontal convection (Re) is verified from the data in table A3.1.

TABLE A3.1

NCCE: Normalized Cumulative Continuity Error.

Gr	Re	Iterations	NCCE
		Sequential Solution	
1.E2	1	12	1.E-4
1.E3	1	30	1.E-4
1.E4	1	86	1.E-4
1.E5	1	Diverged	
1.E5	100	51	1.E-4
1.E6	100	93	1.E-4
1.E7	100	Diverged	

Simultaneous V-T solution

1.E4	1	59	1.E-4
1.E5	1	81	1.E-4
1.E6	1	100	2.2E-4
1.E8	1	100	3.3E-4
1.E10	1	115	1.E-4
1.E15	1	115	1.E-4
1.E20	1	115	1.E-4
1.E25	1	113	1.E-4
1.E10	1	115	1.E-4
1.E10	1.E2	27	1.E-4
1.E10	1.E4	15	1.E-5
1.E25	1	27	1.E-4
1.E25	1.E2	1	1.E-4
1.E25	1.E4	5	1.E-5

This flow was also calculated using the simultaneous solution algorithm. Both the Grashof and Reynolds numbers of the flow were varied, table A3.1. In contrast to the sequential solution algorithm the simultaneous solution algorithm was unconditionally stable for all the Grashof numbers studied up to 1.E25. Also for the same Grashof number the solution converged significantly faster at the higher Reynolds numbers in agreement with the stability analysis.

ii. The buoyancy driven square cavity laminar flow

Following the course of study of Crossley (1975) the sequential solution algorithm was further applied to the buoyancy driven square cavity laminar flow problem, figure A3.5. The flow was calculated for two Grashof numbers 1.E6 and 1.E7 by both the sequential and simultaneous solution algorithms. Since an accurate prediction of the flow itself was not of primary interest only coarse grids were used. Information about the convergence rate of the two algorithms is given in table A3.2.

TABLE A3.2

Grashof number	grid	Iterations for convergence	
		Sequential	Simultaneous
1.E6	7*7	Diverged	624
1.E6	11*11	215	1226
1.E7	7*7	Diverged	1293
1.E7	11*11	354	3694

The table shows that although the simultaneous algorithm enables solutions to be obtained on a given mesh at higher Grashof numbers than the sequential methods,the number of iterations required for convergence in the simultaneous solution was approximately one order of magnitude higher than for the sequential solution when both methods were convergent. Crossley (1975) also reported that the simultaneous solution in the vorticity-stream function formulation required 4300 iterations for a Grashof number of 1.E4 and a 21*21 grid. Roberts (1972) reports a similar

experience from the prediction of strongly swirling flows which exhibit a source term instabilty, similar to the buoyancy related instability. Retardation of convergence rate by one order of magnitude was also observed in this work when simultaneous adjustments of the coupled equations were introduced.

A full explanation of the reasons which cause the retardation of convergence in the flow in question has not been formulated but the following points clarify the observed behaviour. Assume that the calculation is started from a still fluid condition with a temperature equal to the cold wall temperature all over the domain and a uniform pressure. The first solution of the momentum and pressure correction equations will not effect any changes since the stagnant fluid condition satisfies the momentum and mass conservation laws exactly. The first solution of the temperature equation will generate a linearly varying temperature field between the two walls resulting in upwards velocities all over the domain when the vertical momentum equation is eventually solved. The pressure correction procedure, in order to satisfy continuity, will correct the velocities giving a first estimation of the circulation shown in figure A3.5. An important feature of the flow is point symmetry in relation to the centre of the square. Starting from a "cold wall" temperature all over the domain the flow-pattern is initially asymmetrical. When the sequential solution algorithm was applied symmetry was fairly soon established. A closer examination of intermediate results showed that the alternating direction

of the solution-sweeps accelerated the establishment of a symmetric pattern. In the "simultaneous solution" the sweeps of the domain had to have a fixed direction. (When alternating direction sweeps were carried out, the solution changed substantially from iteration to iteration depending on the direction of the sweep and ,after a few iterations, divergence occured). The fixed direction of the sweeps and the point by point solution led to a very slow establishment of the influence of the cold wall all over the domain and hence to the observed very high number of iterations required for convergence. The observed behaviour was described assuming a "cold wall" initial temperature field all over the domain, the same behaviour was however observed when more plau s ible initialisations were applied. Phenomenologically it can be stated that the simultaneous solution resulted in a retardation of the transfer of information from the boundaries in the interior of the solution domain. Roberts (1972), commenting in brief on possible causes of the observed slow convergence, suggested the last general explanation but gave no further details.

The purpose for the development of the simultaneous solution algorithm was to demonstrate the source of instability and to suggest a possible course for the radical removal of the instabilty problem. However the algorithm obviously does not offer a viable alternative to the sequential algorithms for the calculation of practical buoyant flows. Algorithms using point by point solution with simultaneous adjustments are notoriously slow to converge.

The evidence from the present work and from the previous work of Roberts (1972) and Crossley (1975) suggests that methods employing local simultaneous solutions of the coupled momentum and temperature equations retard the convergence rate by a factor of 10.

Because of the above experience the bulk of the buoyant calculations reported in this thesis were carried out using the common sequential algorithm and strong under-relaxation. In the following sections this practice is further discussed.

A3.4. Small amplitude persistent oscillations

A further manifestation of the buoyancy related instability in the sequential solution of stably stratified buoyant flows is the occurence of small amplitude persistent oscillations in the variable fields. In this section attention is mainly concentrated on the characteristics of the solution when strong static under-relaxation is used to overcome the buoyancy instability.

In a systematic iterative method an initial guess is successively refined until subsequent iterations result in changes of the variable field of less than some specified size. Such a process is mathematically convergent if the cumulative "current" error in the variable fields (i.e. the sum of the absolute magnitude of errors for all the nodes) is continuously reduced by successive iterations down to any level within the capabilities of the computer.

In the case of stably stratified buoyant flows, once the

initial unstable error growth problem was overcome through strong static under-relaxation of the momentum equations, the following situation was observed. The cumulative errors in the solution of the variables decreased to a certain limit which however could not be reduced by further iterations. Successive iterations did however result in oscillations of the cumulative errors around the previously mentioned limit and not to a further reduction. At this stage the hydrodynamic and temperature fields did not change substantially over a large number of iterations, however for each node the variables performed irregular small amplitude oscillations.

This situation is illustrated in figure A3.6 for the calculation of a horizontal density jump such as studied in Chapter 4. Three calculations were carried out. For the first calculation, curve A, the boundary conditions were as for the real experimental situation but the buoyancy term in the vertical momentum equation was omitted. The steady state form of the equations was solved and the momentum equations were strongly under-relaxed ($r_U=r_V=\emptyset.15$) for uniformity with the forthcoming buoyant calculation. The normalized cumulative continuity error is more or less continuously reducing down to the set value of 10^{-4} where usually convergence is assumed (curve A). For the second calculation the buoyancy term in the V-momentum equation was introduced; under-relaxation was the same as before (curve C). From figure A3.6 it can be seen that for this case the normalized cumulative error is initially reduced down to a value around 3.10^{-2} and further iterations result only in an oscillation

of the error around this value. In the third calculation (curve B) the false transient approach which will be described in section A3.5 was used; by an appropriate choise of time step the errors could always be reduced at the expense of the number of iterations or time steps required to achieve a steady state situation.

In order to examine the reasons why the cumulative errors could not be continuously reduced in strongly buoyant cases when static under-relaxation was used, the characteristics of the solution were more closely examined and the following features were typically observed. As was previously mentioned when (for a given under-relaxation of the momentum equations) a plateau was reached around which the errors oscillated, the hydrodynamic and temperature fields did not change substantially with further iteration. If the static under-relaxation was sufficiently strong as e.g. in the previous case -curve C- it was observed that the solution practically satisfied overall continuity and thermal energy conservation at each vertical cross-section of the solution domain before (and obviously after) each application of the pressure correction procedure. However an examination of the local continuity errors revealed that the errors remained high in certain areas of the domain and substantially lower in the rest. Such areas were typically areas of low horizontal convection with steep vertical temperature gradients and low values of effective viscosity as e.g. the edge of a buoyant surface mixing layer, the edge of a surface layer after an internal hydraulic jump etc. In such areas the local Grashof numbers are high and the

possibilities of unstable error growth locally are large. The reason that the local instabilities do not result in numerical divergence is that the pressure correction procedure inhibits an uncontrollable growth of the vertical velocity and that the oscillations are bounded due to the strong under-relaxation.

To conclude and further substantiate this qualitative interpretation of the poor convergence of strongly buoyant flows using the static under-relaxation technique the results of the calculation of a surface mixing layer are presented in some detail. The case considered is a simulation of test No 2 of Chu and Baddour (1984); the test conditions were:

Exit velocity $U_{\emptyset}$=14.5 cm/s

Exit depth D =2.Ø1 cm

Buoyancy at the exit $\Delta\rho_{\emptyset}/\rho_a$ =2.1 %

Exit densimetric Froude number Fd=2.29

The steady state form of equations was solved. The static under-relaxation factors for the momentum equations were $r_U=r_V=\emptyset.15$. The solution domain is shown in figure A3.7; the grid had (28*25) nodes and was more concentrated at the edge of the surface layer. In figure A3.7 the Normalized Cumulative Continuity Error (NCCE) is plotted against the number of iterations. A large number of iterations were carried out to allow a demonstration of the previously mentioned characteristics of the solution. It is clear from figure A3.7 that after an initial period of reduction, the error exhibits an oscillatory pattern of more or less constant period varying in the range 5.10^{-3} to 2.10^{-2} .

In figure A3.8 horizontal velocity and temperature profiles are given for three stages of the solution: 600, 1000 and 1400 iterations. The solution did not substantially change between 1000 and 1400 iterations while small changes occured between the 600th and 1000th iteration. To examine the compliance of the solution with the overall constraints of the flow the mass and salt concentration fluxes were calculated -before the application of the pressure correction procedure- at each vertical cross section of the solution domain for the 3 stages of the solution mentioned above; the overall constraints were practically satisfied in all cases. Finally in figure A3.9 the typical pattern of local continuity errors distribution is shown for three cross-sections of the domain. The errors had significant values only at the edge of the layer; in this region the errors were 2 to 3 orders of magnitude higher than in the rest of the solution domain. These details illustrate quite clearly the difficulty of identifying a fully converged solution in strongly buoyant flows.

A3.5. The practice adopted in this project

In certain cases the behaviour described in the previous section could not be inproved by even stronger static under-relaxation. In the prediction of strongly buoyant flows, such as the internal hydraulic jump or the stable form of the vertical buoyant jet in shallow water, the use of static under-relaxation factors as low as $r_U=r_V=0.05$ did not give satisfactory low overall errors. In these cases the

practice of a false-transient solution as described by Markatos (1984) performed considerably better (see figure A3.6 for example). The main features of this practice are:

. The momentum equations are solved by a "false" transient approach assuming a time step sufficiently low to allow satisfactorily low overall errors. The corresponding maximum cell Courant numbers were usually in the range Ø.2-Ø.6. The term "false" transient is used to emphasize the fact that only the momentum equations are solved in an unsteady state form whereas, as discussed below, the remaining equations (e.g. B,k etc) are solved in a steady state form.

The form of the discretised momentum equations becomes:

$$\text{e.g. } U_P^{n+1} = \frac{\sum_i A_i U_i + Su_U + \frac{U_P^n \rho}{\Delta t}}{\sum A_i + \frac{\rho}{\Delta t}} \qquad i = N,S,R...$$

by an appropriate choice of the time step Δt the changes of U_P from iteration to iteration can be controlled.

. It was found beneficial from an overall errors point of view to solve more accurately the pressure correction equation in relation to the "non-buoyant" applications of SIMPLE. A sufficient number of sweeps of the solution domain were carried out until the cumulative error in the solution of the pressure correction equation was reduced to the 1Ø% of its initial value:

$$\frac{\sum_{\text{all nodes}} \left(\sum_i A_i \Delta P_i + Su_{\Delta P} - AP \Delta P_P \right) \Delta V_n}{\sum_{\text{all nodes}} \left(Su_{\Delta P} \Delta V_n \right)} < 0.10$$

At the initial stages of the solution a large number of sweeps per iteration (~3Ø) were found necessary to satisfy the previous constraint; however, when convergence was approached one sweep per iteration was sufficient.

The transport equations for the turbulence quantitities and the mean buoyancy were solved in their steady state form. Static under-relaxation was used for all the turbulence quantities (r_{Φ}=Ø.5) whereas the mean buoyancy equation was not under-relaxed al all.

. For all the (typically) slowly evolving buoyant flows examined in this project it was observed that in agreement with physical observations, the diffusion time scales of the temperature field were substantially longer than the convective time scales (Leschziner, 1979); the number of iterations required to reach a steady state situation was increased due to the naturally slow evolution of the temperature field in areas of low convection and low turbulent diffusion as for example the edge of a buoyant surface layer. (The problem of the slow evolution is far more pronounced for the mean buoyancy than for the remaining transported variables due to the absence of source-sink terms in the mean buoyancy transport equation (a conserved scalar)). To accelerate this evolution the temperature equation was not under-relaxed at all; this practice did not cause any numerical problems since due to the small time-steps the velocity field was changing very slowly.

.Convergence to a steady state situation was assumed when the overall errors were sufficiently low and the variable

fields did not substantially change over a large number of iterations. The procedure applied to ensure this was described in chapter 6.

These practices were found sufficient to obtain converged solutions for all the flows calculated in the present thesis. By an appropriate choice of the time step, the overall errors could be reduced to very low values and the high local continuity errors problem, mentioned in the previous section, could be removed.

The false transient approach relaxes the advancement of the solution in a different way than static under-relaxation does. Assume that at a certain stage of the solution of the transport equation for a variable F, the solution is advanced:

i) with a steady state approach without any under-relaxation:

$$\left(F_P^{n+1} \right)_i = \frac{\Sigma A_{nb} F_{nb} + Su_F}{AP}$$

ii) with a steady state approach using static under-relaxation:

$$\left(F_P^{n+1} \right)_{ii} = r_F \frac{\Sigma A_{nb} F_{nb} + Su_F}{AP} + (1-r_F) F_P^n = r_F \left(F_P^{n+1} \right)_i + (1-r_F) F_P^n$$

iii) with the false transient approach and a time step Δt.

$$\left(F_P^{n+1} \right)_{iii} = \frac{\Sigma A_{nb} F_{nb} + Su_F + \frac{\rho}{\Delta t} F_P^n}{AP + \frac{\rho}{\Delta t}} = \frac{AP}{AP + \frac{\rho}{\Delta t}} \left(F_P^{n+1} \right)_i + \frac{\frac{\rho}{\Delta t}}{AP + \frac{\rho}{\Delta t}} F_P^n$$

On the basis of the previous relations the false transient approach can be considered as equivalent to the use of a spatially varying under-relaxation factor:

$$r'_F(x,y) = \frac{AP}{AP + \frac{\rho}{\Delta t}}$$

It is obvious from this relation that r'_F has its minimum values where convection is low, since:

$$AP \sim a_1 \frac{\rho|U_i|}{\Delta x_i} + a_2 \frac{\mu}{\Delta x_i^2} \qquad \text{where } a_1 \text{ and } a_2 \text{ are constants}$$

and its maximum values where convection is locally strong. It is obvious from the previous analysis that such a distribution of under-relaxation factors is optimal from the buoyancy instability point of view and allows a more flexible and efficient control of the local and overall errors of the solution.

Finally, it should be pointed out that the most important of the measures constituting the false transient method is the transient approach in the solution of the momentum equations. The remaining measures as e.g. the more accurate solution of the pressure correction equation etc were found beneficial from a convergence rate point of view but not necessary to control the instability problem.

REFERENCES

ALBETRTSON M.L., DAI B. and ROUSE H. (1950)
"Diffusion of submerged jets."
Transactions of the ASCE (1950), vol.115, pp. 639-664.

ANWAR H.O. (1972)
"The radial spreading as a free surface layer of a vertical buoyant jet."
J. of Eng. Math. (1972), vol.6, No 3, pp. 257-272.

BADDOUR R.E. AND CHU V.H. (1975)
"Buoyant surface discharge on a step and on a sloping bottom."
Techn. Rep. No 75-2, Dept. Civ. Eng., McGill University, Montreal, 1975.

BRADSHAW P., CEBECI T. and WHITELAW J.H. (1981)
"Engineering calculation methods for turbulent flow."
Academic Press, London (1981)

BRYANT D. and HUMPHREY J.A.C. (1976)
"Conservation equations for laminar and turbulent flows in general three-dimensional curvilinear coordinates."
Report No. CHT/76/2,Mech. Eng. Dept., Imperial College, December 1976.

CHEN C.J. and RODI W. (1980)
"Vertical turbulent buoyant jets - a review of experimental data."

HMT, Volume 4, Pergamon Press (1980).

CHU V.H. and BADDOUR R.E. (1984)

"Turbulent gravity-stratified shear flows."

J. Fluid Mech. (1984), vol. 138, pp. 353-378.

CROSSLEY P.S. (1975)

"Recirculating flows with body forces."

Ph.D. Thesis, Heat Transfer Section, Dept. of Mech. Eng., Imperial College, University of London.

DENNIS S.C.R. and SMITH F.T. (1980)

"Steady flow through a channel with a symmetrical constriction in the form of a step."

Proc. R. Soc. London (1980), vol. A372, pp. 393-414.

ELLISON T.H. and TURNER J.S. (1959)

"Turbulent entrainmemt in stratified flows."

J. Fluid. Mech. (1959), vol. 6, pp. 423-448.

GIBSON M.M. and LAUNDER B.E. (1976)

"On the calculation of horizontal, turbulent, free shear flows under gravitational influence."

Journal of Heat Transfer, Transactions of the ASME (1976), vol. 98c, pp.81-87.

GIBSON M.M. and LAUNDER B.E. (1978)

"Ground effects on pressure fluctuations in the atmospheric boundary layer."

J. Fluid Mech. (1978), vol. 86, pp. 491-511.

GIBSON M.M. and RODI W. (1981)

"A Reynolds-stress closure model of turbulence applied to the calculation of a highly curved mixing layer."

J. Fluid Mech. (1981), vol. 103, pp. 161-182.

HACKMAN L.P., RAITHBY G.D. and STRONG A.B. (1984)

"Numerical predictions of flows over backward facing steps."

Int. J. for Num. Meth. in Fluids (1984), vol. 4, pp.711-724.

HAN T., HUMPHREY J.A.C. and LAUNDER B.E. (1981)

"A comparisom of Hybrid and Quadratic-Upstream differencing in high Reynolds number elliptic flows."

Comp. meth. in appl. mech. and eng. (1981), vol. 29, pp. 81-95.

HANJALIC K. and LAUNDER B.E. (1976)

"Contribution towards a Reynolds-stress closure for low-Reynolds number turbulence."

J. Fluid Mech. (1976), vol.74, pp. 593-610.

HINZE J.O. (1959)

"Turbulence"

McGraw-Hill, New York, 1959.

HOSSAIN Md. S. (1980)

"Mathematishe modellierung von turbulenten Auftriebsstromungen."

Ph.D. Thesis, University of Karlruhe (TH), Germany.

HUANG P.G. and LESCHZINER M.A. (1985)
"Stabilization of recirculating-flow computations performed with second-moment closures and third-order discretisation." Fifth symposium on turbulent shear flows, Cornell University, Ithaka, New York, (1985).

HUNT B. and HSU S.T. (1965)
"Configuration of the free surface above a vertical jet." La Houille Blanche (1965), vol. 6.

IAMANDI C. and ROUSE H. (1969)
"Jet-induced circulation and diffusion."
Journal of the Hydraulics division, ASCE (1969), HY2, pp. 589-600.

JIRKA G.H. and HARLEMAN D.R.F. (1979)
"Stability and mixing of a vertical plane buoyant jet in confined depth."
J. Fluid Mech. (1979), vol. 94, part 2, pp. 275-304.

JIRKA G.H. (1982)
"Multiport diffusers for heat disposal: a summary."
Journal of the Hydraulics division, ASCE (1982), HY12, pp. 1425-1468.

JONES W.P. and LAUNDER B.E. (1973)
"The calculation of low-Reynolds number phenomena with a

two-equation model of turbulence."
Int. J. Heat Mass Transfer (1973), vol 16., pp. 119-1130.

KHEZZAR L., WHITELAW J.H. and YIANNESKIS M. (1985)
"An experimental study of round sudden expansion flows."
Fifth symposium on turbulent shear flows, Cornell University, Ithaka, New York, (1985).

KIM J., KLINE S.J. and JOHNSTON J.P. (1978)
"Investigation of separation and reattachment of a turbulent shear layer: Flow over a backward facing step."
Report MD-37, Thermosciences Division, Mech. Eng. Dept., Stanford University, 1978.

LAUFER J. (1951)
"Investigation of turbulent flow in a two-dimensional channel."
NACA, Report 1053, (1951).

LAUNDER B.E. and SPALDING D.B. (1974)
"The numerical computation of turbulent flow."
Comp. meth. in appl. mech. and eng. (1974), vol. 3, p. 269.

LAUNDER B.E., REECE G.J. and RODI W. (1975)
"Progress in the development of a Reynolds stress turbulence closure."
J. Fluid Mech. (1975), vol. 68, pp. 537-566.

LAUNDER B.E. (1975)

"On the effects of a gravitational field on the turbulent transport of heat and momentum."

J. Fluid Mech. (1975), vol.67, p.p. 569-581.

LEE J.H.W. and JIRKA G.H. (1981)

"Vertical round buoyant jet in shallow water."

Journal of the hydraulics division, ASCE (1981), HY12, pp. 1651-1674.

LEONARD B.P. (1979)

"A stable and accurate convective modelling procedure based on quadratic upstream interpolation."

Comput. meth. in appl. mech. and eng. (1979), vol. 12, pp. 59-98.

LEONARD B.P. (1979)

"A survey of finite differences of opinion on numerical muddling of the incomprehensible defective confusion equation."

ASME, AMD, vol. 34, Finite element methods for convection dominated flows.

LEONARD B.P., LESCHZINER M.A. and McGUIRK J. (1978)

"Third order finite difference method for steady two-dimensional convection."

Proc. Conf. on Numerical methods in laminar and turbulent flows, Swansea, G. Britain (1978).

LESCHZINER M.A. (1979)

"Numerical prediction of the internal density jump."

18th IAHR Congress, Cagliari, Italy, 1979.

LIONG S.Y. (1971)

"Vertical jets in shallow water with high discharge velocities."

Final year project, Institut for Hydromechanics, University of Karlsruhe, Germany,1971.

MANSOUR N.N.,KIM J. and MOIN P. (1983)

"Computation of turbulent flows over a backward facing step."

Fourth symposium on turbulent shear flows, Karlsruhe, Germany, 1983.

MARKATOS N.C., MALIN M.R. and COX G. (1982)

"Mathematical modelling of buoyancy-induced smoke flow in enclosures."

Int. J. Heat and Mass Transfer (1982), vol. 25, No 1, pp. 63-75.

MARKATOS N.C. and PERICLEOUS K.A. (1984)

"Laminar and turbulent convection in an enclosed cavity."

Int. J. Heat and Mass Transfer (1984), vol. 27, No 5, pp. 755-772.

McGUIRK J.J. and RODI W. (1977)

"A mathematical model for a vertical jet discharging into a shallow lake."

17th IAHR Congress, Baden-Baden, Germany, parer a72, (1977).

McGUIRK J.J. and RODI W. (1979)

"Mathematical modelling of three-dimensional heated surface jets."

J. Fluid Mech. (1979), vol. 95, part 4, pp. 609-633.

McGUIRK J.J. ,TAYLOR A.M.K.P. and WHITELAW J.H. (1981)

"The assesment of numerical diffusion in upwind difference calculations of turbulent recirculating flows."

Third symposium on turbulent shear flows, The University of California, Davis, September 1981.

McGUIRK J.J. and TAYLOR A.M.K.P. (1985)

Unpublished RST predictions, Imperial College.

MORTON B., TAYLOR G.I. and TURNER J.S. (1956)

"Turbulent gravitational convection from maintained and instantaneous sources."

Proc. Roy. Soc. (1956) A234, pp. 1-23.

MURAOKA K. and MUROTA A. (1967)

"Experimental study on vertical water jets to free water surface."

Technology reports of the Osaka University, Japan, vol. 17, No 798, 1967.

MUROTA A. and MURAOKA K. (1967)

"Turbulent diffusion of the vertically upward jet."

Proc. of the 12th congress of IAHR, Colorado University, Ft. Collins, Colorado, USA, Sept 1967.

NAKAGAWA H., NEZU I. and UEDA H. (1975)
"Turbulence of open channel flow over smooth and rough beds."
Proc. of Japan. Soc. Civ. Eng. (1975), No 241, pp. 155-167.

NEMEROW N.L. (1978)
"Industrial water pollution."
Addison-Wesley publishing company, Reading-Massachussets (1978).

PAN F. and ACRIVOS A. (1967)
"Steady flows in rectangular cavities."
J. Fluid Mech. (1967), vol. 28, pp. 643-655.

PATANKAR S.V. and SPALDING D.B. (1972)
"Heat and mass transfer in boundary layers."
Intertext books, London (1970).

PATANKAR S.V. and SPALDING D.B. (1972)
"A calculation procedure for heat, mass and momentum transfer in 3-D parabolic flows."
Int. Journal of Heat and Mass Transfer (1972), vol. 15.

PATANKAR S.V. (1980)
"Numerical heat transfer and fluid flow."
McGraw-Hill book company, 1980.

POLLARD A. and SIU A.L.W. (1982)

"The calculation of some laminar flows using various discretisation schemes."

Comp. meth. in appl. mech. and eng. (1982), vol. 35, pp. 293-313.

POPE S.B. and WHITELAW J.H. (1976)

"The calculation of near-wake flows."

J. Fluid Mech. (1976), vol. 13, part 1, pp. 9-32.

PRONCHICK S.W. and KLINE S.J. (1983)

"An experimental investigation of the stucture of a turbulent reattaching flow behind a backward facing step."

Report MD-42, Thermosciences Division, Mech. Eng. Dept., Stanford University, 1983.

PRYPUTNIEWICZ R.J. and BOWLEY W.W. (1975)

"An experimental study of vertical buoyant jets discharged into water of finite depth."

Journal of Heat Transfer, Transactions of the ASME (1975), Paper no 75-HT-RR, pp 274-281, May 1975.

REYNOLDS W.C. and CEBECI T. (1976)

"The calculation of turbulent flows"

from : "Turbulence", editor: Bradshow P.,

Topics in applied Physics, vol. 12, Springer Verlag Berlin, 1976.

ROACHE P.J. (1982)

"Computational Fluid Dynamics."

Hermosa Publishers, Albuquerque, New Mexico (1982).

ROBERTS L.W. (1972)

"Turbulent swirling flows with circulation."

Ph.D. Thesis, Heat Transfer Section, Dept. of Mech. Eng., Imp. College, University of London, 1972.

RODI W. (1979)

"Influence of buoyancy and rotation on equations for the turbulent length scale"

Second symposium on turbulent shear flows, Imperial College, London , 1980.

RODI W. (1980)

"Turbulence models and their application in Hydraulics."

IAHR, Srate-of-the art paper, Presented by the IAHR-Section on Fundamentals of Division II: Experimental and Mathematical Fluid Dynamics.

SHIR C.C. (1973)

"A preliminary numerical study of atmospheric turbulent flows in the idealized planetary boundary layer."

J. Atmos. Sci. (1973), vol. 30, pp. 1327-1339.

STANFORD CONFERENCE (1980)

1980-1981 AFOSR HTM Stanford Conference on complex turbulent flows, Proceedings vol. 1,2 and 3, 1982.

STEFAN A.M. (1970)

"Stratification of flow from channel into deep lake."
Journal of Hydraulics division (1970), ASCE, HY7, pp. 1417-1434.

TAYLOR A.M.K.P. and WHITELAW J.H. (1984)

"Velocity characteristics in the turbulent wakes of confined axisymmetric bluff bodies."
J. Fluid Mech. (1984), vol.139, pp. 391-416.

TENNEKES H. and LUMLEY J.L. (1972)

"A firt course in turbulence."
The MIT Press, Cambridge-Massachussets, 1972.

TRENT D.S. and WELTY J.R. (1973)

"Numerical thermal plume model for outfalls in shallow water."
Environmental Protection Technology Series, EPA-R2-73-162, U.S. Environmental Protection Agency, (1973).

TRENT D.S. (1980)

Private communication reported by W. Rodi in "Turbulence models and their application in Hydraulics.", Rodi (1980).

WEBSTER C.A.G. (1964)

"An experimental study of turbulence in a density stratified shear flow."
J. Fluid Mech. (1964), vol. 19, pp. 221-245.

WILKINSON D.L. and WOOD I.R. (1971)

"A rapidly varied flow phenomenon in a two-layer flow."

J. Fluid Mech. (1971), vol.47, pp. 241-256.

FIGURES

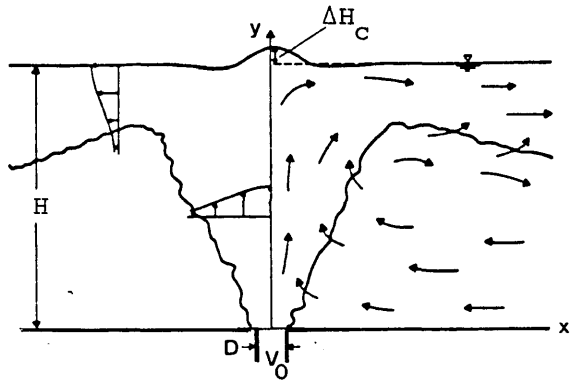


FIGURE 1.1 : Isothermal plane jet.
Flow configuration.

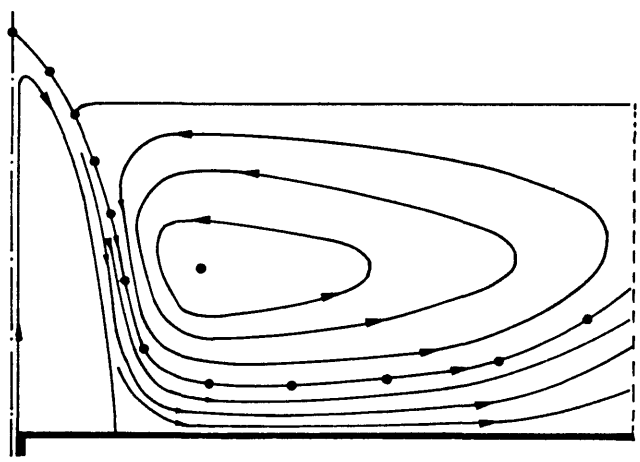


FIGURE 1.2 : Isothermal plane jet with high initial momentum.

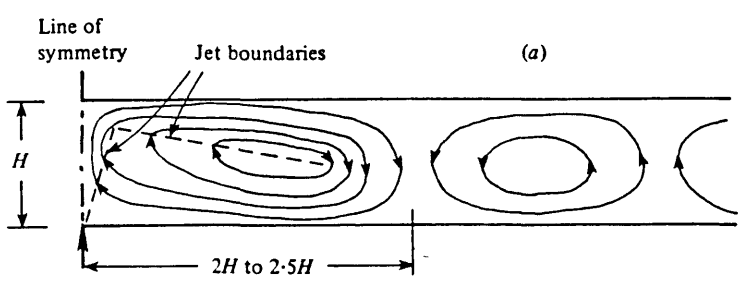
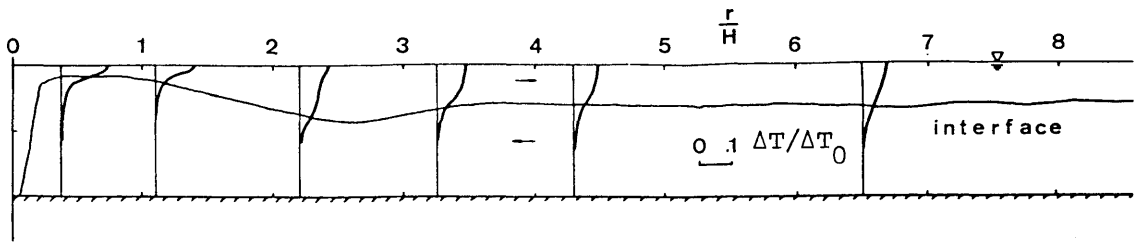
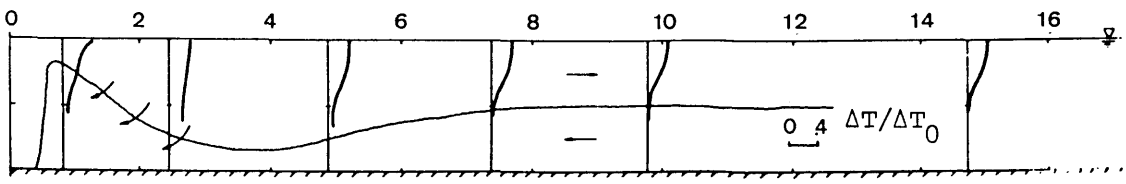


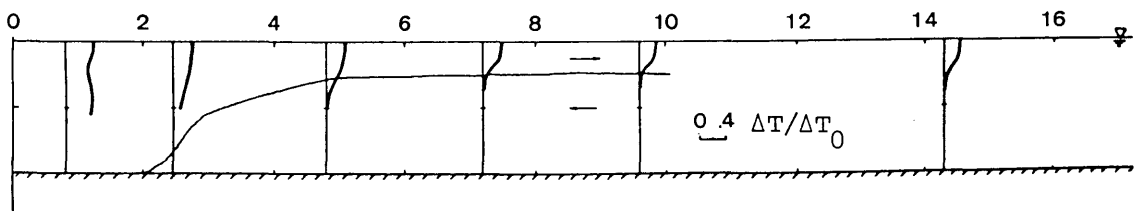
FIGURE 1.3 : Isothermal plane jet. Flow-pattern suggested by Jirka and Harleman.



Case 1 : Stable form F_d = 46 , H/D = 11



Case 2 : "Submerged jump" F_d = 8 , H/D = 2.2



Case 3 : Unstable form F_d = 205 , H/D = 10

FIGURE 1.4 : Temperature profiles for three axisymmetric configurations (figure from Lee and Jirka , 1981)

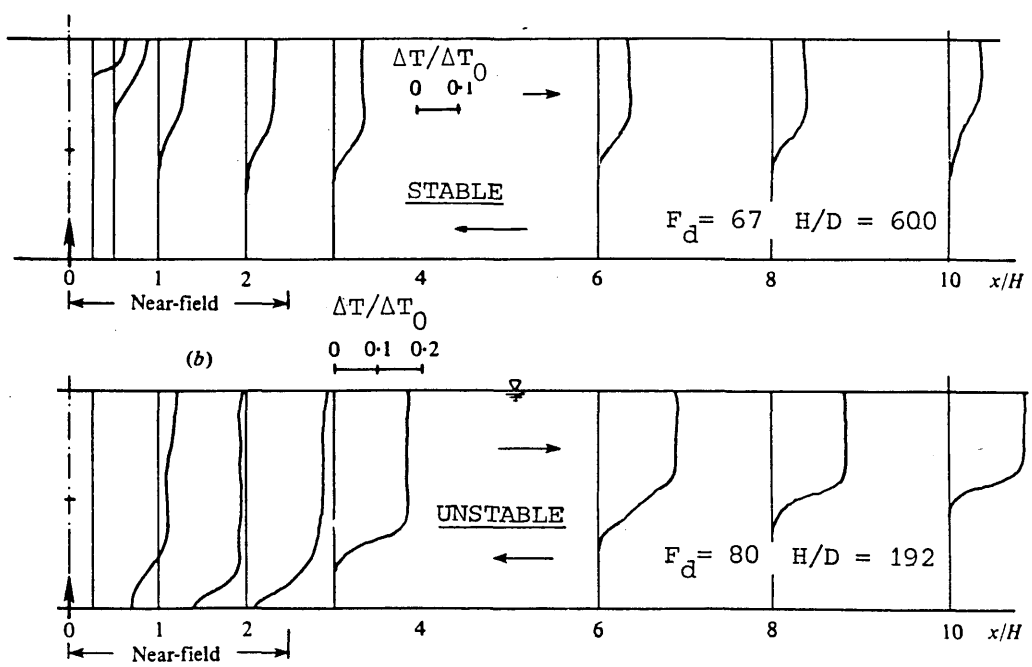
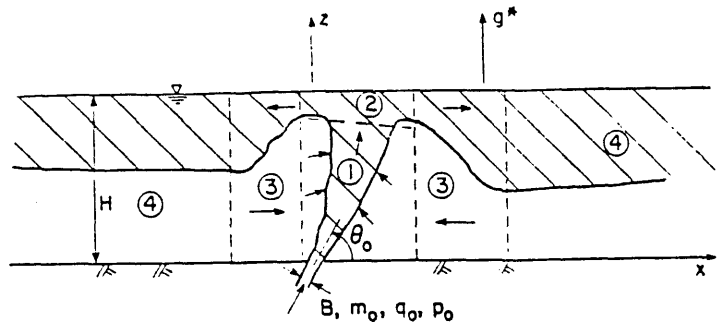
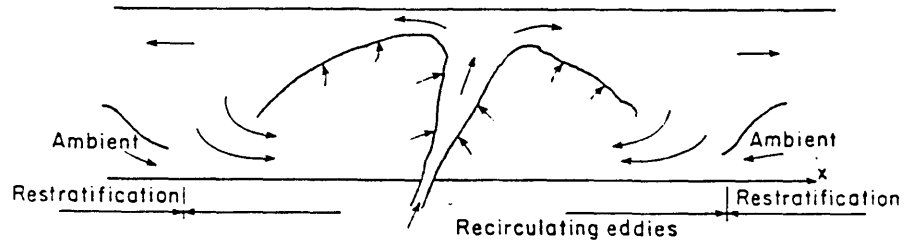


FIGURE 1.5 : Temperature profiles for two plane configurations. (figure taken from Jirka and Harleman , 1979)



1. Vertical buoyant jet region
2. Surface impingement and surface jet regions
3. Internal hydraulic jump region
4. Stratified counterflow region

a) Stable discharge configuration



b) Unstable discharge configuration

FIGURE 1.6 : Two-dimensional submerged buoyant jet in shallow water : definition of flow field configurations. (figure taken from Lee and Jirka , 1981)

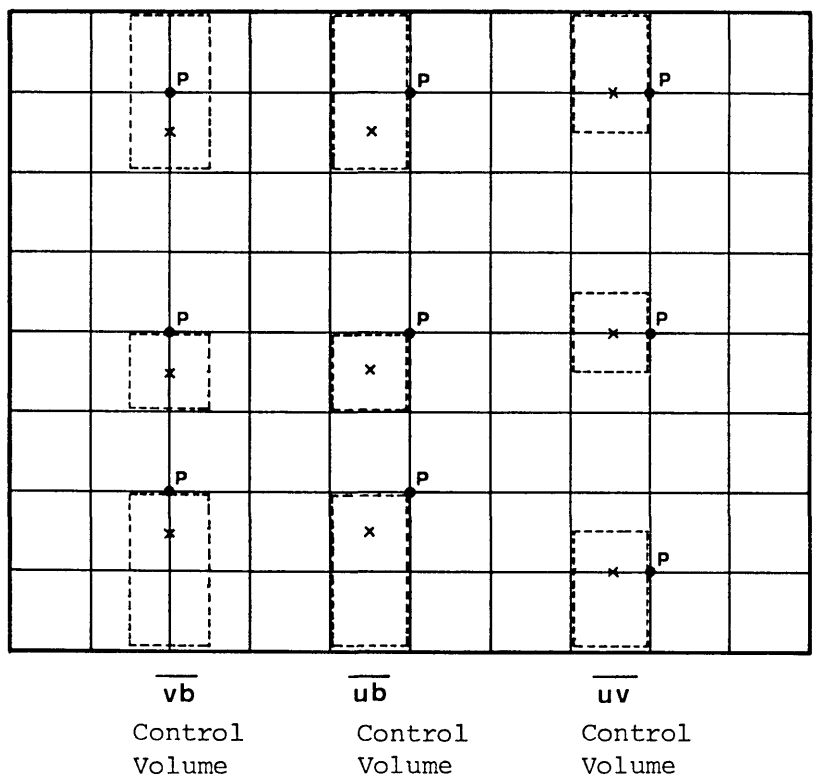
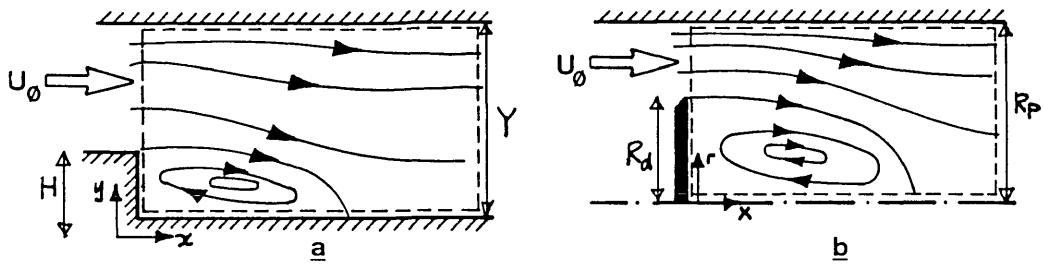


FIGURE 2.1 : Control volumes for the scalar fluxes and the Shear stress.



$U_\emptyset = 18.5$ m/s, H = 3.81 cm, air. $U_\emptyset = 1.37$ m/s, $R_d = 1.27$ cm, water.

FIGURE 3.1 : Flow configurations considered.
(a): Plane single-sided expansion, Y/H=3
(b): Axi-symmetric disc blockage in a pipe, Rd/Rp=0.5

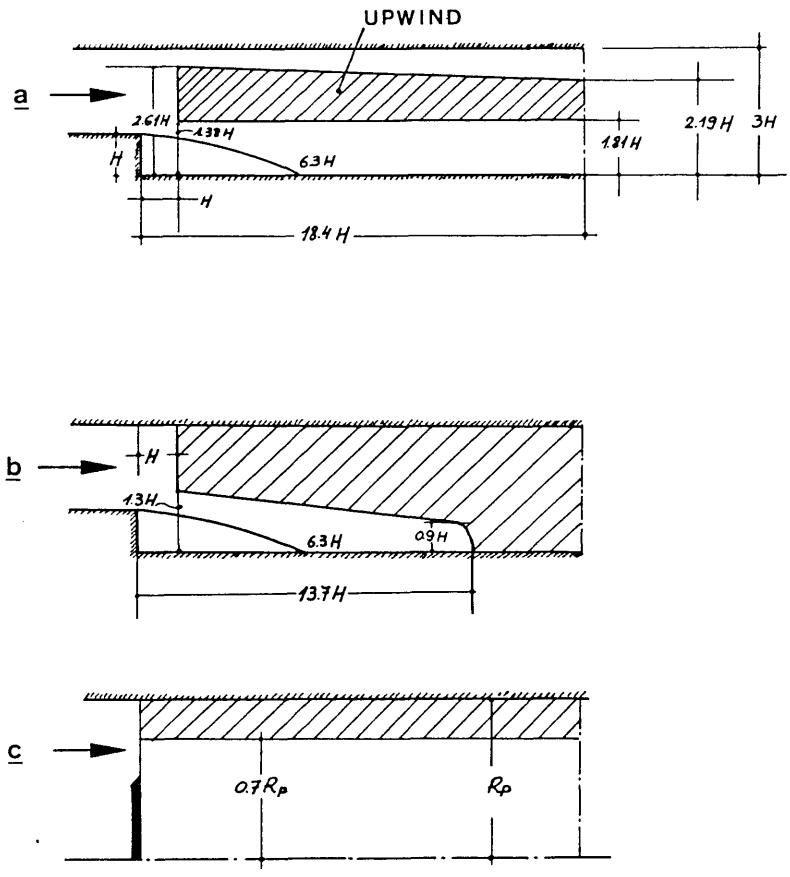


FIGURE 3.2 : Zones of the domain where Upwind discretisation was applied:
(a): Step-flow. Turbulence equations, horizontal convection, k-ε and RST.
(b): Step-flow. Momentum equations, horizontal convection, RST.
(c): Disc-flow. Momentum equations, horizontal convection, RST.

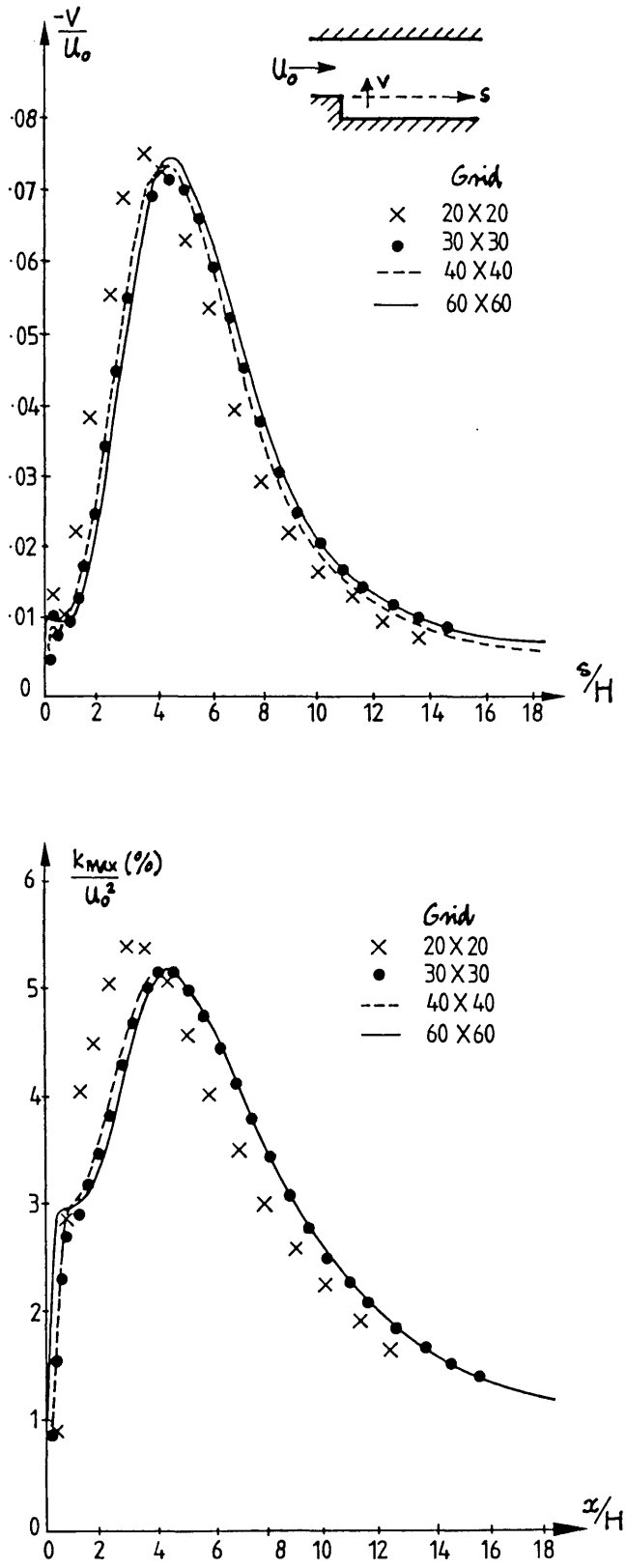


FIGURE 3.3 : Grid independence checks, k-ε predictions, step-problem.
(A) : Vertical velocity at the level of the expansion
(B) : Maximum cross-sectional turbulence energy

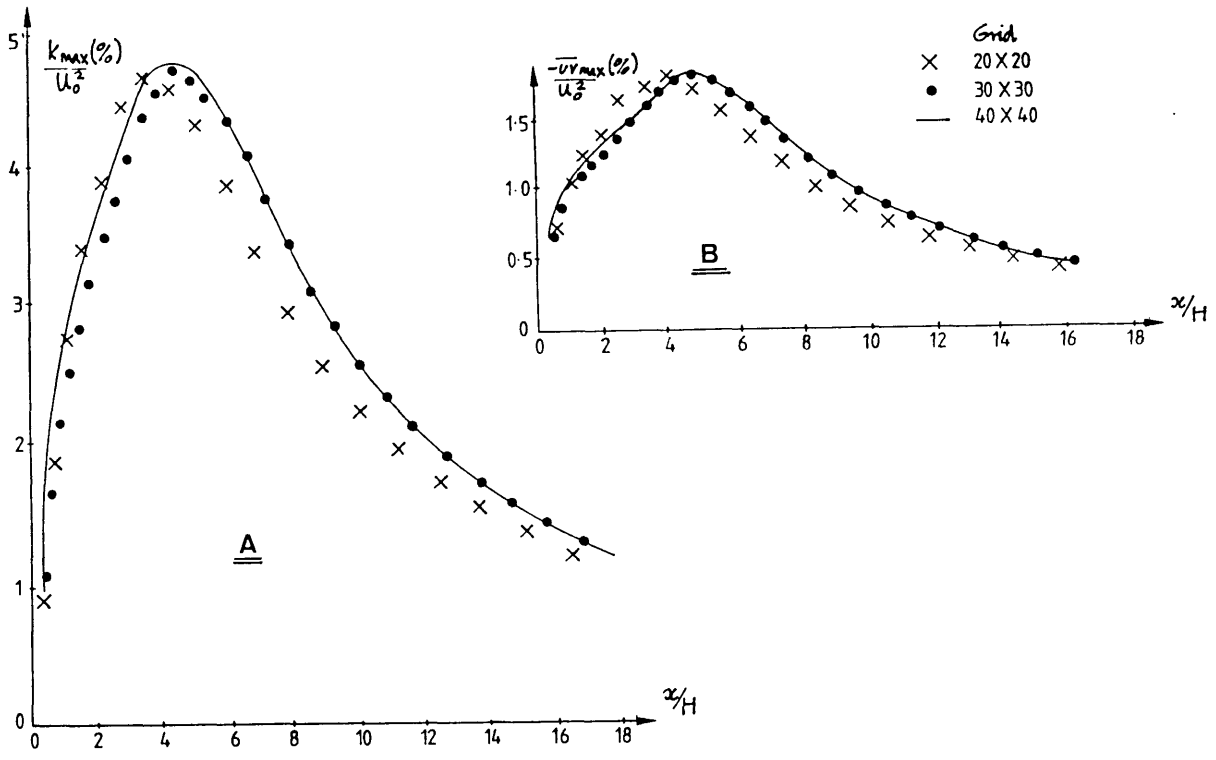


FIGURE 3.4 : Grid independence checks RST predictions, Step-problem.
(A): Maximum cross-sectional turbulence energy
(B): Maximum cross-sectional shear stress

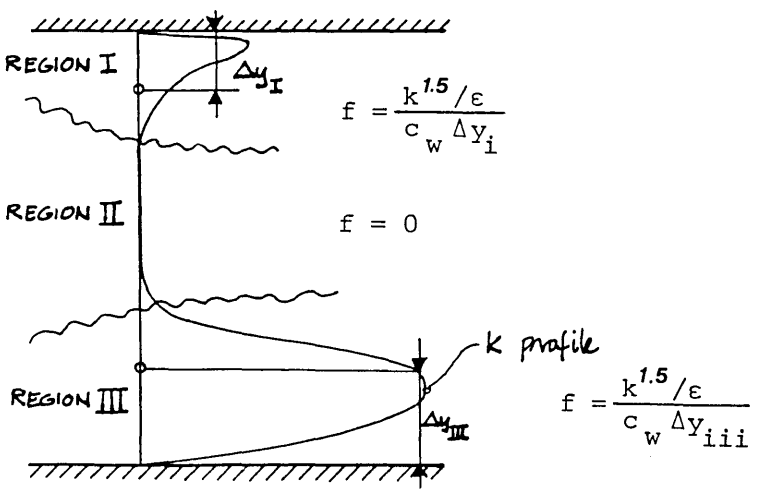


FIGURE 3.5 : Plane single-sided step. Definition of the wall effects function f.

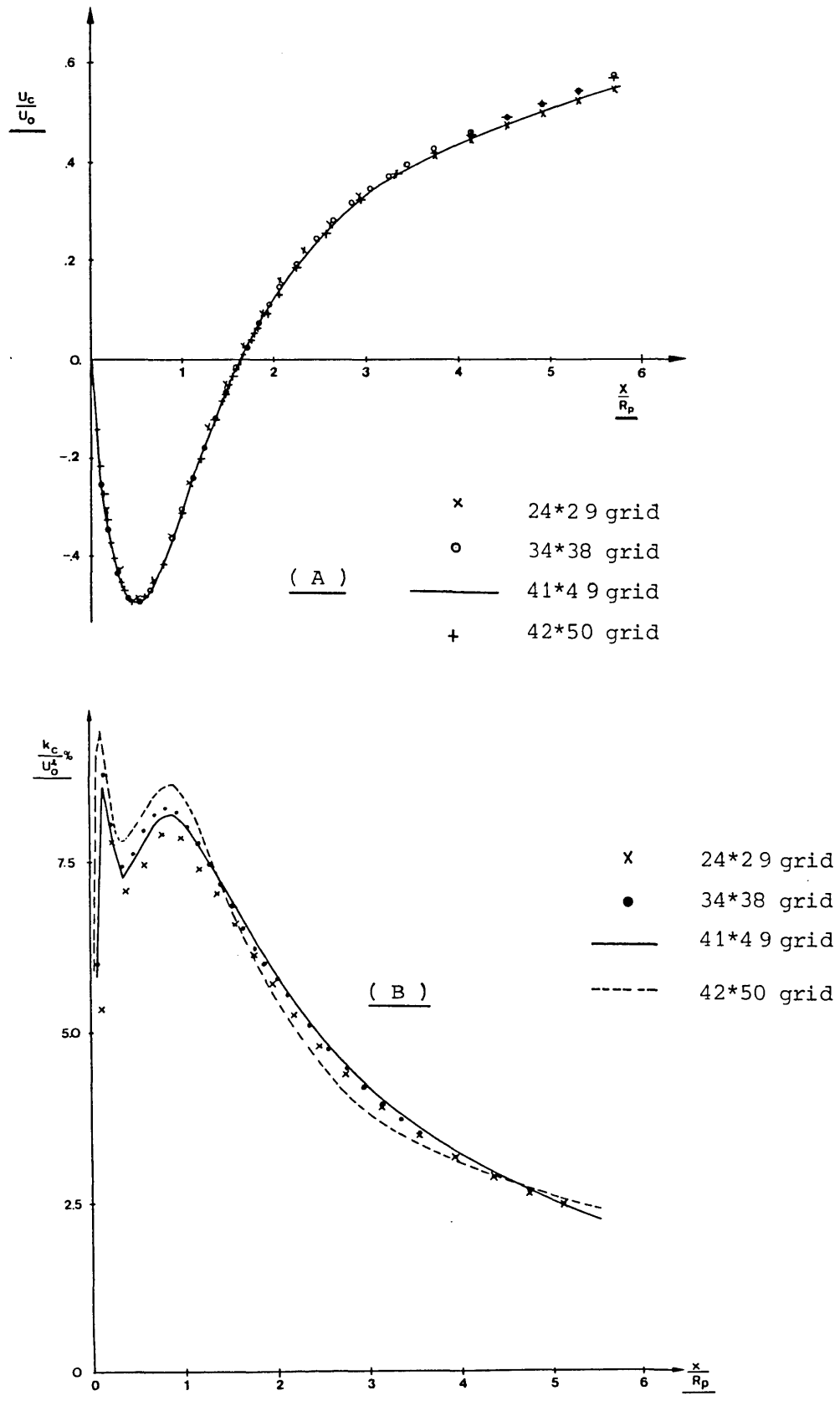


FIGURE 3.6 : Grid-independence checks, k-ε predictions, disc-flow.
(A) : Centreline velocity
(B) : Centreline turbulence energy

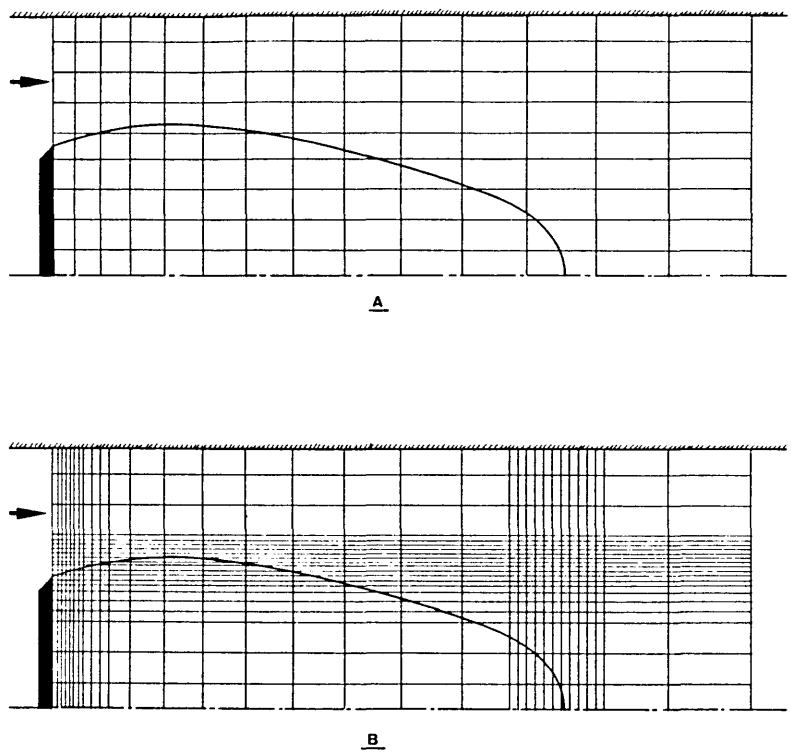


FIGURE 3.7 : Disc-flow, selective refinement of the grid from the (24*29) level to the (42*50) level. (sketch)

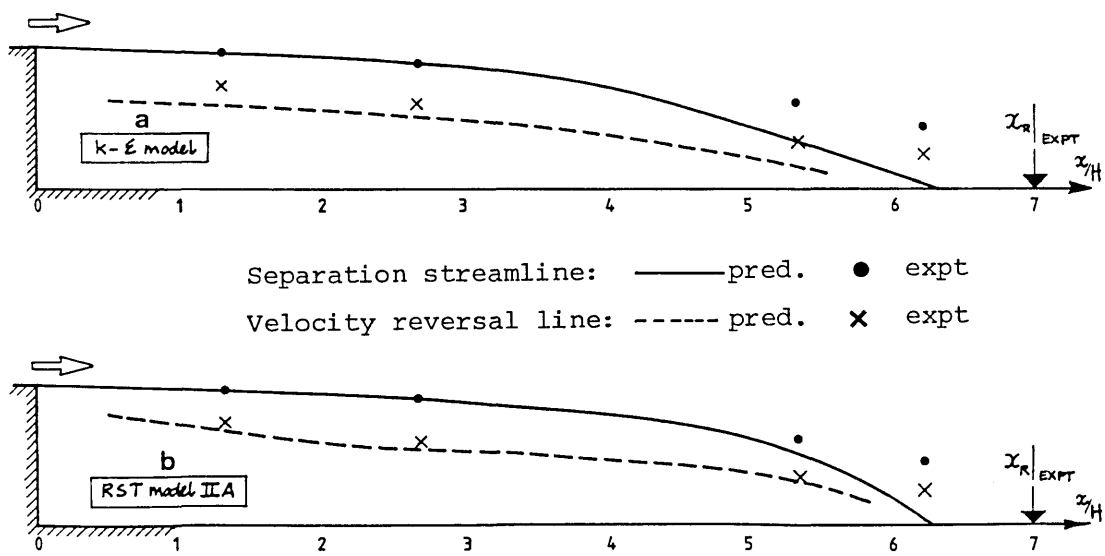


FIGURE 3.8 : Recirculation zone, step-flow.

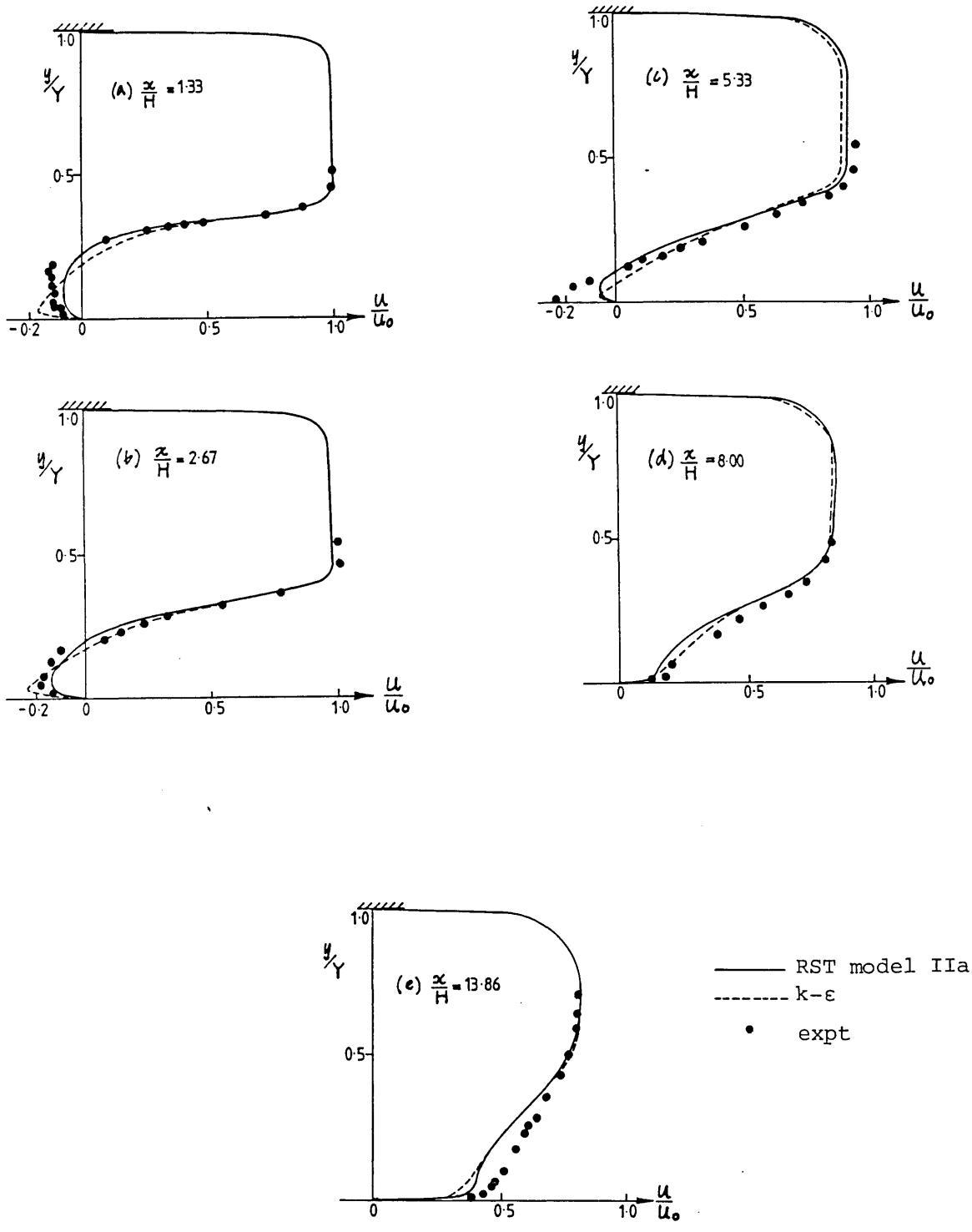


FIGURE 3.9 : Axial velocity profiles, step-flow.

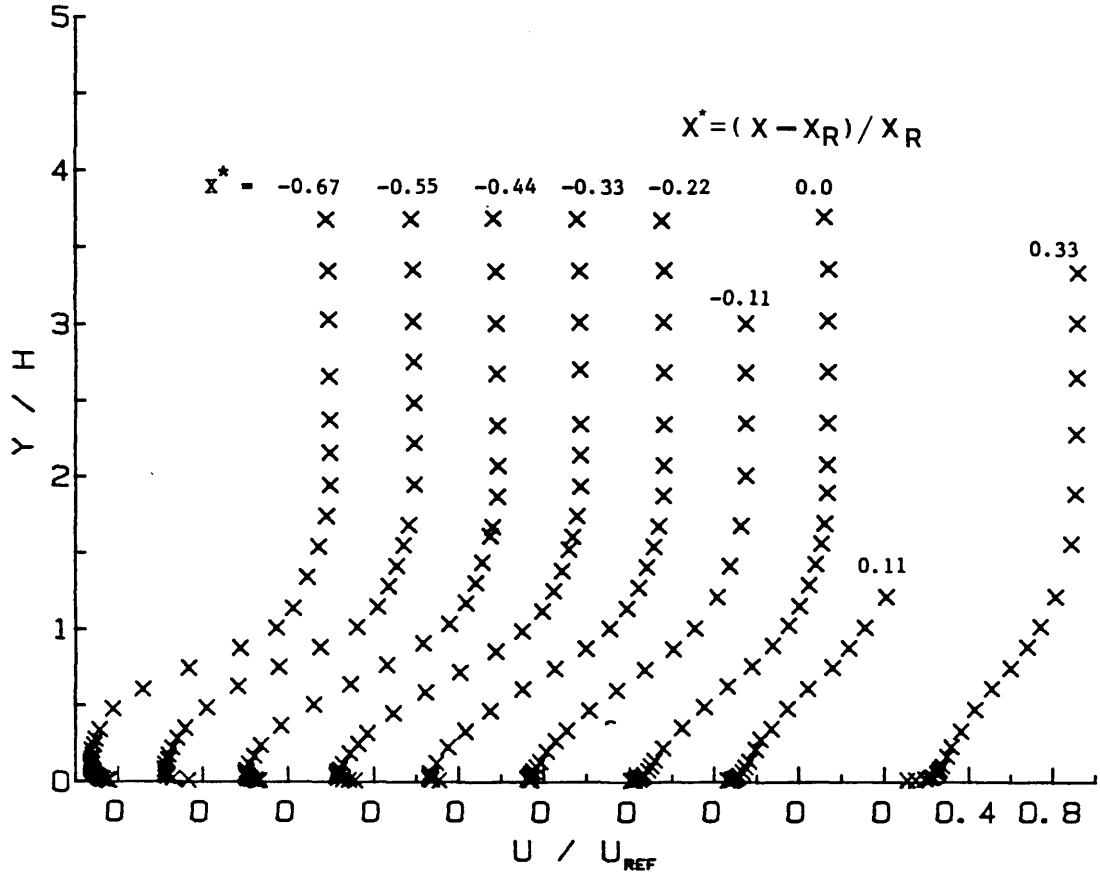


FIGURE 3.10 : Experimental data of Pronchick et al (1983). Longitudinal velocity profiles before and past reattachment. (x_R is the reattachment length)

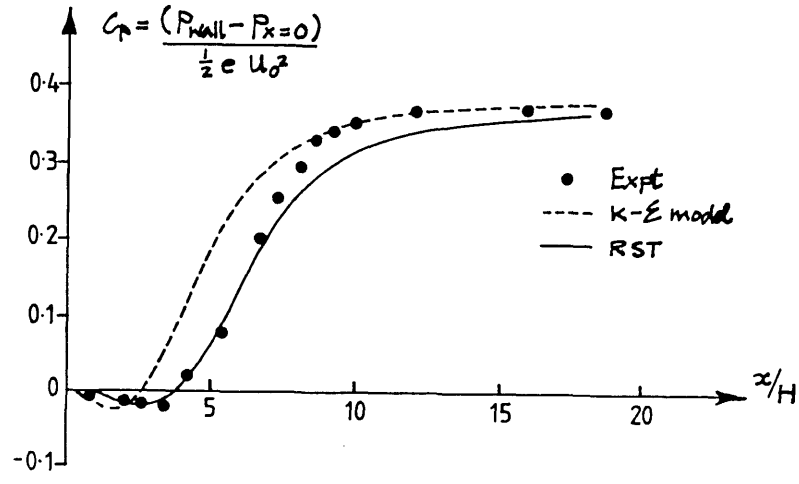


FIGURE 3.11 : Static pressure coefficient at the expansion wall of the channel.

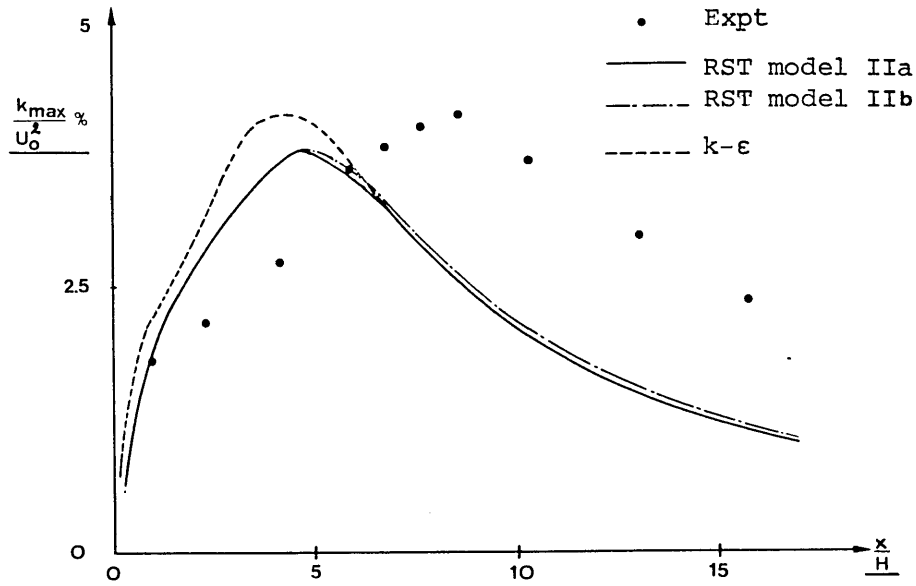


FIGURE 3.12 : Cross-sectional maximum of turbulence kinetic energy (Step-flow)

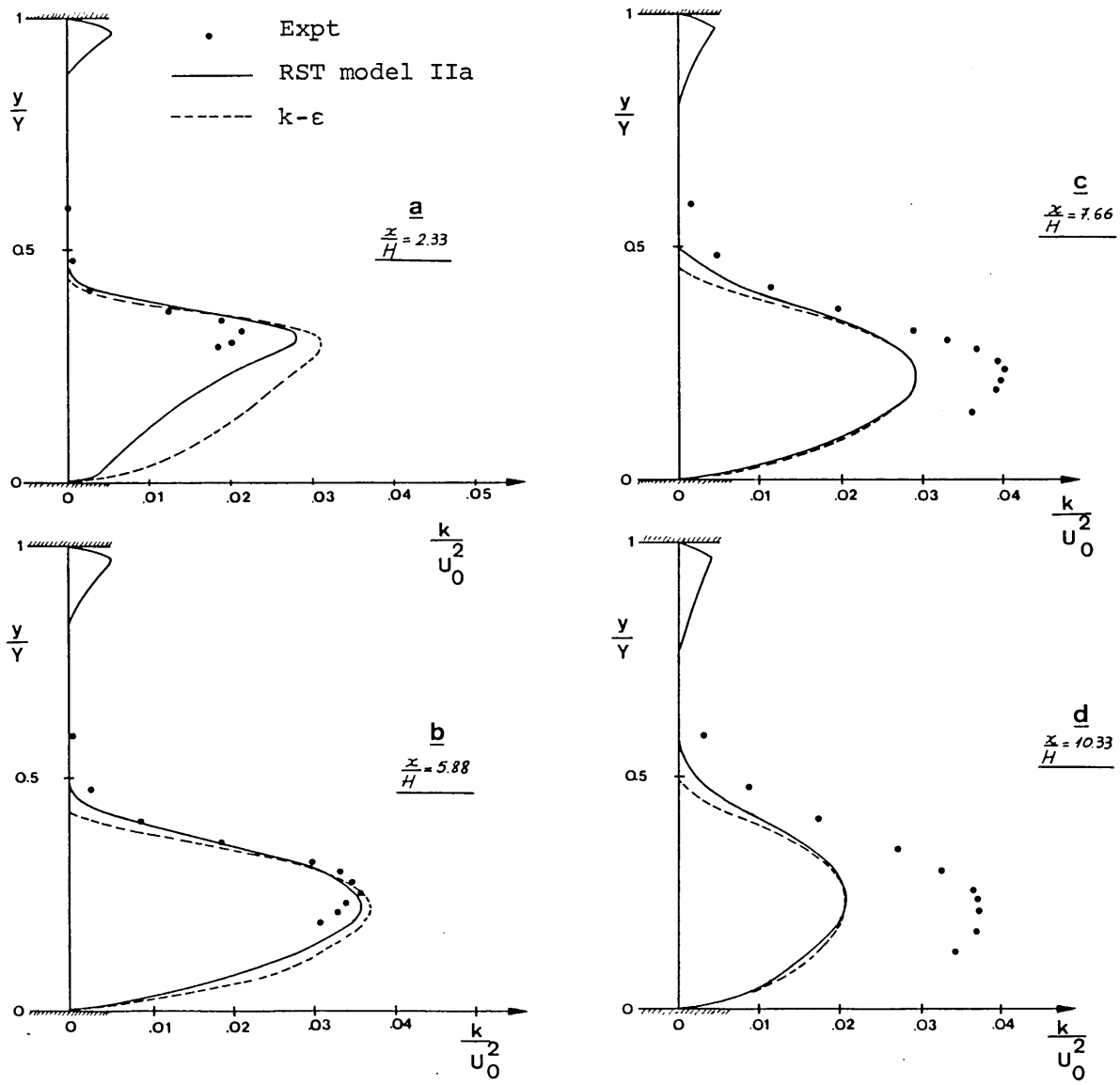


FIGURE 3.13 : Turbulence kinetic energy profiles, step-flow.

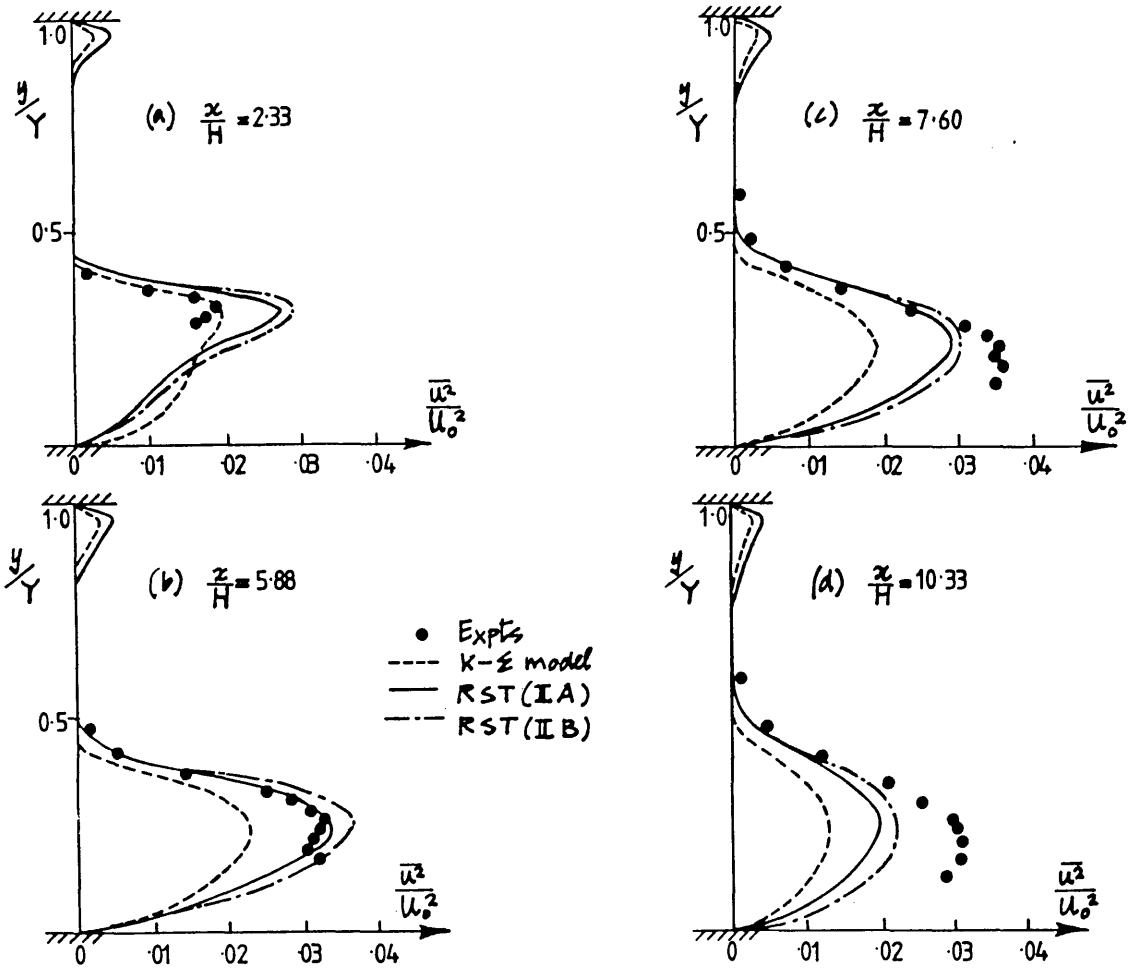


FIGURE 3.14 : Axial normal Reynolds stress ($\overline{u^2}$) profiles, Step-flow.

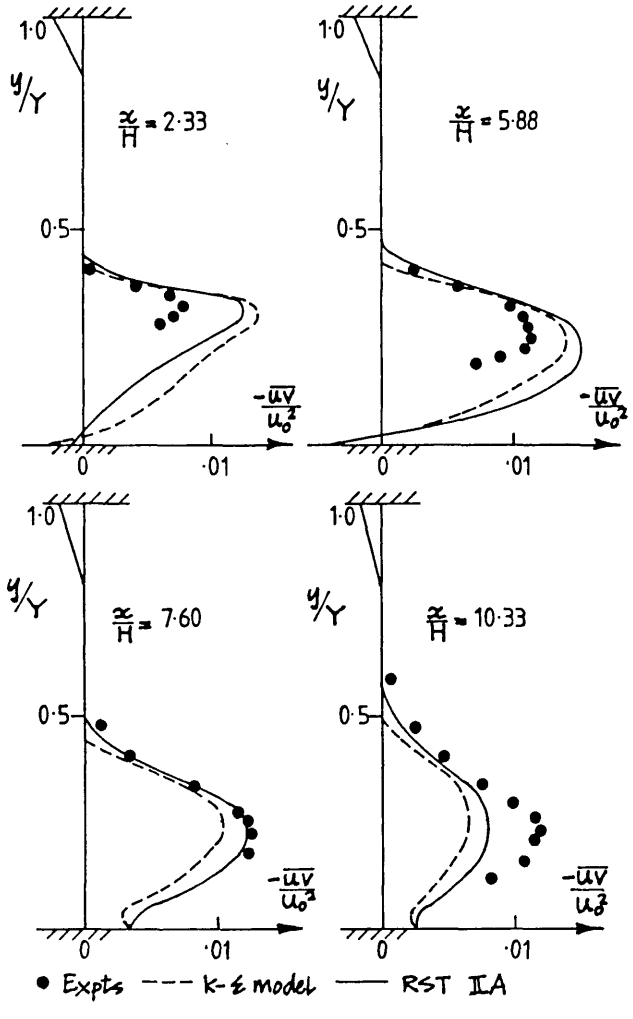


FIGURE 3.15 : Shear stress profiles, Step-flow.

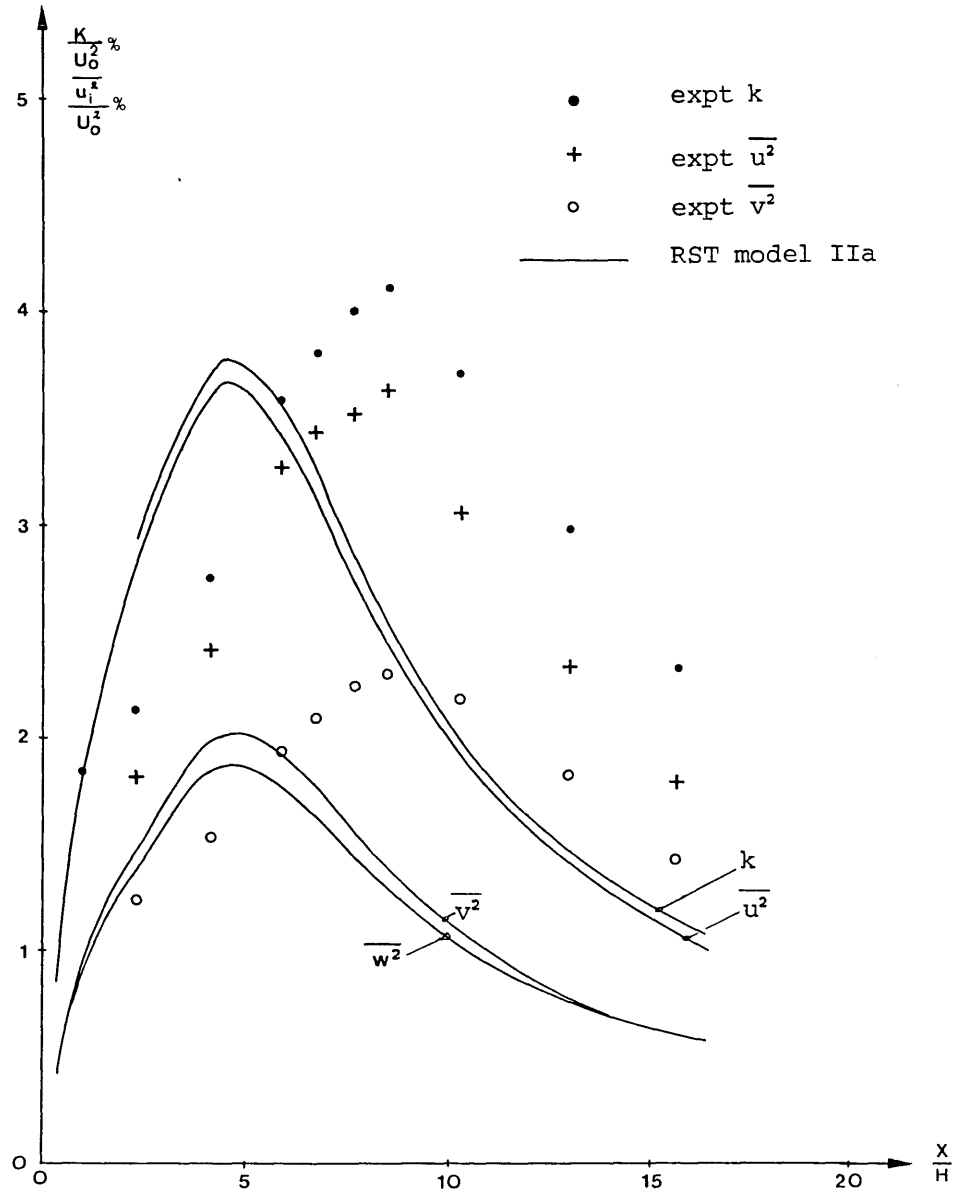


FIGURE 3.16 : Cross-sectional maxima of $\overline{u^2}$, $\overline{v^2}$, $\overline{w^2}$ and k. Step-flow.

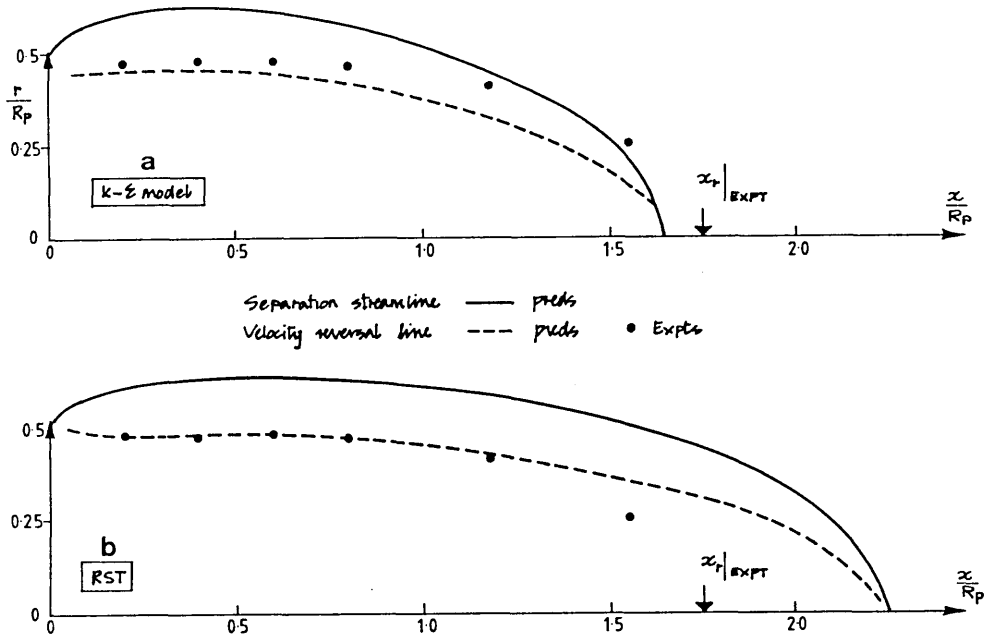


FIGURE 3.17: Recirculation zone, disc-flow.

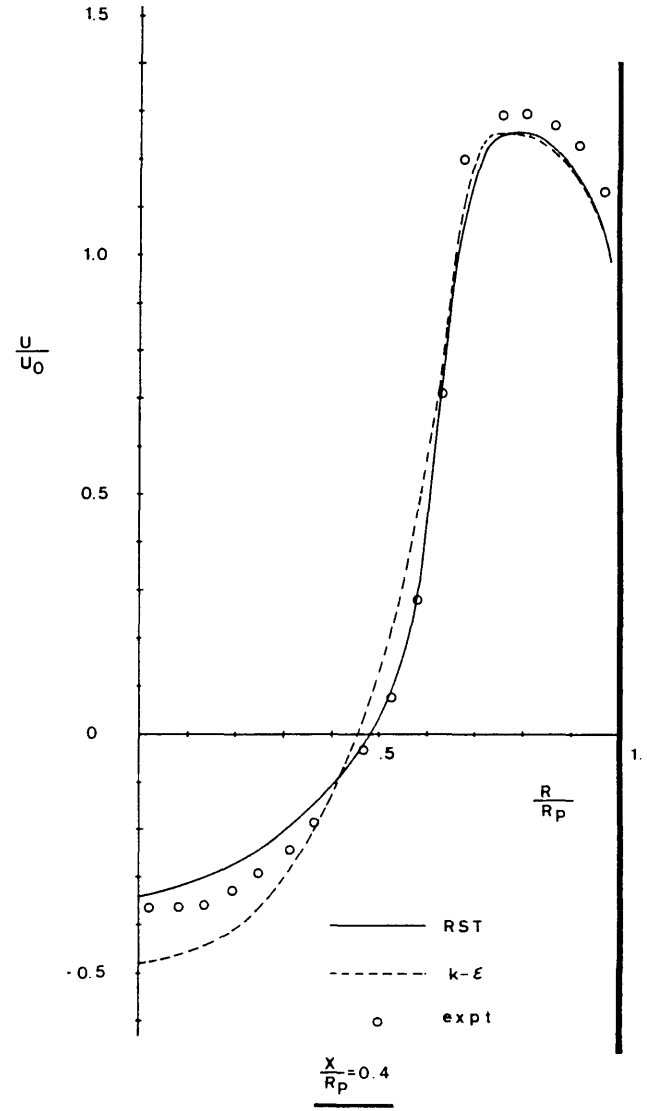


FIGURE 3.18 : Axial velocity profile at x/Rp=0.4, disc-flow.

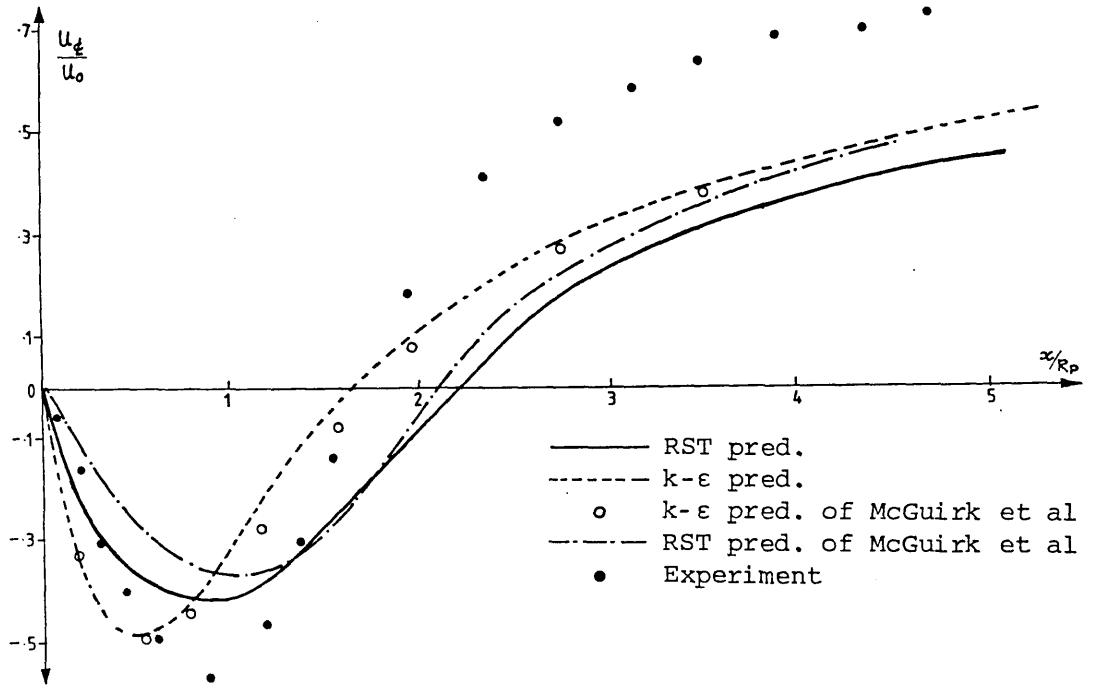


FIGURE 3.19 : Centreline velocity development, disc-flow.

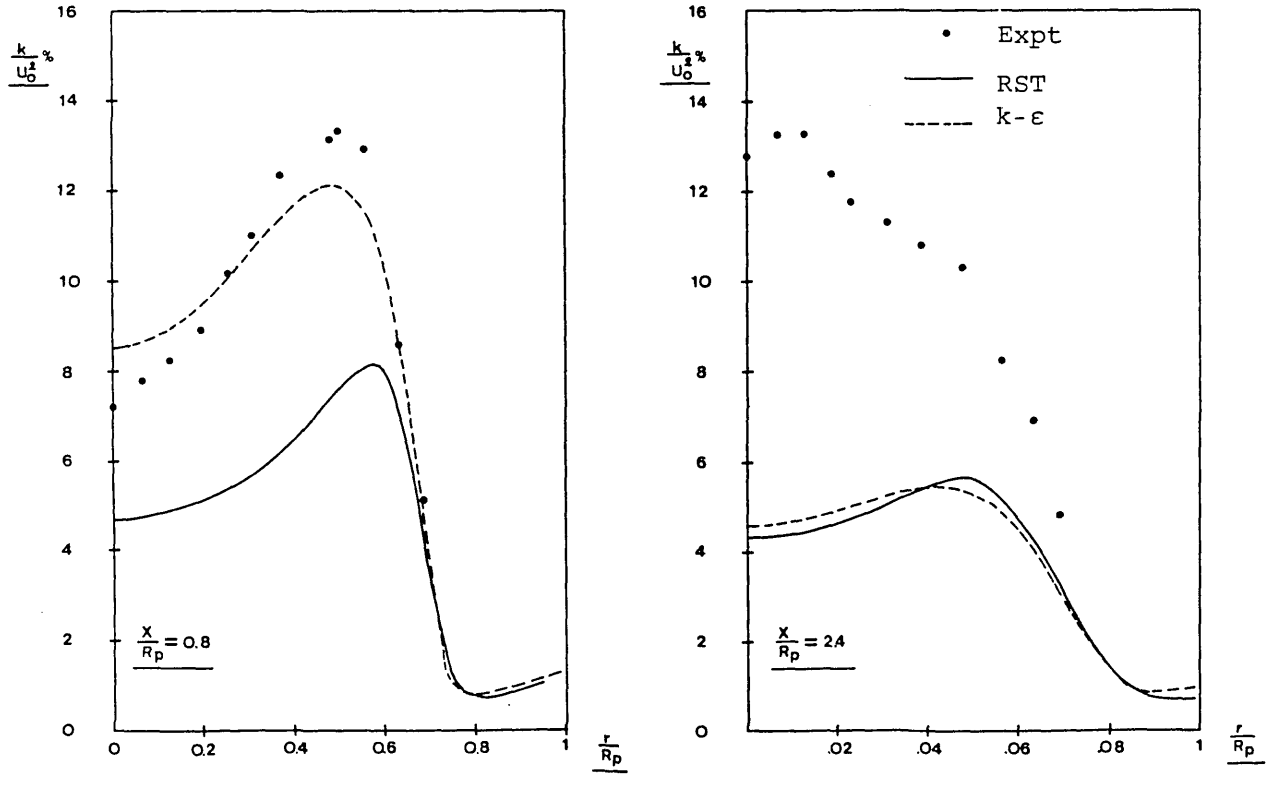


FIGURE 3.20 : Turbulence kinetic energy profiles, disc-flow.

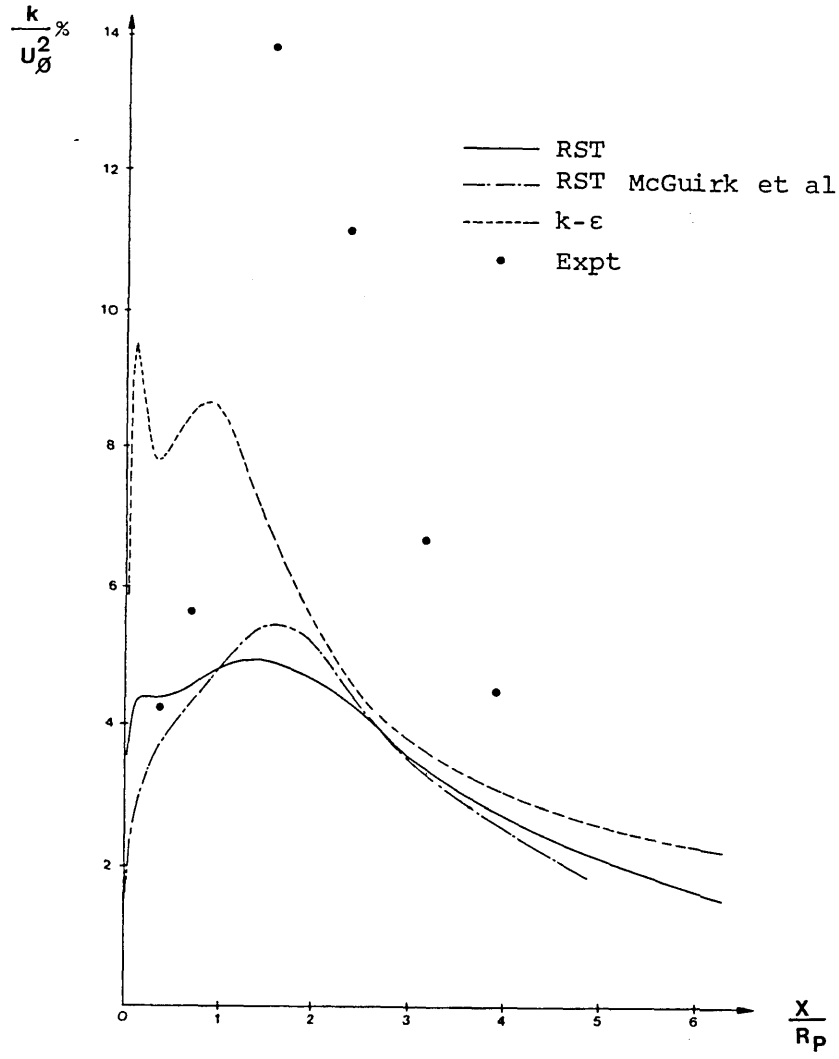


FIGURE 3.21 : Centreline turbulence kinetic energy, disc-flow.

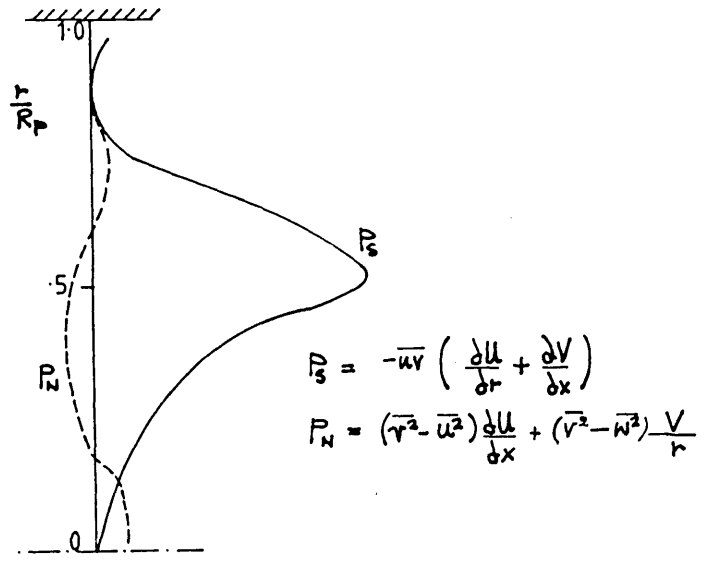
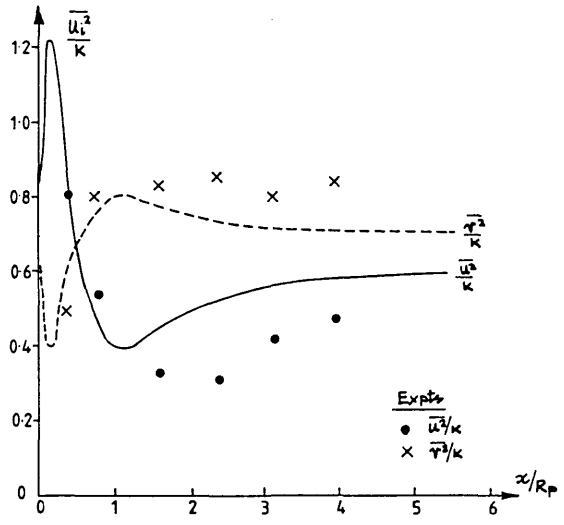
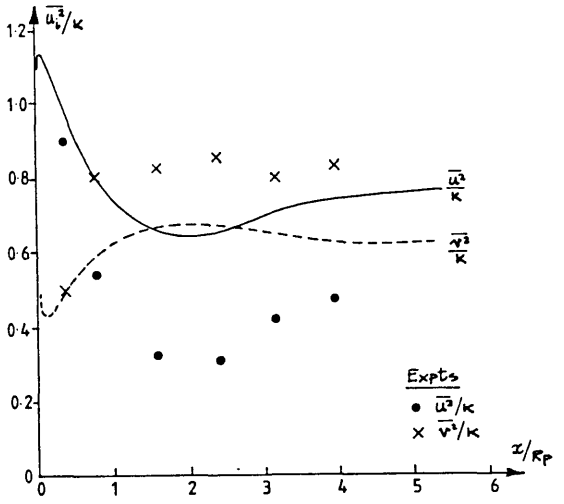


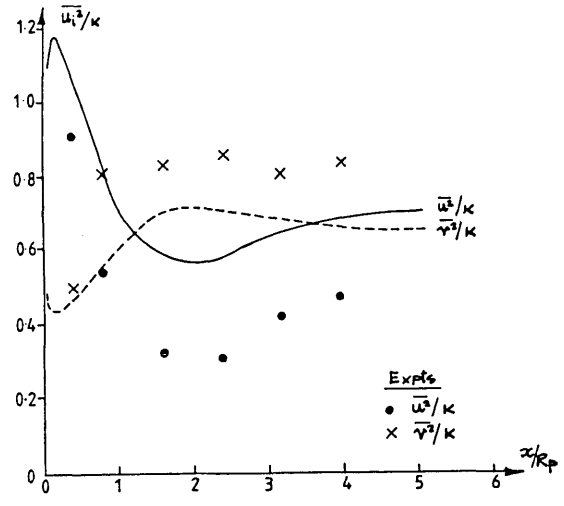
FIGURE 3.22 : Normal (P_N) and shear stress (P_S) contribution to the production of turbulence kinetic energy at a cross section close to the stagnation point.



k-ε model



RST model



RST model, McGuirk et al.
(complex form of Π_{ij})

FIGURE 3.23 : Turbulence anisotropy along the axis of symmetry.
Disc-Flow.

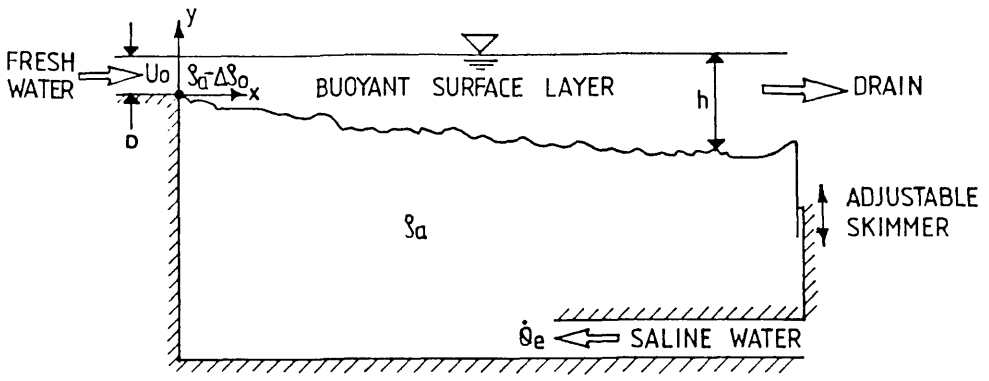


FIGURE 4.1 : Sketch of the experimental apparatus. Experiments of Chu and Baddour (1984).

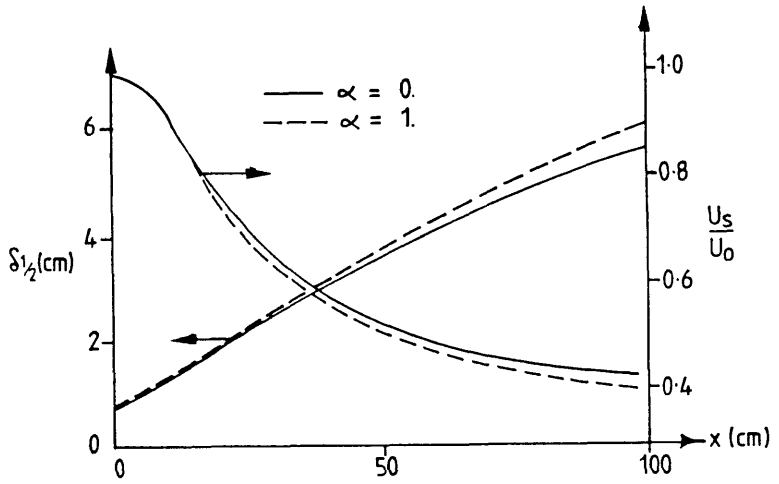


FIGURE 4.2 : Parametric study of the form of the production term in the dissipation rate equation. (Surface jet , Fd= 12)

$$\lambda_1 = \frac{\int U\, B\, dy}{U_0 B_0 D}$$

$$\lambda_2 = \frac{\int U^2\, dy + \int P\, dy}{U_0^2\, D + D^2\, B_0/2}$$

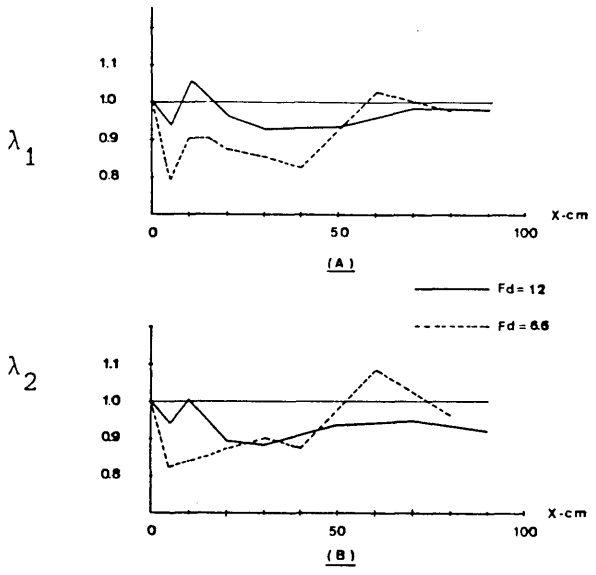


FIGURE 4.3 : Surface jet experiments of Chu and Baddour (1984). Experimental data compliance with the integral constraints of the flow.
(A) Salinity conservation
(B) Momentum conservation

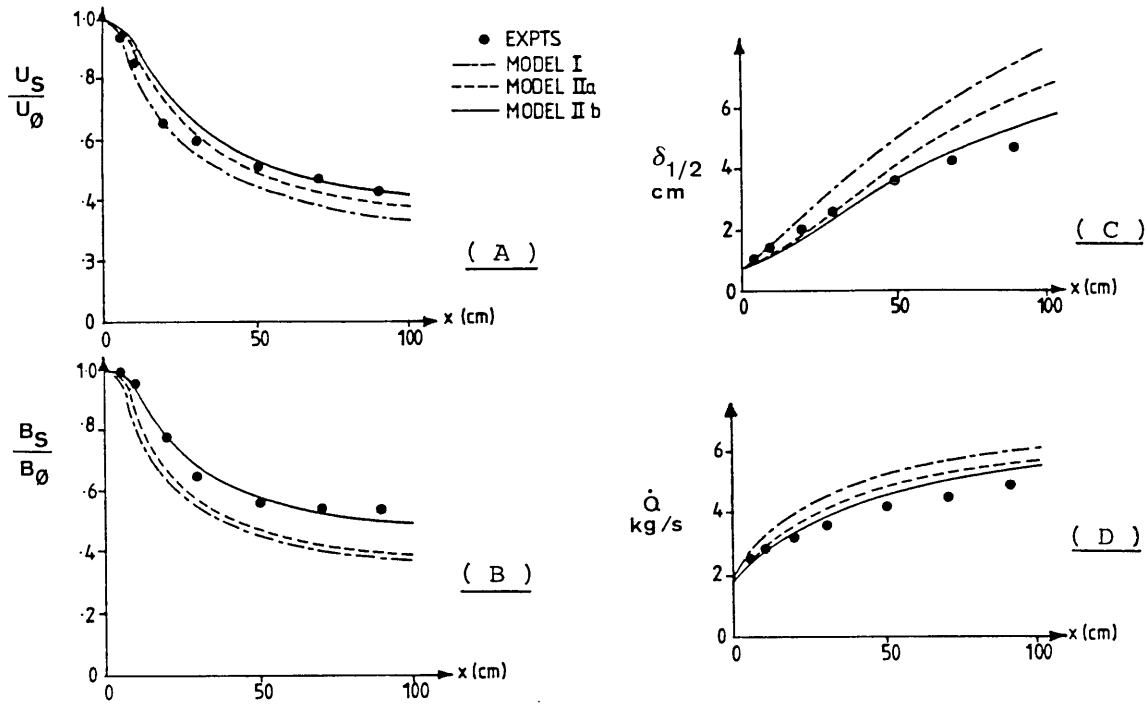


FIGURE 4.4 : Longitudinal development of the flow (Surface jet, F_d= 12). (A) Surface velocity, (B) Surface buoyancy, (C) Jet half-velocity width, (D) Mass flowrate in the layer.

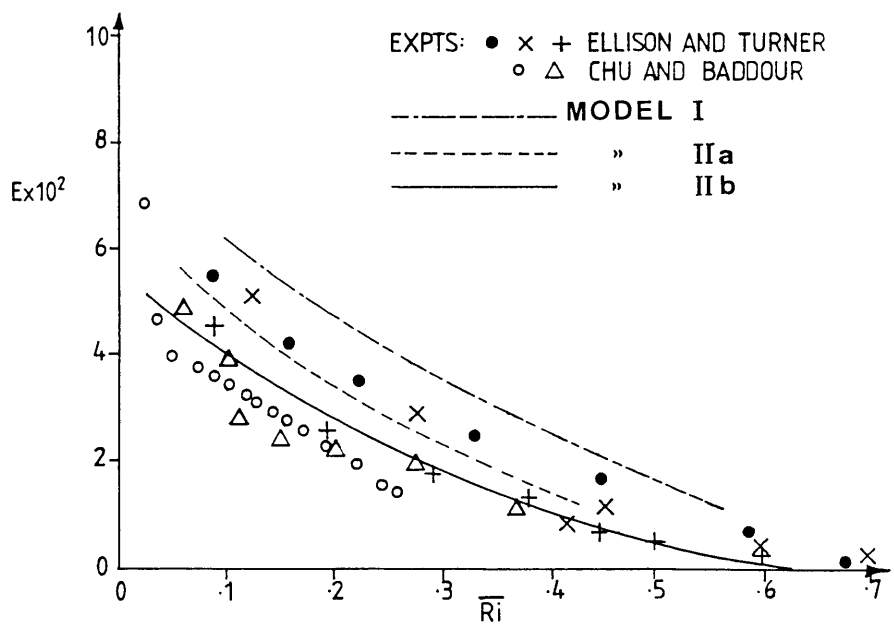


FIGURE 4.5 : Relation of the cross-sectional Richardson number with the entrainment coefficient. Surface jet , F_d= 12.

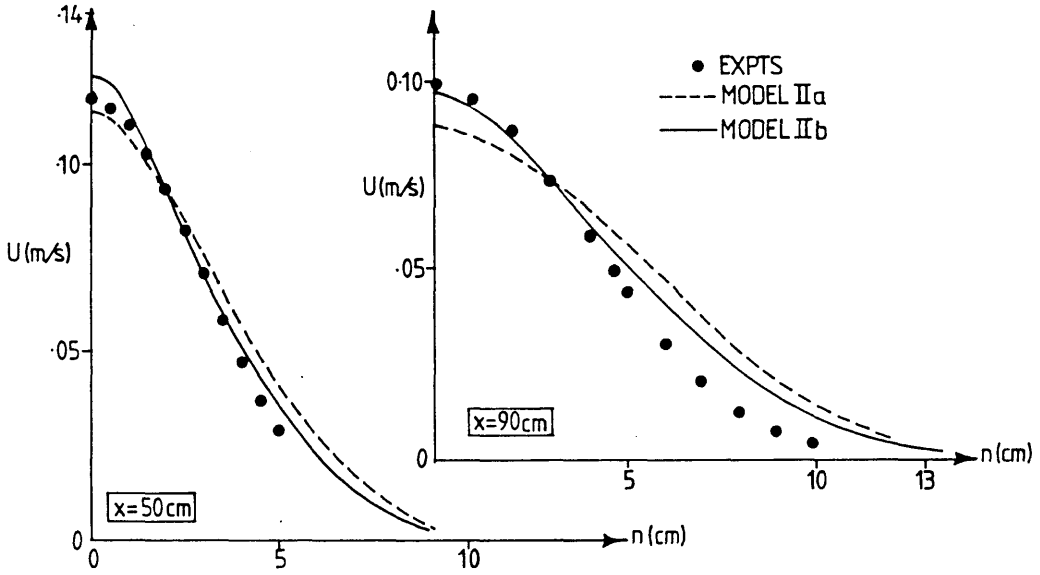


FIGURE 4.6 : Velocity profiles (Surface jet, F_d= 12)

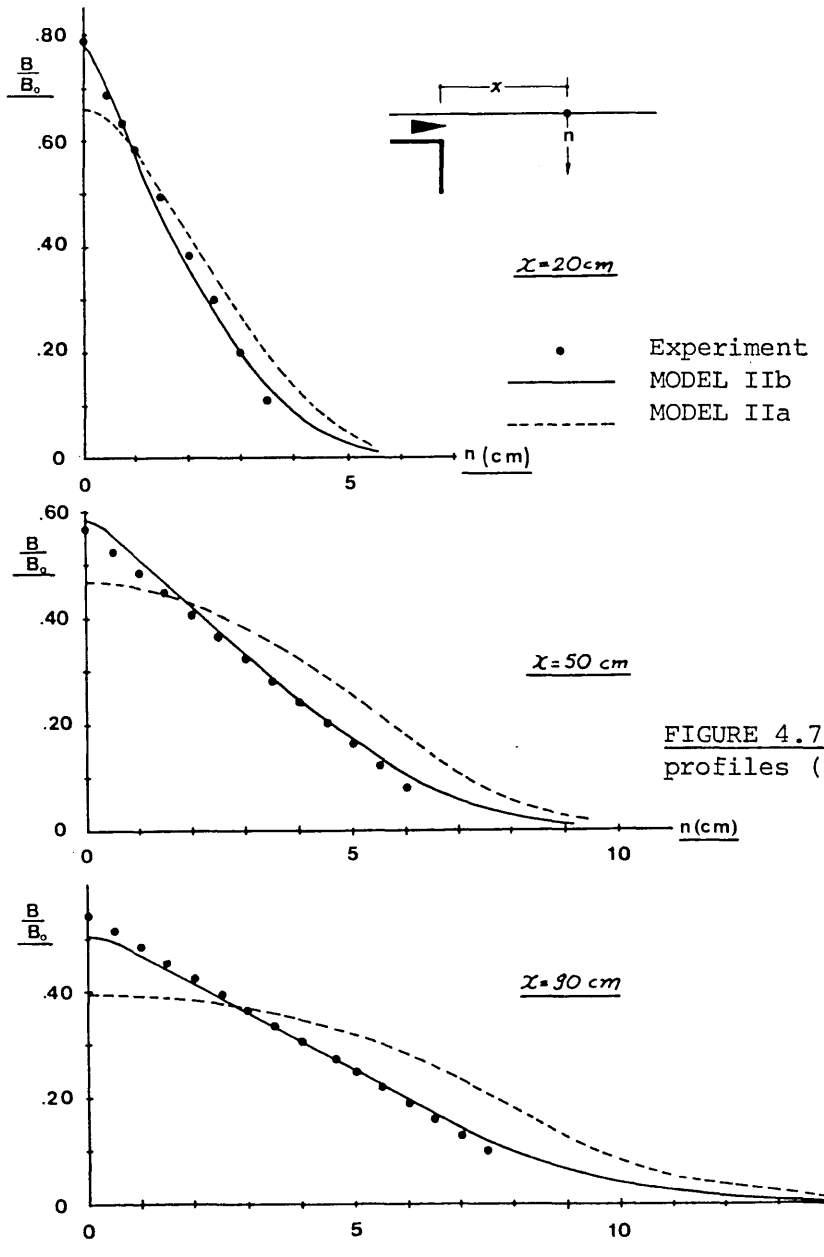


FIGURE 4.7 : Mean buoyancy profiles (Surface jet F_d= 12)

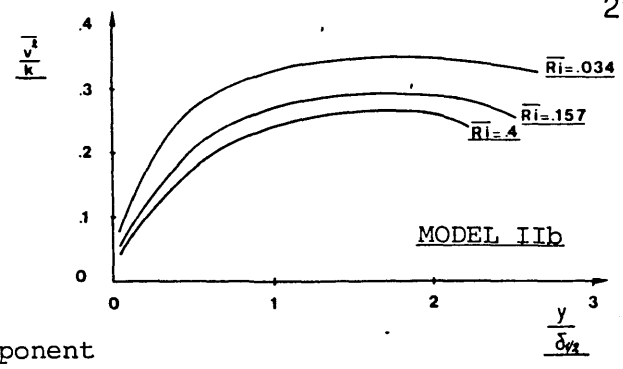
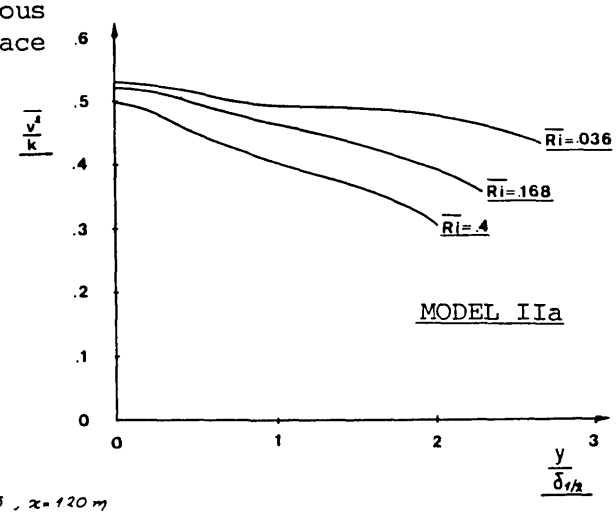


FIGURE 4.8 : Vertical component ($\overline{v^2}/k$) profiles for various Richardson numbers. (Surface jet , F_d= 12).



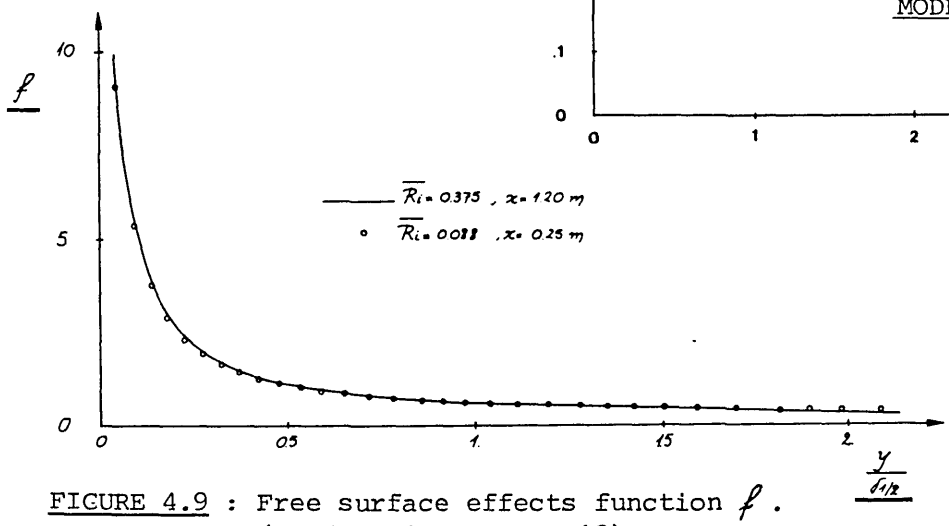


FIGURE 4.9 : Free surface effects function f . (surface jet , F_d = 12)

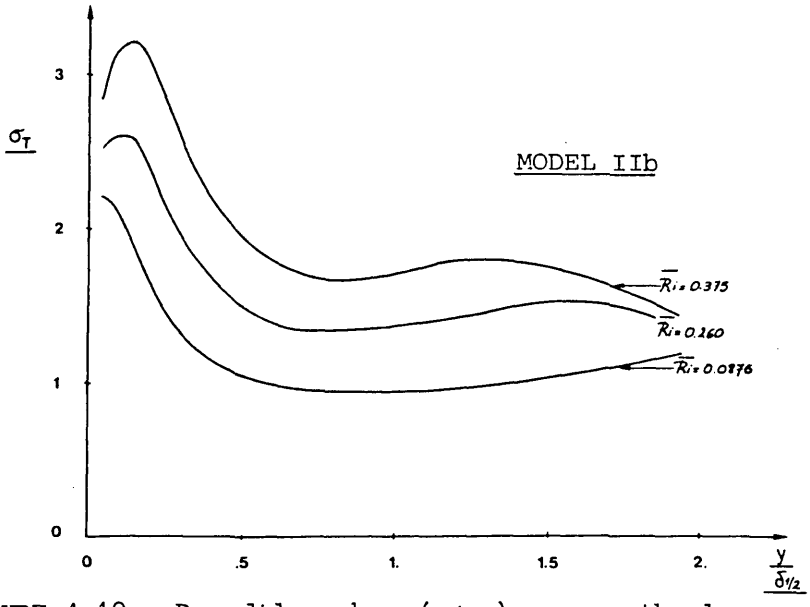
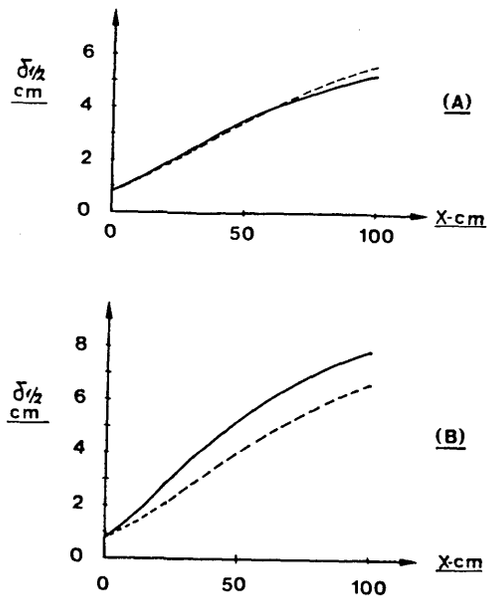


FIGURE 4.10 : Prandtl number (σ_T) across the layer (Surface jet , F_d = 12).



——— buoyancy based layer width
------- velocity based layer width

FIGURE 4.11 : Layer width (Surface jet, F_d= 12). (A) MODEL IIb
(B) MODEL IIa

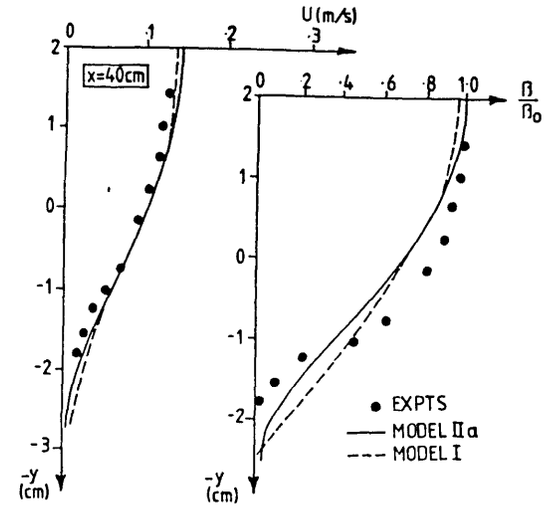
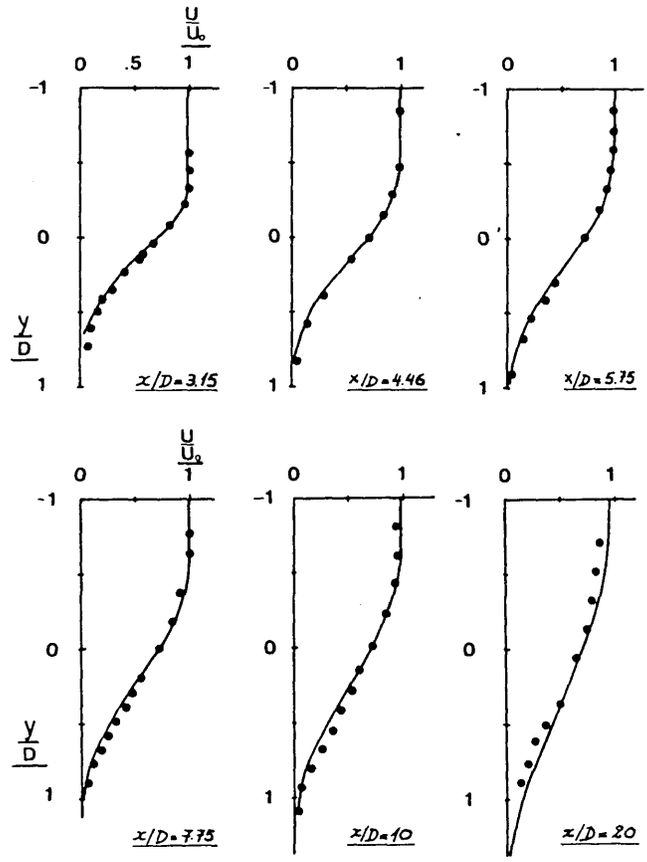


FIGURE 4.12

Comparison between k-ε and RSFT predictions (Mixing-layer, F_d= 2.3).



——— Predictions , MODEL IIa

• Experiment

FIGURE 4.13 : Velocity profiles (Mixing-layer, F_d= 2.3)

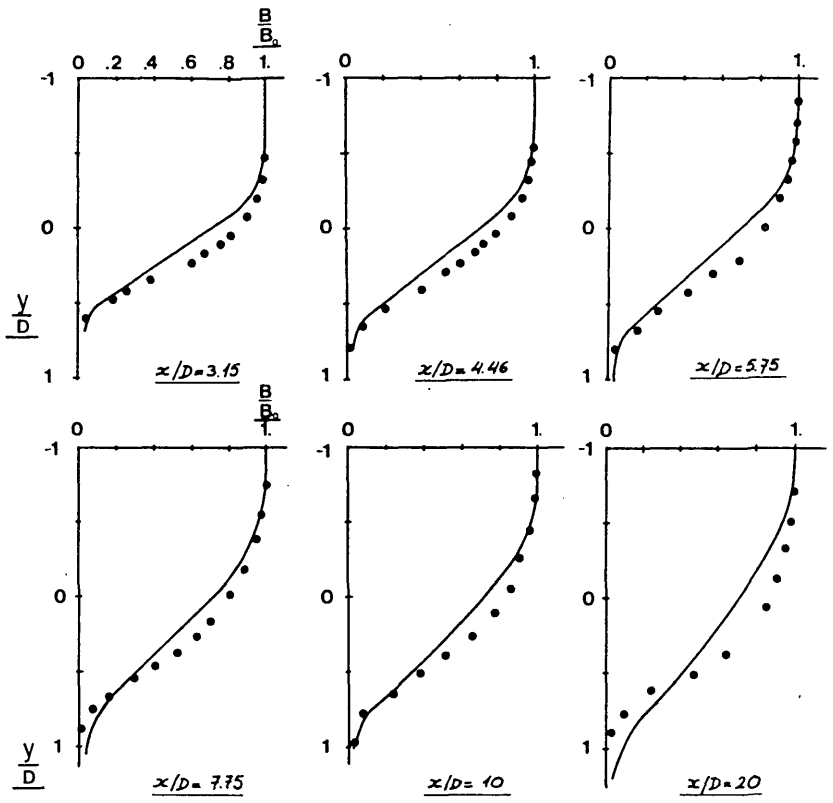


FIGURE 4.14 : Mean buoyancy profiles (Mixing-layer , F_d= 2.3)

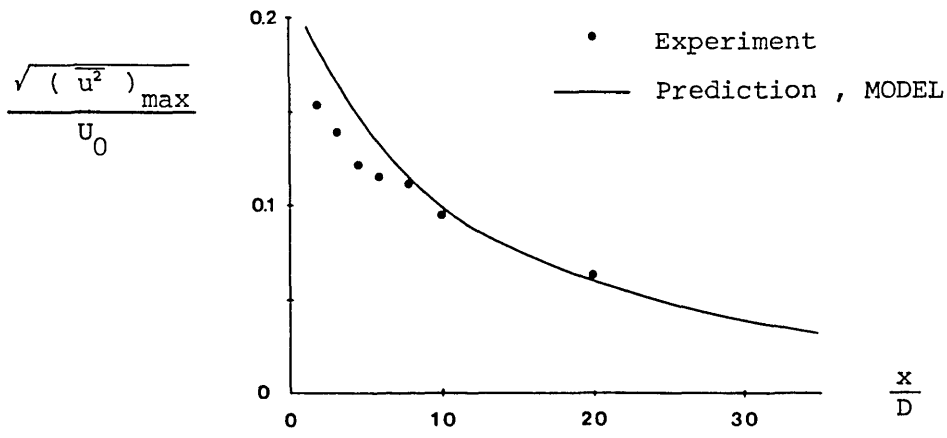


FIGURE 4.15 : Longitudinal development of the cross-sectional peak value of $\overline{u^2}$ (Mixing-layer, F_d= 2.3).

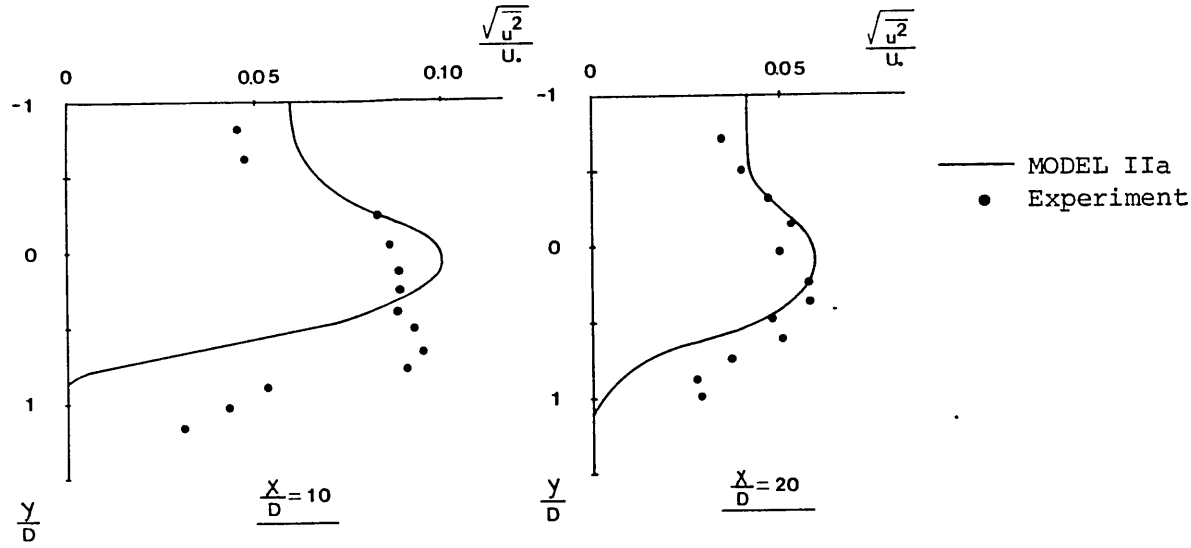
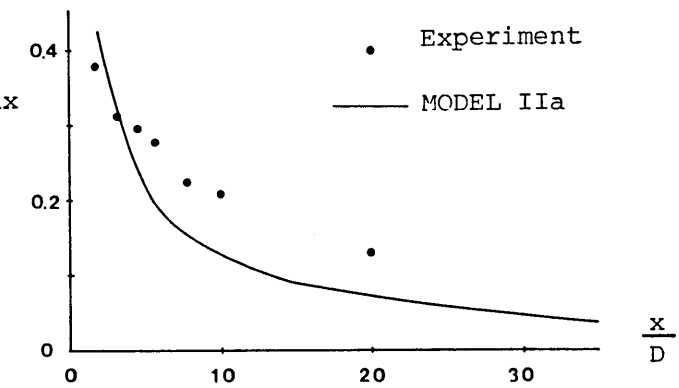


FIGURE 4.16 : Axial normal stress profiles (Mixing-layer F_d= 2.3).

FIGURE 4.17

Longitudinal development of the cross-sectional peak value of $\overline{b^2}$ (Mixing-layer F_d= 2.3).



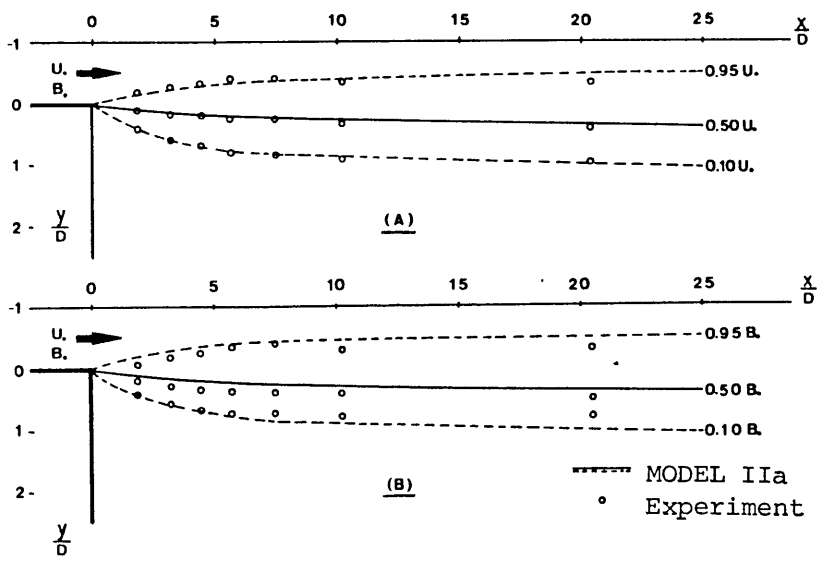


FIGURE 4.18 : Longitudinal layer development, Centreline and boundaries. (A) based on the velocity predictions, (B) based on the buoyancy predictions.

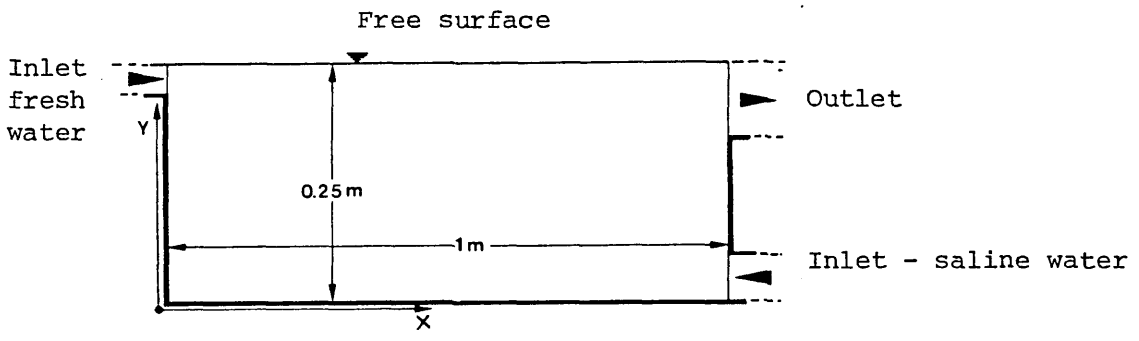


FIGURE 4.19 : Internal Hydraulic Jump , Solution domain and boundary conditions.

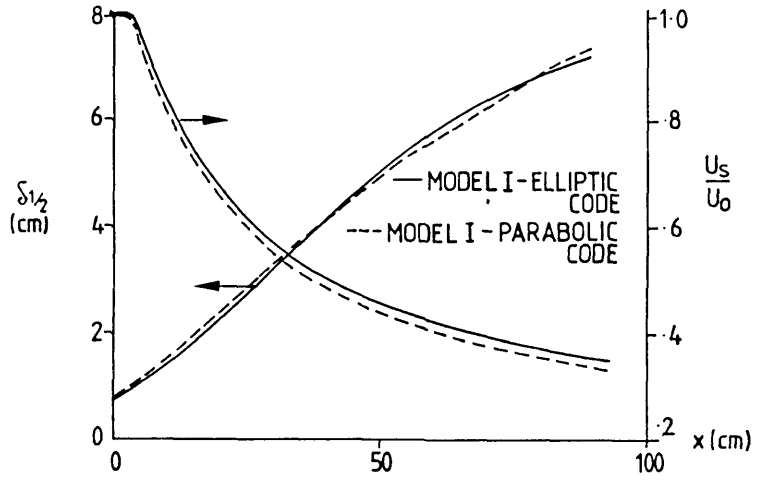


FIGURE 4.20 : Surface jet , F_d= 12.
Comparison of the prediction of two parameters using elliptic and parabolic codes. Surface velocity and jet half-velocity width.

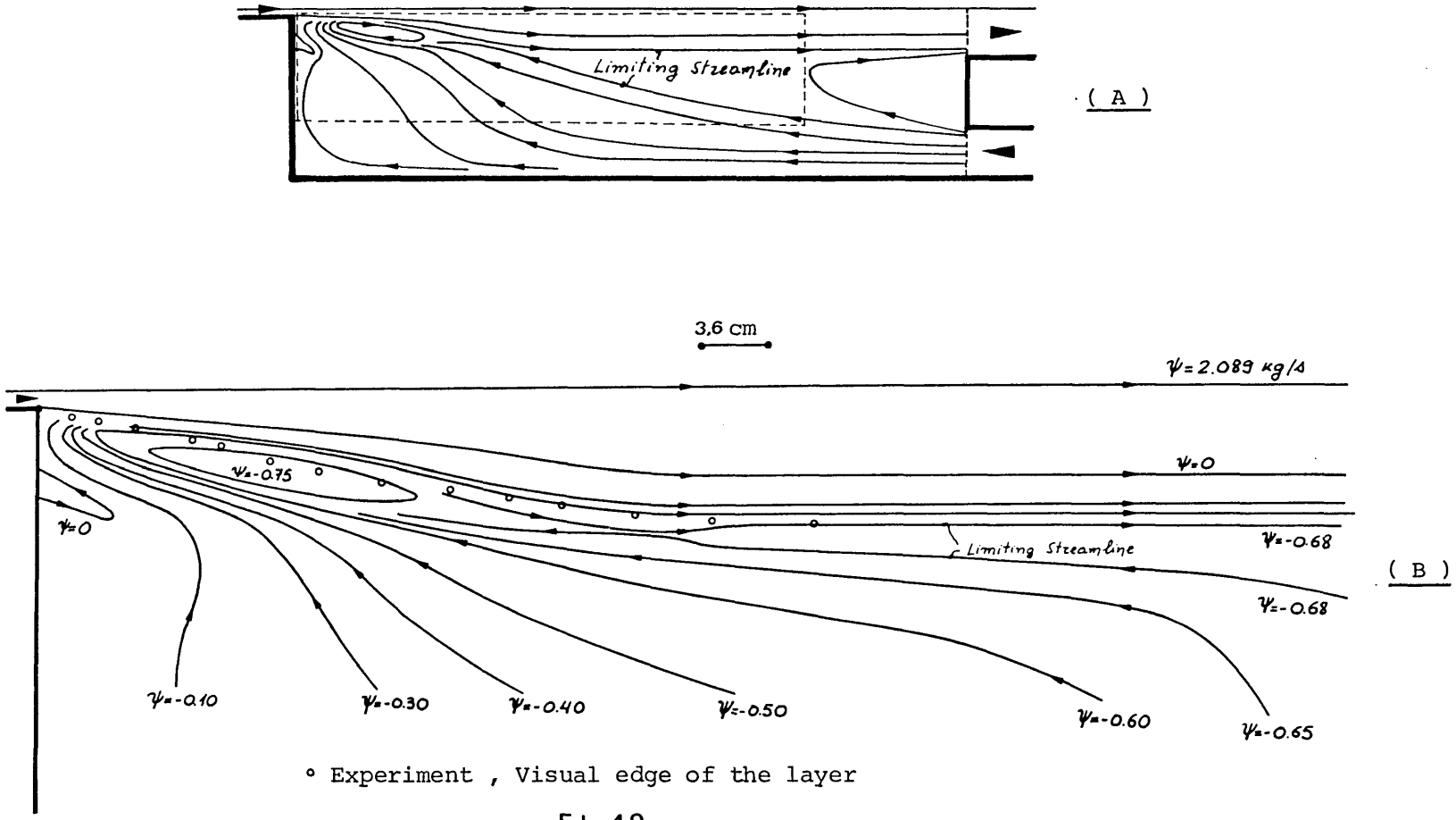


FIGURE 4.21 : Internal Hydraulic Jump, k-ε prediction. Streamline pattern.
(A) Sketch of the streamlines all over the solution domain.
(B) Predicted Streamlines. (Part of the domain enclosed by the dashed lines in the previous sketch).

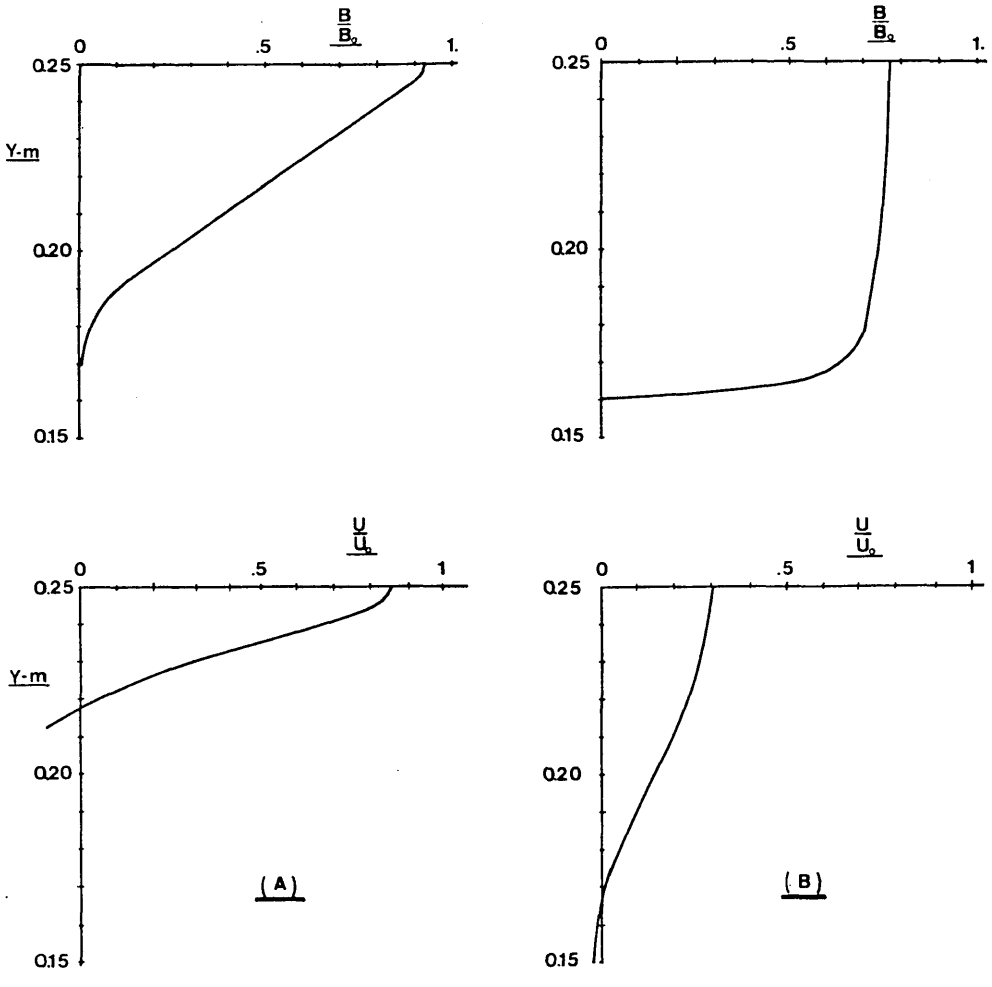


FIGURE 4.22 : Internal Hydraulic jump F_d= 4.9 , k-ε prediction. Velocity and mean buoyancy profiles.
(A) before the roller, x = 6 cm.
(B) after the roller, x = 50 cm.

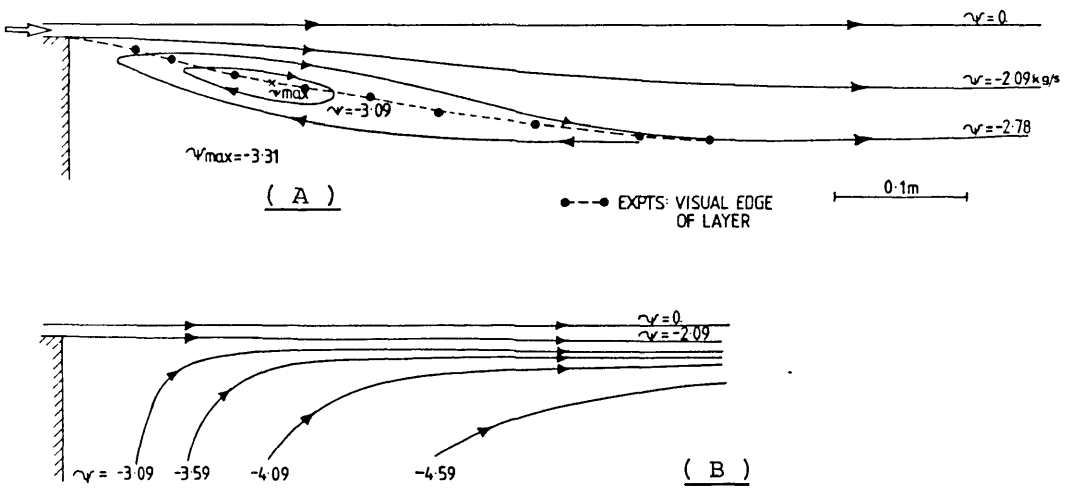


FIGURE 4.23 : The influence of the downstream control on the evolution of a buoyant surface layer.
F_d= 6.39 , k-ε prediction. (A) Internal Hydraulic Jump , (B) Fully entraining jet.

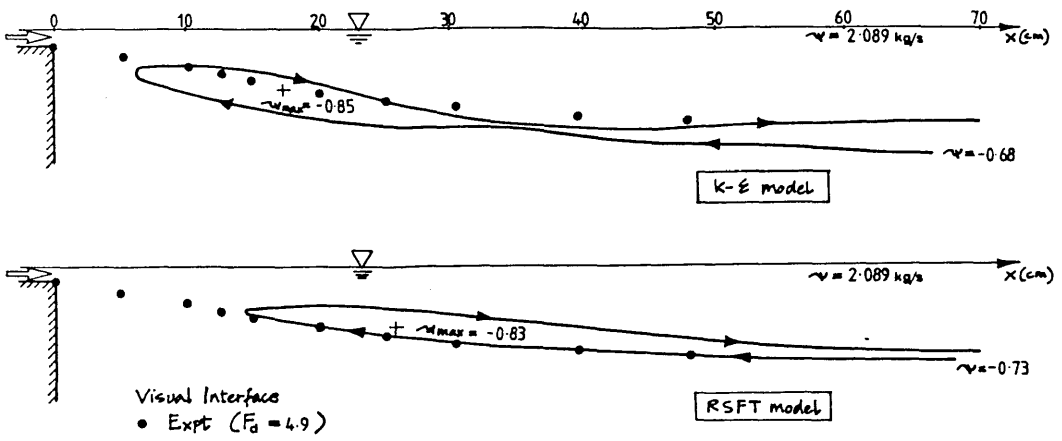


FIGURE 4.24 : Internal Hydraulic Jump , F_d= 4.9 . Location of the limiting streamline.

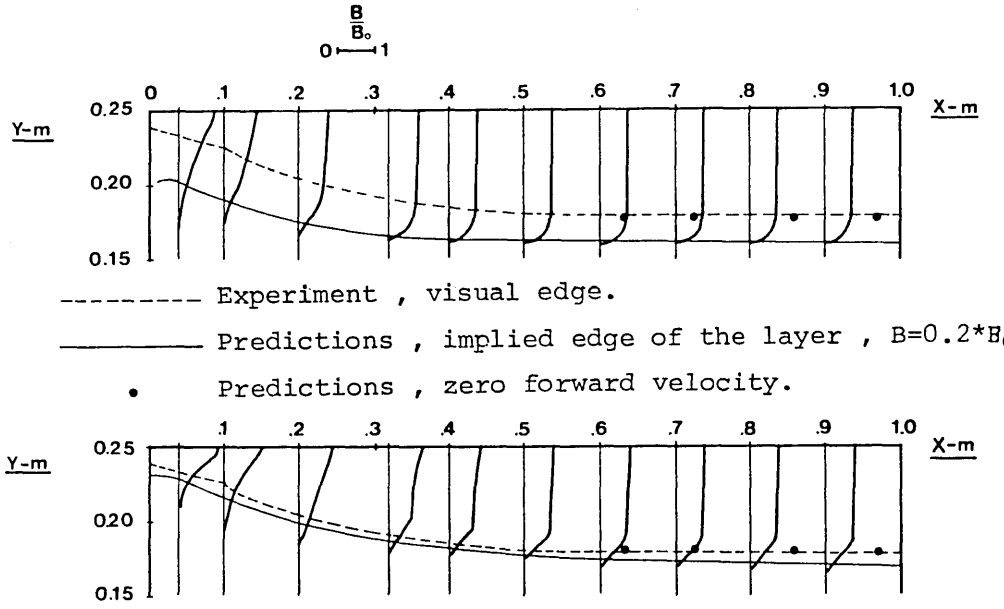


FIGURE 4.25 : Internal Hydraulic Jump , F_d= 4.9 . Mean buoyancy profiles and interface of the layer. (A) k-ε , (B) RSFT .

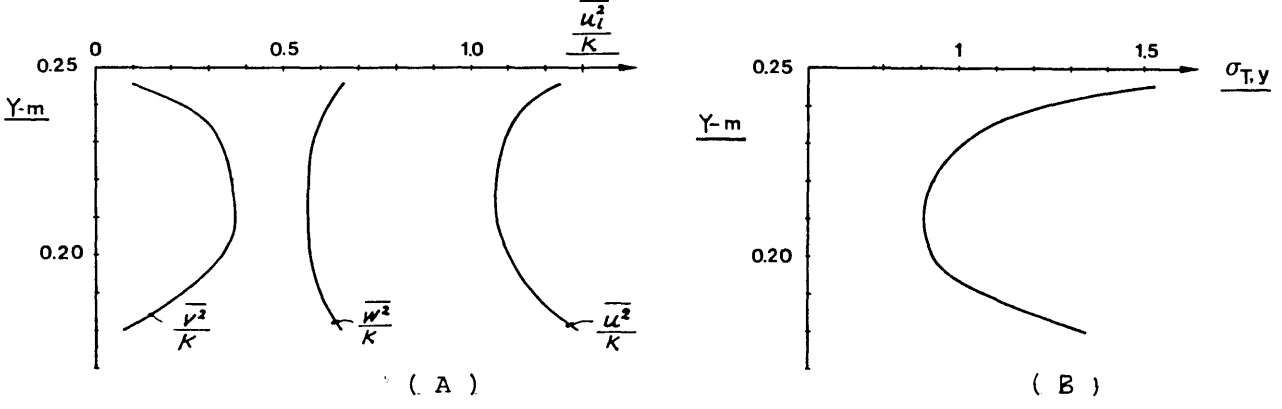
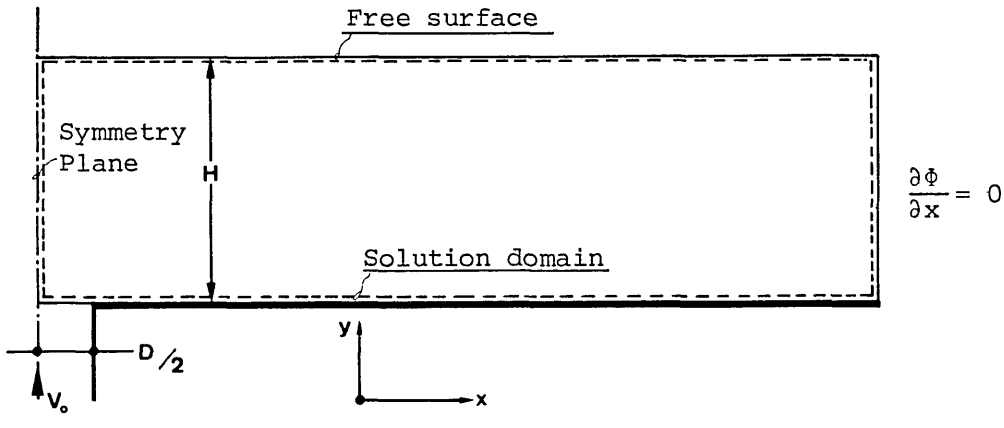


FIGURE 4.26 : Internal Hydraulic Jump , F_d= 4.9 . Turbulence anisotropy (A) and Prandtl number (B) across the layer.



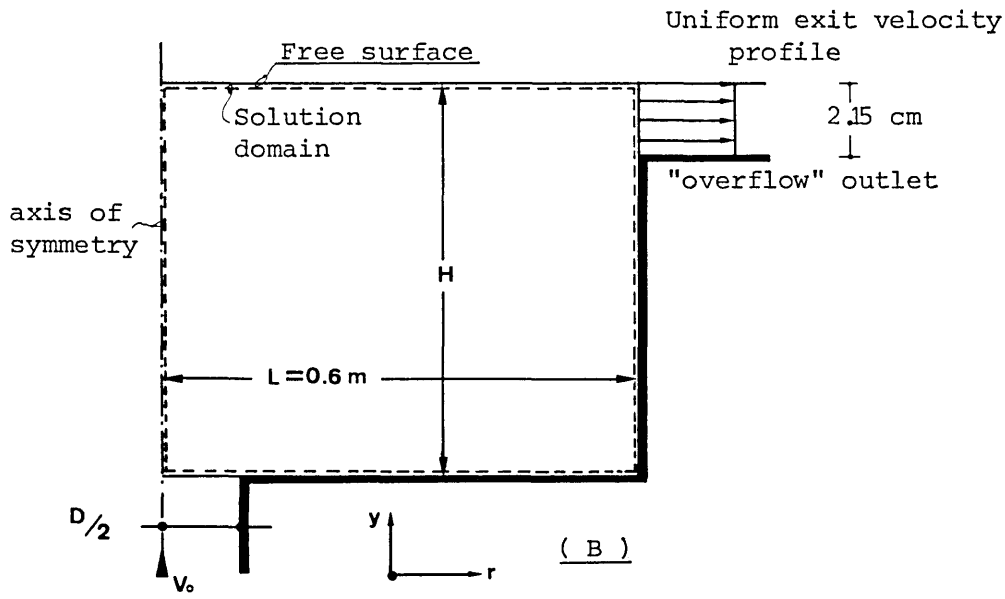


FIGURE 5.1 : 2-D vertical non-buoyant discharge in shallow water. Solution domain and boundary conditions.
(A) Plane configuration
(B) Axisymmetric configuration.

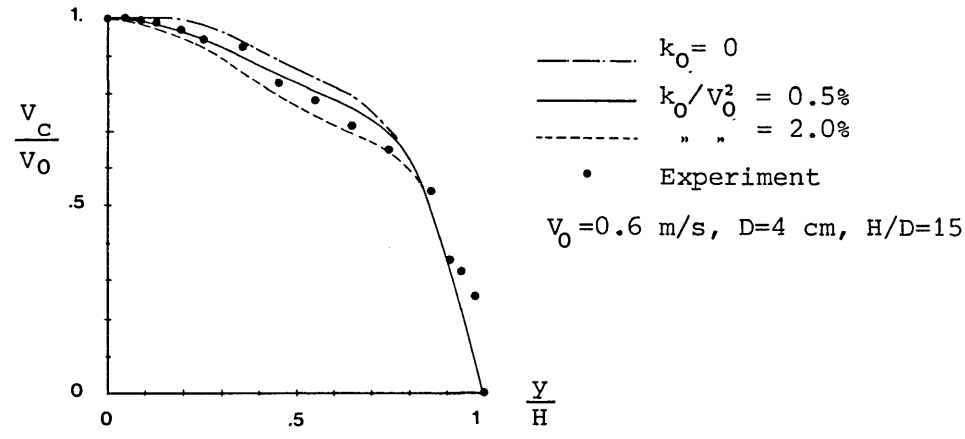


FIGURE 5.2 : The influence of the inlet turbulence intensity on the centreline velocity decay.

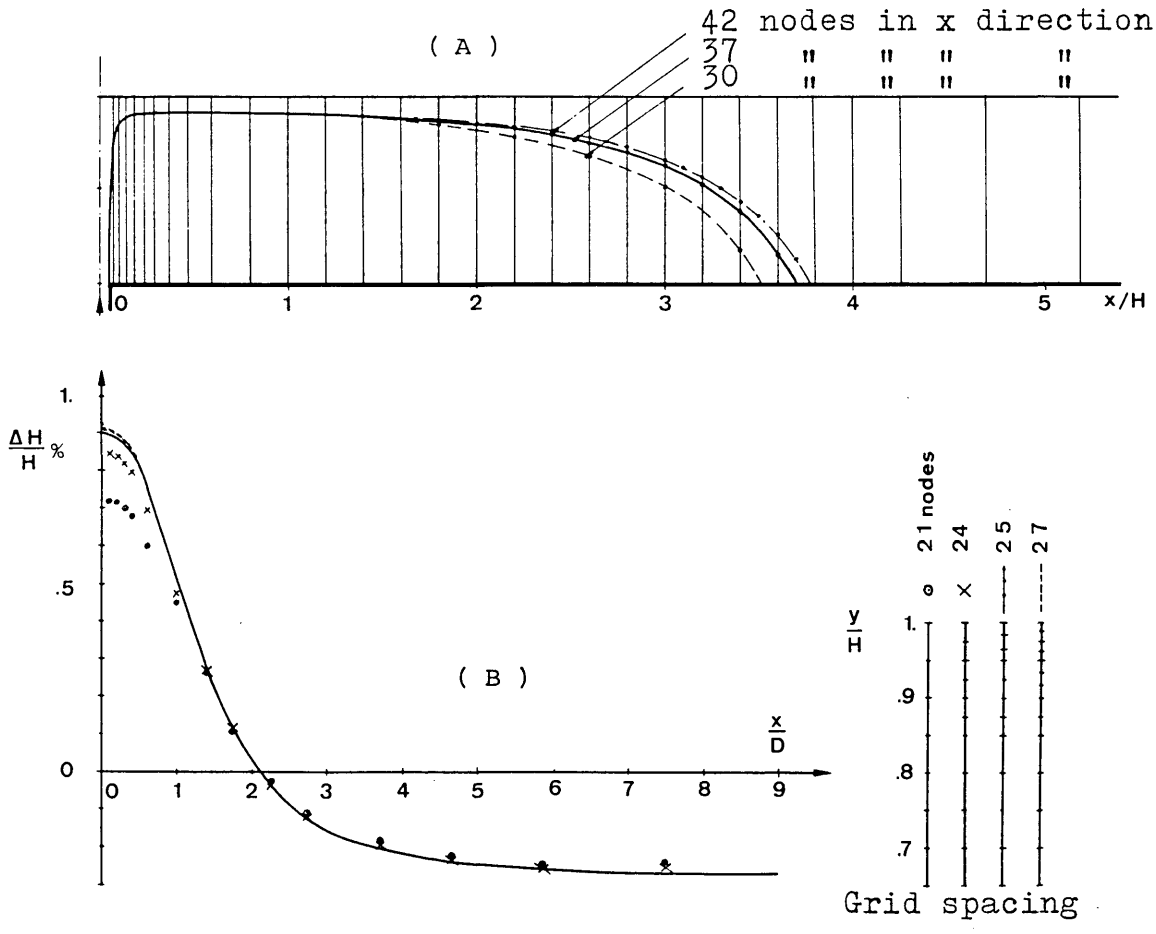


FIGURE 5.3 : Grid dependence checks. Plane discharge V_0= 0.6 m/s, D= 4 cm, H/D= 10.
(A) Separation streamline.
(B) Surface shape.

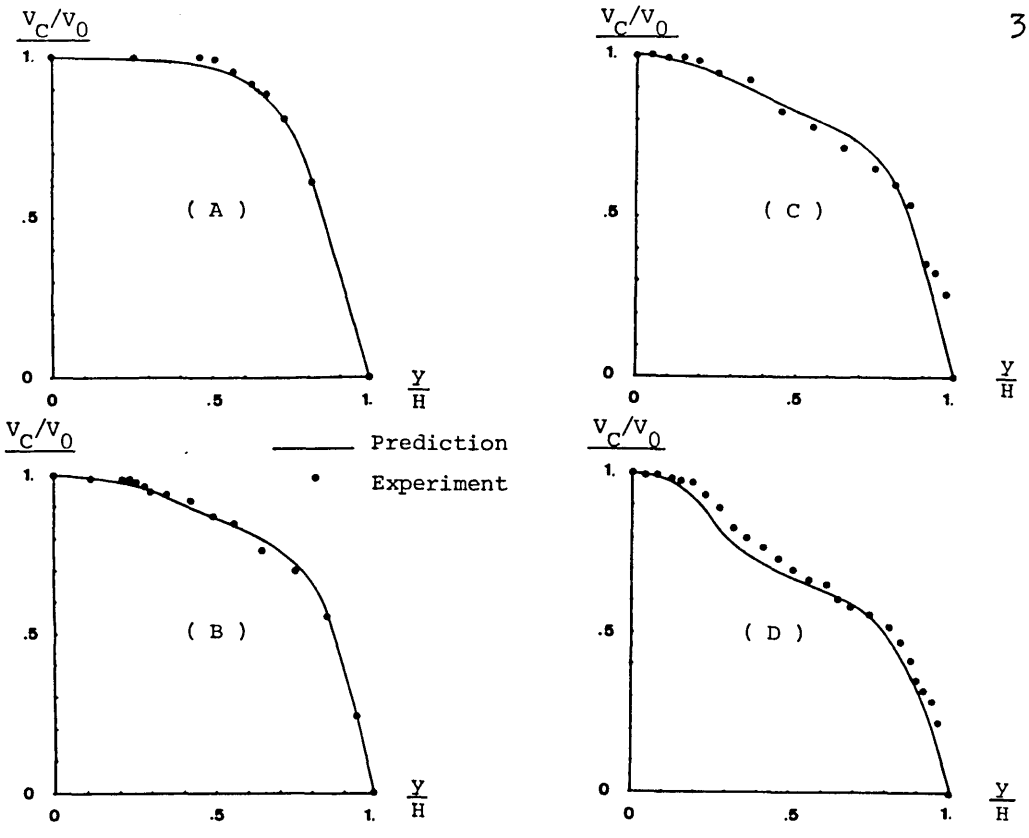


FIGURE 5.4 : Symmetry plane velocity decay , Plane configuration. (A): V_0=0.26 m/s, D=4cm, H/D=4.9 . For the remaining configurations V_0=0.60 m/s, D=4cm and H/D= (B) 10, (C) 15, (D) 20.

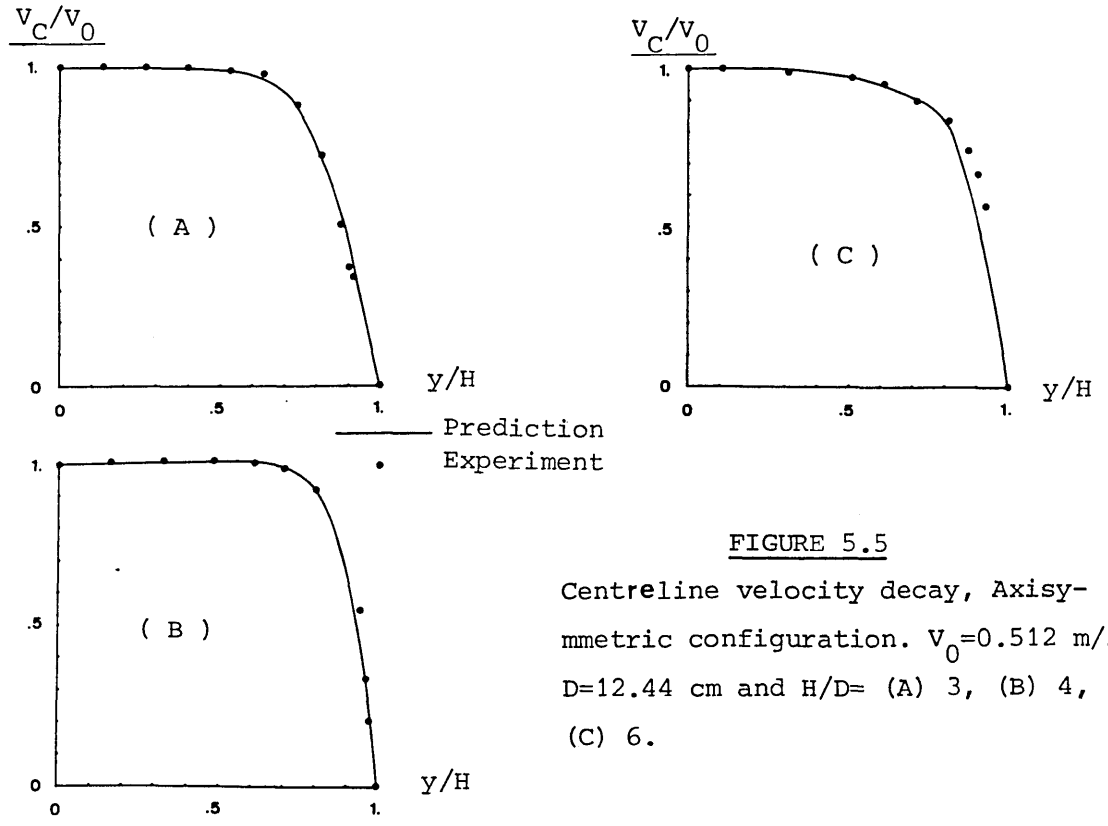


FIGURE 5.5

Centreline velocity decay, Axisymmetric configuration. V_0=0.512 m/s D=12.44 cm and H/D= (A) 3, (B) 4, (C) 6.

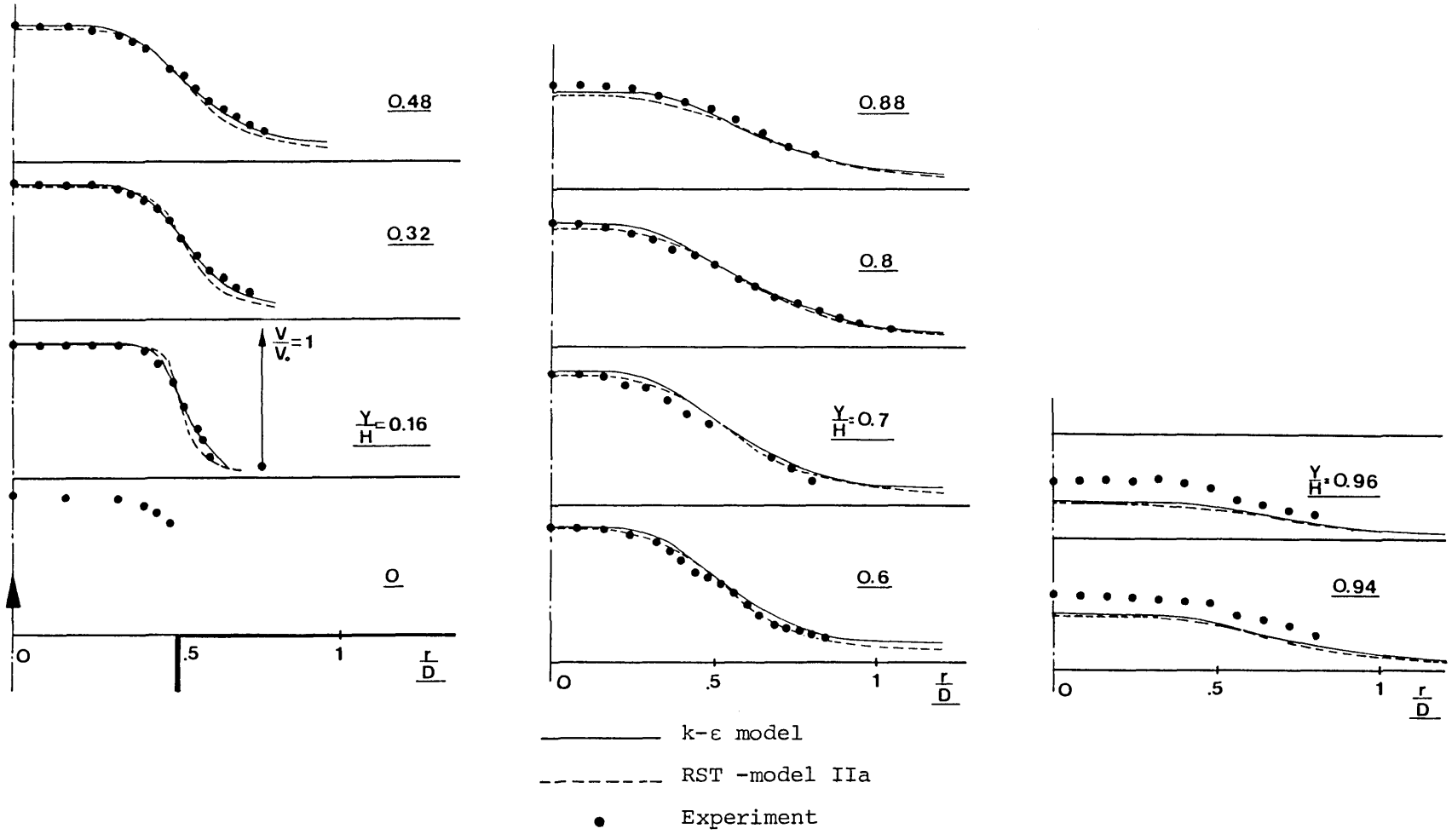
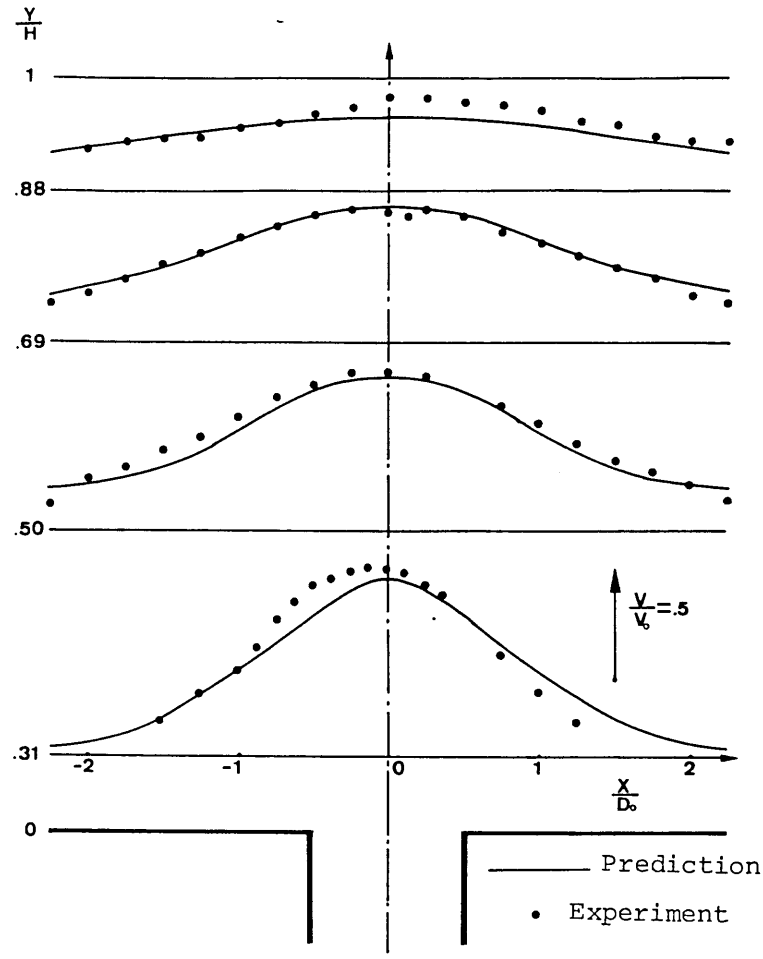


FIGURE 5.6 : Round discharge V_0=0.512 m/s , D=12.44 cm , H/D=4 .
Vertical velocity close to the axis of symmetry.

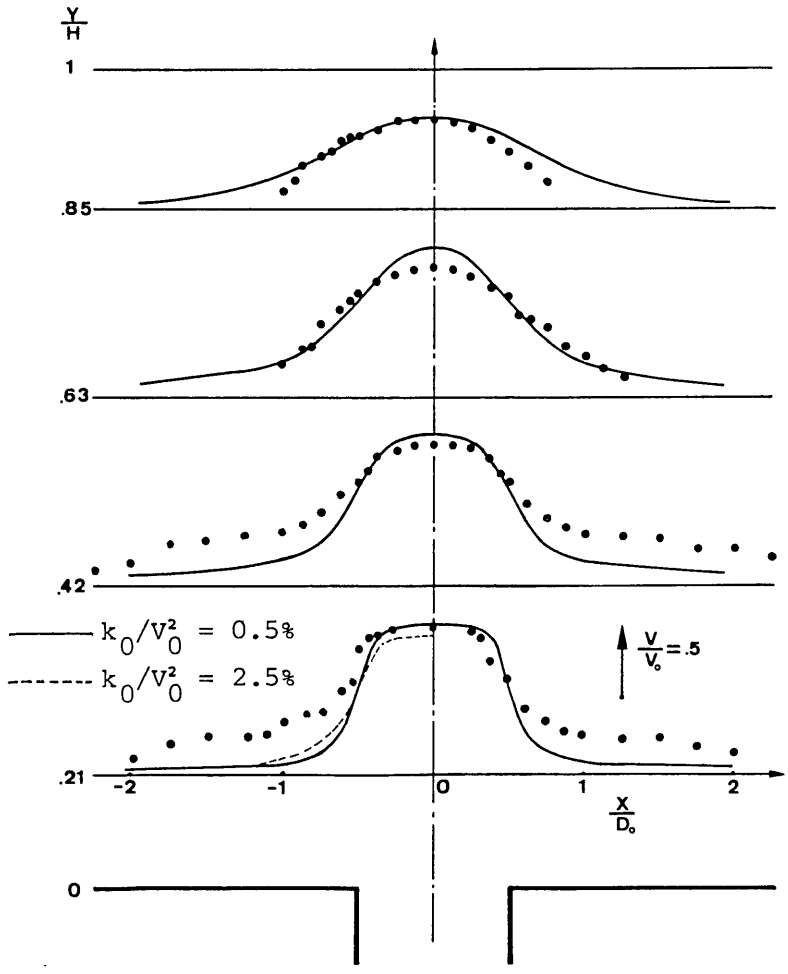


(A)

V_0 = 0.6 m/s

D = 4 cm

H/D = 20



(B)

V_0 = 0.4 m/s

D = 4 cm

H/D = 5.92

FIGURE 5.7

Vertical velocity profiles. Plane configuration.

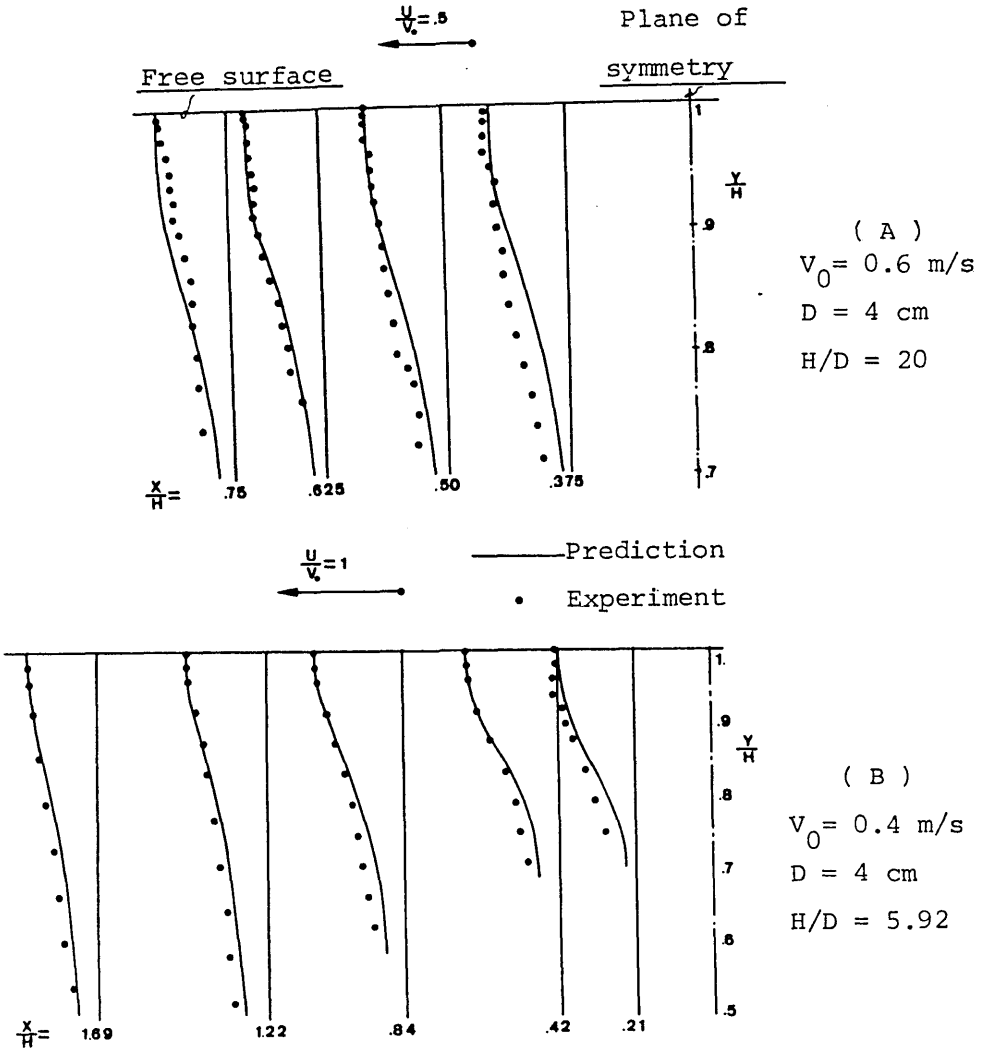


FIGURE 5.8 : Horizontal velocity profiles, Plane configuration.

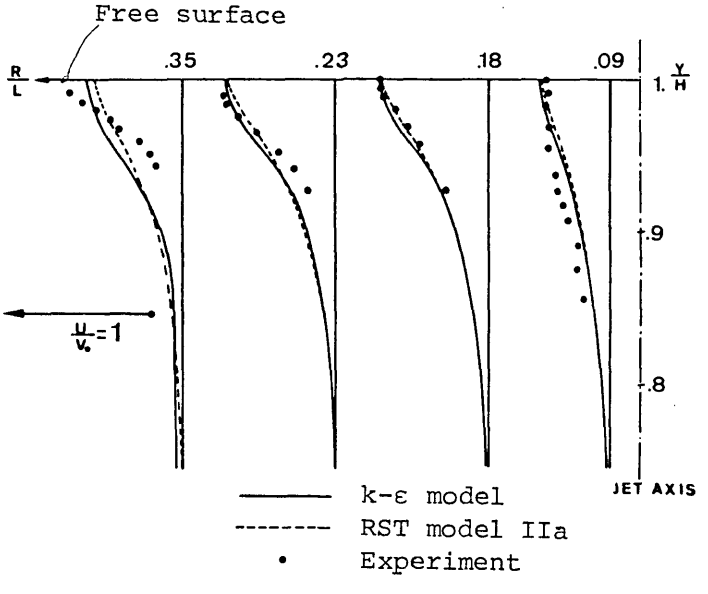


FIGURE 5.9 : Round jet , V_0=0.512 m/s, D=12.44 cm, H/D= 4. Horizontal velocity profiles.

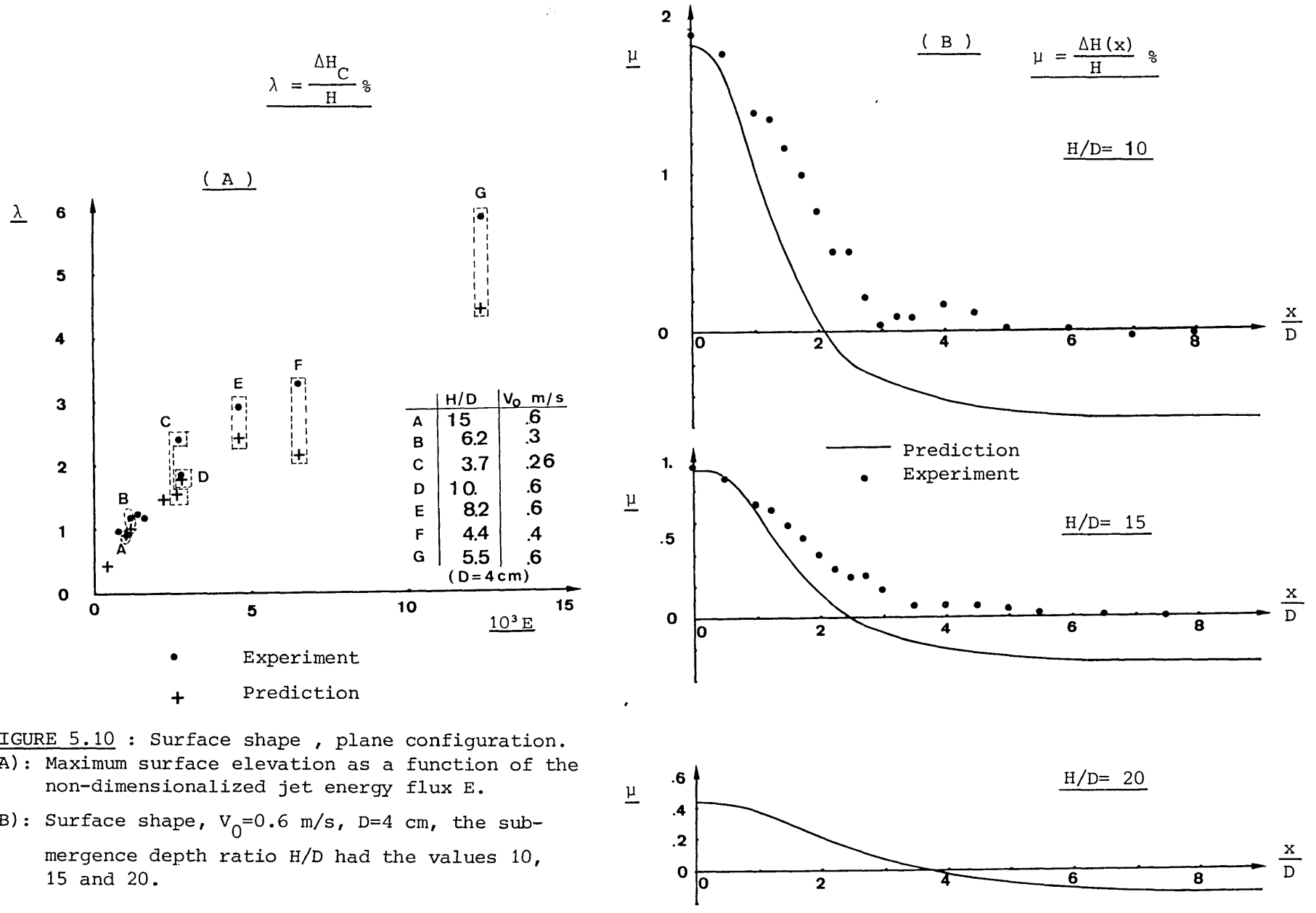
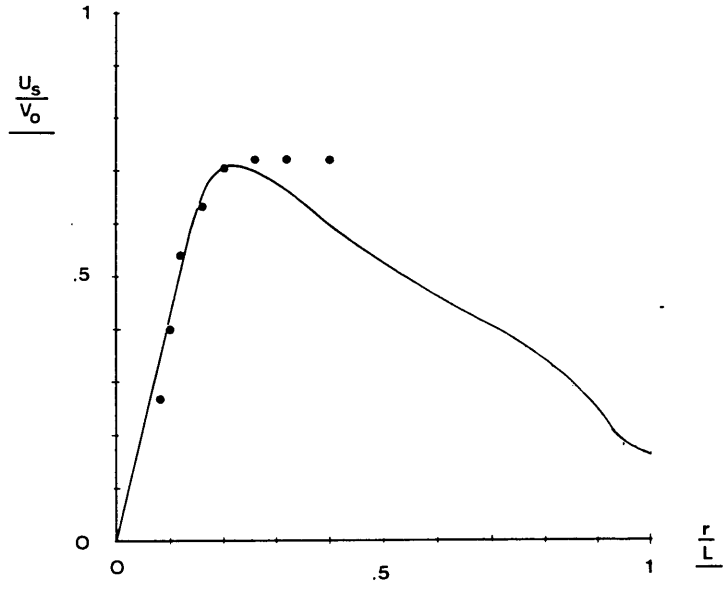


FIGURE 5.10 : Surface shape , plane configuration.
(A): Maximum surface elevation as a function of the non-dimensionalized jet energy flux E.

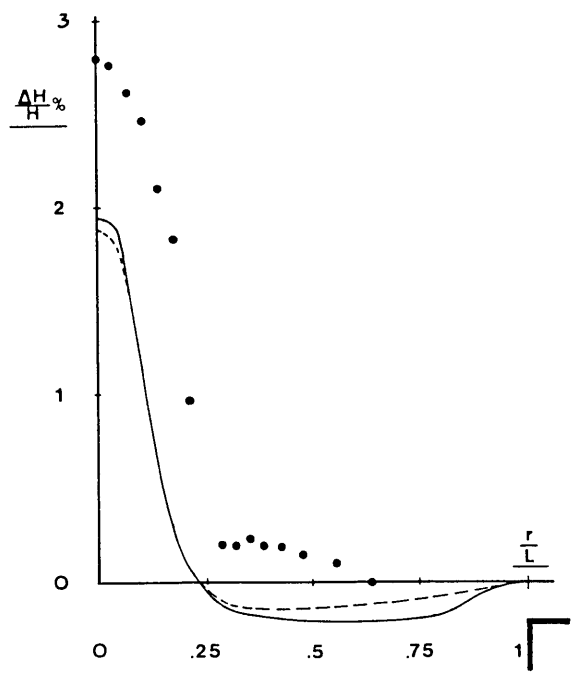
(B): Surface shape, V_0=0.6 m/s, D=4 cm, the submergence depth ratio H/D had the values 10, 15 and 20.



——— Prediction, k-ε

• Experiment

FIGURE 5.11 : Round jet, V_0= 0.512 m/s, D=12.44 cm H/D= 4. Surface velocity evolution.



——— k-ε model

------ RST model IIa

• Experiment

FIGURE 5.12 : Round jet, V_0= 0.512 m/s, D=12.44 cm , H/D= 4. Surface shape.

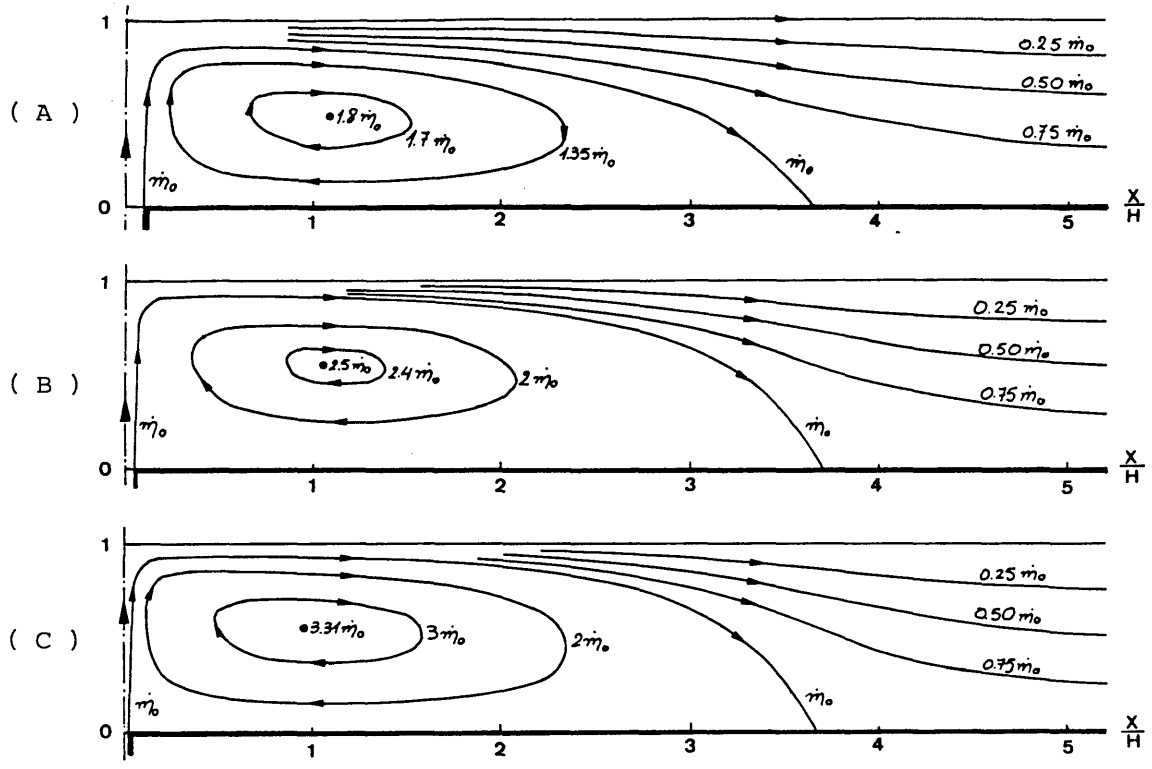
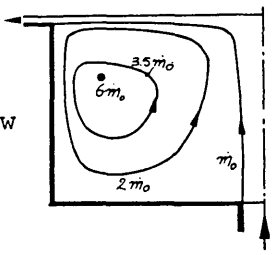


FIGURE 5.13 : Plane configuration , Streamline patterns.

(A) V_0= 0.26 m/s, D= 4 cm, H/D= 5.
(B) V_0= 0.60 m/s, D= 4 cm, H/D=10.
(C) V_0= 0.60 m/s, D= 4 cm, H/D=20.

(A) confined flow



(B) Infinite horizontal extent flow

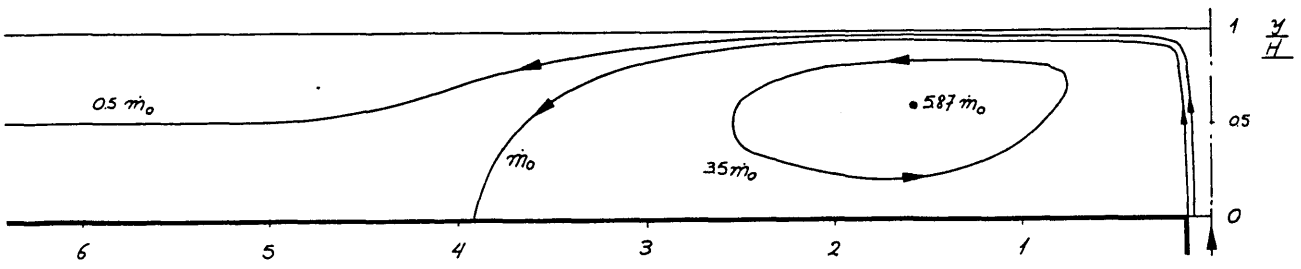
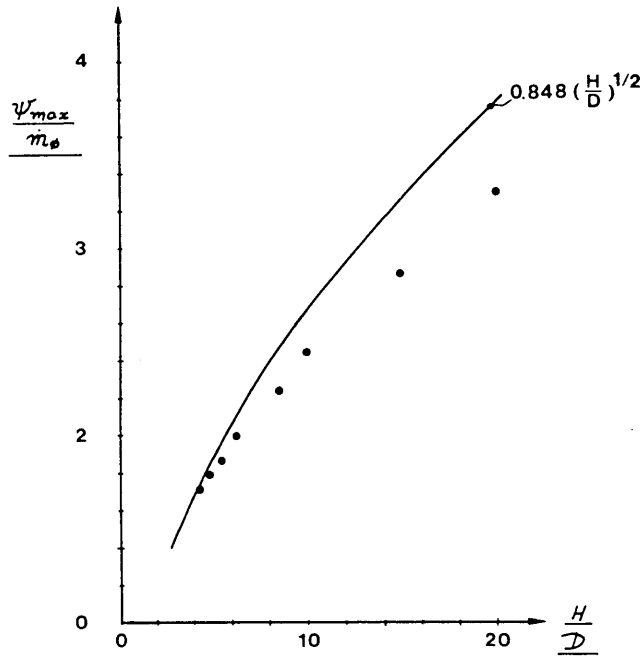
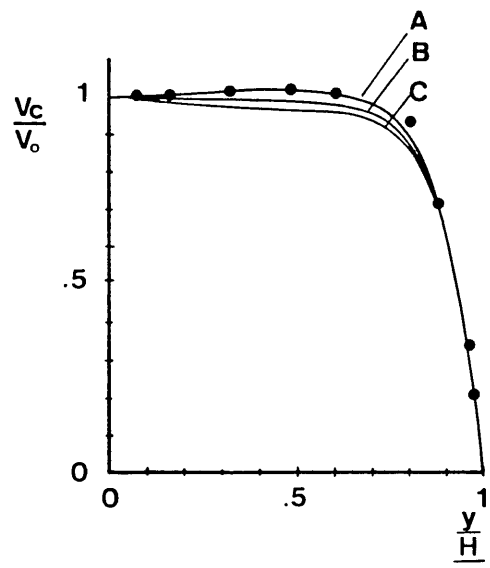


FIGURE 5.14 : Axisymmetric configuration, Streamline patterns. V_0=0.512 m/s, D=12.44 cm, H/D= 4.



• Numerical predictions.

FIGURE 5.15 : Plane discharge, Strength of the recirculation cell.



A: Zero shear stress at the discharge
B: Linear shear stress profile
C: Uniform shear stress profile

FIGURE 5.16 : Round jet, RST prediction. The influence of the inlet shear stress on the centreline velocity decay.

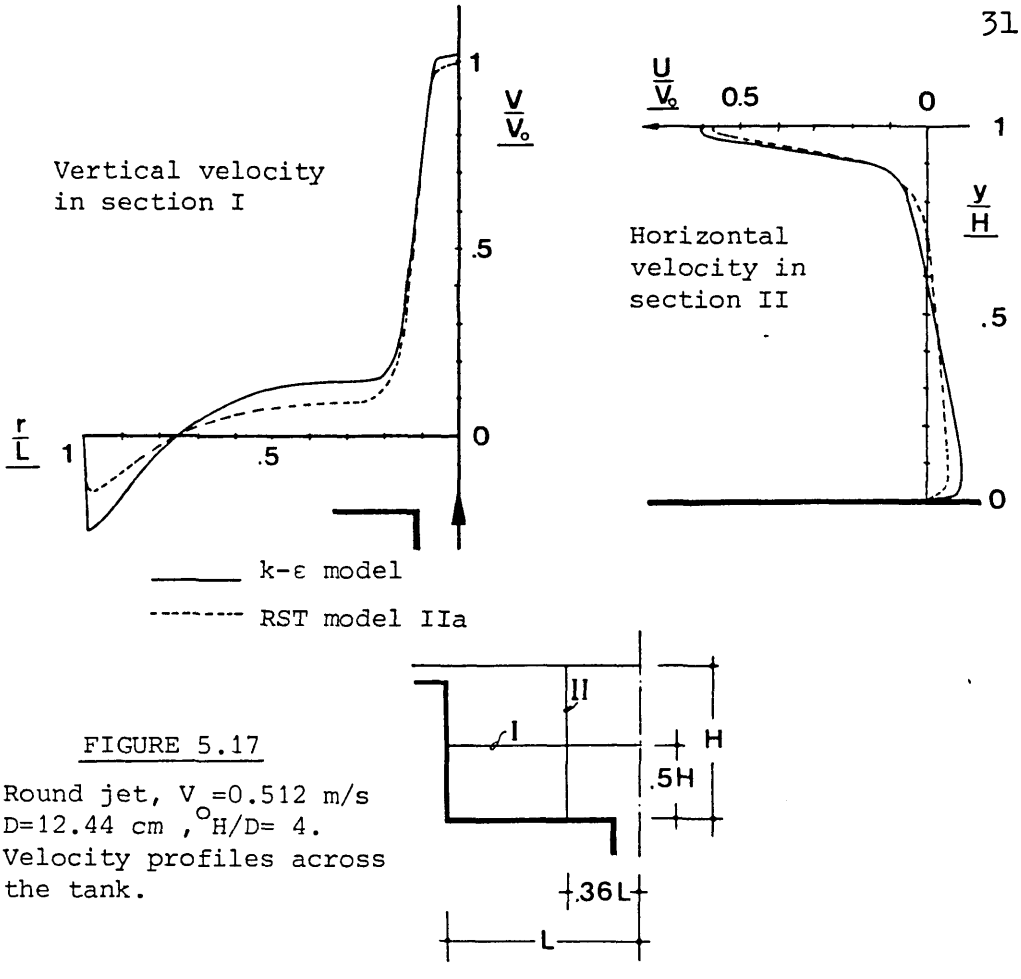


FIGURE 5.17

Round jet, V_o=0.512 m/s
D=12.44 cm , H/D= 4.
Velocity profiles across
the tank.

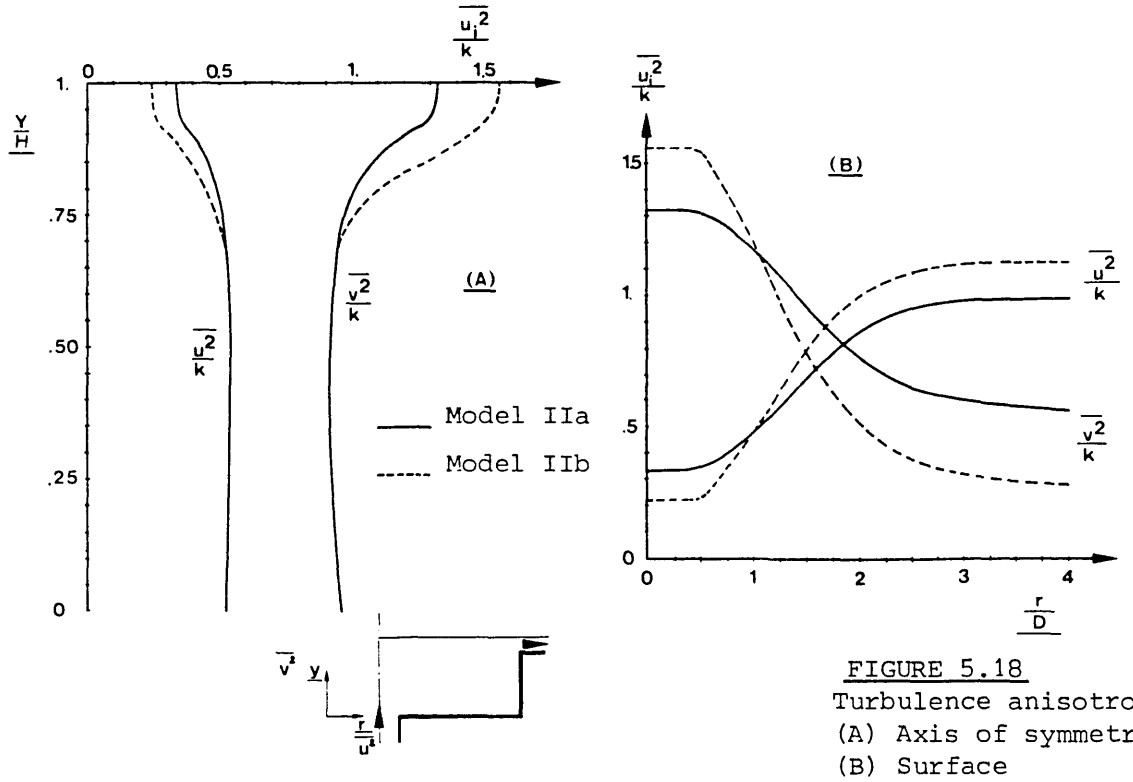


FIGURE 5.18

Turbulence anisotropy
(A) Axis of symmetry
(B) Surface

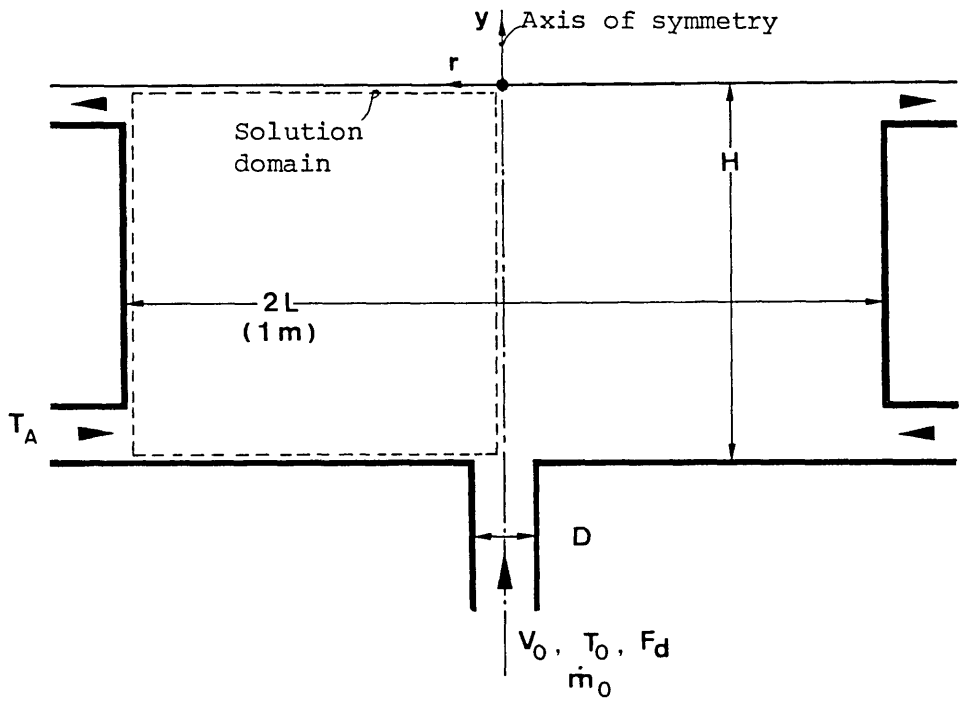


FIGURE 6.1 : Vertical buoyant jet in a shallow tank.
Flow configuration and solution domain.

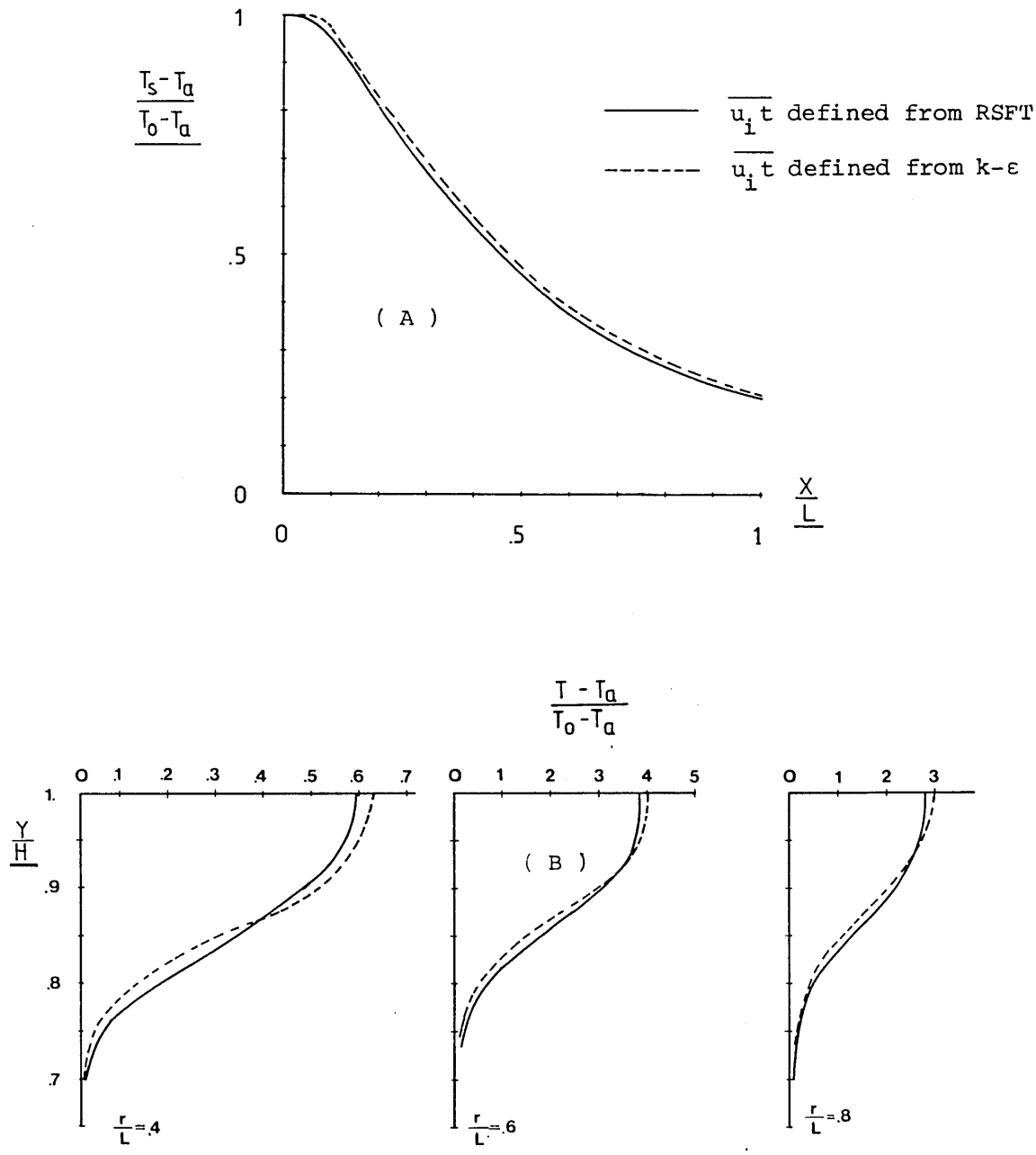


FIGURE 6.2 : Vertical buoyant jet (Fd= 5, H/D= 1.6).

(A): Surface excess temperature.
(B): Temperature profiles.

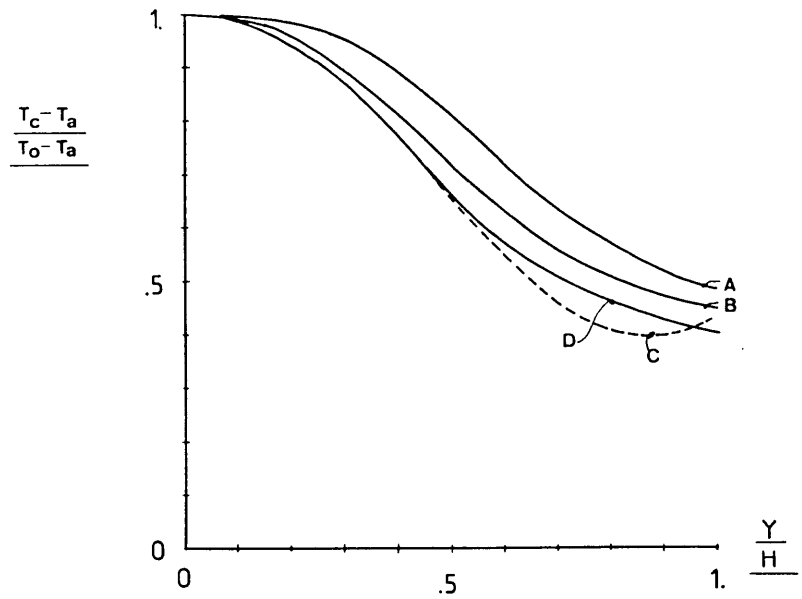


FIGURE 6.3 : Vertical buoyant jet (Fd= 4, H/D= 10). RSFT and k-ε predictions. Centreline temperature.
(A): RSFT, buoyancy set equal to zero in all equations.
(B): RSFT, buoyancy set equal to zero in the turbulence equations.
(C): RSFT, buoyancy taken into account in all equations.
(D): RSFT for the turbulence quantities, but diffusion terms in T equation from k-ε

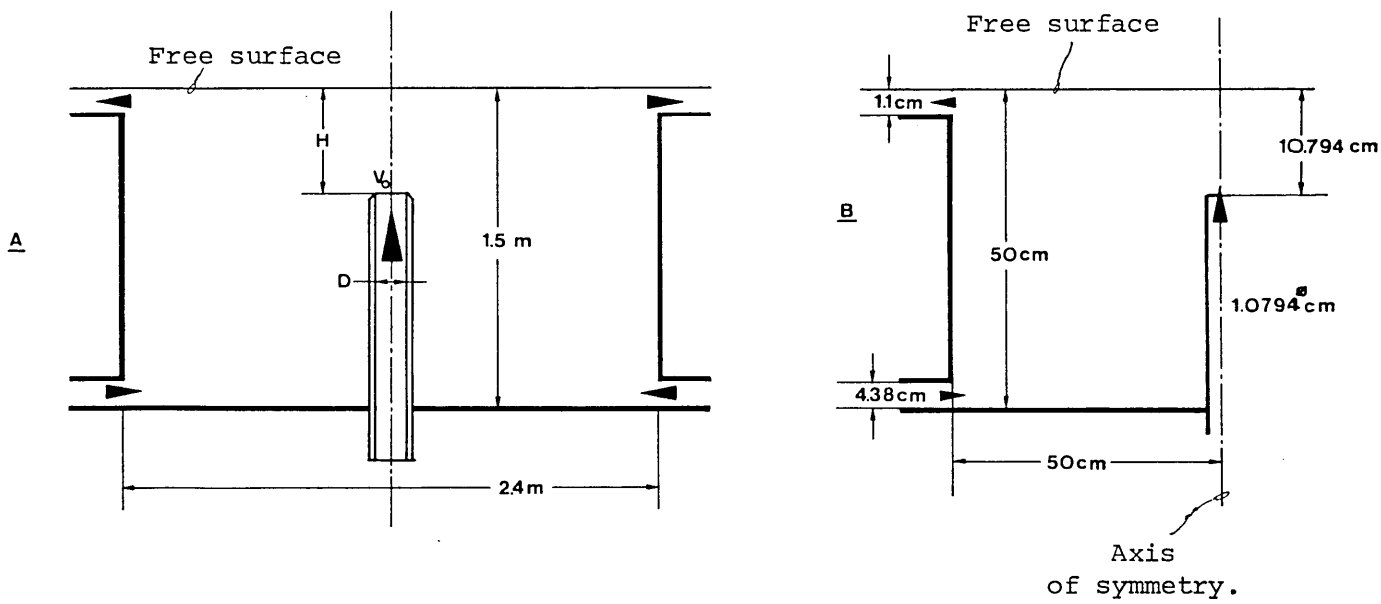


FIGURE 6.4 : (A) sketch of the experimental apparatus of Pryputniewicz and Bowley (1975).
(B) Solution domain.

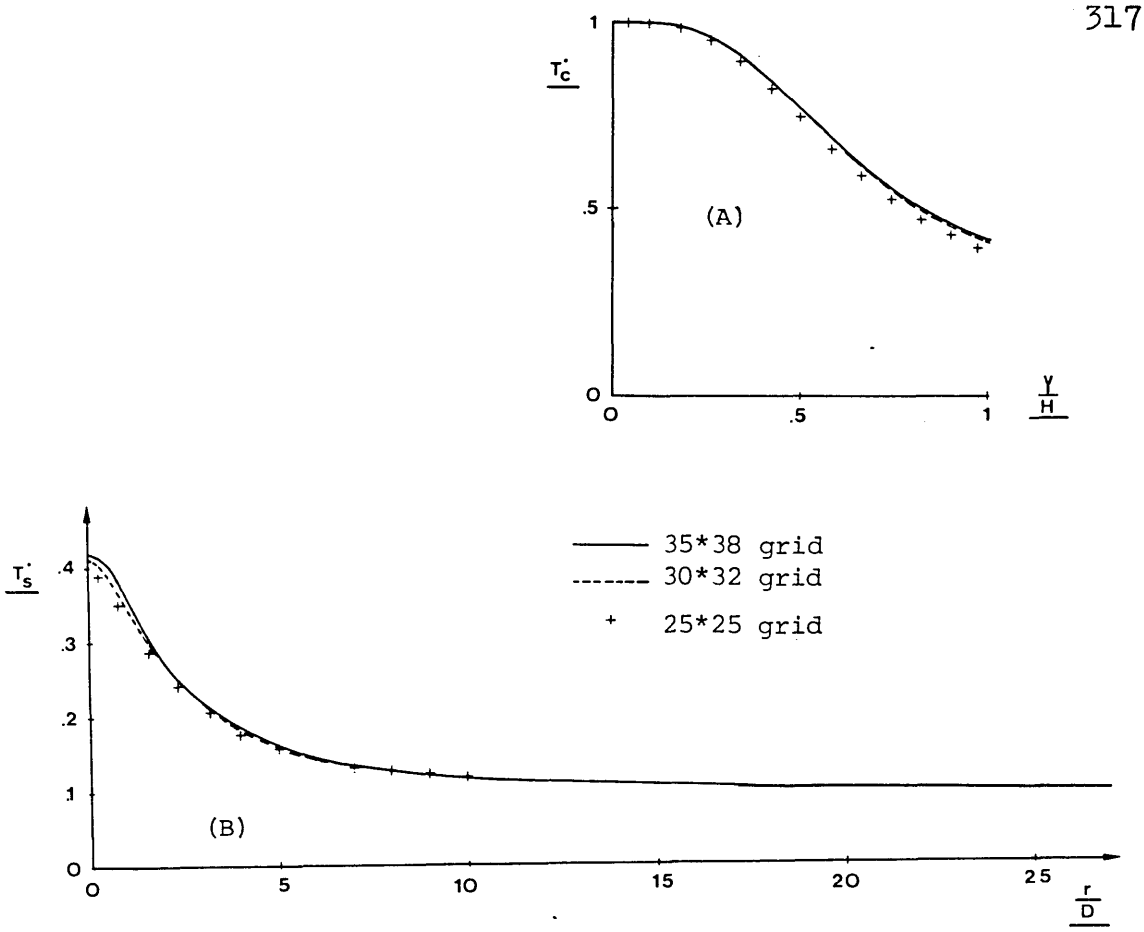


FIGURE 6.5 : Grid independence checks (Fd= 4 , H/D= 10).
(A): Centreline excess temperature
(B): Surface excess temperature

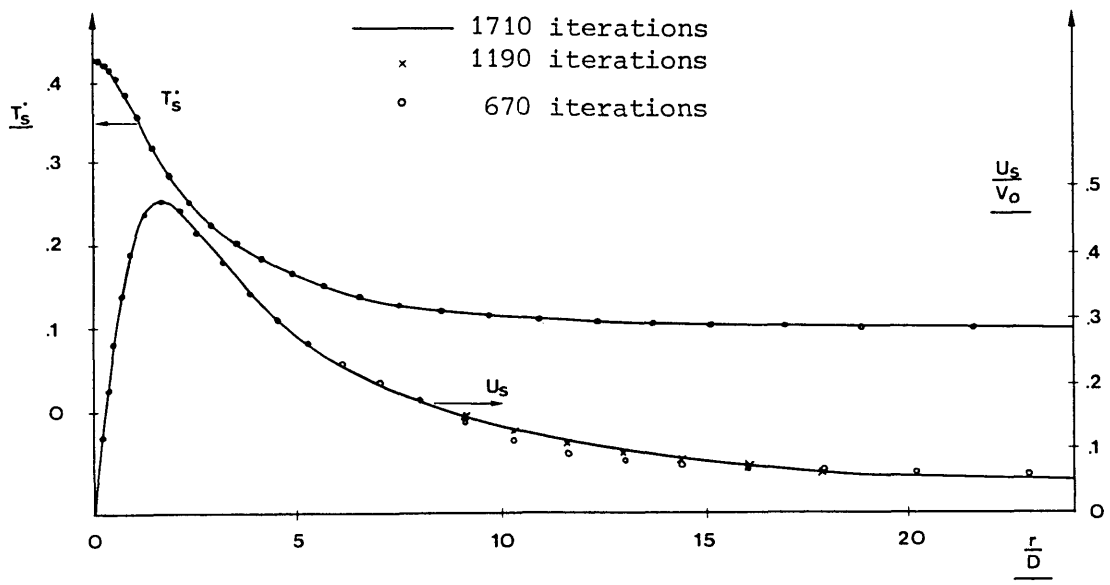


FIGURE 6.6A : Evolution of the solution (Fd=4, H/D=10).
Surface excess temperature and velocity.

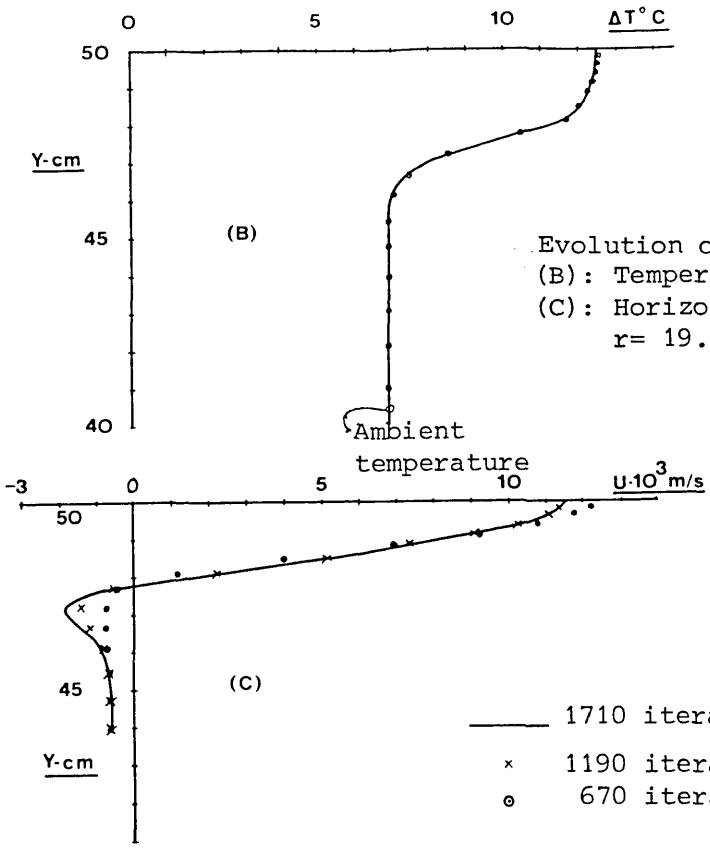


FIGURE 6.6

Evolution of the solution (Fd=4, H/D=10)
(B): Temperature profile at r=20 cm.
(C): Horizontal velocity profile at r= 19.3 cm.

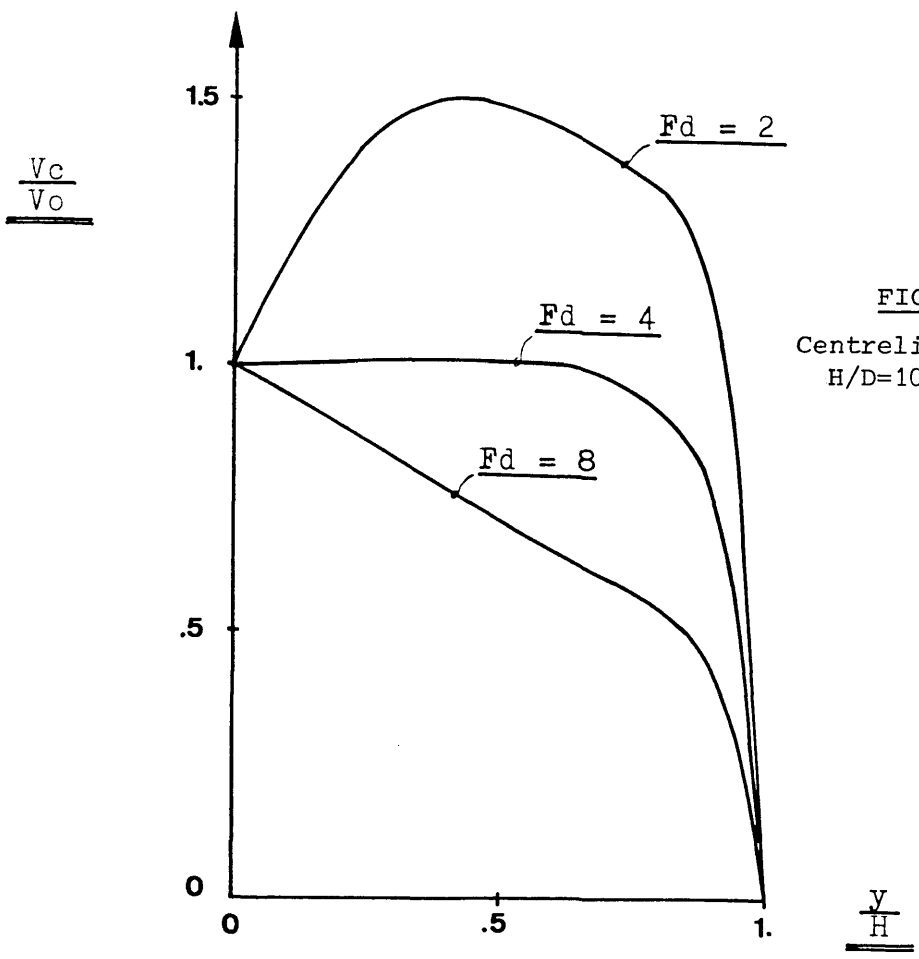


FIGURE 6.7

Centreline velocity.
H/D=10, Fd= 2, 4, 8.

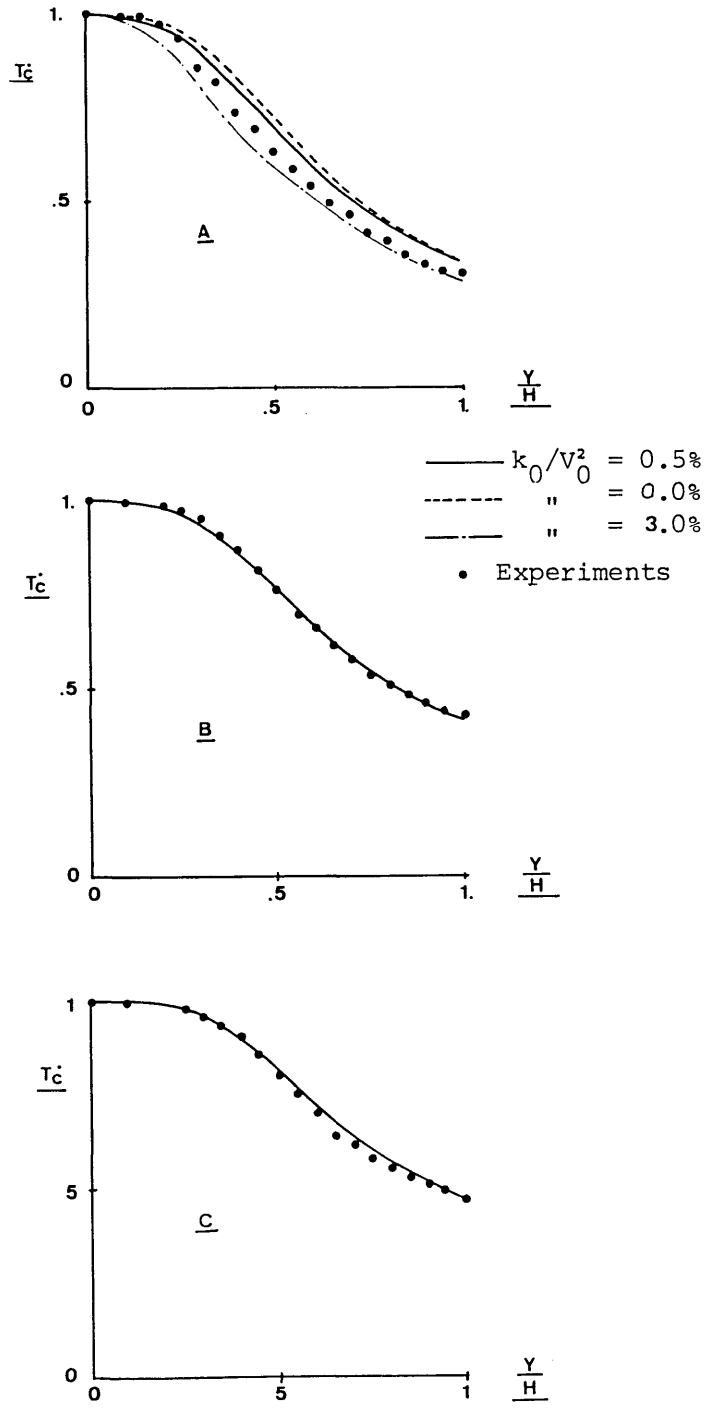
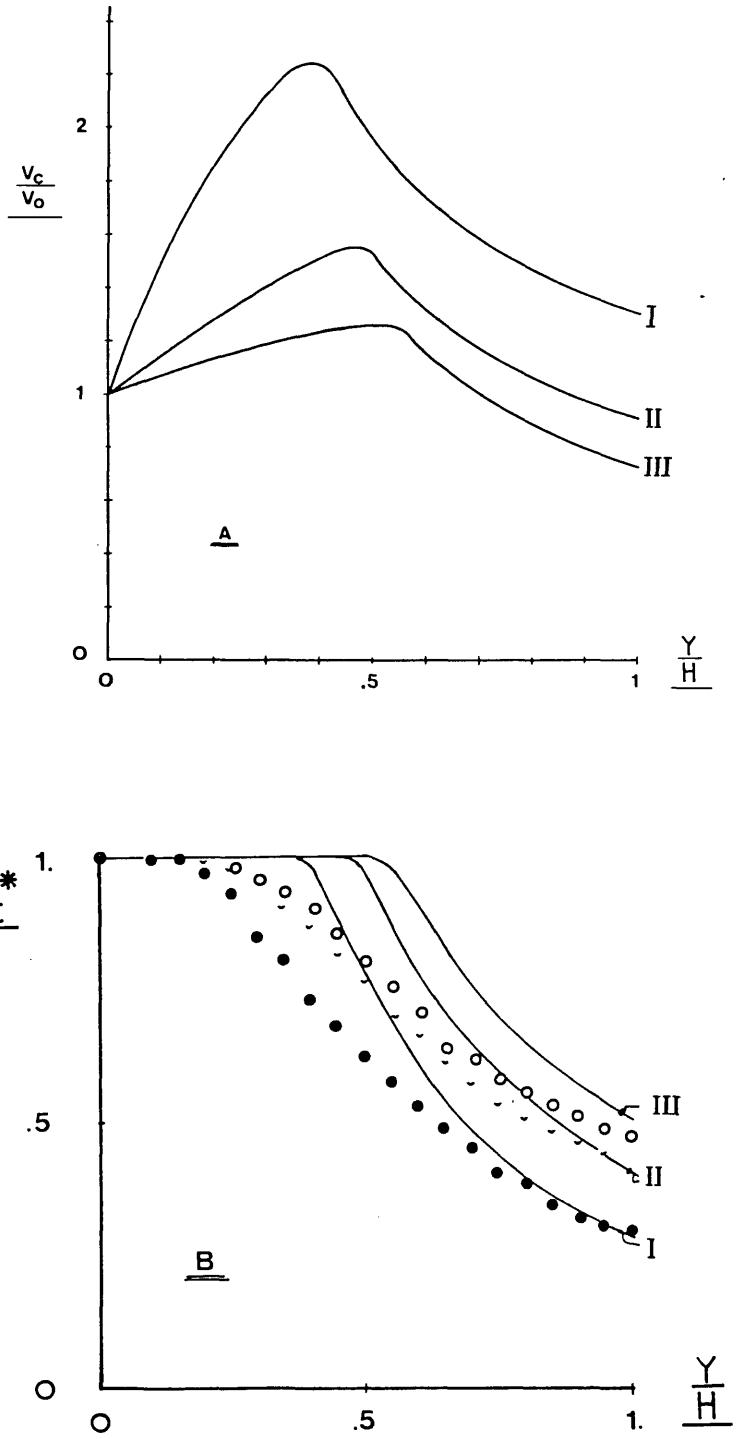


FIGURE 6.8: Centreline excess temperature, H/D= 10.
(A) : Fd = 2
(B) : Fd = 4
(C) : Fd = 8

(k_0 is the turbulence energy at the discharge)



o Experiment, Fd=8

- Experiment, Fd=4

• Experiment, Fd=2

——— Predictions,
I : Fd=2, II : Fd=4, III : Fd=8

FIGURE 6.9 : Centreline velocity and excess temperature (H/D=10). Predictions of the integral analysis of Jirka e.a. (1981).
(A): Centreline velocity
(B): Centreline excess temperature

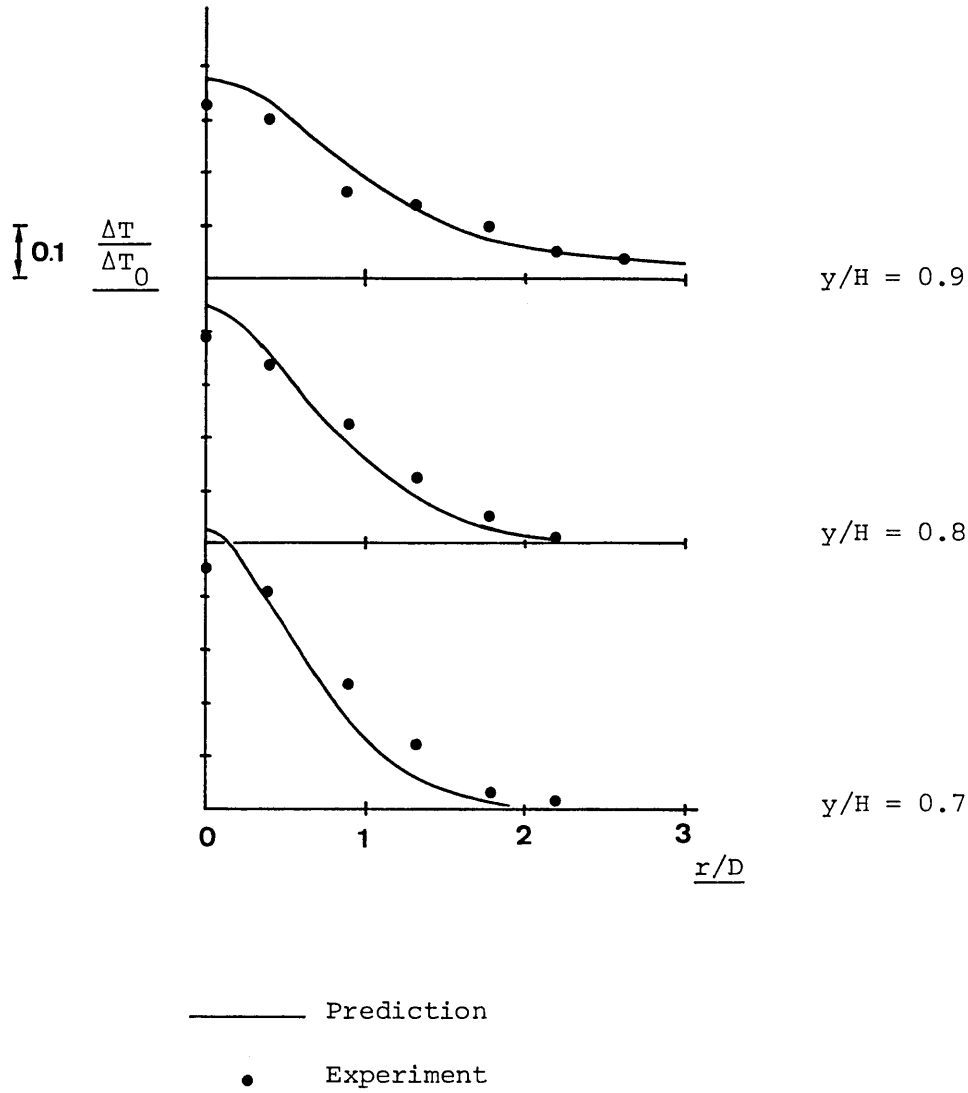


FIGURE 6.10 : Temperature profiles close to the axis of symmetry, H/D=10, Fd=2.

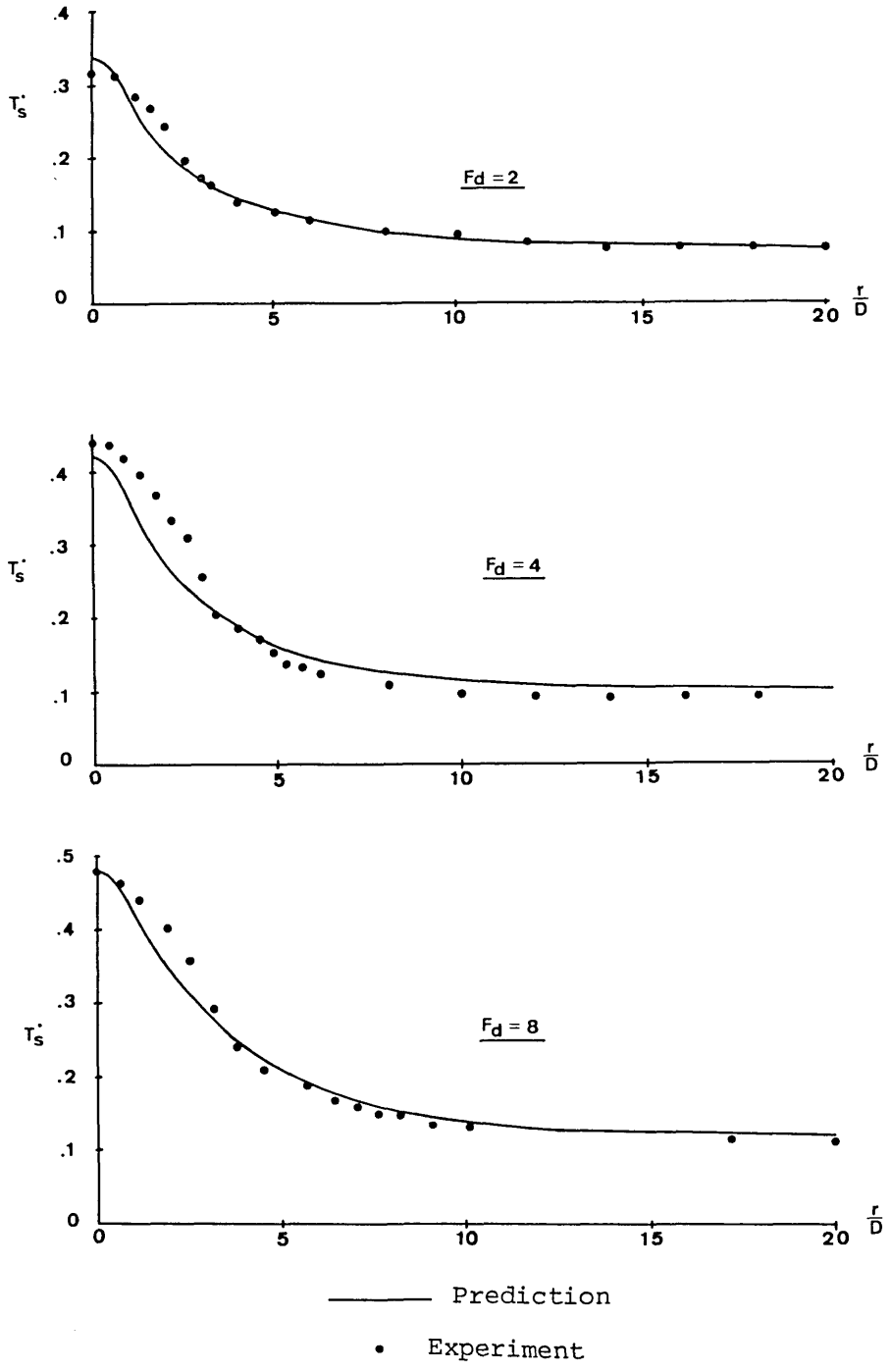


FIGURE 6.11 : Surface excess temperature, H/D=10.

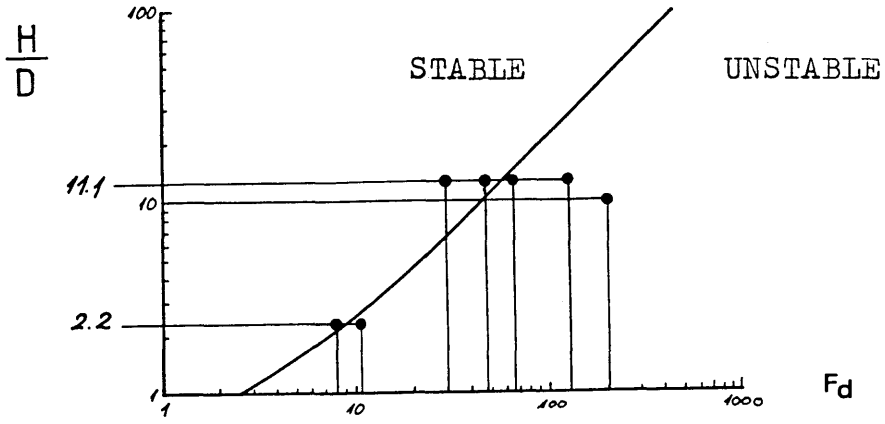


FIGURE 6.12 : Stability map of Jirka and Lee (1981). Axisymmetric geometry. Location of the predicted configurations.

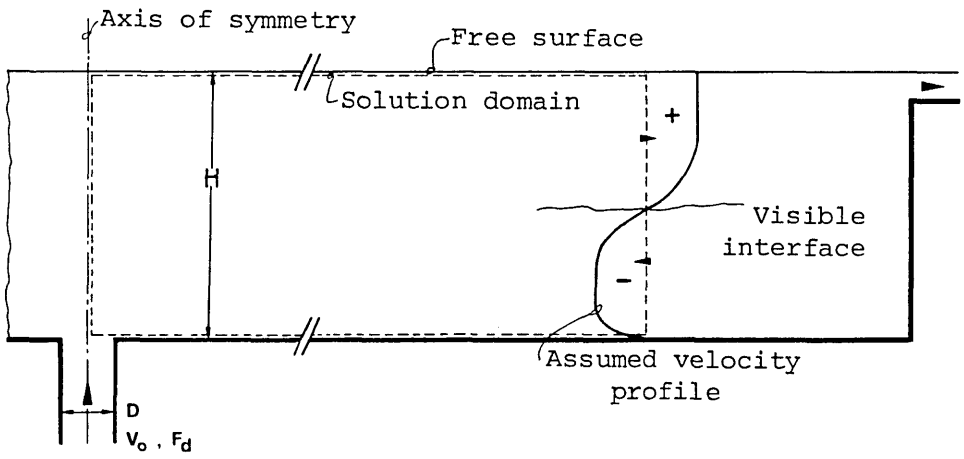


FIGURE 6.13 : Solution domain for the buoyant vertical discharge in shallow water. Steady state solutions.

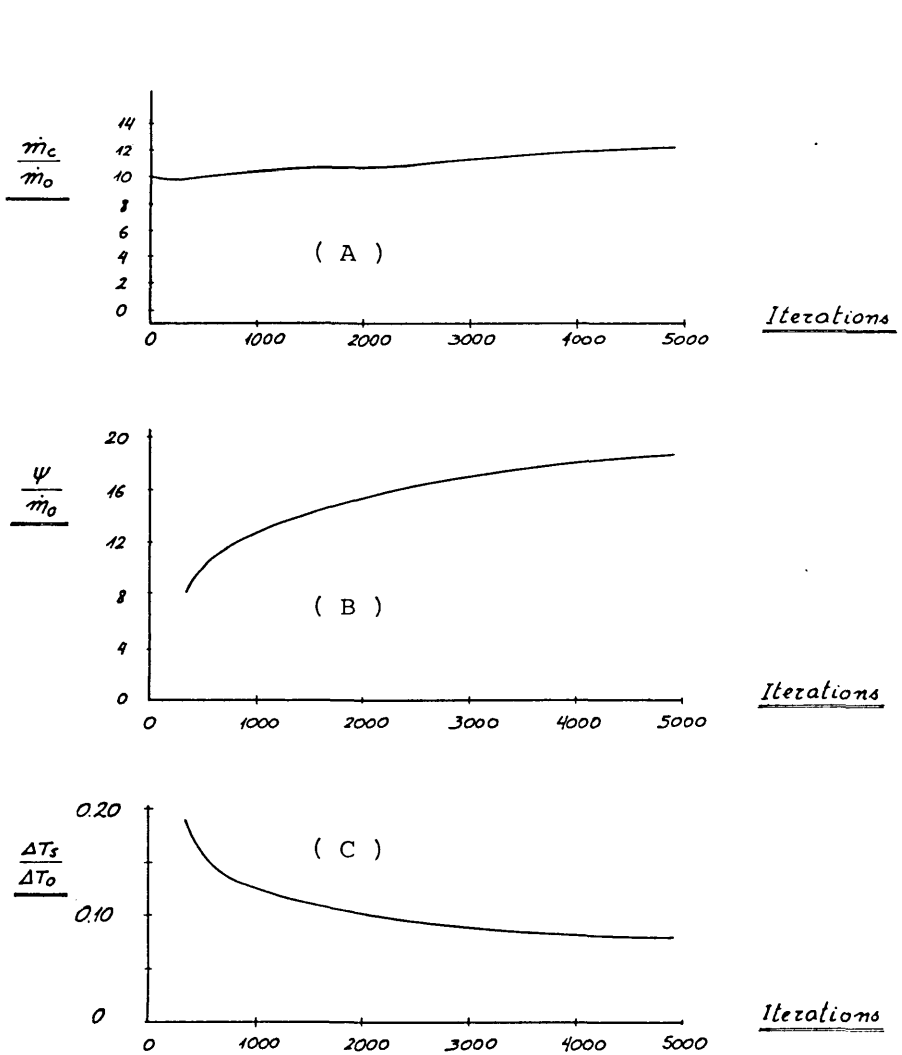


FIGURE 6.14 : Evolution of the solution for the case (H/D=11.1, Fd=46). (A):ambient water entrainment, (B): Stream function at a characteristic location, (C): Downstream surface temperature.

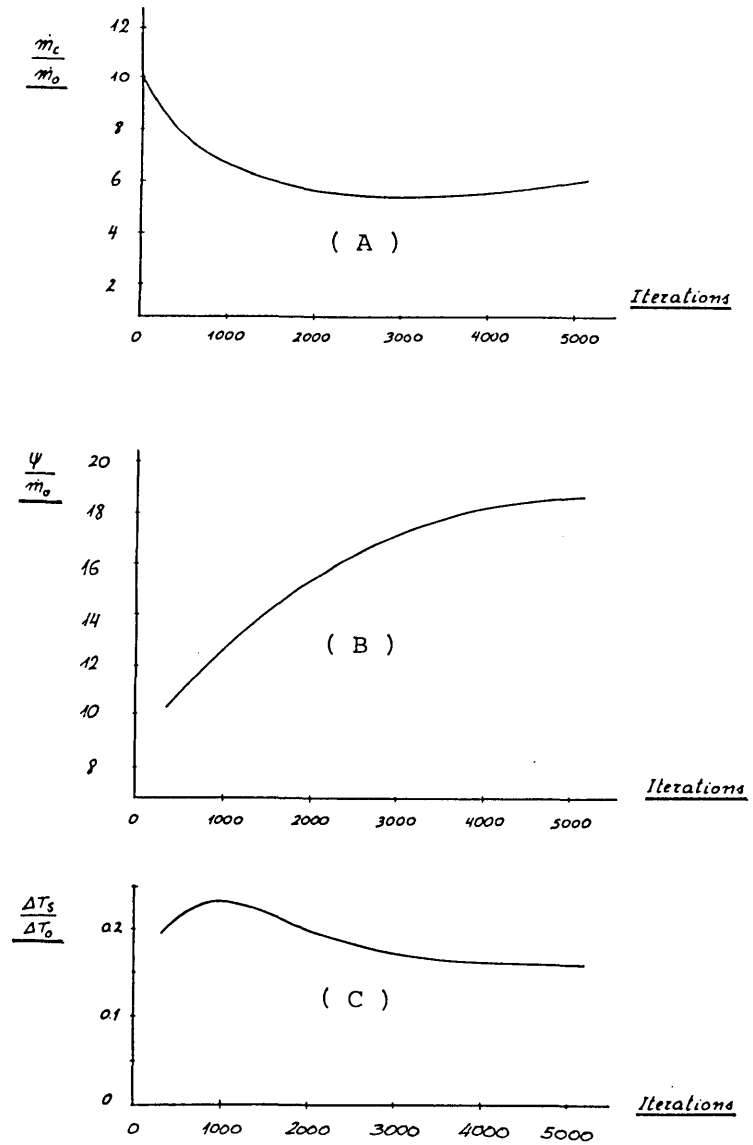


FIGURE 6.15 : Evolution of the solution for the case (H/D=11.1, Fd=110). (A): ambient water entrainment, (B): Stream function at a characteristic location, (C): Downstream surface temperature.

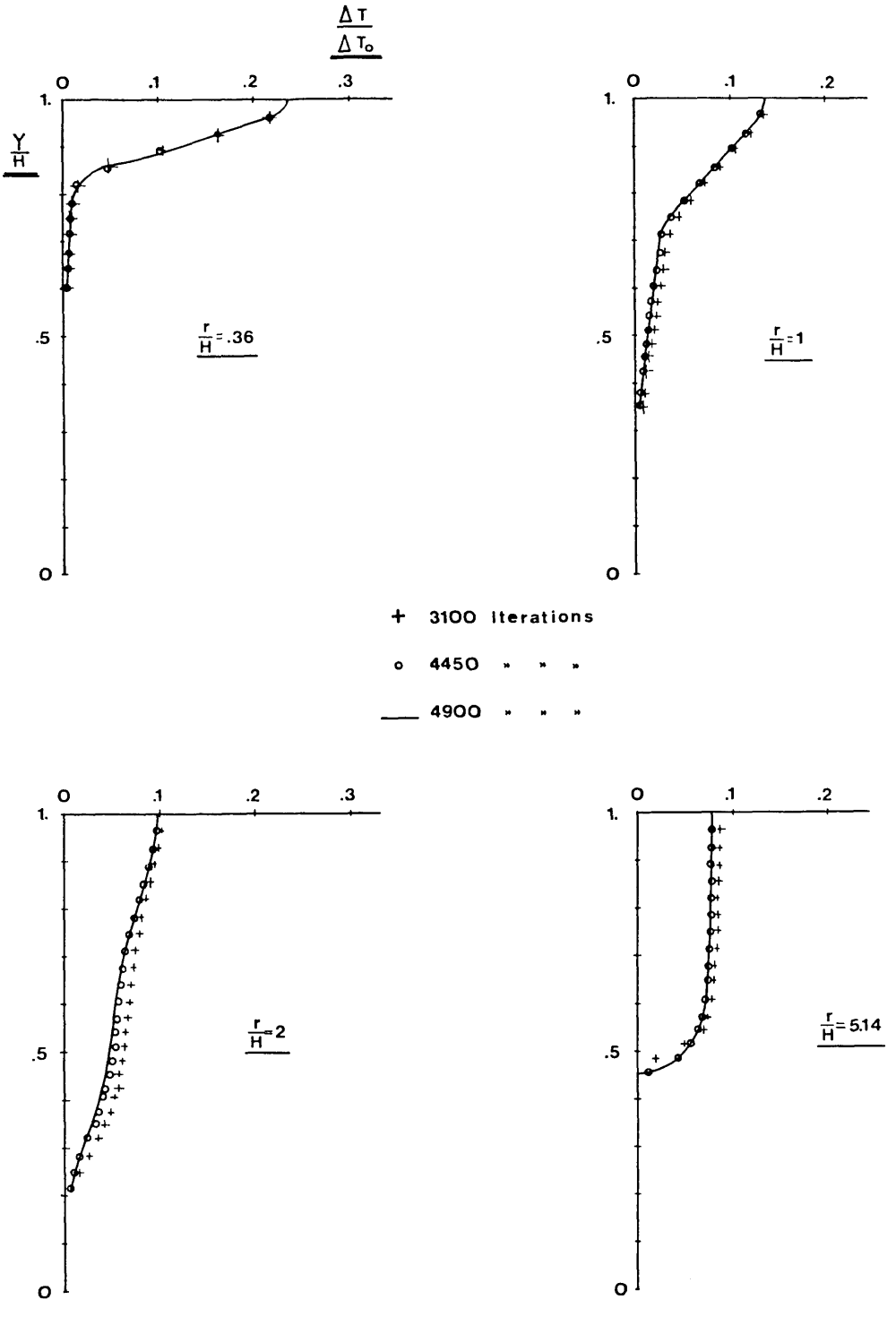


FIGURE 6.16 : Evolution of the temperature field for the case H/D= 11.1, Fd=46.

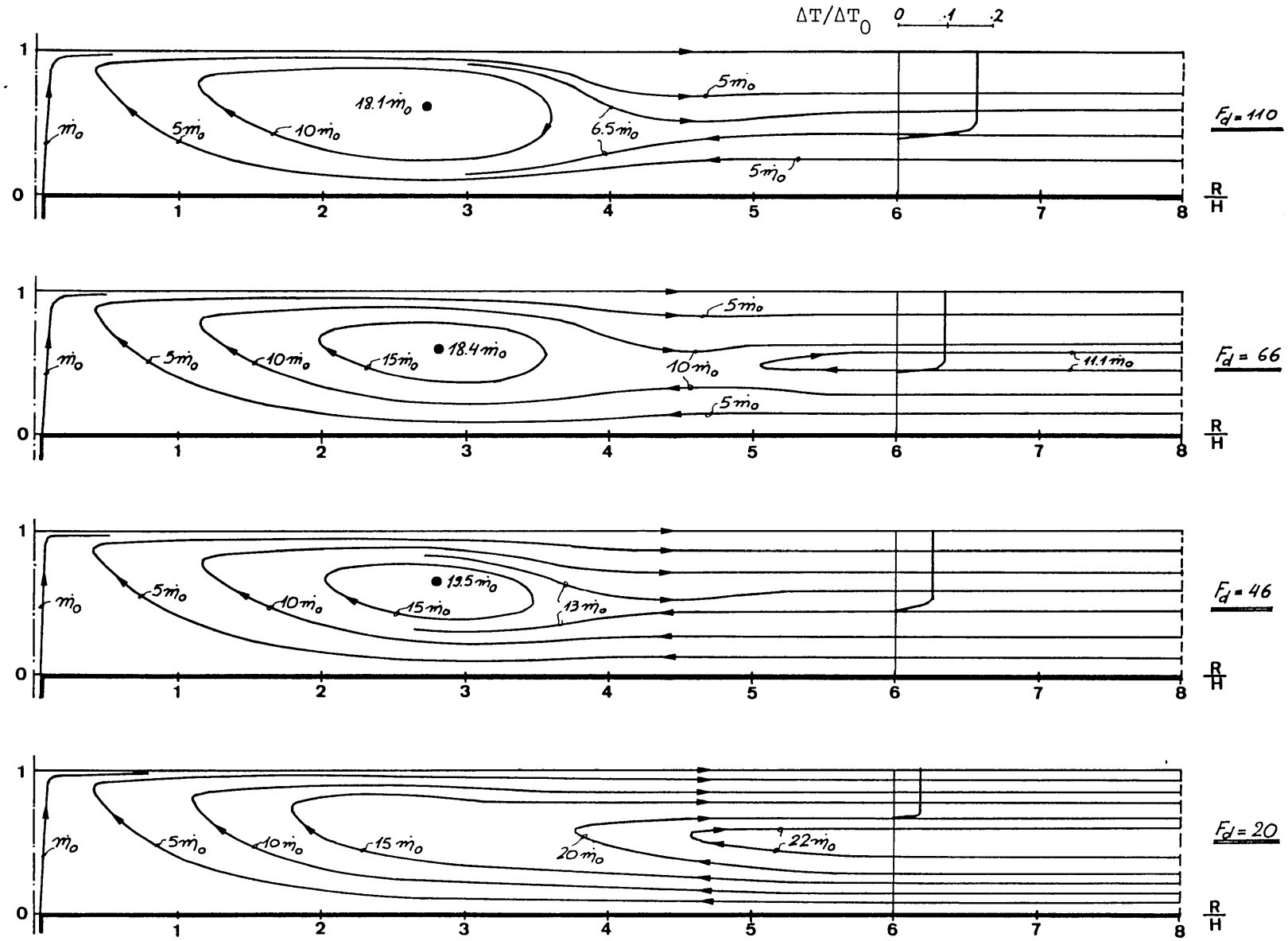


FIGURE 6.17 : Predicted streamline patterns for four discharge Froude numbers. (Fd= 20, 46, 66, 110 and H/D= 11.1). Steady state solution approach.

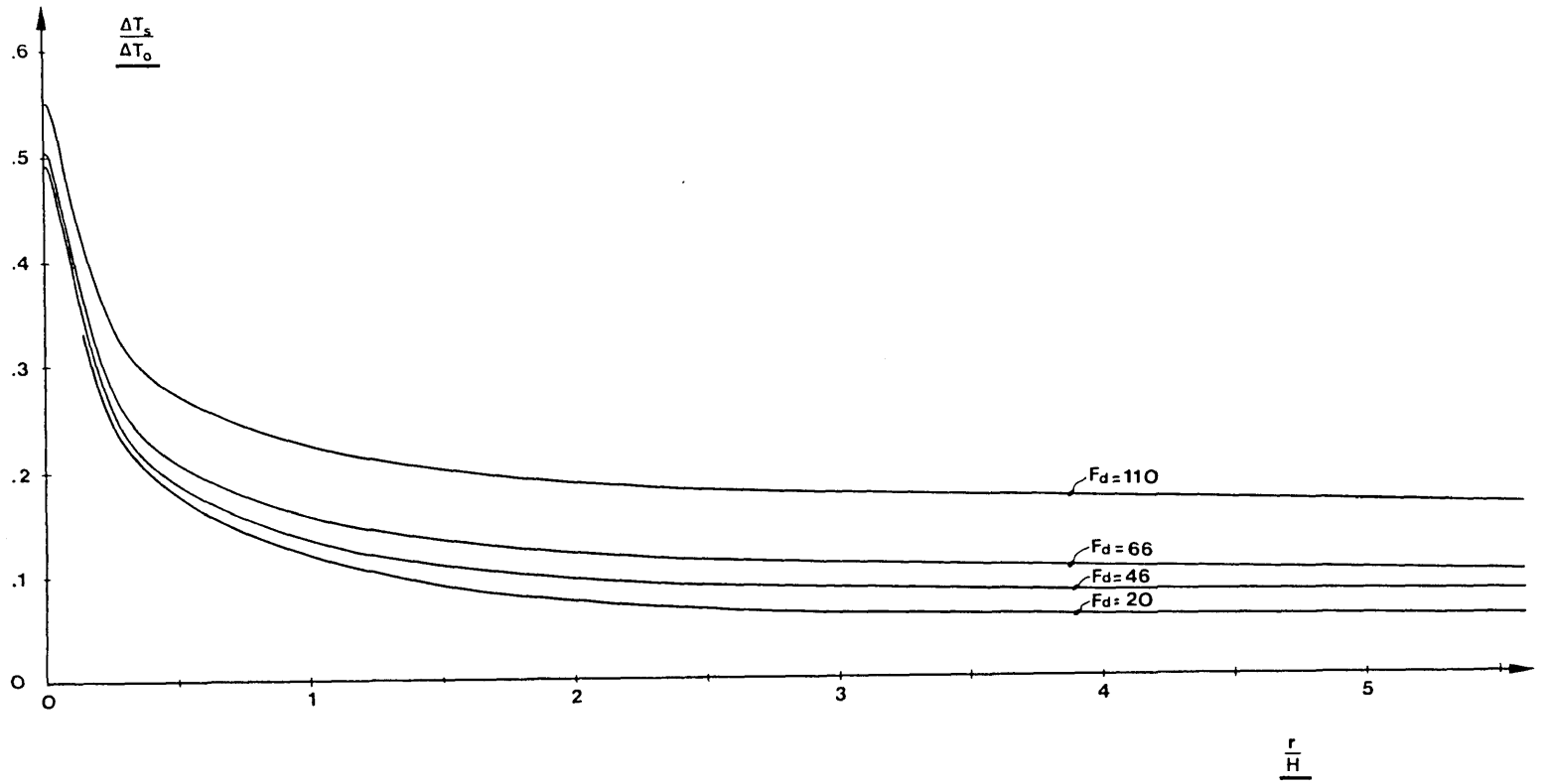


FIGURE 6.18 : Predicted surface temperature for four discharge Froude numbers Fd = 20, 46, 66, 110 and H/D=11.1. Steady state approach.

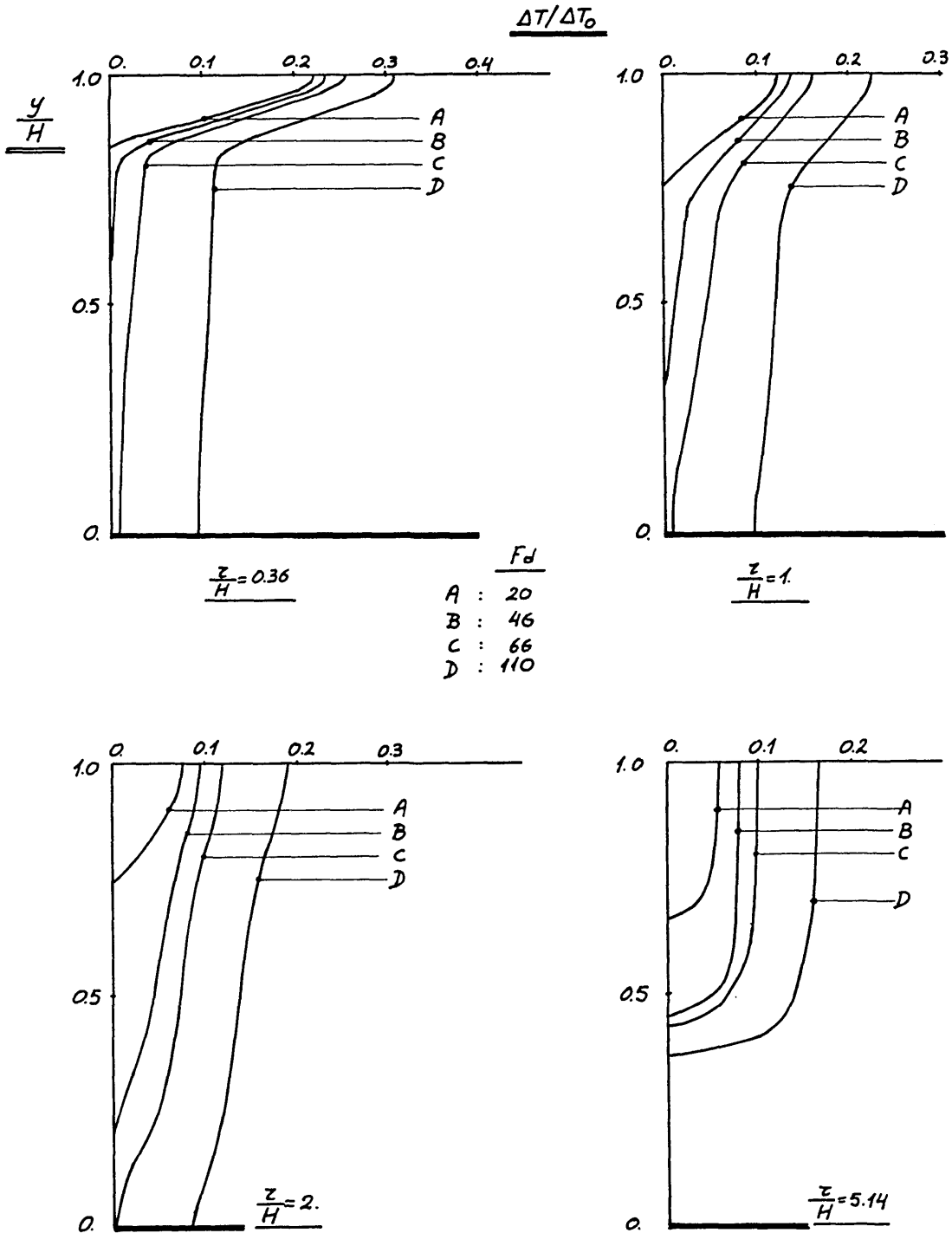


FIGURE 6.19 : Predicted temperature profiles for four discharge Froude numbers Fd = 20, 46, 66, 110 and H/D= 11.1 . Steady-state approach.

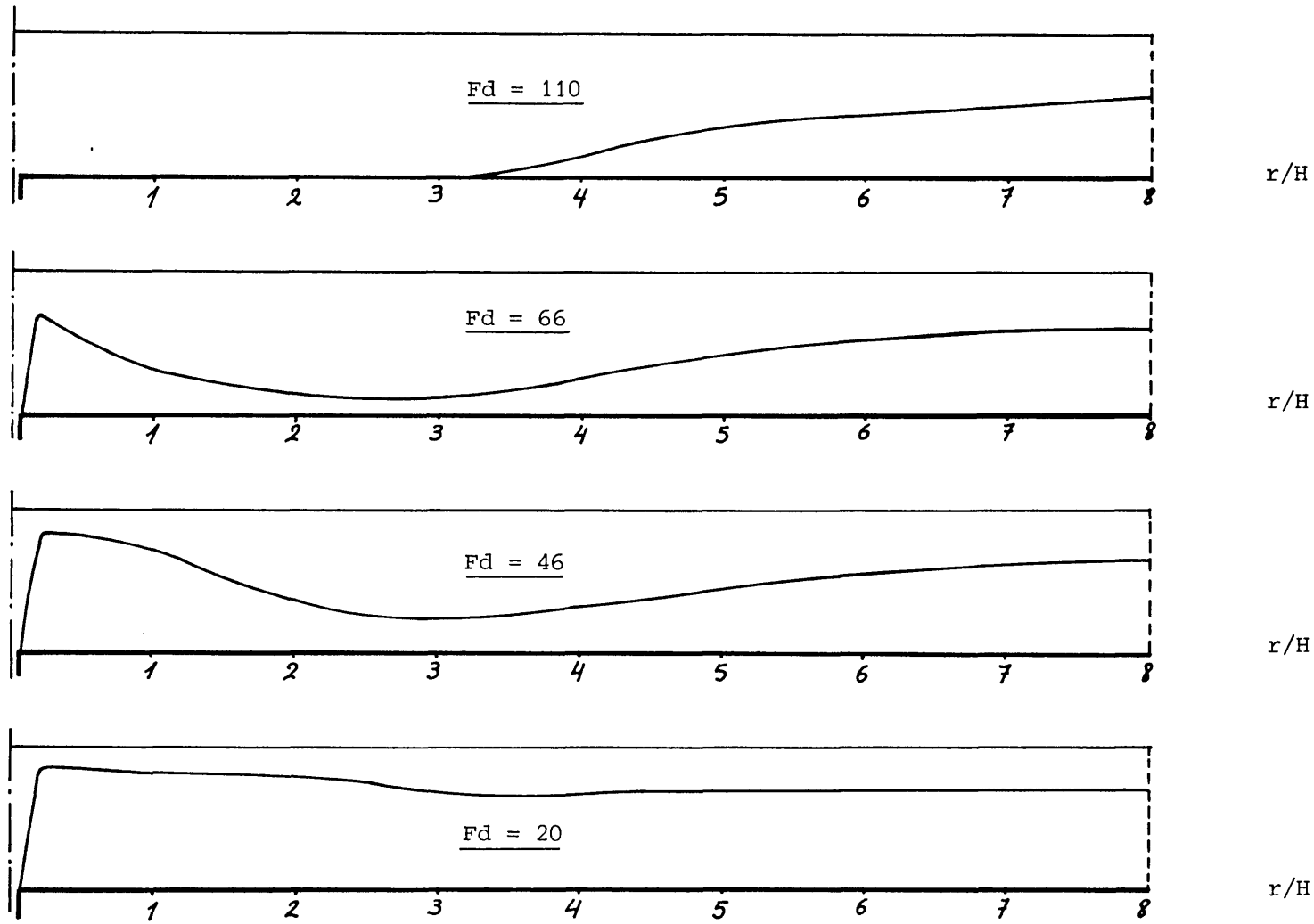


FIGURE 6.20 : Predicted visible interface ($\Delta T/\Delta T_0$ = 3%) for four discharge Froude numbers Fd= 20, 46, 66, 110 and H/D=11.1. Steady-state approach.

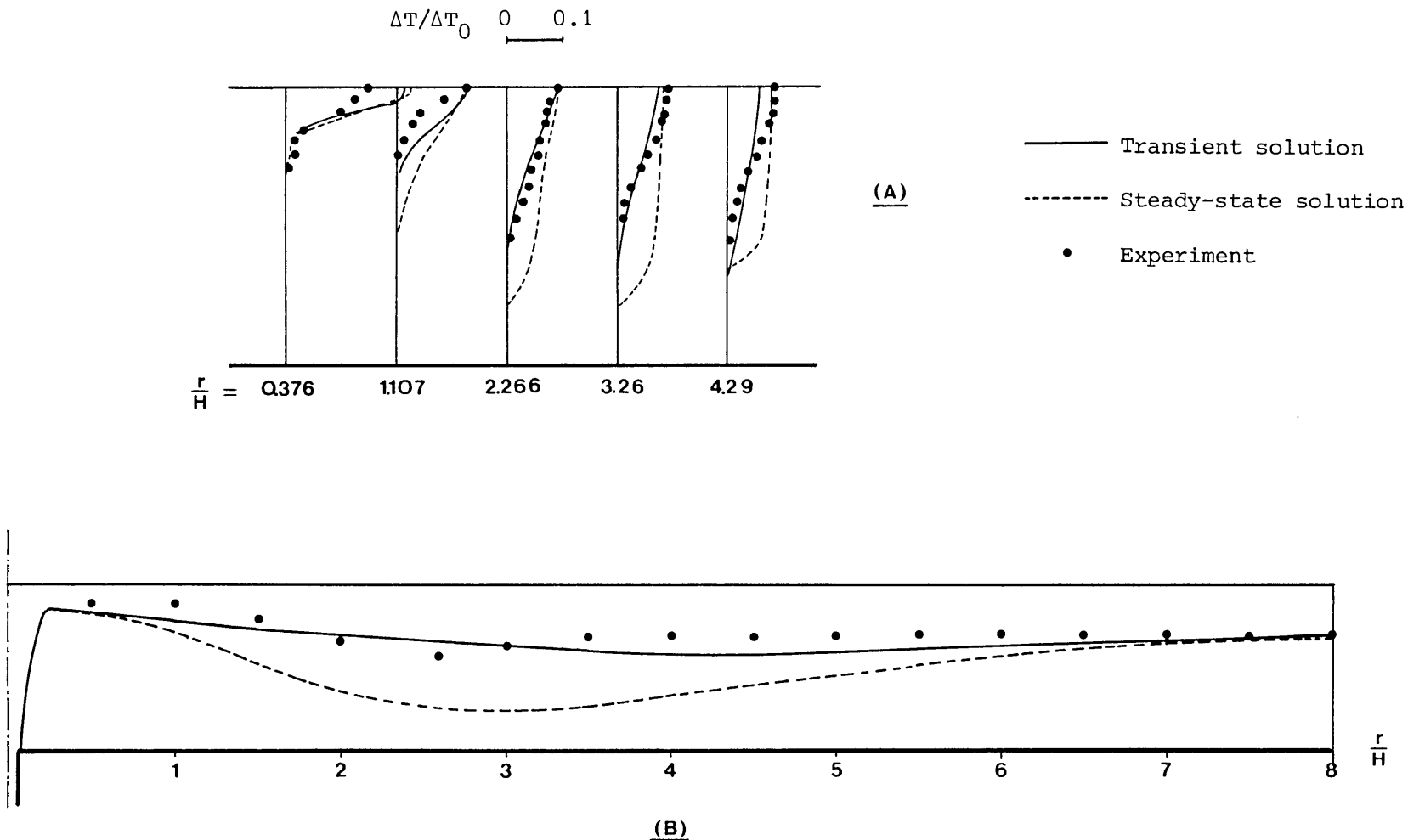


FIGURE 6.21 : Comparison of temperature field predictions with the experimental data H/D=11.1, Fd=46. (A): Temperature profiles, (B): Visible interface.

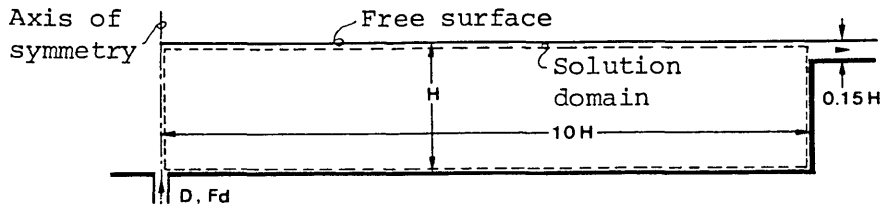
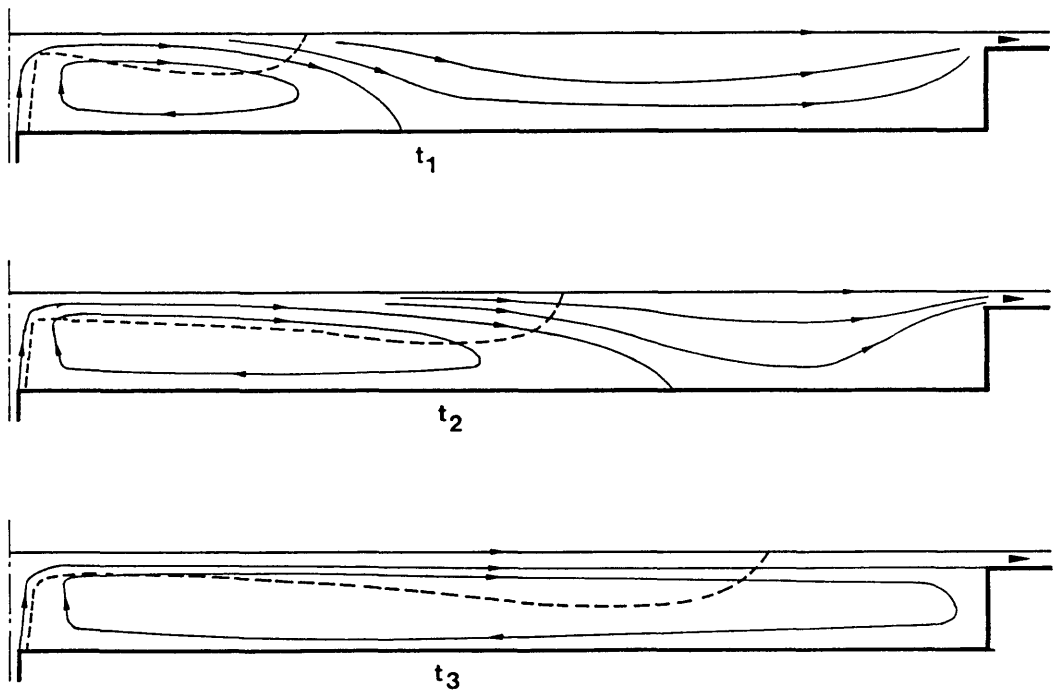


FIGURE 6.22 : Solution domain for the buoyant vertical discharge in shallow water. True transient solution.



_____ Visible interface ($\Delta T/\Delta T_0$=3%)

$t_1 < t_2 < t_3$

FIGURE 6.23 : Vertical buoyant jet in shallow water - stable form. Transient solution. Sketch of the predicted evolution of the flow.

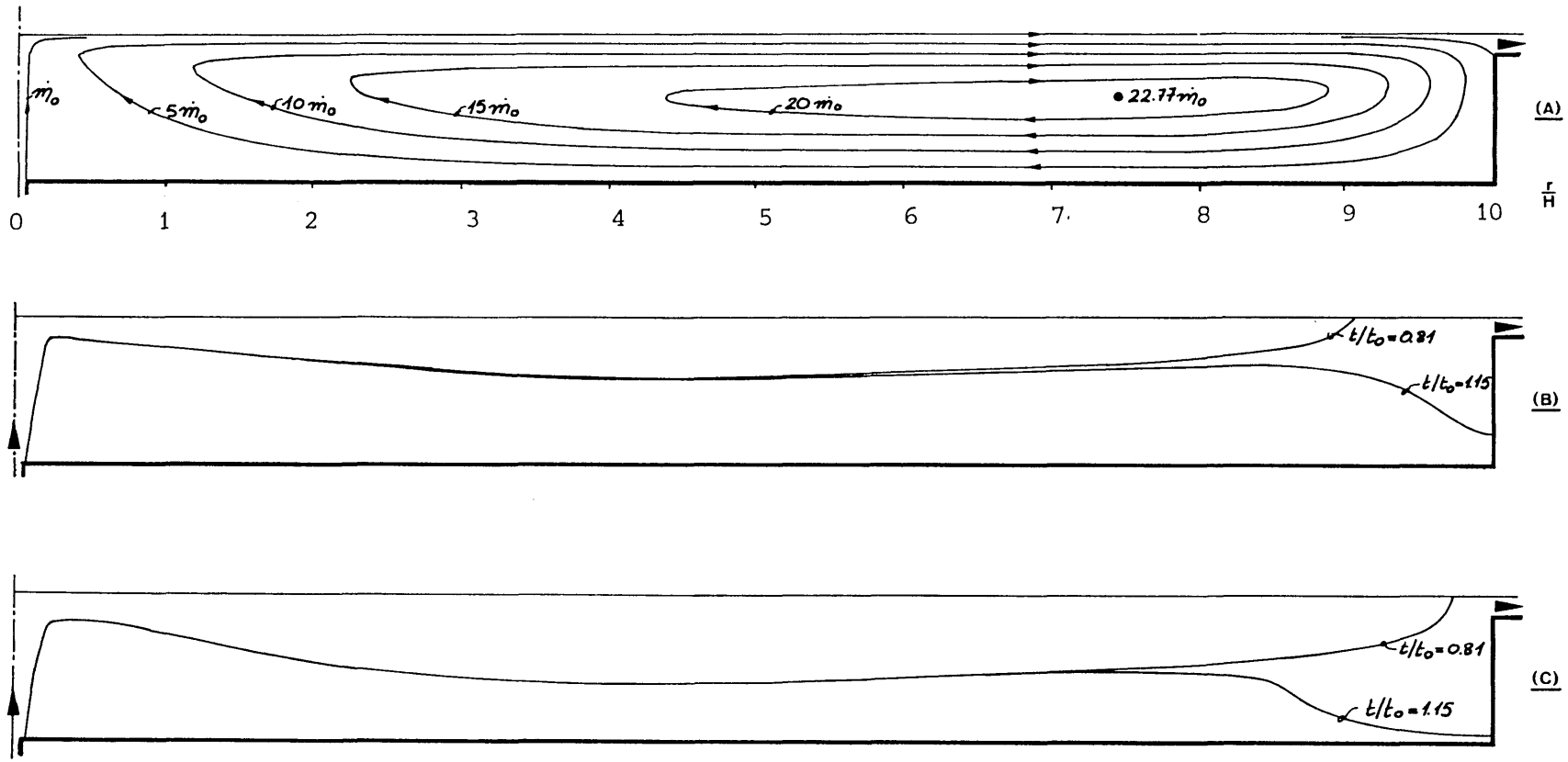


FIGURE 6.24 : Stable discharge H/D= 11.1, Fd=46, transient solution. (A): Streamline pattern at t/t_0=1, (B): Predicted visible interface (locus of points where $\Delta T/\Delta T_0$=3%), (C): Locus of points $\Delta T/\Delta T_0$=1%.

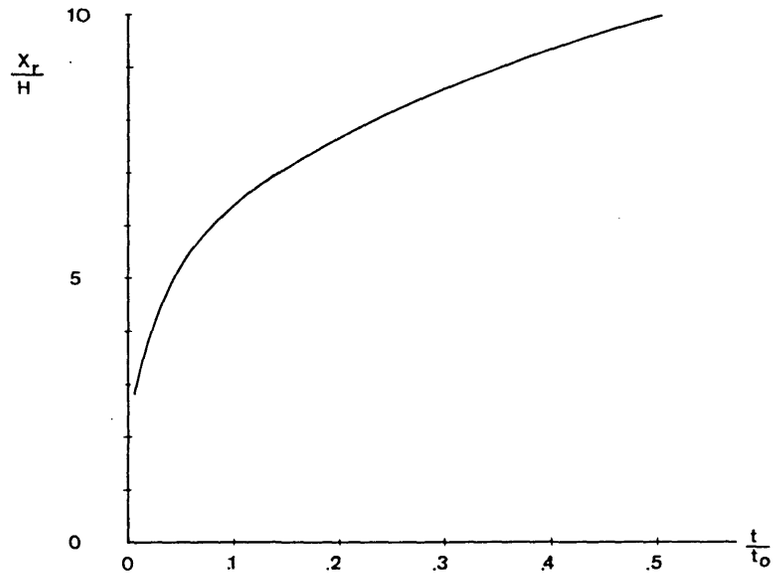
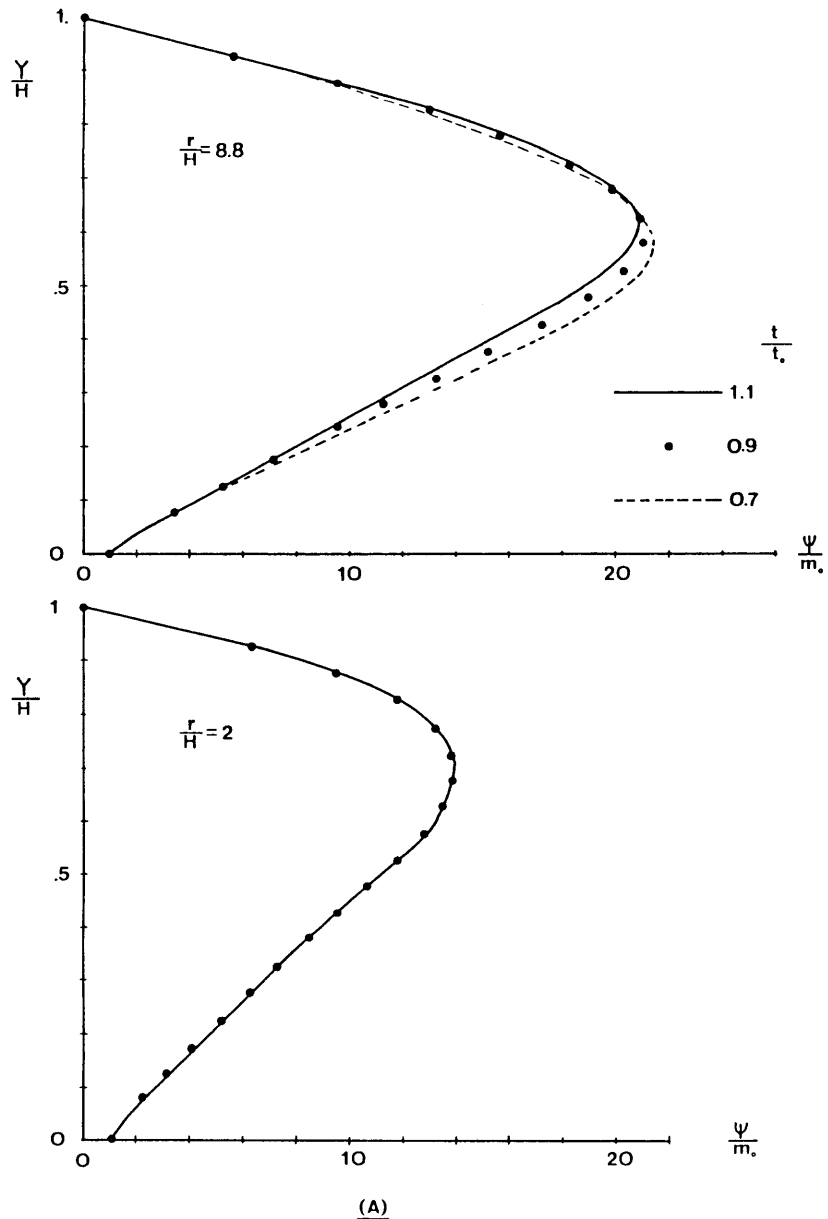


FIGURE 6.25 : H/D=11.1, Fd=46 - transient solution. Reattachment length as a function of time.



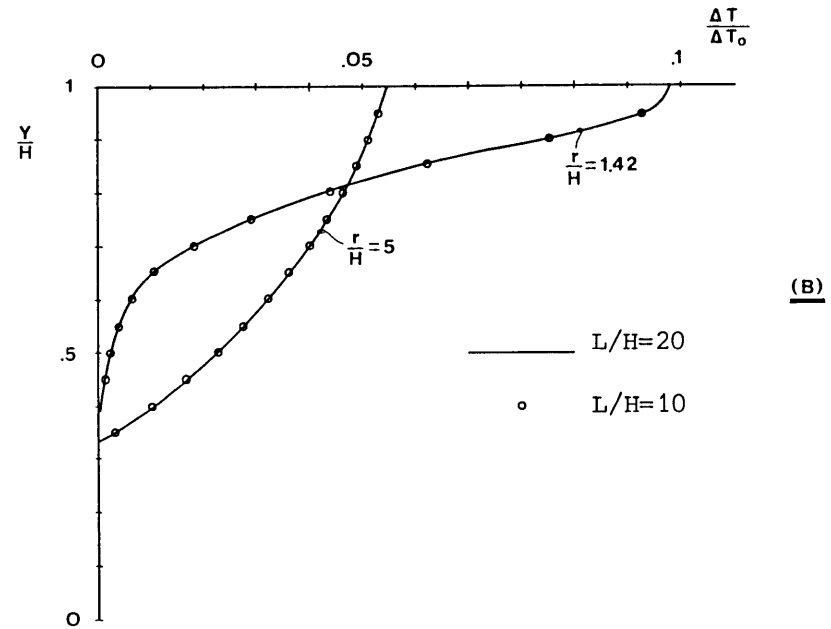


FIGURE 6.26: (A): H/D=11.1, Fd=46. Evolution of the predicted stream function profile at two radial locations (m_0 is the discharge flowrate).
(B): H/D=11.1, Fd=46. The influence of the tank length on the near-field temperature predictions.

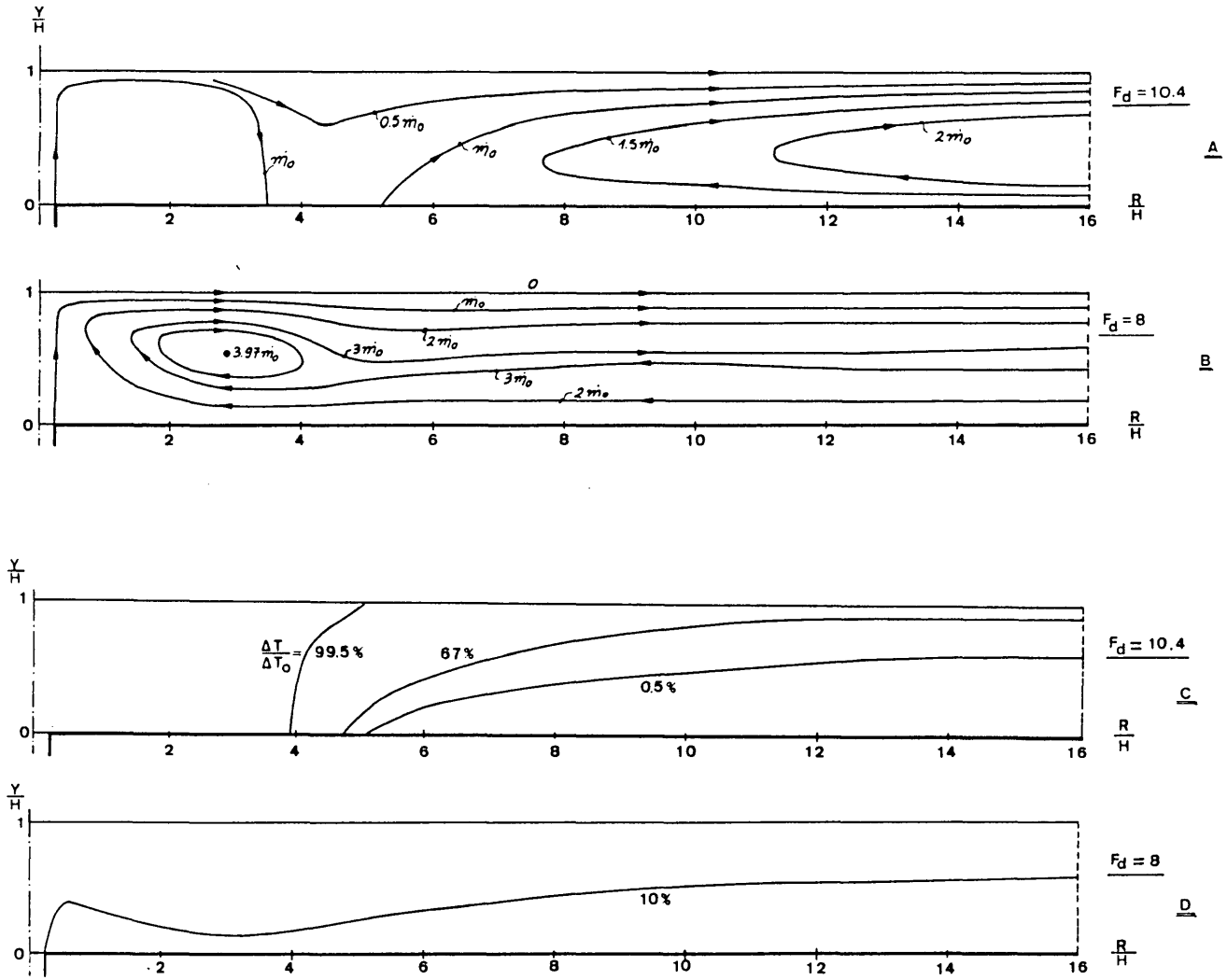


FIGURE 6.27 : Steady-state approach calculations for the geometry H/D=2.2, D=2.54 cm. (A): Fd=10.4, unstable form. Streamline pattern. (B): Fd=8, stable form. Streamline pattern. (C): Fd=10.4. Equal temperature contours. (D): Fd=8. $\Delta T/\Delta T_0$=10% contour.

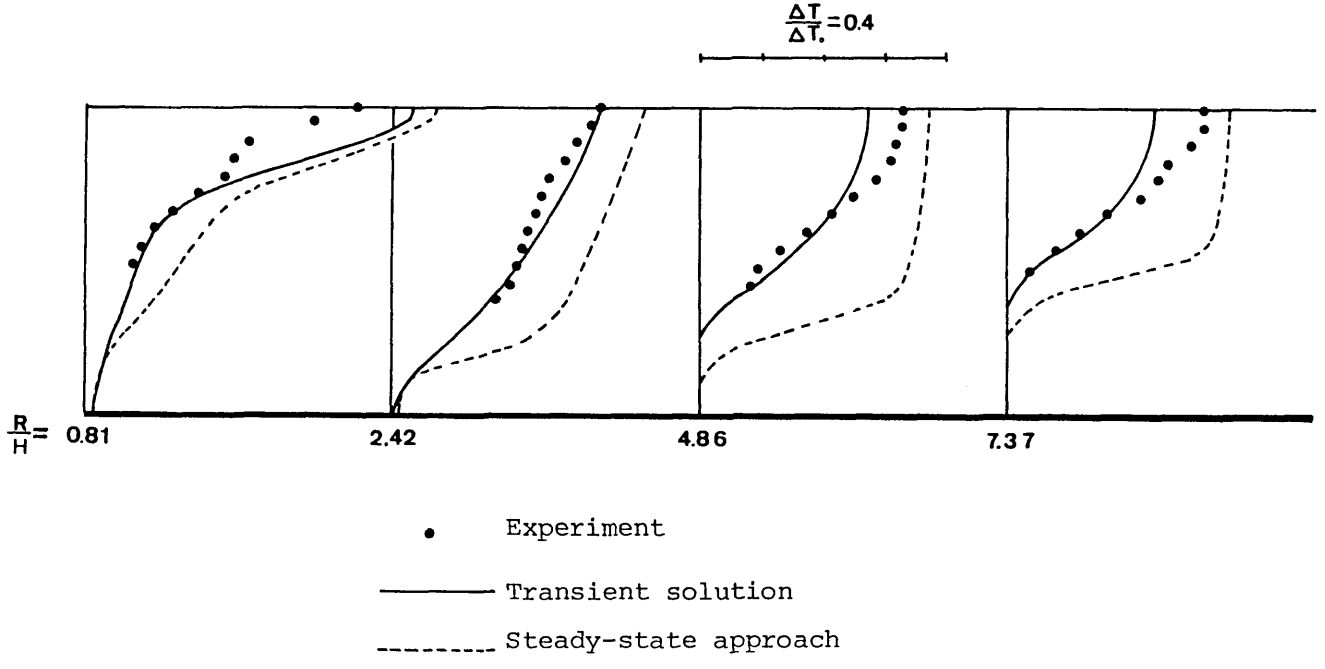


FIGURE 6.28 : Stable configuration Fd=8, H/D=2.2. Temperature field predictions.

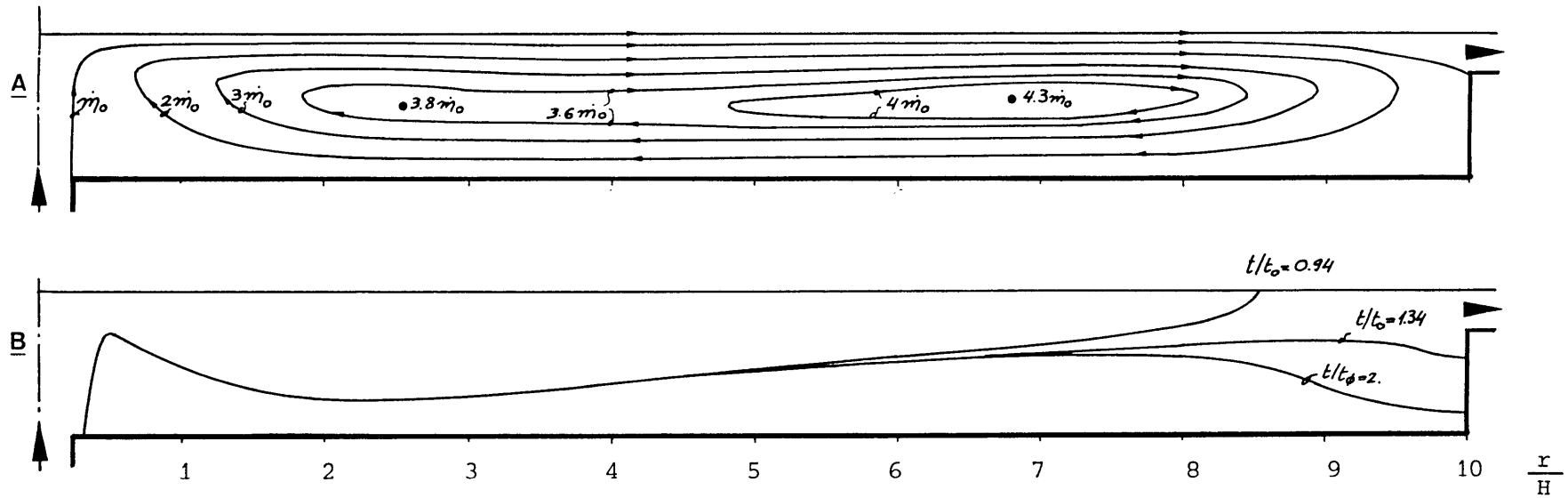


FIGURE 6.29 : Stable discharge, H/D=2.2, Fd=8, transient solution. (A): Streamline pattern at t/t_0=1.34. (B): Locus of points where $\Delta T/\Delta T_0$= 10%.

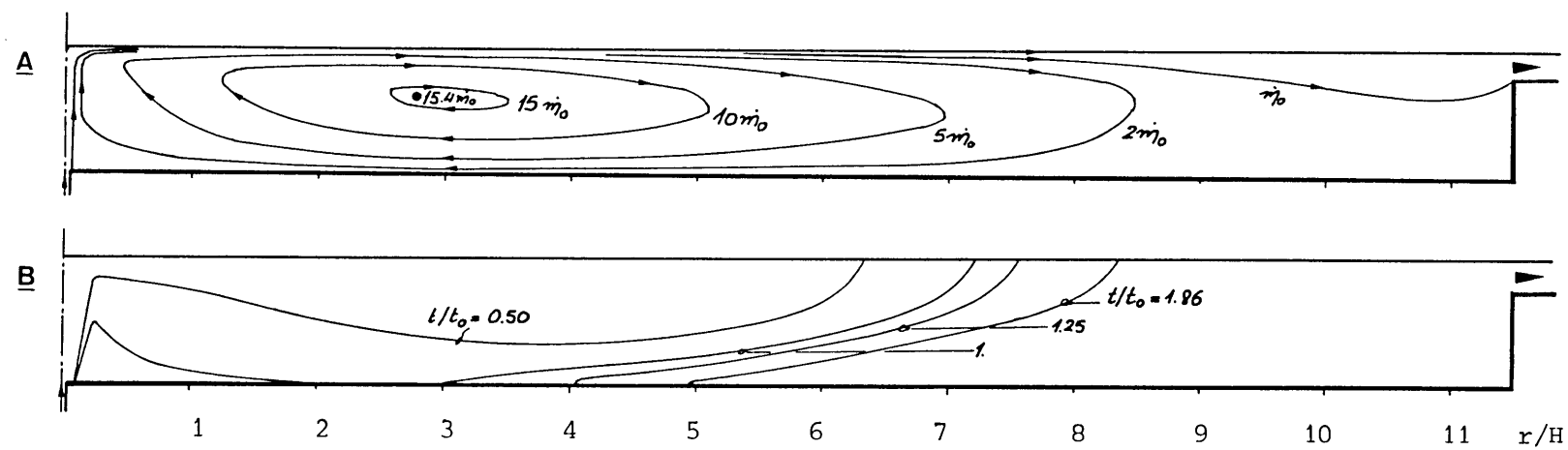


FIGURE 6.30: Unstable discharge, H/D=10, Fd=205 - transient solution. (A): Streamline pattern at t/t_0=1.50, (B): Visible interface ($\Delta T/\Delta T_0$=3%)

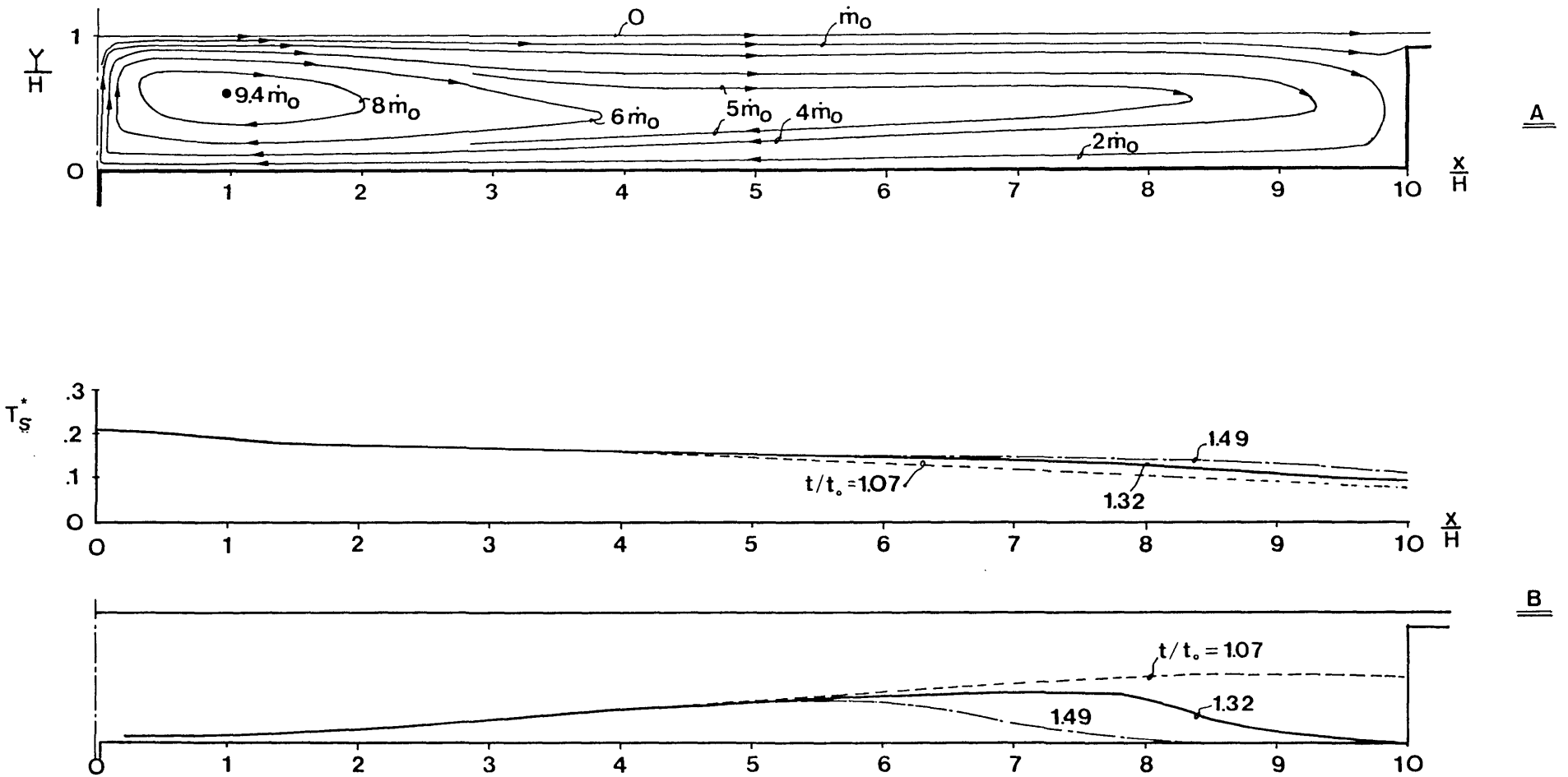


FIGURE 6.31: Unstable discharge H/D=190.6, Fd=80. (A): Streamline pattern at t/t_0=1.17.
(B): Surface temperature and location of the visible interface $\Delta T/\Delta T_0$=3%.
(PLANE GEOMETRY)

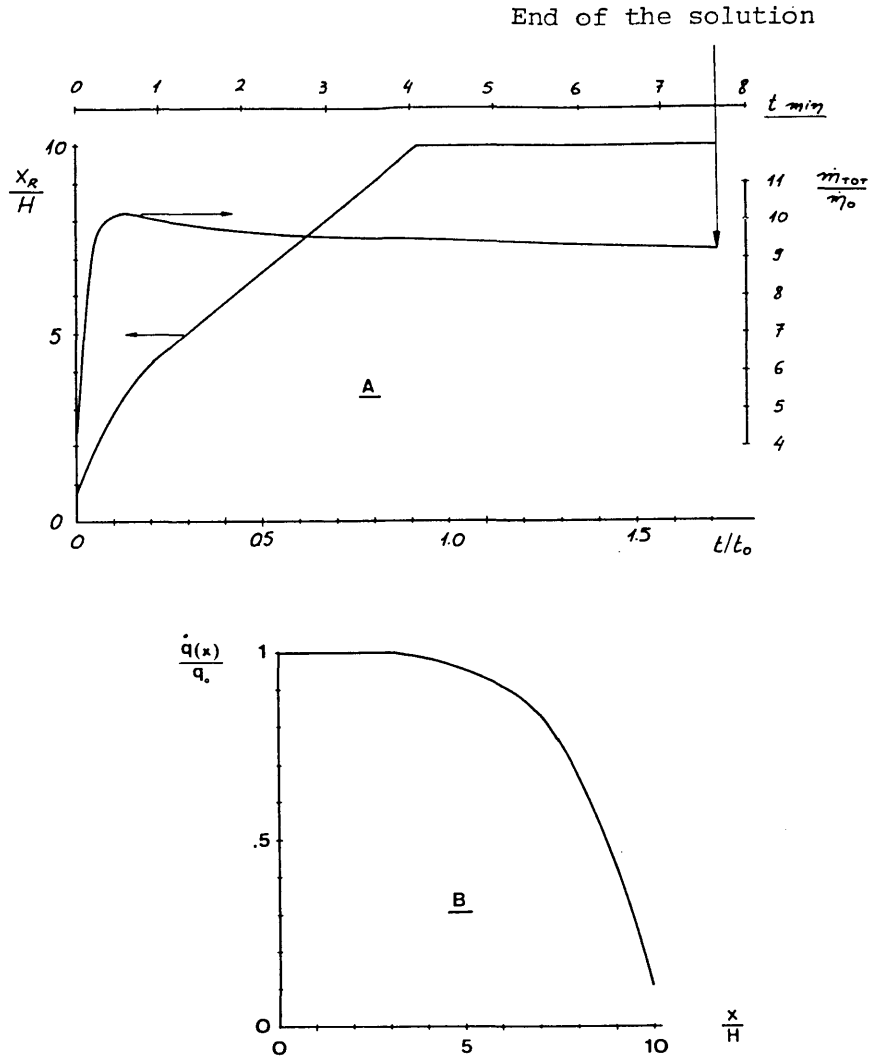


FIGURE 6.32 : Unstable discharge H/D=190.6, Fd=80.(A): Evolution of the solution. Reattachment length (X_R) and total circulation in the tank ($\dot{m}_{TOT}$) as functions of time. (B): Longitudinal heat flux $\dot{q}(x)$ along the solution domain.

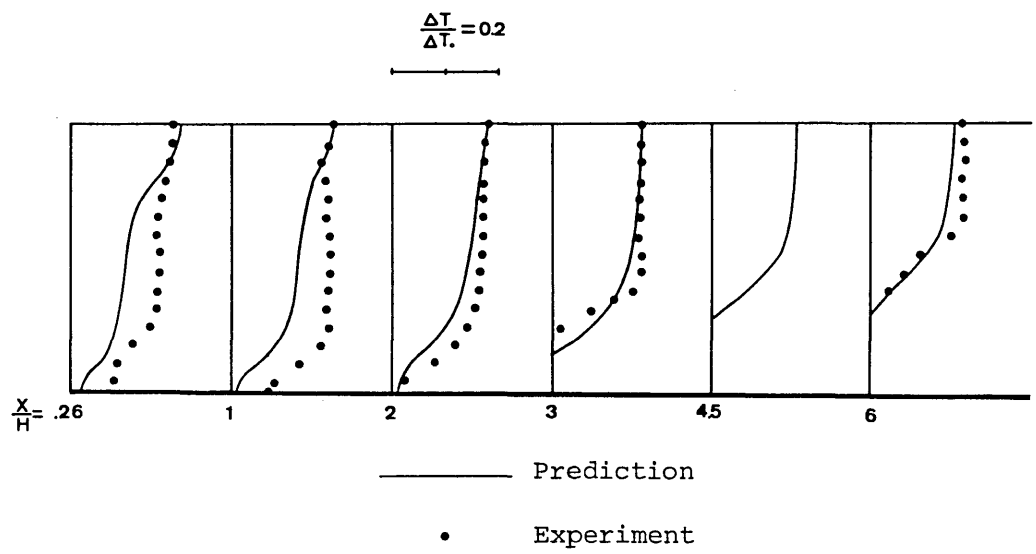


FIGURE 6.33 : Unstable discharge H/D=190.6, Fd=80. Temperature field predictions.

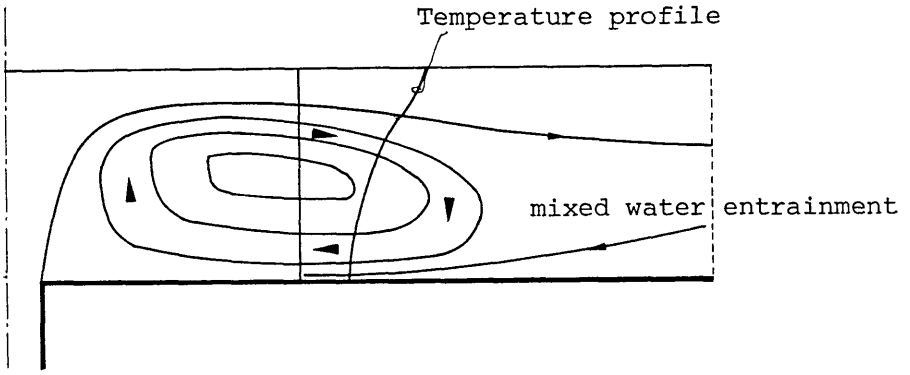


FIGURE 6.34 : Unstable discharge. Mixed water reentrainment within the near-field recirculation and effects on the temperature profile.

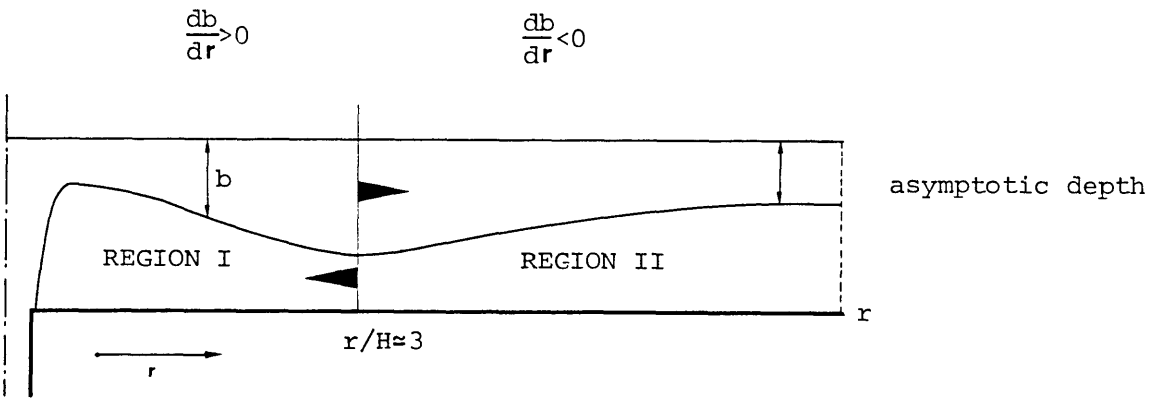


FIGURE 6.35 : Stable discharge. Dye-trace interface shape observed in the experiments

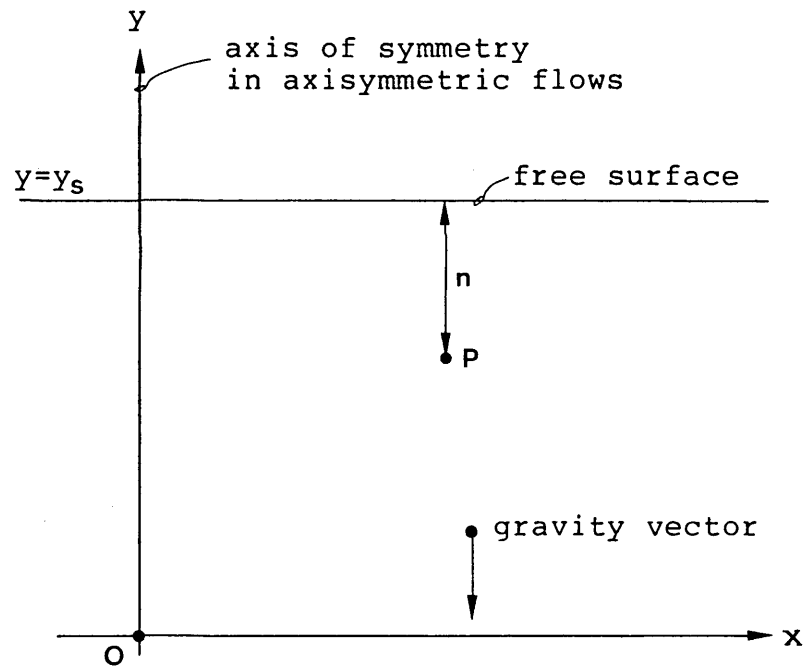


FIGURE A1.1 : Coordinate system

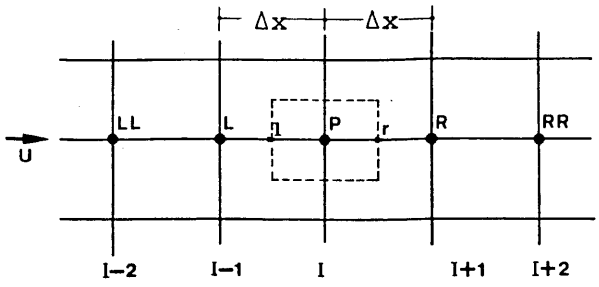


FIGURE A2.1 : Scalar variable control volume.

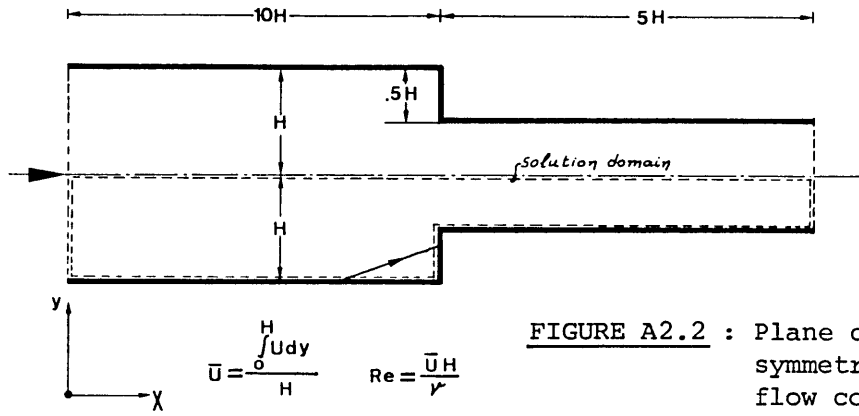
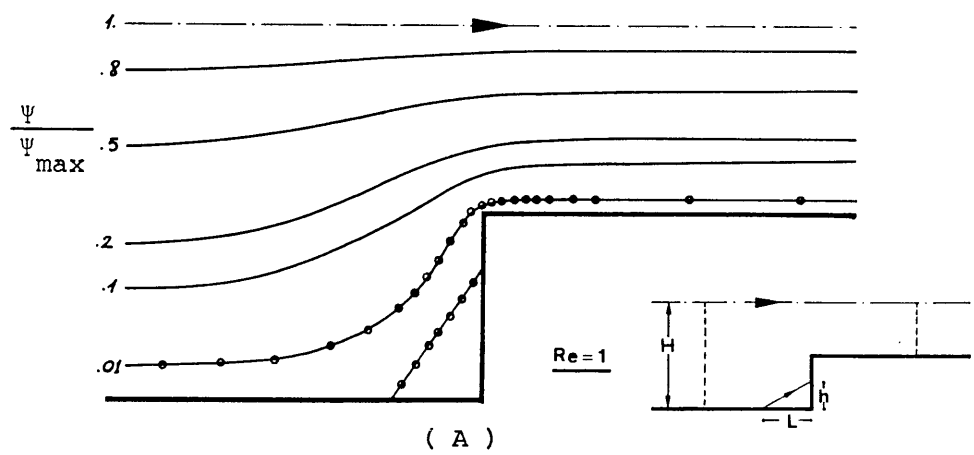


FIGURE A2.2 : Plane channel with a symmetric contraction, flow configuration and solution domain.



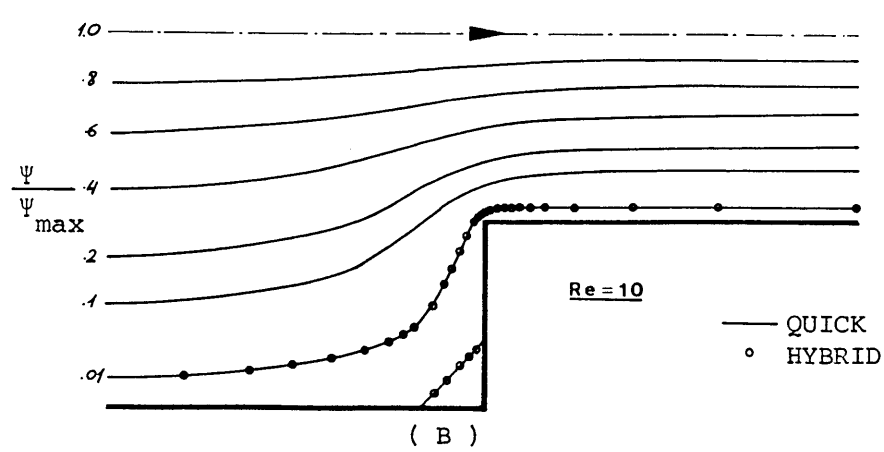


FIGURE A2.3 : Streamline pattern at low Reynolds numbers, (A) Re= 1, (B) Re= 10.

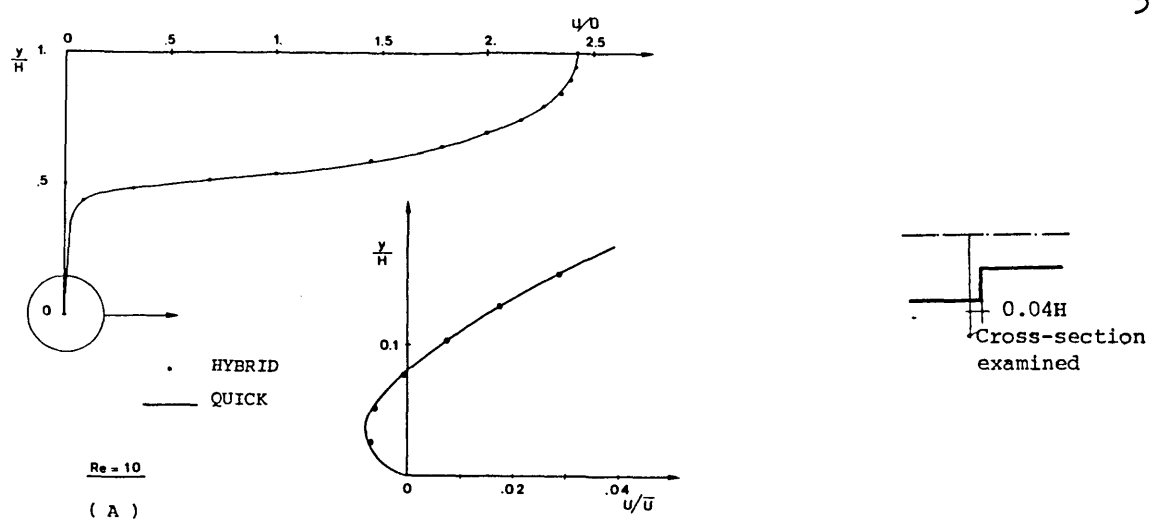
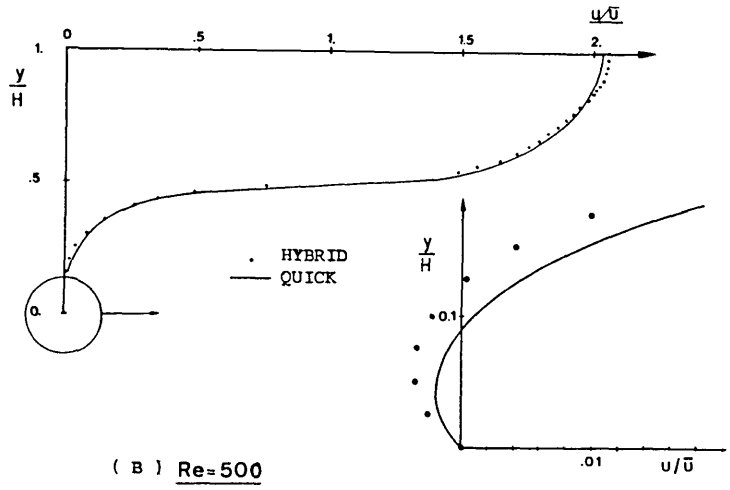


FIGURE A2.4

Axial velocity profiles at two Reynolds numbers. (A) Re = 10 , (B) Re = 500



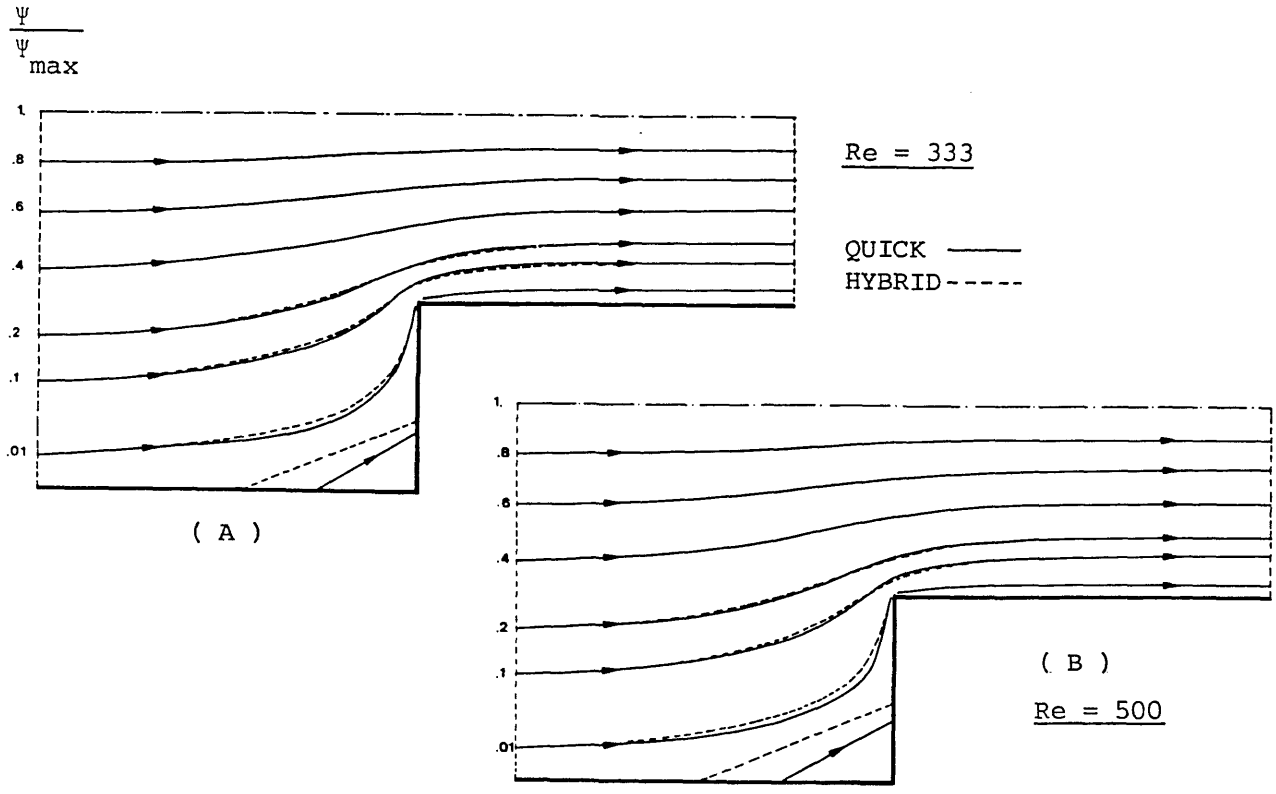


FIGURE A2.5 : Streamline pattern at high Reynolds numbers (A) Re = 333 , (B) Re = 500 .

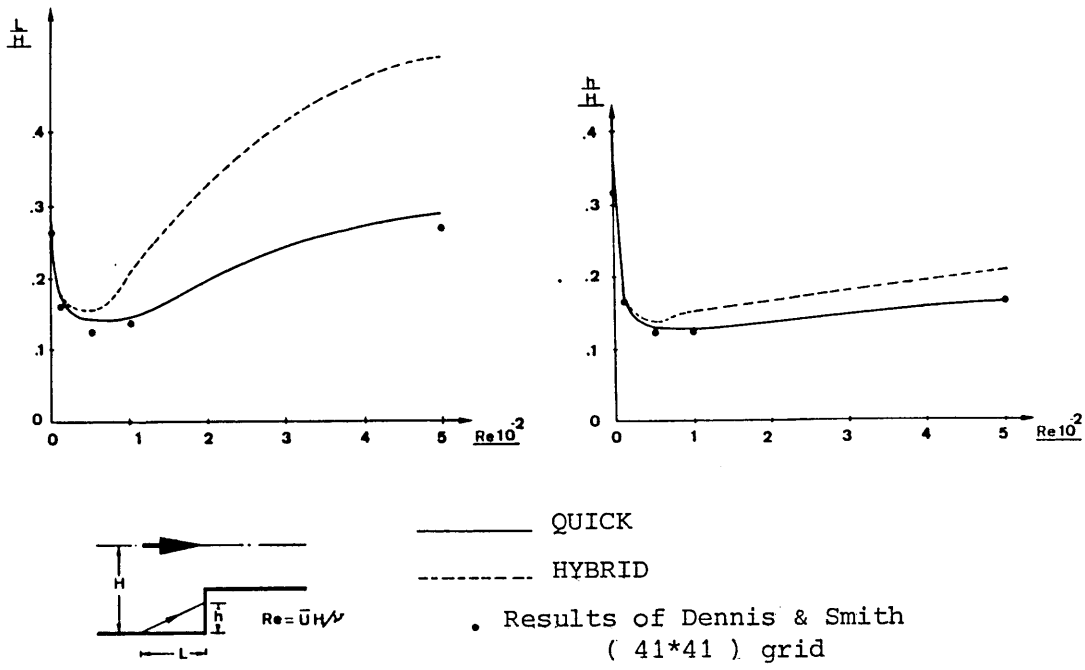


FIGURE A2.6 : Size of the corner eddy, QUICK and HYBRID predictions for a 42*40 grid.

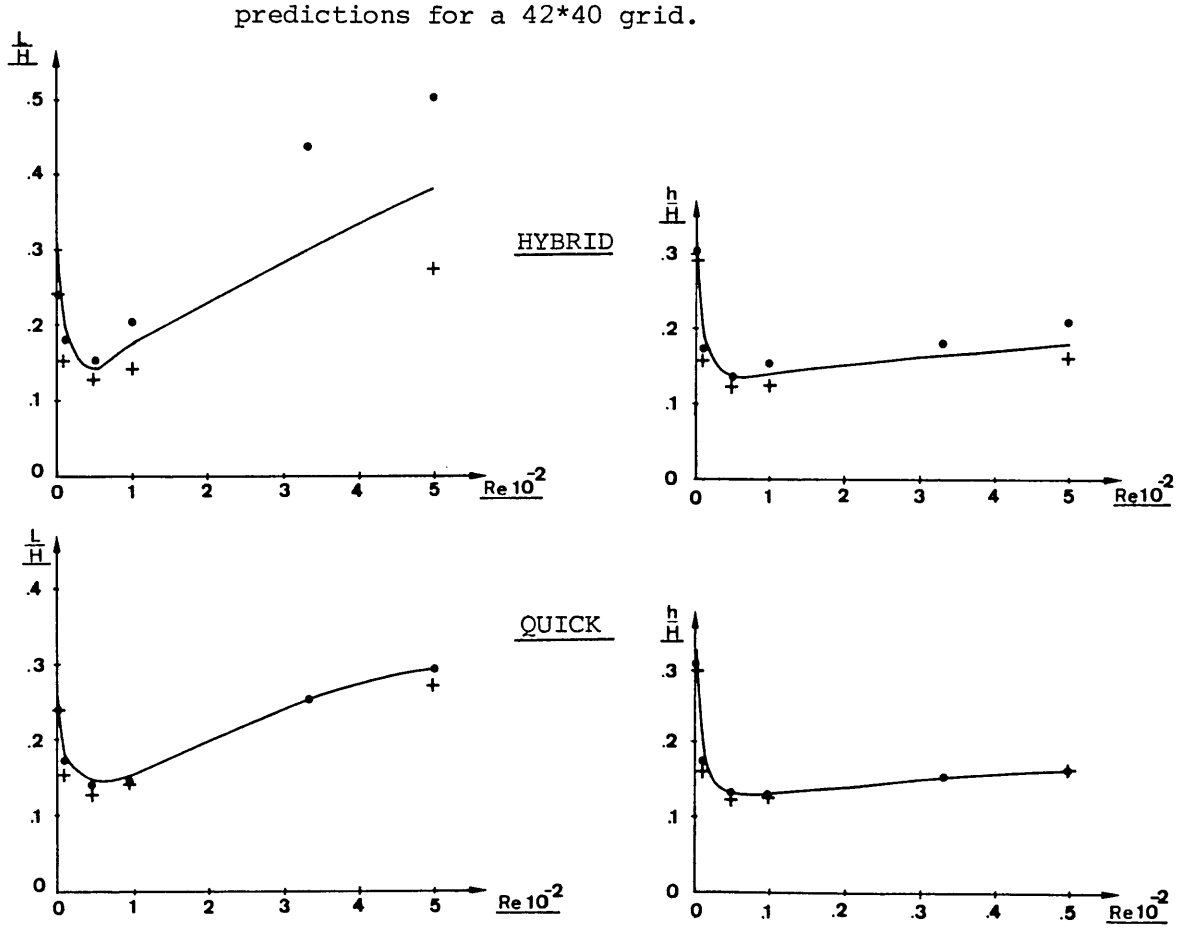
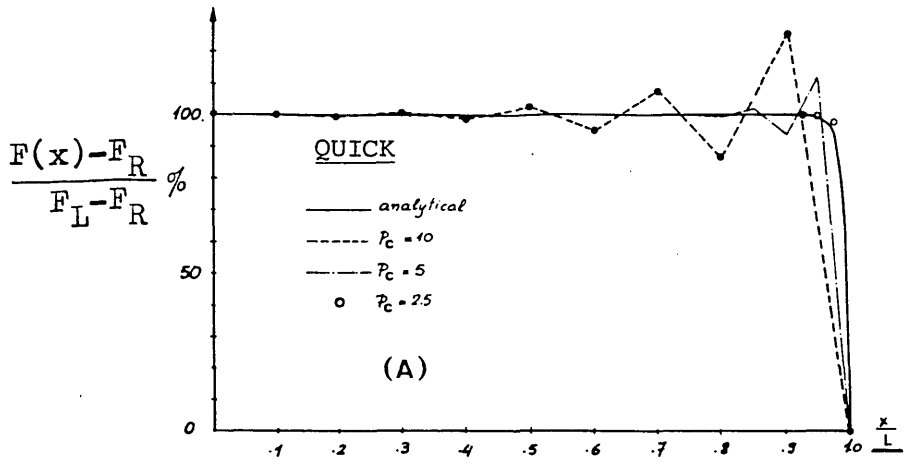


FIGURE A2.7 : Grid independence study, size of the corner eddy.



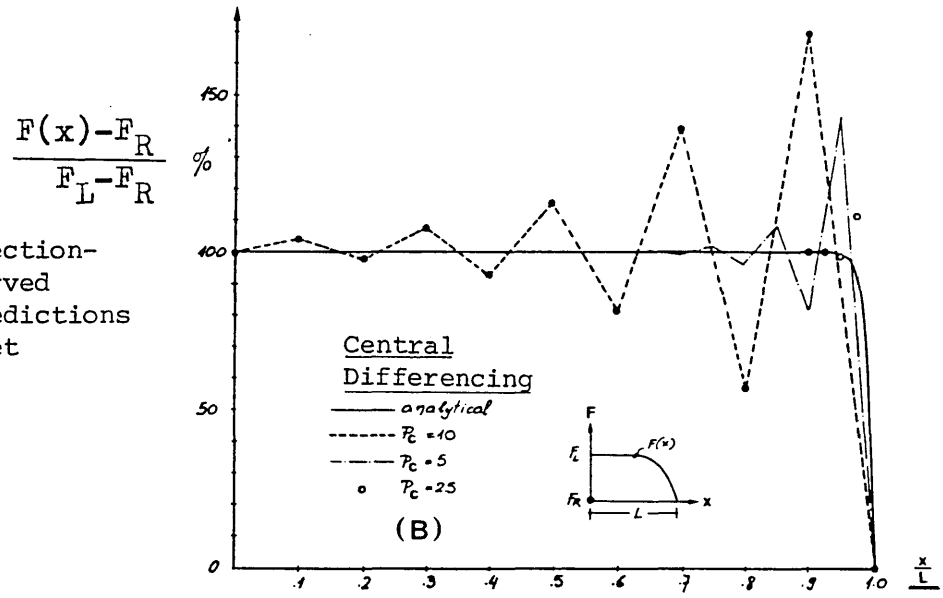


FIGURE A2.8

One-dimensional convection-diffusion of a conserved scalar. Numerical predictions at various Cell Peclet numbers P_c.

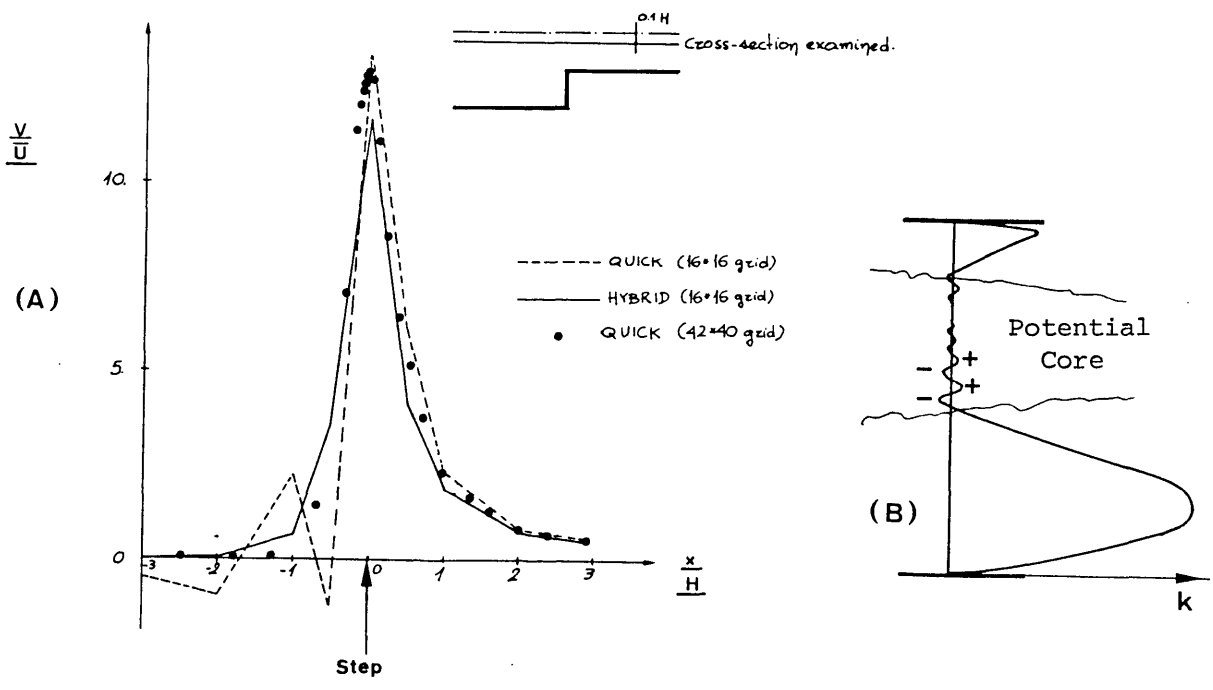


FIGURE A2.9 : Wiggles in QUICK solutions.
(A) Wiggles in the velocity field. Flow in plane channel with a symmetric contraction. (B) Wiggles in the turbulence energy field. Turbulent flow in a channel with a one-sided step.

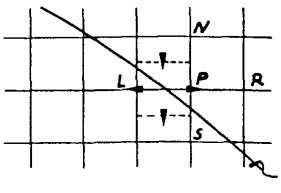
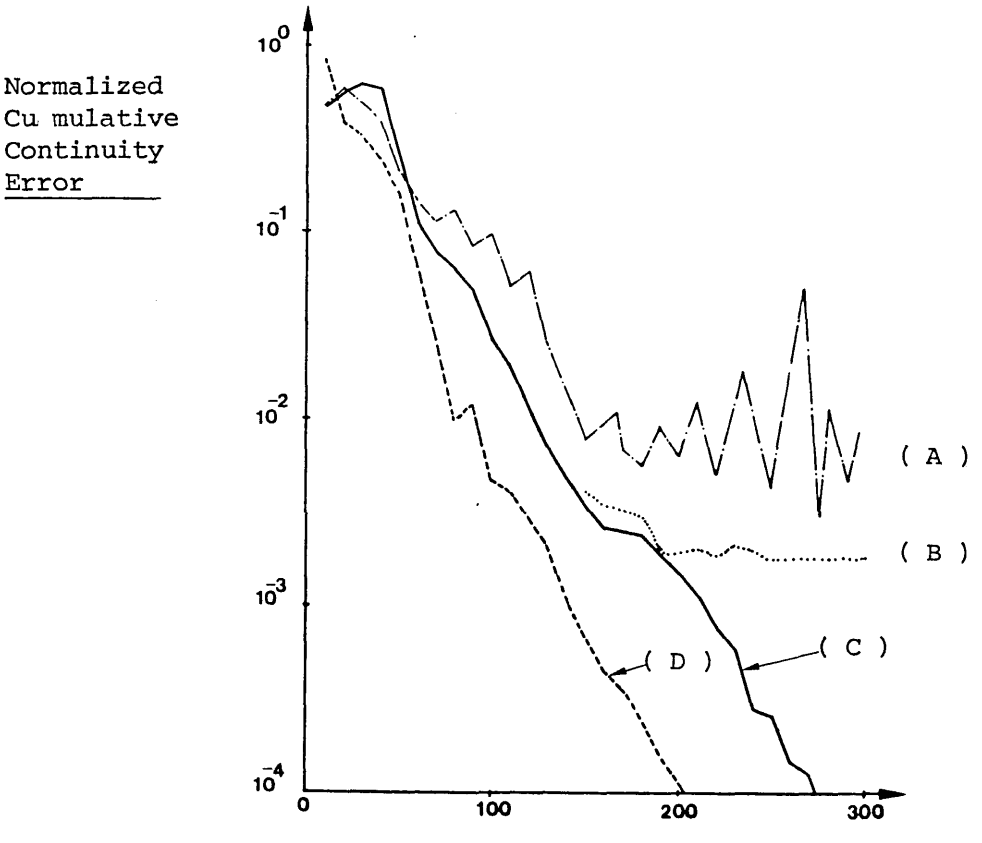


FIGURE A2.10 : U-velocity control volume.



QUICK : (A) $P_{k\varepsilon} = 10^{6}$, (B) $P_{k\varepsilon} = 10^{3}$, (C) $P_{k\varepsilon} = 5$

HYBRID : (D)

FIGURE A2.11 : Convergence rate of the solution for the flow in a plane channel with a one-sided step. k-ε model, 21*21 grid. $P_{k\varepsilon}$ is the value of the limiting cell Peclet number where the shift QUICK - UPWIND took place.

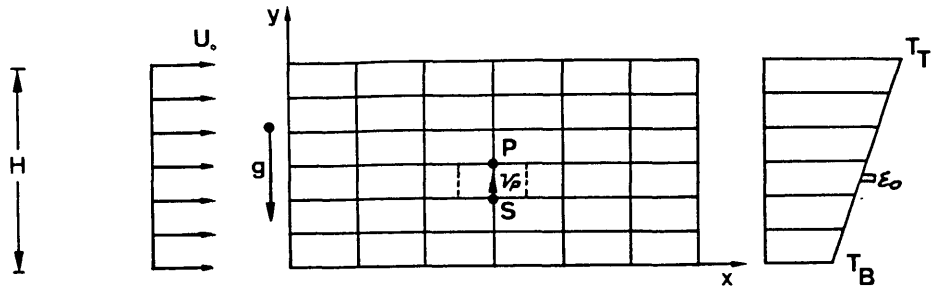


FIGURE A3.1: Horizontal convection with stable stratification.

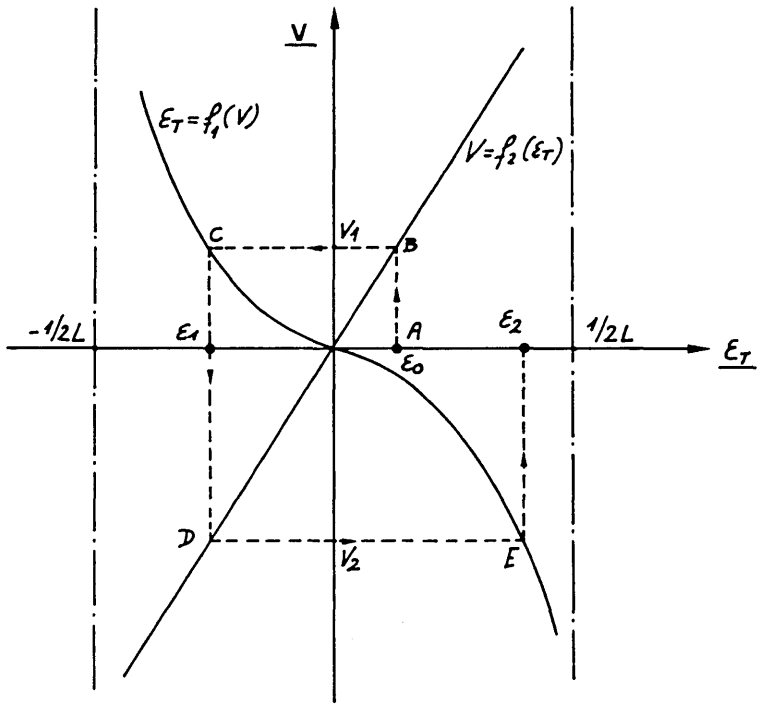
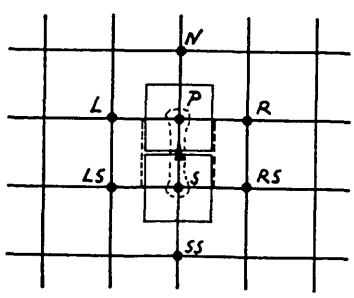


FIGURE A3.2 : Horizontal convection with stable stratification. Temperature and momentum equations ; diverging iteration path.

FIGURE A3.3

Local simultaneous solution of the vertical momentum and temperature equations.



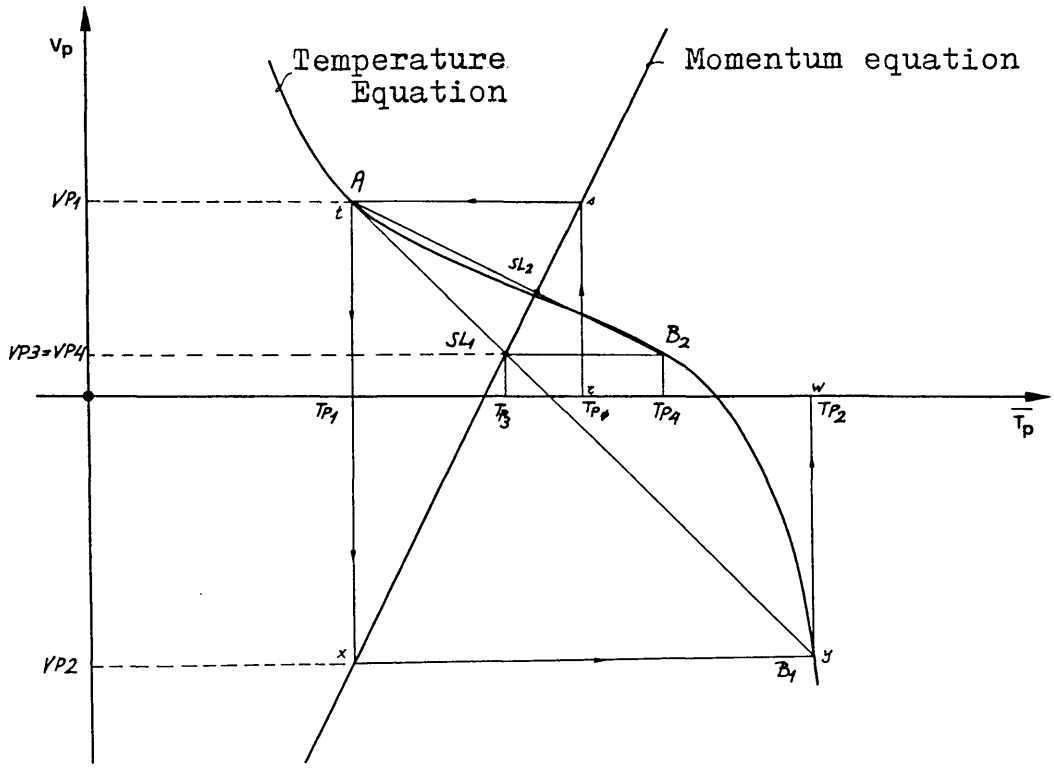
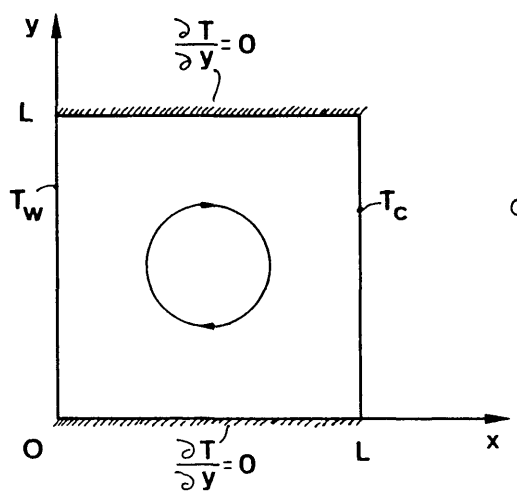


FIGURE A3.4 : Simultaneous solution of momentum and temperature equations. The Newton-Raphson method.



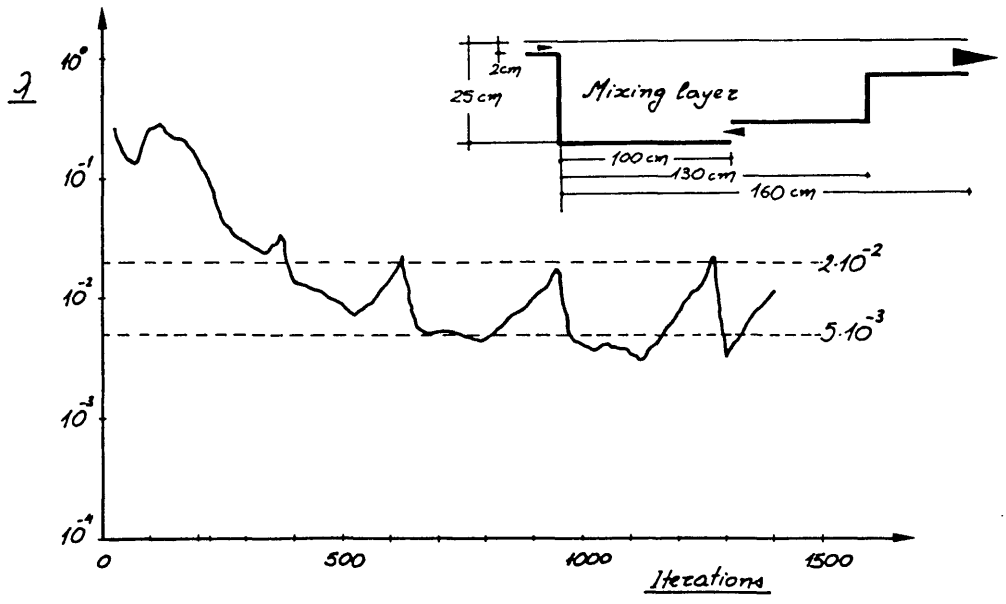
$$Gr = \frac{L^3 \beta g \, (T_w - T_c)}{\nu^2}$$

FIGURE A3.5 : The buoyancy driven square cavity flow. Solution domain and boundary conditions.



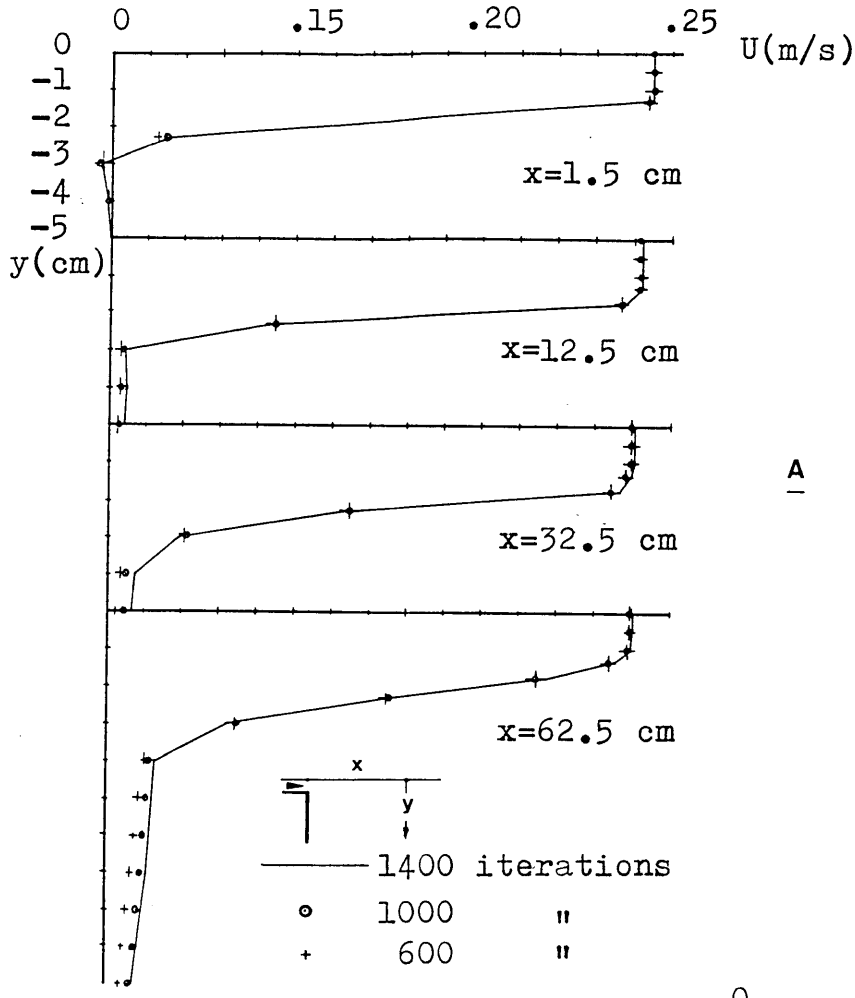
λ : Normalized cumulative continuity error.

FIGURE A3.6 : Convergence rate of buoyant and non-buoyant solutions.
(A) : Non-buoyant flow, Static under-relaxation $r_U=r_V=0.15$.
(B) : Buoyant flow , internal hydraulic jump , False-transient solution.
(C) : Buoyant flow , internal hydraulic jump , Static under-relaxation , $r_U=r_V=0.15$.

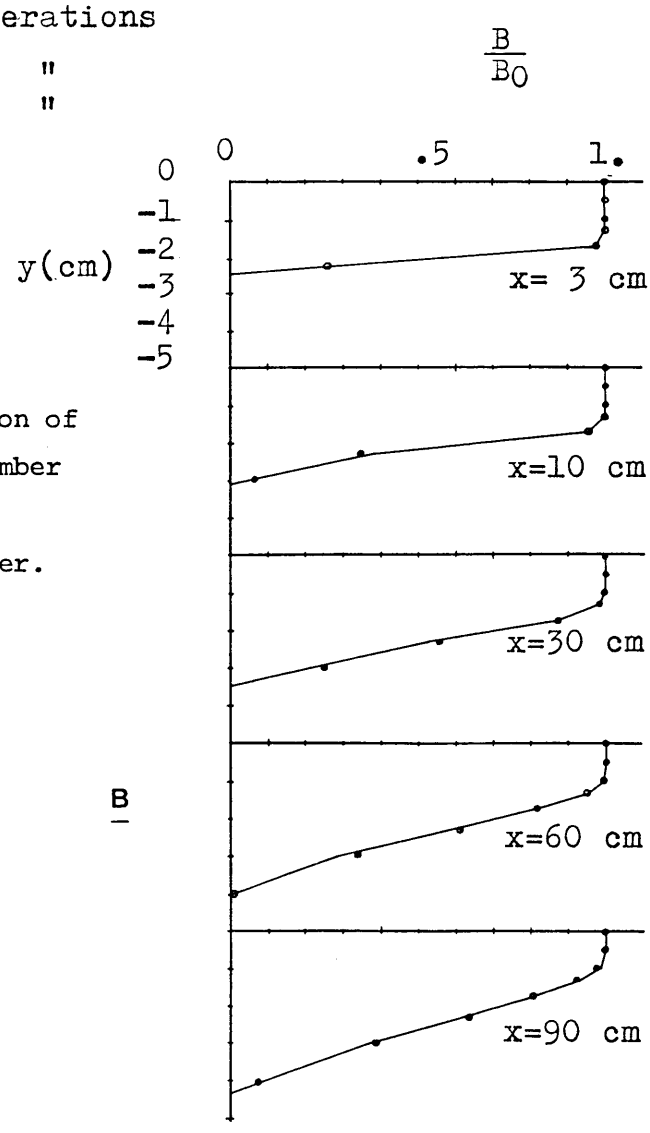


λ : Normalized cumulative continuity error.

FIGURE A3.7 : Mixing layer , $F_d=2.3$. Static under-relaxation $r_U=r_V=.15$



A



B

FIGURE A3.8

Mixing layer F_d=2.3. Evolution of the solution over a large number of iterations.

(A): Velocity across the layer.

(B): Mean buoyancy.

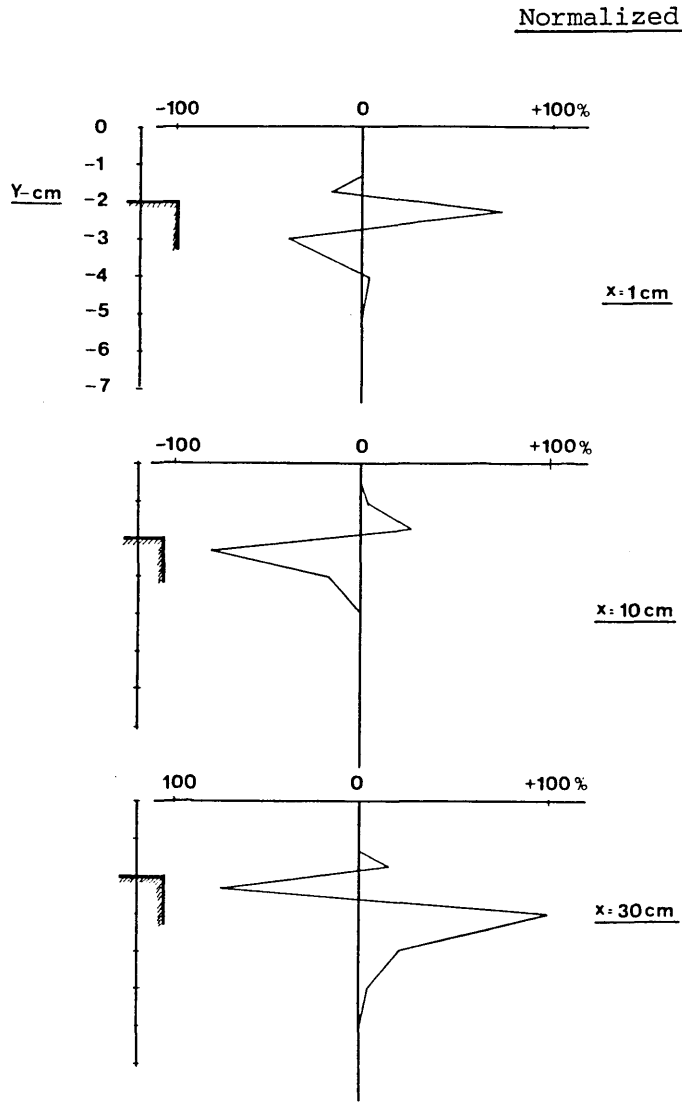


FIGURE A3.9 : Mixing layer , F_d=2.3. Local continuity error distribution. Normalization by the maximum error in the solution domain. (1000th iteration)